Magnetic Resonance Imaging of Hyperpolarised ^{129}Xe Gas in the Human Lungs

(Spine Title: MRI of Hyperpolarised ^{129}Xe)

(Thesis Format: Integrated Article)

by

Xiaojun Xu

Postgraduate PhD in Magnetic Resonance Physics

A thesis submitted in partial fulfilment of the requirements for the degree of doctor of philosophy.

Unit of Academic Radiology

Department of Cardiovascular Science

The University of Sheffield
Sheffield, Yorkshire, United Kingdom.

Co - Authorship

Chapter 3 of this thesis was co-authored by Xiaojun Xu[1], Graham Norquay[1], Steven R. Parnell[1], Martin H. Deppe[1], Salma Ajraoui[1], Ralph Hashoian[2], Helen Marshall[1], Juan Parra-Robles[1], Jim M. Wild[1] [1]Academic Radiology, University of Sheffield, Sheffield, UK [2]Clinical MR Solutions, and is published in Magnetic Resonance in Medicine (2012 Jan 31. doi: 0.1002/mrm.24190).

Chapter 4 of this thesis was co-authored by Xiaojun Xu[1], Martin H Deppe[1], Nicola De Zanche[2,3], and Jim M. Wild[1] [1]Academic Radiology, University of Sheffield, Sheffield, South Yorkshire, United Kingdom, [2]Department of Medical Physics, Cross Cancer institute and [3]Department of Oncology, University of Alberta, Edmonton, Canada, and is being prepared for submission to Magnetic Resonance in Medicine.

Chapter 5 of this thesis was co-authored by Xiaojun Xu[1], General Leung[1], Graham Norquay[1], Helen Marshall[1], Juan Parra-Robles[1], and Jim M. Wild[1] [1]Academic Radiology, University of Sheffield, Sheffield, United Kingdom, and is being prepared for submission to Magnetic Resonance in Medicine (MRM).

To my mother Hongyu, who always wanted the best for me and provided all the love and discipline a child needed to become independent and strong willed.

To my father Zhuyun, who held the gentlest heart, always supported my decisions without questioning.

Acknowledgments

This thesis is made possible because of the support of many to whom I would like to say thank-you. The first person I would like to thank is of course my PhD supervisor, Prof. Jim Wild, who gave me the opportunity to come to Sheffield and join a very knowledgeable and welcoming group and guided me in the past three years with just the right amount of freedom to allow me to explore the field of hyperpolarised xenon imaging. Jim is very resourceful and his expertise in MRI provided a solid ground I can always count on. Even when he is extremely busy, he will always find the time if I needed to ask or communicate about a certain project. Alongside him, I would like to thank my co-supervisor, Dr. Juan Parra-Robles, whose expertise on diffusion imaging is very fascinating and who is always available to help me with my questions. There are also two graduated students, Martin Deppe and Salma Ajraoui, I would like to acknowledge for teaching me many things on the 1.5 T and 3 T scanners respectively from their own experiences. Next, I'd like to thank my colleague Graham Norquay, , who spent many, many hours collecting xenon, which made all the imaging possible, and Helen Marshall, who scanned for me when I needed her to. I would like to thank every single member in the group, to everyone who had volunteered for imaging for me on many occasions, and are much more than just colleagues as they made my experience in Sheffield in the past three years memorable.

I would also like to acknowledge a few other people collaborating with the group: Fraser Robb, for helping and letting us use equipment at the GE plant in Cleveland, Ohio; Nicola deZanche at the University of Alberta, for RF simulations which helped me with the iterative tuning of the RF coil project. Last, but not least, I'd like to thank everyone in the Unit of Academic Radiology at the Royal Hallamshire Hospital in Sheffield for giving me a wonderful working environment, and friendly help whenever I needed.

Table of Contents

List of Tables

List of Abbreviations

2D	2 dimensional
3D	3 dimensional
ADC	Apparent diffusion coefficient
COPD	Chronic obstructive pulmonary disease
CT	Computed Tomography
FEV_1	Forced expiratory volume in one second
FID	Free induction decay
Fig.	Figure
FOV	Field of view
FVC	Functional vital capacity
HNG	Hyperpolarised noble gas
HU	Hounsfield unit
IFT	Inverse Fourier transform
MR	Magnetic resonance
MRI	Magnetic resonance imaging
NMR	Nuclear magnetic resonance
ROI	Region of interest
SNR	Signal-to-noise ratio
SEOP	Spin exchange optical pumping
SPECT	Single photon emission computed tomography
T_1	Longitudinal relaxation time
T_2	Transverse relaxation time
TE	Echo time
TR	Repetition time

Thesis Abstract

Chapter 1: Theoretical Background of Hyperpolarised Gas Magnetic Resonance Imaging

Nuclear Magnetic Resonance (NMR) forms the basis of many scientific applications from studying protein structures in biochemistry to imaging just about every body part possible using magnetic resonance imaging (MRI). This chapter provides the background to the physics and theory in this thesis. In Section 1.1, the physics of MRI is briefly explained. In Section 1.2, an overview and introduction to basic MRI hardware and radio-frequency (RF) engineering construction will be discussed. Lastly, a brief summary of hyperpolarisation is summarised in Section 1.3.

Chapter 2: Advances in Diagnostic Methods for Respiratory Diseases Using Hyperpolarised Gas Magnetic Resonance Imaging

In this chapter, imaging techniques for respiratory diseases using hyperpolarised ^{3}He and ^{129}Xe will be reviewed. Respiratory disease is the fourth leading cause of death in the world. The incidence is increasing annually and it is predicted to become the third leading cause of death in a decade. Chronic obstructive pulmonary disease (COPD) is the most common respiratory disease, and displays one or a mix of symptoms including chronic bronchitis and asthma in the larger airways, as well as terminal airways and alveolar diseases like emphysema. There are other types of respiratory diseases such as restricted lung disease that manifest mostly in pulmonary cystic fibrosis (CF), respiratory tract infection, as well as cancer and tumours in the lungs. Scientists have been searching for early detection and diagnostic methods that have regional sensitivity to early signs of lung disease to help diagnose and treat the significant increase in patients with respiratory disease, as well as lowering the financial burden to the health system.

Chapter 3: Imaging of Hyperpolarised gas phase ^{129}Xe in lung MRI – B_0 field strength comparisons at 1.5 T and 3 T

For hyperpolarised gas MRI to be a viable imaging modality for lung diseases, it needs to be readily implemented on clinical MRI systems. In Chapter 3, the signal-to-noise ratio of hyperpolarised ^{129}Xe gas human lung magnetic resonance imaging was compared at 1.5 T and 3 T, the two standard clinical MRI field strengths. Experiments were performed at both B_0 fields with quadrature double Helmholtz transmit–receive chest coils of the same geometry with the same subject loads. Differences in sensitivity between the two field strengths were assessed from the signal-to-noise ratio of multi-slice 2D ^{129}Xe ventilation lung images obtained at the two field strengths with a spatial resolution of 15 mm × 4 mm × 4 mm. There was a systematically higher signal-to-noise ratio observed at 3 T than at 1.5 T by a factor of 1.25. Mean image signal-to-noise ratio was in the range 27–44 at 1.5 T and 36–51 at 3 T. T_2^* of ^{129}Xe gas in the partially inflated lungs was measured to be 25 ms and 18 ms at 1.5 T and 3 T, respectively. T_2^* of gas in fully inflated lungs was measured to be 52 ms and 24 ms at 1.5 T and 3 T, respectively. We conclude that HP ^{129}Xe MRI is equally feasible at 1.5 T and 3 T, with slightly better signal-to-noise ratio at 3 T.

Chapter 4: An Unshielded Asymmetric Split Insert Quadrature Birdcage Coil for Hyperpolarised ^{129}Xe Lung MRI at 1.5 T

In Chapter 4, the design, construction and testing of an un-shielded asymmetric quadrature insert birdcage body coil for hyperpolarised ^{129}Xe lung imaging on a 1.5 T MR system is presented. For patient comfort, the coil inner space was maximised to fill the magnet bore and the coil detaches into two parts to allow easy access for the subject. The quadrature design creates a circularly polarised B_1 field to maximise the efficiency of the radio-frequency power at the xenon frequency of 17.7 MHz. A conformal mapping

method was used for the birdcage geometry, and the initial capacitor values were calculated using an algebraic method based on the inductance matrix of the coil network. Further empirical iterations in the testing process were needed to compensate for the coupling of the xenon body coil with the proton body coil of the magnet. Two major iterations of a working coil are presented side by side in this Chapter to show improvements made, and the functionality of the coil is demonstrated. The function of the coil is demonstrated with in-vivo ^{129}Xe images and B_1 maps. The transparency of the coil to ^{1}H radio-frequency pulses is demonstrated in this Chapter with ^{1}H images acquired with the ^{129}Xe coil in-situ.

Chapter 5: Apparent T_2^* Measurements of Dissolved-Phase ^{129}Xe in the Human Lungs at 1.5 T and 3 T

^{129}Xe gas is soluble in blood and tissue with a large observable chemical shift that can be utilised to image and quantify gas exchange in the lungs. Knowing the *in vivo* relaxation constants is important in determining sequence parameters for optimal dissolved phase ^{129}Xe imaging. Imaging measurements of the apparent T_2^* of dissolved phase ^{129}Xe in human lungs at 1.5 T and 3 T are presented. T_2^* measurements were made from whole lung coronal slices with a 2D interleaved gradient echo imaging sequence with 2 echo times. The echo times were chosen with consideration of the phase evolution of the signal due to the chemical shift difference between ^{129}Xe dissolved in red blood cells (RBCs) with respect to ^{129}Xe dissolved in plasma. The apparent T_2^* of dissolved ^{129}Xe as measured from the imaging experiments were 1.6 ms and 1.0 ms at 1.5 T and 3 T, respectively. Measurements of the T_2^* made from whole lung spectroscopy gave values of 1.65 ms/ 1.3 ms for RBC/Plasma at 1.5 T in vitro and 1.26 ± 0.03 ms / 0.94 ± 0.04 ms for RBC/Plasma respectively at 3 T in vivo. Whereas the transverse relaxation time is long for gas phase xenon (see Chapter 3), dissolved-phase ^{129}Xe T_2^* is on the order of 1 ms, which is

extremely short and as such faster imaging techniques utilising short echo times must be adopted to effectively image dissolve ^{129}Xe *in vivo*.

Chapter 6: Summary and Future Work

The final Chapter of this thesis consists of the following sections: in Sections 6.1 to 6.3, ongoing projects will be described and discussed, and section 6.4 of this Chapter serves as a summary of this thesis. Section 6.1 is an extension of Chapter 4, as a clinical 8 channel array proton chest coil was retuned to perform as a receive array in combination with the asymmetrical birdcage body coil. In Section 6.2, a methodology is under investigation as we imaged simultaenously both the gas-phase ^{129}Xe as well as ^{129}Xe in the dissolved phase, providing insights into ventilation and perfusion information that could be useful for clinical applications. Section 6.3 describes the limitation and difficulties when measuring the dissolved ^{129}Xe in the chemical shift satuation recovery (CSSR) type experiments. Lastly, a summary of the thesis is presented in Section 6.4.

CHAPTER 1: Theoretical Background of Hyperpolarised Gas Magnetic Resonance Imaging

1.1 Nuclear Magnetic Resonance and Magnetic Resonance Imaging

1.1.1 Nuclear spin, magnetic moment and magnetisation

Classically, a particle's angular momentum is associated with its rotation around its own centre of mass. Spin, however, is quantum mechanical in nature and is an intrinsic physical property of elementary particles. It is associated with only the magnitude of the intrinsic angular momentum of a particle and elementary particles simply possess spin, even at a temperature of absolute zero.

The nuclear magnetic moment $\vec{\mu}$ of a nuclear spin is a measure of its nuclear magnetism associated with its nuclear angular momentum, $\vec{J}$, by

$$\vec{\mu} = \gamma \vec{J} \tag{1.1}$$

where the proportionality constant γ is called the gyromagnetic ratio given by

$$\gamma = \frac{q}{2m} \tag{1.2}$$

Its magnitude can be approximated for a point particle with charge q and mass m in circular motion, specific to a given nucleus. The corresponding angular momentum is given by

$$\vec{J} = \vec{I}\hbar \tag{1.3}$$

where $\hbar$ is the reduced Planck's constant and $|\vec{I}|$ is the total angular momentum quantum number of a nuclear spin in its ground state that can take on an integer or half-integer value depending on spin pairing of protons and neutrons. For a nucleus of spin *I*, there are a total of (2*I*+1*)* degenerate energy states from –*I* to *I*, denoted by the quantum number I_z (The projection of the total angular moment along an arbitrary axis of quantisation). When there is no external magnetic field present, the values of the spin angular momentum along an arbitrary axis for each state of I_z are the same. In the presence of an external magnetic field ($\overrightarrow{B_0}$), however, a magnetic moment can adopt one of the two energy levels for spin ½ nucleus, with a potential energy difference of $E = -\vec{\mu} \cdot \overrightarrow{B_0}$ and the degeneracy is lifted. The quantum Hamiltonian along the direction of the magnetic field thus becomes:

$$\widehat{H} = -\gamma \hbar B_0 I_z \tag{1.4}$$

The potential energy depends on the orientation of the spin with respect to the direction of the external magnetic field. This is known as the Zeeman resonance effect (2) (Fig. 1.1).

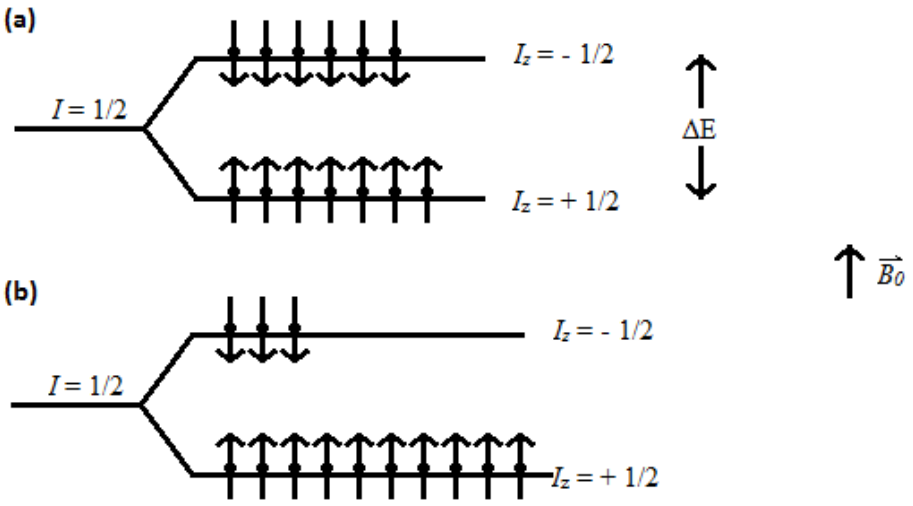

Figure 1.1. **The Zeeman energy levels of a spin ½ ensembles in an applied magnetic field under thermal equilibrium (a), the population difference is very small compared to the non-equilibrium state found with a hyperpolarised sample (b).**

All nuclei considered and used in this thesis (^{1}H, ^{3}He, and ^{129}Xe) have a spin quantum number *I* of ½, hence I_z can take the values of - ½ and + ½, and the Hamiltonian given by equation 1.4 has two energy levels which differ by $\gamma\hbar B_0$.

The bulk magnetisation, M_0, of a total number of *N* spins in a sample at thermal equilibrium is determined by the number of $n_\uparrow$ (I_z = + ½) spins in excess of $n_\downarrow$ (I_z = - ½) spins which follows from Boltzmann statistical mechanics(2),

$$n_\uparrow - n_\downarrow = N\frac{\hbar\omega_0}{2kT} \qquad \text{when } \frac{\hbar\omega_0}{kT} << 1 \tag{1.5}$$

where $\frac{\hbar\omega_0}{kT}$ is typically on the order of 10^{-11} at room temperature, and *k* is the Boltzmann constant. The magnitude of the equilibrium magnetisation is given by

$$M_0 = \frac{1}{2}\gamma\hbar NP \tag{1.6}$$

where *P* is the polarisation which can take any value between 0 and 1, and is usually expressed in percentage between 0 and 100%. It is expressed as the fraction of total spins aligned in the Zeeman ground state:

$$P = \frac{|n_\uparrow - n_\downarrow|}{n_\uparrow + n_\downarrow} \tag{1.7}$$

The nuclear magnetic moment $\vec{\mu}$ will tend to align with the magnetic field to minimise the energy through T_1 relaxation (to be discussed later) in an external magnetic field $\overrightarrow{B_0}$.

Since the magnetic moments of aligned and anti-aligned spins largely cancel out, the total magnetisation measured is proportional to the "spin excess" or net polarisation, which is very small at thermal equilibrium. The polarisation in thermal equilibrium can be approximated by:

$$P \cong \frac{\Delta E}{2kT} = \frac{\gamma\hbar B_0}{2kT} \tag{1.8}$$

where ΔE is the energy difference between the two spin states (Fig. 1.1 (a)), and *T* is temperature in Kelvin. The polarisation is typically of the order of 10^{-6} at room temperature for nuclear spins in thermal equilibrium. In the case of hyperpolarised media

(Fig. 1.1 (b)), the polarisation is greatly increased (see Section 1.3) with a highly populated spin state, giving a net spin excess in the order of 10 – 50%.

Combining eqns. 1.6 and 1.8, Curie's Law gives the net magnetisation for nucleus' spin I = ½:

$$M_0 = \frac{N\hbar^2\gamma^2 B_0}{4kT} \tag{1.9}$$

Equations 1.5 through 1.9 only apply to I = ½ spin nuclei. For nuclei with I >1/2, such as ^{83}Kr, the polarisation can be calculated by:

$$P = Z^{-1}\frac{1}{\hbar I}\left|tr\{\rho\hat{I_z}\}\right| \tag{1.10}$$

where Z in equation 1.10 is the partition function and ρ is the density matrix operator.

1.1.2. Alternating magnetic fields

Even though spin is a quantum phenomenon, with the understanding of classical electrodynamics, a particle can be treated as a magnetic moment and its associated rotation around its own centre of mass. A magnetic moment $\vec{\mu}$ of a nucleus inside a magnetic field $\overrightarrow{B_0}$ experiences a torque given by

$$\vec{\tau} = \vec{\mu} \times \overrightarrow{B_0} \tag{1.11}$$

which can be equated to the rate of change of the angular momentum

$$\vec{\tau} = \frac{d\vec{J}}{dt} \tag{1.12}$$

By differentiating eqn. 1.1 with respect to time and substitution of eqns. 1.11 and 1.12, the equation of motion of a single spin can be expressed as

$$\frac{d\vec{\mu}}{dt} = \gamma\frac{d\vec{J}}{dt} = \gamma\vec{\mu} \times \overrightarrow{B_0} \tag{1.13}$$

Eqn. 1.13 can be solved with the solution for the magnitude of the magnetic moment as

$$|\vec{\mu}| = \mu_0 e^{-i\omega_0 t} \tag{1.14}$$

where the expression for the well-known Larmor angular frequency ω_0, assuming the magnetic moment is perpendicular to the magnetic field is:

$$\omega_0 = \gamma B_0 \tag{1.15}$$

The equation of motion predicts the precessing motion of the magnetic moments of the nuclei around the axis pointing in the direction of the magnetic field. The frequency of the precession is determined by the Larmor frequency, related to the angular frequency as:

$$\nu = \frac{\omega_0}{2\pi} = \left(\frac{\gamma}{2\pi}\right) B_0 \tag{1.16}$$

Values of the gyromagnetic ratios for nuclei of interest in hyperpolarised gas lung imaging can be found in **Table 1.1**.

Nucleus	Gyromagnetic ratio: $\frac{\gamma}{2\pi}$ [MHz/T]	ν at 1.5 T	ν at 3 T
^{1}H	+ 42.576	+ 81.86	+ 127.73
^{3}He	+ 32.434	+ 48.65	+ 97.30
^{13}C	+ 10.705	+ 16.06	+ 32.11
^{129}Xe	- 11.777	- 17.67	- 35.33

Table 1.1. Gyromagnetic ratio for nuclei of interest and the resonant frequencies at 1.5 T and 3.0 T.

The sum of all the magnetic moments per unit volume is called the magnetisation and is given by

$$\vec{M} = \lim_{\Delta V \to 0} \left(\frac{\Sigma \vec{\mu_i}}{\Delta V}\right) \tag{1.17}$$

From equation 1.13 and 1.17, the equation of motion for the bulk magnetisation in the applied magnetic field $\vec{B}$ is then given by

$$\frac{d\vec{M}}{dt} = \gamma \vec{M} \times \vec{B} \tag{1.18}$$

Equation 1.18 describes the motion of $\vec{M}$ in the laboratory frame (denoted by lab). In MR physics, a more convenient and simplified coordinate system called the rotating frame (denoted by rot) is usually adopted. Given the laboratory frame unit vectors $\hat{\imath}, \hat{\jmath}, \text{and } \hat{k}$ for the Cartesian x-, y-, and z- axis respectively, the rotating frame has the corresponding vectors $\hat{\imath}', \hat{\jmath}', \text{and } \hat{k}'$. By convention, $\hat{k} = \hat{k}'$ is the direction of the static magnetic field B_0 along the z-axis, and their orthogonal counterparts make up the transverse plane, which rotates at an angular frequency of ω in the rotating frame of reference. A useful relation

between the two frames was derived by Slichter (1989), and the equation of motion in the rotating frame is given by:

$$\left(\frac{d\vec{M}}{dt}\right)_{rot} = \left(\frac{d\vec{M}}{dt}\right)_{lab} - \vec{\omega} \times \vec{M}$$

$$= \gamma\vec{M} \times \vec{\mathrm{B}} + \vec{M} \times \vec{\omega}$$

$$= \gamma\vec{M} \times \left(\vec{B} + \frac{\vec{\omega}}{\gamma}\right) \quad (1.19)$$

Now assuming a total magnetic field strength is a combination of a static magnetic field $\overrightarrow{B_0}$ along the z-axis, as well as a rotating magnetic field B_1 at an angular frequency of ω with the nuclear spin, the combined magnetic field in the laboratory frame of reference is then given by:

$$\vec{B} = \overrightarrow{B_0} + \overrightarrow{B_1}(t) = B_0\vec{k} + B_1(\vec{\imath}\cos\omega t + \vec{\jmath}\sin\omega t) \quad (1.20)$$

By substituting equation 1.20 into equation 1.19, and again applying the relationship between the two reference frames,

$$\left(\frac{d\vec{M}}{dt}\right)_{rot} = \left(\frac{d\vec{M}}{dt}\right)_{lab} - \vec{\omega} \times \vec{M}$$

$$= \gamma\vec{M} \times \left(B_0\overrightarrow{k'} + B_1(\overrightarrow{\imath'}\cos\omega t + \overrightarrow{j'}\sin\omega t)\right) + \vec{M} \times \vec{\omega}$$

$$= \gamma\vec{M} \times \left(B_0\overrightarrow{k'} + B_1(\overrightarrow{\imath'}\cos\omega t + \overrightarrow{j'}\sin\omega t) + \frac{\vec{\omega}}{\gamma}\right)$$

$$= \gamma\vec{M} \times \left(\left(B_0 + \frac{\vec{\omega}}{\gamma}\right)\overrightarrow{k'} + B_1\overrightarrow{\imath'}\right)$$

$$\left(\frac{d\vec{M}}{dt}\right)_{rot} = \gamma\vec{M} \times \left(\left(B_0 - \frac{\omega}{\gamma}\right)\overrightarrow{k'} + B_1\overrightarrow{\imath'}\right) \quad (1.21)$$

where $\vec{\omega} = -\omega\widehat{k'}$ and B_1 is static along $\overrightarrow{\imath'}$. This gives an effective magnetic field, $\overrightarrow{B_{eff}}$, in the presence of a static magnetic field B_0 and a rotating magnetic field B_1 of:

$$\overrightarrow{B_{eff}} = B\left(B_0 - \frac{\omega}{\gamma}\right)\overrightarrow{k'} + B_1\overrightarrow{\imath'} \quad (1.22)$$

If in equation above, $\omega = \omega_0$, B_1 is said to be on-resonance and equation 1.22 simplifies to $\overrightarrow{B_{eff}} = B_1\vec{\imath'}$.

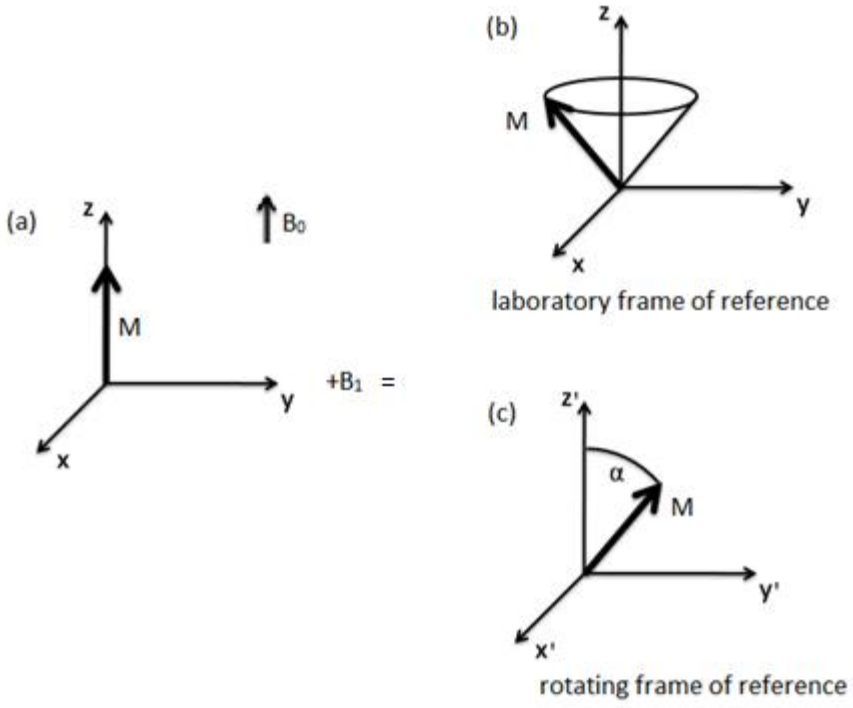

Figure 1.2. (a): Total magnetisation in a constant external magnetic field B_0. After applying an alternating magnetic field, $B_1(t)$, orthogonal to the main magnetic field by a voltage oscillating at the Larmor frequency for a time τ, the net magnetisation is nutated by a flip angle, α, defined by equation 1.23. The net magnetisation is illustrated for the laboratory frame (b) as well as the rotating frame of reference (c).

The B_1 field is usually generated by a sinusoidal voltage applied to a resonator or coil, generating a radio frequency (RF) pulse orthogonal to the main magnetic field. When the voltage is pulsed over time τ, the angle at which the magnetisation nutates about the direction of the main magnetic field is then called the flip angle (Fig. 1.2), and is determined by the duration and magnitude of the B_1 field by

$$\alpha = \int_0^\tau \gamma B_1(t)dt \qquad (1.23)$$

Note that, if only one B_1 field is applied oscillating as described above, B_1 does not rotate around the z-axis, but linearly along an axis. It can be separated into two RF fields, one in the direction of precession of the magnetisation, the other in the counter direction, thus only half of peak amplitude of the B_1 field is effective with a linear RF field (3).

1.1.3 The Bloch Equation

So far, the net magnetisation has been treated in simplified expressions as the summation of all non-interacting spins in the bulk medium. The spins, however, do interact with their environment (lattice) as well as each other characterised by relaxation constants T_1 and T_2.

The Bloch equation (4) describes the behaviour of the total magnetisation, $\overrightarrow{M}$. It is a phenomenological expression for the time dependence of the net magnetisation within a sample. By convention, the external magnetic field, $\vec{B}$, points in the positive z direction. The general form of the Bloch equation within a general magnetic field $\vec{B}$ is

$$\frac{dM}{dt} = \gamma\vec{M} \times \vec{B} - R(\vec{M} - \overrightarrow{M_0}) \tag{1.24}$$

where R is the relaxation matrix described by T_1 and T_2 relaxation (see the next section).

$$R = \begin{bmatrix} \frac{1}{T_2} & 0 & 0 \\ 0 & \frac{1}{T_2} & 0 \\ 0 & 0 & \frac{1}{T_1} \end{bmatrix} \tag{1.25}$$

In component form,

$$\begin{aligned} \frac{dM_x}{dt} &= \gamma\left(M_y B_z - M_z B_y\right) - \frac{1}{T_2} M_x \\ \frac{dM_y}{dt} &= \gamma(M_z B_x - M_x B_z) - \frac{1}{T_2} M_y \\ \frac{dM_z}{dt} &= \gamma\left(M_x B_y - M_y B_x\right) - \frac{1}{T_1}(M_z - M_0) \end{aligned} \tag{1.26}$$

where

$$\begin{aligned} \vec{M} &= \left(M_x\hat{\imath}, M_y\hat{\jmath}, M_z\hat{k}\right) \\ \vec{B} &= (B_x\hat{\imath}, B_y\hat{\jmath}, B_z\hat{k}) \end{aligned} \tag{1.27}$$

In the rotating frame where B_1 is on resonance, $\omega = \omega_0$, as described earlier. With a second perturbating field $B_1(t)$, the Bloch equation becomes

$$\left(\frac{dM_{x'}}{dt}\right)_{rot} = -\frac{1}{T_2}M_{x'}$$
$$\left(\frac{dM_{y'}}{dt}\right)_{rot} = \gamma M_z B_1 - \frac{1}{T_2}M_{y'} \quad (1.28)$$
$$\left(\frac{dM_z}{dt}\right)_{rot} = -\gamma M_{y'} B_1 - \frac{1}{T_1}(M_z - M_0)$$

Where $$B = (B_1 \cos(\omega t)\,\hat{j}, B_0\hat{k}) \quad (1.29)$$

and $B_1 \cos(\omega t)$ is the perturbing RF pulse. Solving eqn. 1.28, the magnetisation in the direction of the magnetic field (M_z) and its associated transverse magnetisation resolved in the xy-plane (M_{xy}) can be expressed as

$$M_z(t) = M_0\left(1 - \exp\left(-\frac{t}{T_1}\right)\right) \quad (1.30)$$

$$M_{xy} = M_0 \exp\left(-\frac{t}{T_2}\right) \quad (1.31)$$

1.1.4. Spin-lattice relaxation (T_1)

After the magnetisation has been tipped by the B_1 magnetic field into the transverse plane, the magnetisation regrowth is characterised by the constant T_1, the spin-lattice relaxation constant. It is also referred to as the longitudinal relaxation time constant, characterising the rate at which the longitudinal magnetisation recovers back to thermal equilibrium in a magnetic field $\overrightarrow{B_0}$ by convention in the z-direction. Some typical *in vivo* values of T_1 for ^{1}H at 1.5 T are shown in Table 1.2.

Tissue	T_1 [ms]
muscle	900
fat	250
blood	1200

Table 1.2 Representative T_1 values in ms for ^{1}H in different tissues at 1.5 T and body temperature (1).

Unlike conventional ^{1}H MRI, for hyperpolarised gases, in the case of Fig. 1.1 (b), where the spins are in a non-thermal equilibrium state, relaxing back towards thermal equilibrium means a decrease in magnetisation. There are a few factors that contribute to T_1 relaxation including surface relaxation, oxygen-induced relaxation, gradient-induced relaxation and dipolar self-relaxation.

The surface relaxation mechanism of hyperpolarised ^{3}He and ^{129}Xe were described by Fitzsimmons et al. and Driehuys et al. (5,6) given by:

$$\frac{1}{T_{1,surface}} = \frac{1}{\eta}\frac{S}{V} \tag{1.32}$$

where η is a coefficient depending on the surface material, temperature and the magnetic field strength and S/V is the surface-to-volume ratio of the gas container. $T_{1,\,surface}$ of ^{3}He is about 100 h in an iron-free glass cell. $T_{1,surface}$ of ^{129}Xe on the other hand is shorter. $T_{1,surface}$ of 3 h was measured for gas contained in a 7.5 cm diameter quartz cell (7).

Oxygen-induced relaxation cause by the oxygen paramagnetic electron spin to nuclear spin dipole-dipole interaction is a very large contributor to T_1 relaxation of hyperpolarised gases. It can be empirically determined for ^{3}He (8) and ^{129}Xe (9) in the temperature range from 200 – 400 K by:

$$\frac{1}{T_{1He,O_2}} = \frac{0.45p_{O2}}{1.013}\frac{273}{T}\left(\frac{299}{T}\right)^{0.42} s^{-1} \tag{1.33}$$

$$\frac{1}{T_{1Xe,O_2}} = \frac{0.388p_{O2}}{1.013}\frac{273}{T}\left(\frac{300}{T}\right)^{0.03} s^{-1} \tag{1.34}$$

T here is temperature in degrees Kelvin and pO_2 is the oxygen partial pressure in units of bar.

Field gradient-induced relaxation is another contributor to T_1 relaxation of the hyperpolarised gases by (10-12):

$$\frac{1}{T_{1,\,gradient}} = D\,\frac{|\nabla B_x|^2+|\nabla B_y|^2}{B_0^2} \tag{1.35}$$

where D is the diffusion constant, and ∇B_x and ∇B_y are spatial gradients in the x and y directions respectively.

The dipolar self-relaxation contribution comes from atomic collisions via nuclear spin to nuclear spin dipole interaction. The relaxation rates at room temperature were derived by Newbury et al. for ^{3}He (13) and Hunt and Carr for ^{129}Xe (14,15), with gas pressure p in units of bar:

$$\frac{1}{T_{1He,dipole}} = \frac{p}{809} h^{-1} \quad (1.36)$$

$$\frac{1}{T_{1Xe,dipole}} = \frac{p}{61} h^{-1} \quad (1.37)$$

Dipolar relaxation is thus insignificant except at very high gas pressure.

Lastly, ^{129}Xe has a special case of spin-rotation coupling in Xe-Xe van der Waals molecules which is constant under most circumstances (7) given by:

$$\frac{1}{T_{1Xe,vdW}} = 0.24\ h^{-1} \quad (1.38)$$

Finally, the total T_1 relaxation constant for i denoting surface relaxation, oxygen-induced relaxation, etc. of hyperpolarised gases is given by:

$$\frac{1}{T_1} = \sum_i \frac{1}{T_{1,i}} \quad (1.39)$$

1.1.5 Spin-spin relaxation (T_2)

Spin-spin interactions of individual nuclei determine the rate of magnetisation decay in the xy-plane due to dephasing and loss of phase coherence between the individual spins as a function of local differences in magnetic field. Dephasing causes each spin to precess at a slightly different rate, causing an increase rate of intrinsic spin dispersion (T_2). In addition to spin-spin interaction, there are also other causes for dephasing of the spins and transverse decay caused by field inhomogeneities in the magnetic field, such as magnet imperfections and localised differences in magnetic susceptibility of the sample. Since the observed transverse relaxation is larger than $1/T_2$, which is the decay constant

associated with static and dynamic field changes, an apparent transverse relaxation constant, T_2^*, is usually used and has been defined as

$$\frac{1}{T_2^*} = \frac{1}{T_2} + \frac{1}{T_2'} \tag{1.40}$$

where T_2' is the component due to static field inhomogeneities. The equation above is generally applied in the static dephasing regime, where diffusion is neglected, which is not the accurate case for ^{129}Xe and ^{3}He as they are very highly diffusive and would lead to additional time dependent relaxation. More details of the transverse relaxation decay constants of both gas phase (Chapter 3) and dissolved phase (Chapter 5) xenon will be discussed and measured in later Chapters.

In the presence of spin-spin relaxation, transverse relaxation is generally faster than that of the longitudinal relaxation, i.e.:

$$T_1 \geq T_2 \geq T_2^* \tag{1.41}$$

1.1.6 Signal Detection

MR signals are generated by transverse magnetisation, thus a component of the magnetic field must be in the transverse plane in order for a MR signal to be detected.

In the laboratory frame of reference, the precession of the transverse magnetisation causes varying magnetic flux φ, which generates an electromotive force (EMF), detectable in the coil according to Faraday's law:

$$emf = -\frac{d\phi}{dt} = -\frac{d}{dt}\int \vec{B}_{receive}(\vec{r})\vec{M}(\vec{r},t)d^3r \tag{1.42}$$

where $\vec{B}_{receive}$ is the induced magnetic field defined as the magnetic field per unit volume. This time varying *emf* signal is also known as the free induction decay (FID). The total signal can be simplified by introducing spin density $\rho(\vec{r})$ and is given by:

$$s(t) = \int e^{-\frac{t}{T_2(\vec{r})}}\rho(\vec{r})e^{i\left(\omega_0 t+\phi(\vec{r},t)\right)}d^3r \tag{1.43}$$

The spin density $\rho(\vec{r})$ can be calculated using equation 1.43 from the measured signal, $s(t)$, obtained from a MRI scanner. It consists of a large cryogenically cooled superconductive magnet with the hardware components illustrated in Figure 1.3. The two systems used for this thesis are 1.5 T Signa HDx (GE, Milwaukee, WI, USA) with maximum axis continuous gradient of 33 mT/m and a slewrate of 120 T/m/s and a 3 T Philips Achieva (Best, Netherlands) with maximum axis continuous gradient of 40 mT/m and a slewrate of 200 mT/m/ms. There is hardware limitation of gradient and slewrate (change in gradient / time) set on clinical systems to avoid peripheral nerve stimulation (16).

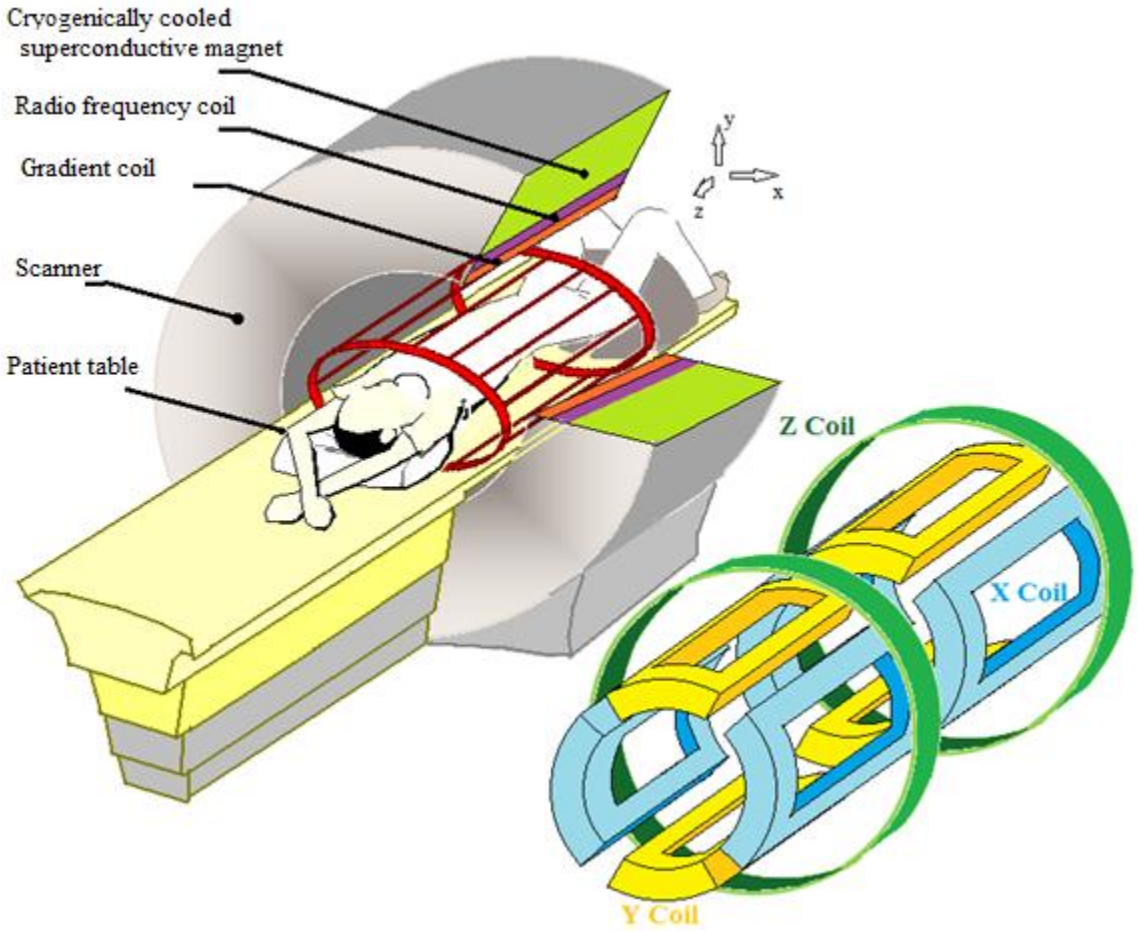

Figure 1.3. Hardware components of a clinical MRI system. Different types of transmit-receive coils can be used including an elliptical birdcage coil (red) as used in Chapter 4. Field gradient coils are illustrated in more detail on the right in x (blue), y (yellow), and z (green) - directions.

1.1.7 Spatial Encoding

The magnet bore inside an MR imaging system provides a uniform external magnetic field for the sample, B_0. Signals are generated by induced magnetic field flux in response to an orthogonal B_1 pulse of RF radiation through Faraday's law (eqn. 1.42). To obtain spatial information, we need to artificially change the resonant frequency or phase of the nuclear spin resonance by applying spatially dependent magnetic field gradients along x, y, z or a combination of all three directions.

Slice selection

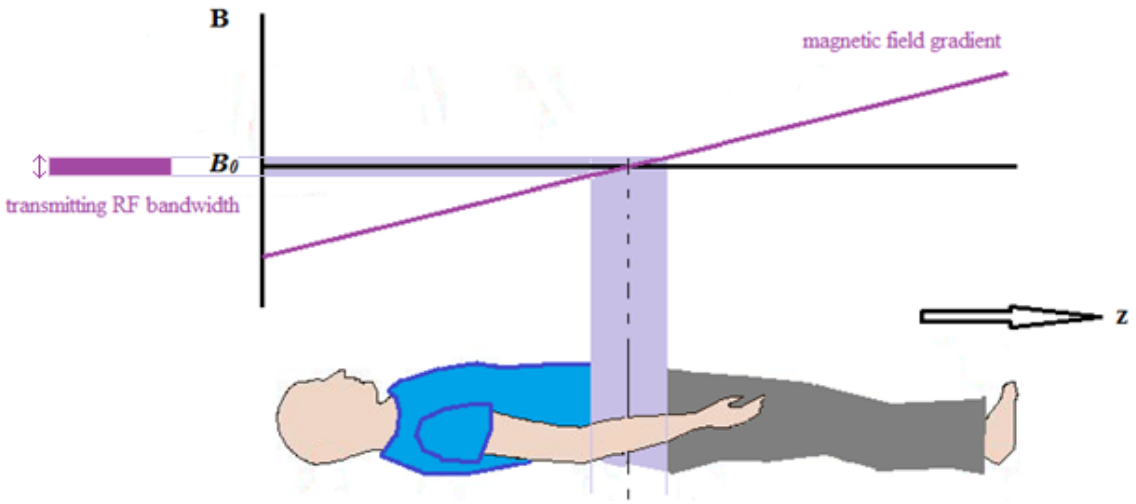

Figure 1.4. Slice selection in the z – direction

To select a slice, a linear gradient is first applied to the static magnetic field in the direction of the slices (let us assume in the *z*-direction of axial images with the patient feet in first). This implies that the resonant frequency is unchanged at the iso-centre, higher towards the feet and lower towards the head. Since an RF pulse has a finite bandwidth of transmitted frequencies depending on its pulse width (τ) and shape ($BW \propto \frac{1}{\tau}$), the spins will only be excited in the isolated plane that resonates in the frequency range of the RF pulse window (Fig. 1.4). By this method, a selective slice of excitation can be determined

where the slice thickness, Δ*z,* or position is determined by the gradient strength, $G_z = \frac{dB}{dz}$ and the RF pulse bandwidth (BW_{RF}) by

$$\Delta z = 2\pi \cdot \frac{BW_{RF}}{\gamma G_z} \tag{1.44}$$

Figure 1.5 shows how the slice thickness changes with the slice select gradient strength; one can also use the same diagram to see how the transmitting RF bandwidth would affect the slice thickness.

During the spatially dependent selective excitation of an isolated slice, dephasing of the spins occur dependent on their positions along the gradient. This leads to signal loss that can be recovered by a rewinding/rephasing gradient with a negative gradient amplitude whose area is half the area of the initial slice selective gradient for simple, low flip angle RF pulses.

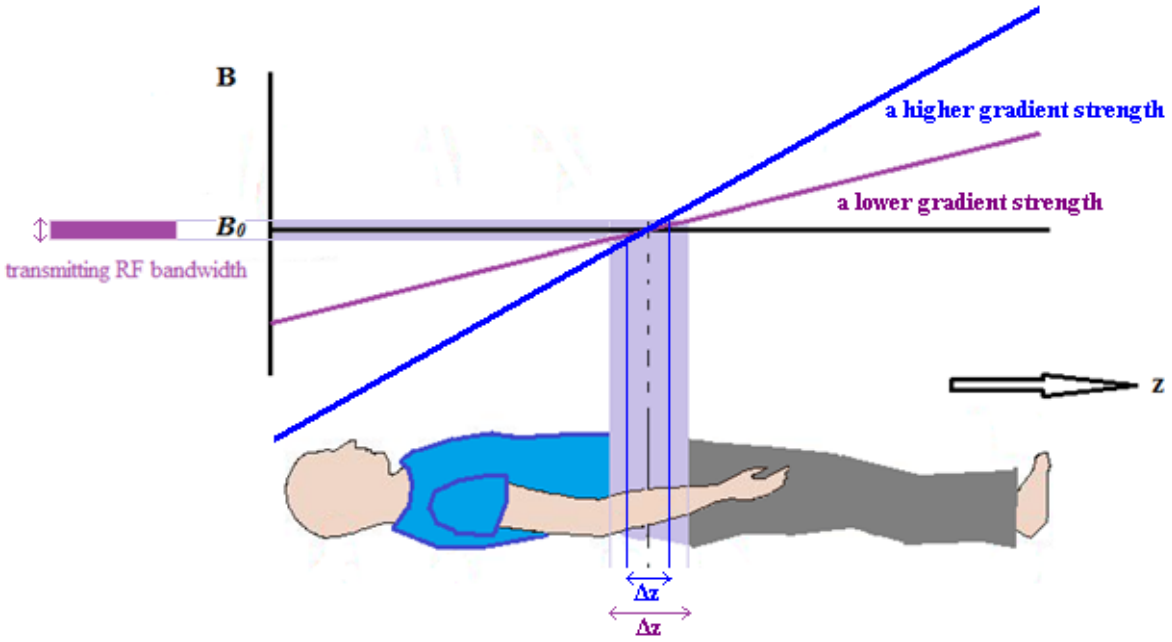

Figure 1.5. Schematics of the influence of gradient strength on slice thickness denoted by Δ*z*, colour matched to the applied gradient, with the same transmit RF pulse bandwidth.

Frequency encoding

After an isolated plane is selected, we now need to encode in the other two dimensions. By applying a magnetic field gradient, G_x, linearly in the direction of x, the effective magnetic field strength, B_x, is:

$$B_x(t) = B_0 + xG_x(t) \tag{1.45}$$

which leads to a dispersion of the resonance and spatially different Larmor frequency:

$$\omega(x,t) = \gamma B_0 + \gamma x G_x(t) \tag{1.46}$$

Again, if the same patient position (supine, feet first) is used, the resonating frequency would be unchanged at the iso-centre, faster towards the right arm, and slower towards the left arm (Fig. 1.6). The inverse Fourier Transform of a frequency-encoded free induction decay (FID) is a one dimensional projection image (Fig. 1.6).

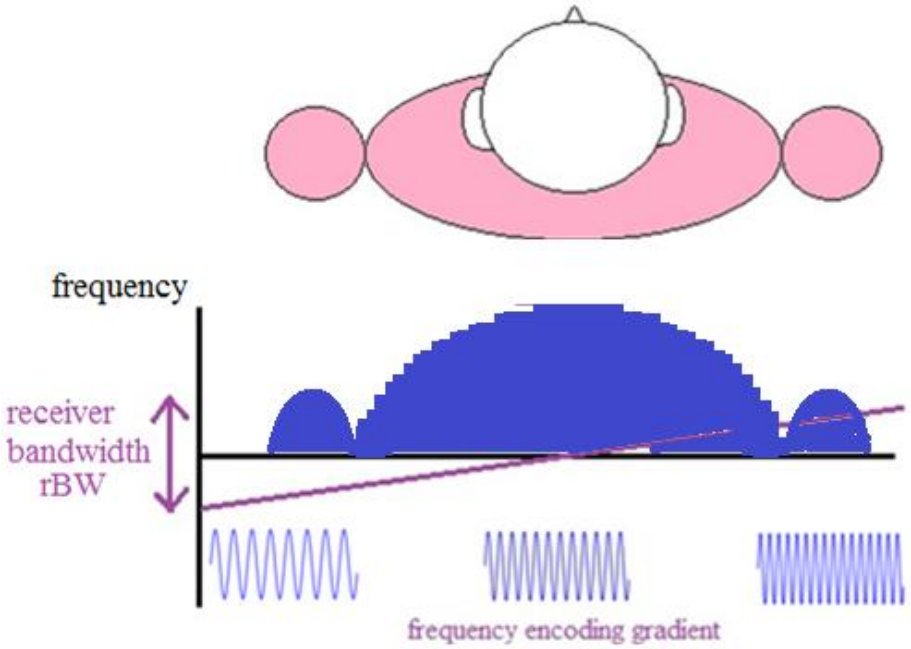

Figure 1.6. Frequency encoding in the x-direction, the Fourier Transform of the dispersed FID signal produces a 1D profile of the object (blue).

This is often referred to as the read direction as it is present during data acquisition. The receiver bandwidth (*rBW*) during readout is dependent on how steep the readout gradient strength is. A higher gradient strength would enable faster rephasing of the spins, which in turn shortens the TE. This is especially beneficial for a nucleus with a very short T_2^* constant (i.e. dissolved ^{129}Xe, see Chapter 5).

The constraint of using a larger gradient strength is its effect on the signal to noise ratio (SNR, discussed more in Chapter 3) of the image by:

$$SNR \propto \frac{1}{\sqrt{rBW}} \tag{1.47}$$

Lastly, the field of view (FOV) of the image in the readout direction cannot be decreased infinitely because it is affected by the receiver bandwidth, *rBW*, and the maximum G_x, by the following relationship:

$$FOV_x = \frac{rBW}{\gamma G_x} \tag{1.48}$$

In practice, frequency encoding is not directly applied for measurement of FIDs; instead, it is a part of a gradient echo formation in a pulse sequence (see Section 1.1.8).

Phase encoding

Phase encoding, also known as spin warping (17), is the third spatial encoding process. Much like frequency encoding, a gradient is applied perpendicular to the slice, continuing the case with the patient in the scanner bore (Fig. 1.4 – 1.6), phase encode direction would be in the y -direction, producing an effective magnetic field, B_y, for a time of Δt. The cumulative gradient in the y-direction for phase encoding is an applied gradient prior to read out. It is turned off before the readout gradient in the frequency encoding direction, thus the spins would now have the same frequency again in the phase encoding direction, but a different phase depending on their location (Fig 1.7) with a 2π phase difference between spins at the opposite edges of the FOV in the phase direction. Phase encoding can be applied in two orthogonal directions and is routinely used for 3D Cartesian imaging.

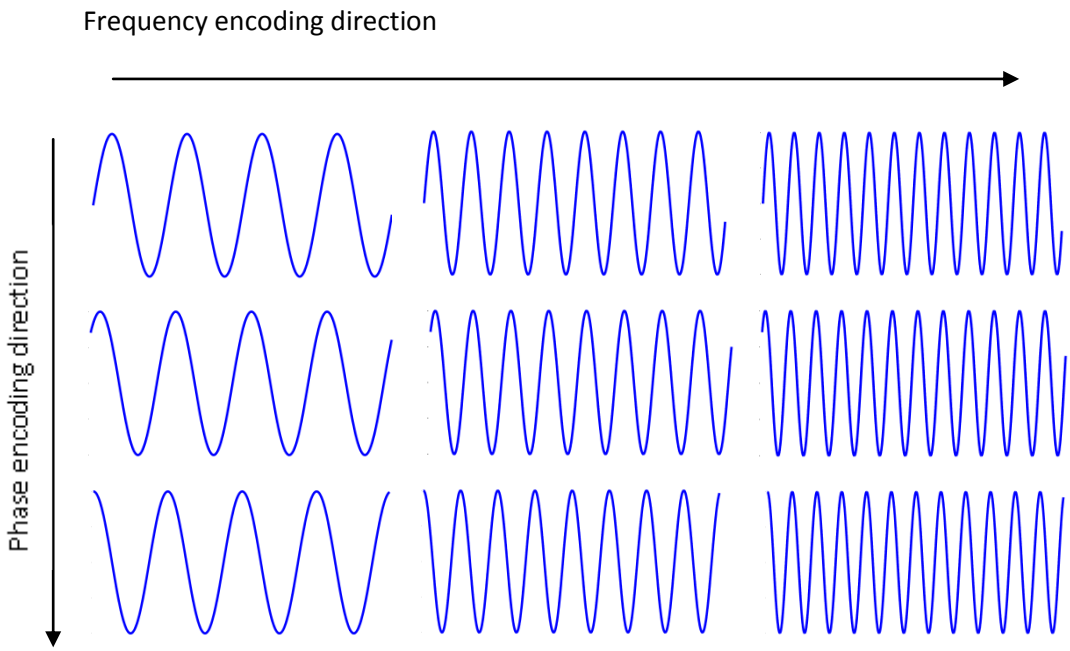

Figure 1.7. 2D spatial encoding.

The resolution in the phase encoding direction is given by equation 1.49 where the variables are illustrated in Fig. 1.8:

$$FOV_y = \frac{1}{\frac{\gamma}{2\pi}\Delta G_y \Delta t} \tag{1.49}$$

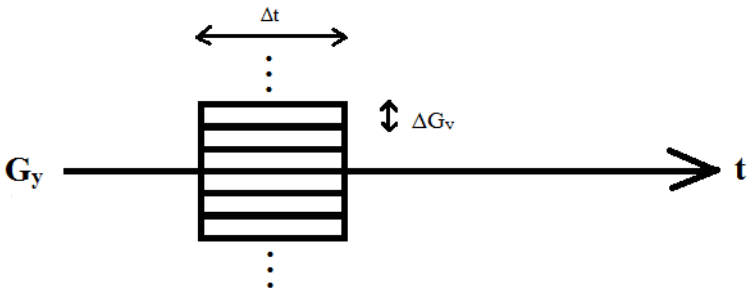

Figure 1.8. Phase – encoding gradient.

Now, by using all three spatial encoding gradients together with synchronised timing with RF excitation pulses and sampling of the echo or FID, one can spatially resolve and produce an image using a pulse sequence. There are many pulse sequences used for MRI,

one specific sequence that is used consistently throughout this thesis is a gradient echo sequence.

1.1.8 Pulse sequence

Gradient echo sequence

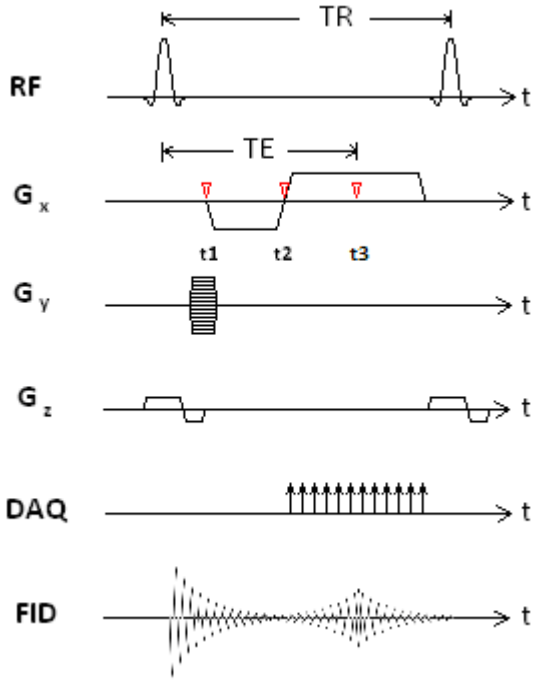

Figure 1.9. Gradient-echo pulse sequence timing diagram, where TR is the repetition time between RF pulses, and TE is the echo time between the RF pulse and the formation of a gradient recalled echo.

Fig. 1.9 shows a timing diagram of a basic 2D gradient echo pulse sequence, which is used throughout this thesis for ^{129}Xe MRI. Here we can see the spatial encoding gradients discussed earlier, where a slice selective gradient G_z is applied at the time of the RF pulse followed by a rewinder, the gradient G_y is the phase encoding gradient, and G_x is used for a gradient echo formation, which also serves as the readout gradient in the frequency direction.

To demonstrate this sequence, it can be shown in the form of individual isochromats (sum of a group of spins with the same frequency as a single vector). A spatial gradient (G_x) is first applied to dephase the isochromats from t1 to t2, also refers to as a pre-compensation gradient. The inversion of the magnitude of the gradient in the second half of this sequence (t2 to t3) ensures the highest frequency isochromats are now the lowest. Therefore, after the same duration of time, the spins re-phase and a gradient echo is formed at t3 (Fig. 1.9 and 1.10), the remaining gradient in the x direction is the readout gradient when the data acquisition takes place.

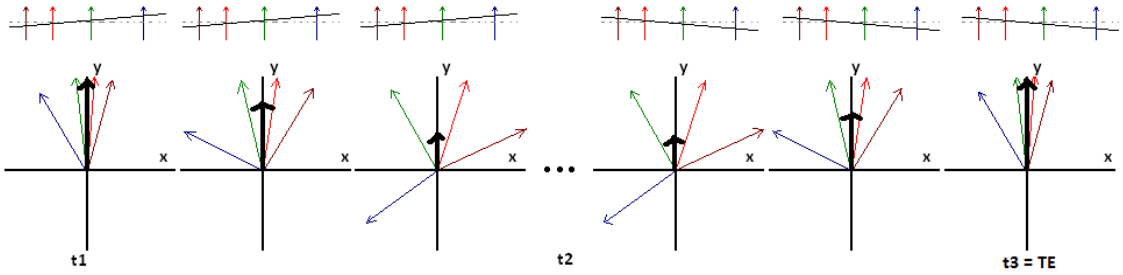

Figure 1.10. Schematic of a gradient echo sequence. The four representative isochromats are presented in their relative spatial coordinates, and the dotted line is where the gradient is zero. t_1, t_2, and t_3=TE correspond to Fig. 1.9.

When imaging thermally polarised spins with a gradient echo sequence, the repetition time, TR, is usually small compared to the T_1 relaxation constant of the sample, thus a complete relaxation of M_z to thermal equilibrium cannot be achieved between acquisitions, but reaches a steady-state magnetisation, M_{ss}, given by

$$M_{ss} = \frac{M_0\left(1-\exp\left(-\frac{TR}{T_1}\right)\right)}{1-cos\alpha\cdot\exp\left(-\frac{TR}{T_1}\right)} \tag{1.50}$$

where α is the flip angle. Knowing that the transverse magnetisation between pulses is related to the steady-state magnetisation, M_{ss}, by $M_{xy} = M_{ss}\sin\alpha$, the steady-state magnetisation can be maximised for a value of α, known as the Ernst angle (1) given by:

$$\alpha_{ernst} = \arccos\left(\exp\left(-\frac{TR}{T_1}\right)\right) \quad (1.51)$$

When imaging hyperpolarised spins with such a sequence, there is no thermal recovery of the signal so the optimal flip angle depends on the size of the image acquisition in the RF encoding dimension. Since M_z is not recovered between RF pulses, each RF pulse of flip angle α will decrease the total magnetisation by (1-cos α). Assuming negligible T_1 decay, the transvers magnetisation, M_{xy}, after *n* RF pulses is given by:

$$M_{xy}(n) = M_0 \sin\alpha \cos^{n-1}\alpha \quad (1.52)$$

The optimal flip angle for maximising the signal at the centre of k-space in an N phase encoding sequential image, α_{opt}, can be calculated from equation 1.52 (18) :

$$\alpha_{opt} = arctan\left(\frac{1}{\sqrt{(N-1)}}\right) \quad (1.53)$$

1.1.9 k-space

By means of spatial encoding with a pulse sequence, MR signals containing frequency and phase information are spatially recorded in the time domain (Fig. 1.11). Fig. 1.11 (a) is taken from the pulse sequence in Fig. 1.9 to show how a single k-space line is acquired, the phase encoding gradient then changes incrementally to cover the entire k-space.

This data is referred to as k-space or inverse space, with low-frequency information in the centre and high-frequency at the edges. The beauty of k-space is that linear shifts in gradient amplitude translate to linear shifts in k-space. Inverse Fourier transformation (IFT) can then convert the signals back into the spatial domain, so that an image can be produced (Fig. 1.12). The resolution (Δx) along direction *x* in the spatial domain is related to the sampling number, N_x, acquired in k-space along k_x, at a frequency step of Δk by:

$$\Delta x = \frac{1}{N_x \Delta k_x} \quad (1.54)$$

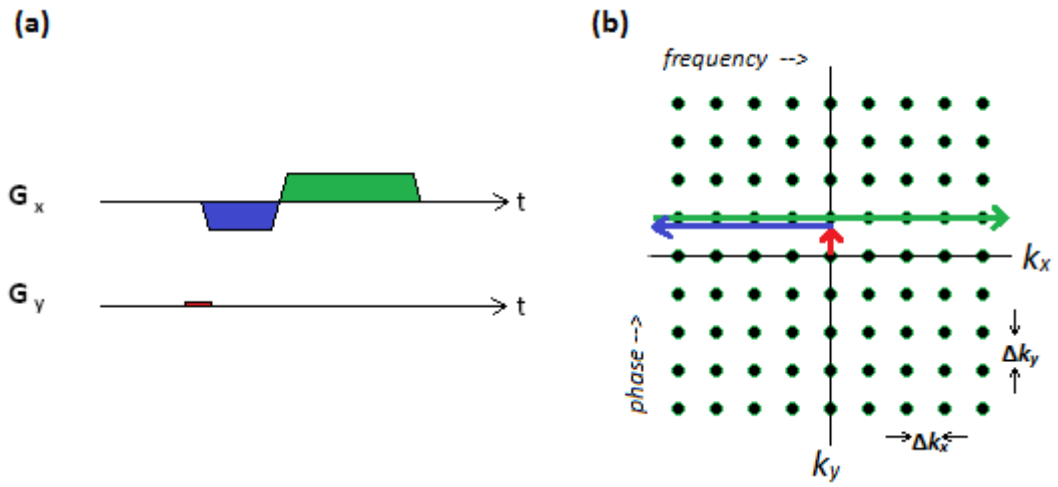

Figure 1.11. Schematics of *k*-space data acquisition of a single k-space line (b), which corresponds to phase and frequency encoding gradients illustrated in (a), where the pulse sequence (Fig. 1.9) acquires a single line in k-space, and is then repeated with a different incrementing G_y phase encoding gradient each time to fill up the rest of the k-space. The k-space trajectories are colour coded in (b) to match the gradients in (a).

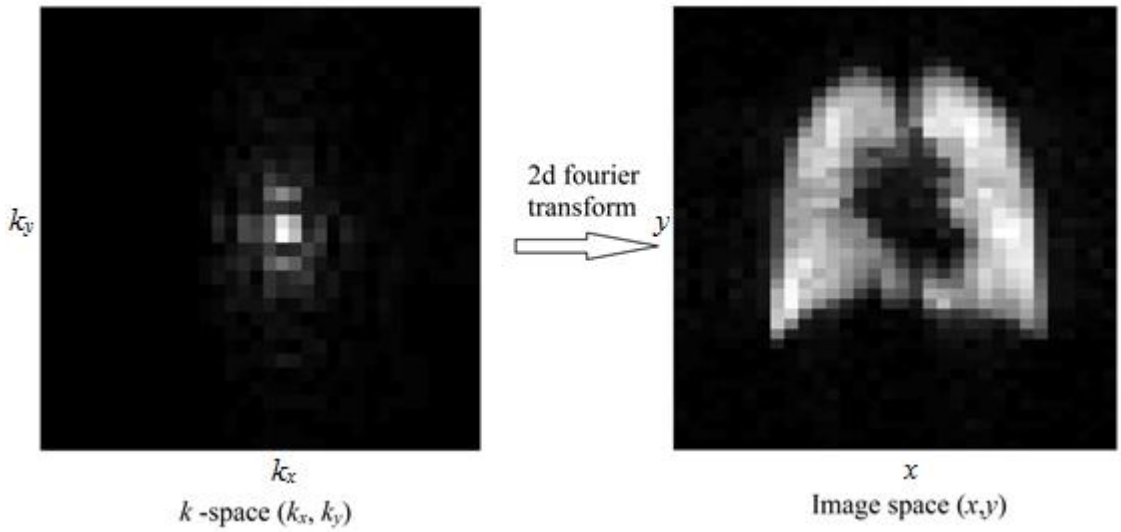

Figure 1.12. *k* – space raw data post data acquisition of a MRI experiment, and the resulting image after inverse Fourier transform with homodyne reconstruction (19).

1.1.10 Partial Fourier Imaging and Reconstruction

In cases where imaging time is essential, *k*-space can be obtained in an asymmetric fashion to shorten the total imaging time. The amount of time saved is called the degree of asymmetry, asym, for a k-space coverage region of [$-n_- \Delta k$, $n_+ \Delta k$] is defined as

$$asym = \frac{n_+ - n_-}{n_- + n_+} \tag{1.55}$$

and can take on all values between 1 (completely asymmetric) to 0 (completely symmetric). One of the most popular ways to achieve partial Fourier imaging is to use asymmetric echoes (partial echoes) in the readout direction where the dephasing gradient is reduced and the duration of the readout gradient is shortened (see Figure 1.13). Asymmetric echoes are useful for hyperpolarised gas MRI as they serve to (i) reduce T_2^* dephasing with shorter TE, (ii), reduce diffusion dephasing of the readout gradient and (iii) reduce sequence TR and hence imaging acquisition time. Some of the missing negative k-space data can be compensated for by the process of homodyne reconstruction (20). In a similar fashion, the number of k-space lines can also be reduced in the imaging acquisition. Unlike asymmetric echo, the reduction of phase encoding lines does not shorten the echo time, but shortens the total imaging time by reducing the number of acquisitions.

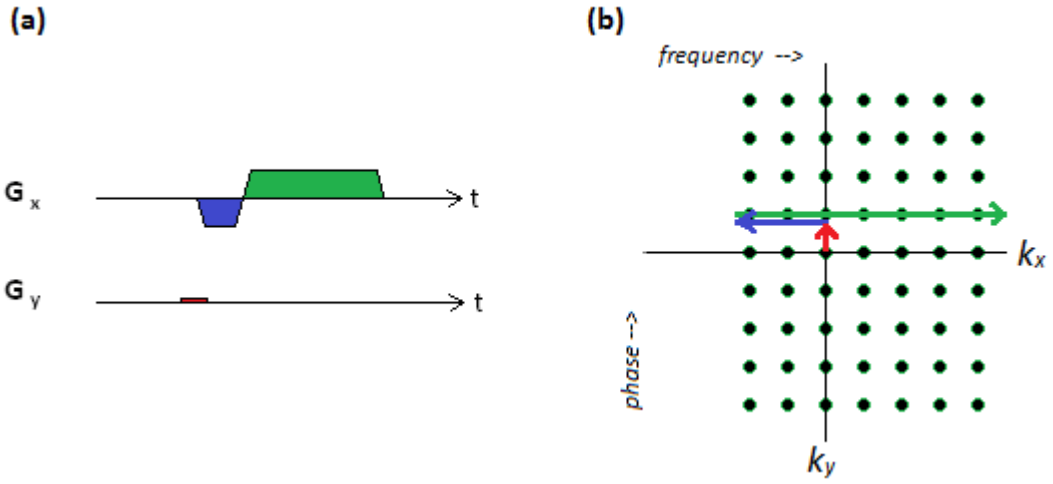

Figure 1.13. Partial echo data acquisition of a single k-space line. Notice the dephasing gradient in blue in (a) is shortened compared to the one in Fig.1.11, and k-space raw data is in this case acquired only partially (b).

Depending on the order in which k-space line acquisitions are taken, images can be obtained either centrically encoded (Fig. 1.14 (a)) or sequentially encoded (Fig. 1.14 (b)). In hyperpolarised gas MRI, the lack of polarisation recovery means the order of data acquisition is very important as the signal decays after each RF pulse. If an image is obtained using centric encoding, the SNR is higher since most of the signal comes from the centre of k-space, however, a sequentially encoded imaging sequence would provide finer details and less blurring as the highest weighted signals are on the edge of k-space.

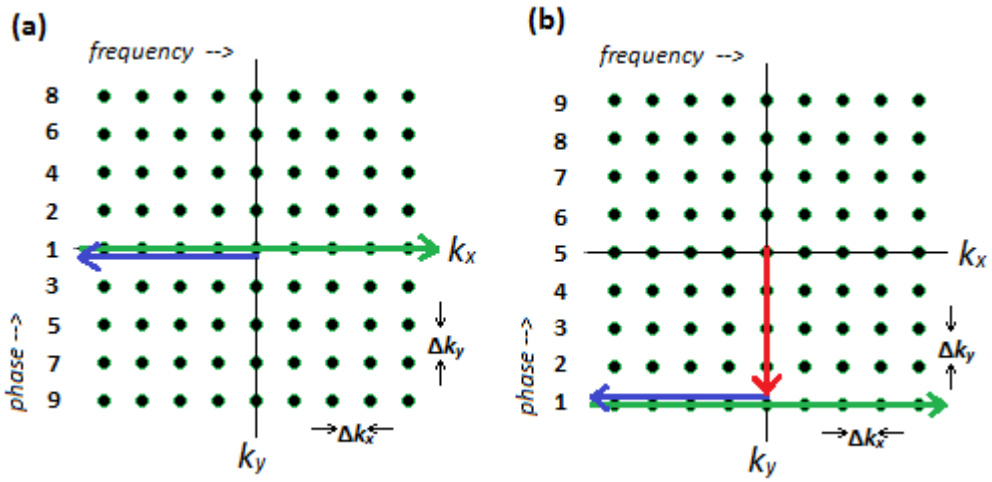

Figure 1.14. Cartesian k-space acquisitions: (a) centric encoding: when the centre of k-space is acquired first; (b) sequential encoding: when the k-space is acquired for the first line to the last in order. The numbers on the left indicate the order of RF phase encoded acquisitions.

1.1.11 Discrete sampling and the Nyquist criterion

The inverse Fourier Transform (FT) is defined for continuous variables, i.e. the integral of the full infinite k-space is required, which is impossible and impractical for finite scanning times. In reality, discrete data points are acquired in a finite k-space. The convolution theorem for Fourier Transforms states that the product of two functions is equivalent to

the convolution of the functions' Fourier transforms individually. Figure 1.15 shows the effect of discrete sampling using a 1D example of a rectangular object, whose FT is given by a Sinc function. If the sampling spacing in k-space is Δk, as shown in Figure 1.15 (e), then the spacing in imaging space is given by L, which is $1/\Delta k$ (Figure 1.15 (b)). If the object is larger than L, the original image would alias in the final image reconstruction as the images of the adjacent periodic images overlap. This aliasing artefact can be avoided as long as the object size, A, is smaller than L. This is known as the Nyquist criterion (expression (1.56)), where L is the FOV of the acquisition (1).

$$\Delta k < \frac{1}{A} \tag{1.56}$$

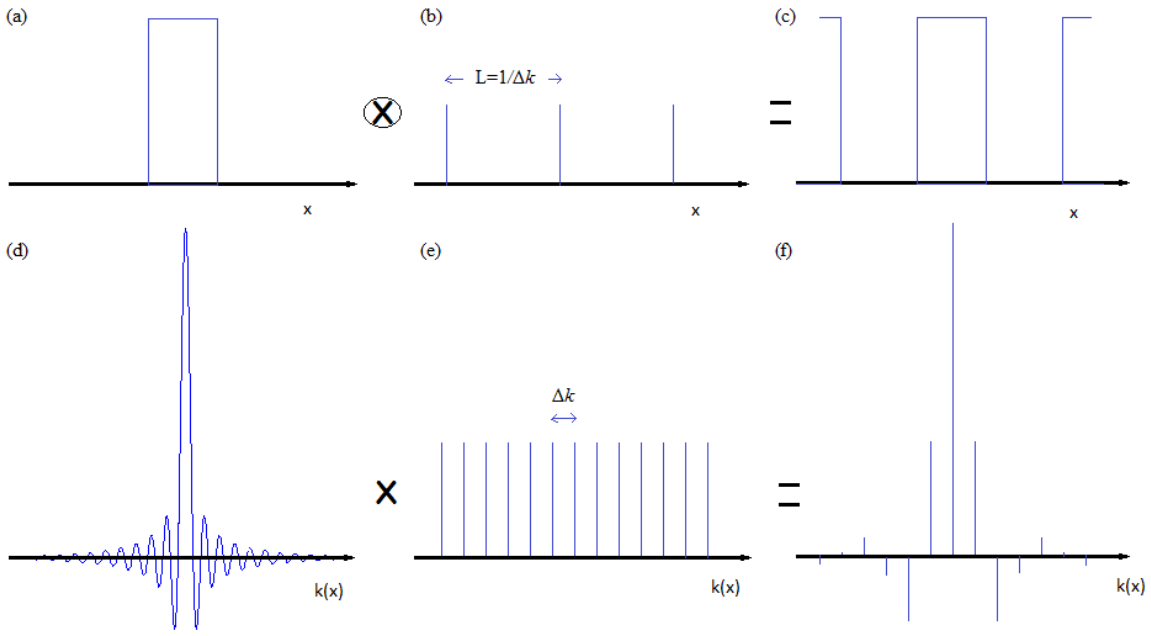

Figure 1.15. Discrete sampling in imaging space (top row) and their FT in k-space (bottom row) related by the convolution theorem of Fourier Transforms.

1.2 Radiofrequency engineering

Transmission of radio-frequency (RF) pulses into the sample at the Larmor frequency and reception of the received spatially encoded signal is accomplished by the use of tuned RF coils. A coil can excite via a generated B_1 field, and receive via the *principle of reciprocity*,

which states that if we were to apply direct current to a receive coil and then measure the field created at the sample, the induced signal in the coil by the sample would be proportional to the strength of this hypothetical field. An MRI–RF coil is made of a single loop or more of conducting elements that transmits an RF pulse and/or receives signal as current is induced by magnetic flux during the precession of the nuclei in MRI. It is built to produce a homogeneous imaging field (more important for transmit coils) resonating at the Larmor frequency.

1.2.1 Oscillating circuit

LCR circuit

An LCR circuit is the simplest resonant RF circuit; it consists of one resistor, an inductor and a capacitor, and resonates as a harmonic oscillator.

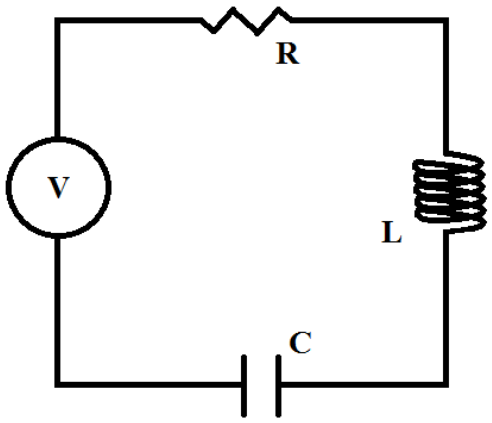

Figure 1.16. **An LCR circuit, named after the components of the circuit.**

In this oscillating circuit, the complex resistances, or impedances, Z_C and Z_L, of the capacitor *C* and inductor *L* are given by:

$$Z_c = \frac{1}{i\omega C} = -\frac{i}{\omega C} \quad (1.57)$$

$$Z_L = i\omega L \quad (1.58)$$

The total impedance is equal to zero at the resonating frequency, i.e., Z_C = Z_L, the frequency can be calculated from equations 1.57 and 1.58 as:

$$\omega_0 = \frac{1}{\sqrt{LC}} \quad (1.59)$$

where ω_0 is the resonating frequency of the resonator. The resistor and resistance in the circuit serve as a damping factor of the oscillating resonating frequency ω_0, much like friction in an oscillating weight on a spring. The quality factor (Q) of an oscillating circuit is defined as the fractional loss of energy per one cycle and is given by:

$$Q = \frac{\omega L}{R} \quad (1.60)$$

1.2.2 Common coil designs

Surface coil

The simplest design of a RF coil is a surface coil, which is sensitive when placed very close to the sample. It offers a high sensitivity, however, a very poor B_1 homogeneity, especially in the direction perpendicular to the coil surface with a depth of penetration comparable to the coil radius.

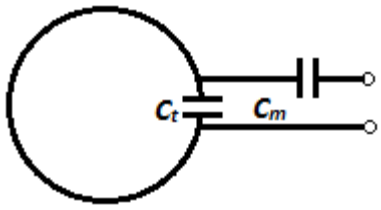

Figure 1.17 A surface coil in circular shape.

Helmholtz pair

A Helmholtz coil pair (21) (22) consists of two identical coils symmetrically placed on either side of the sample of interest separated on a common axis. An equal current flows in the same direction in each coil. The optimal distance between the two coils is equal to the radius of the coil, and the field map summation of the two coils is shown in Fig. 1.18. The coils used in Chapter 3 and Chapter 5 of this thesis are of the design of double Helmholtz coil pairs.

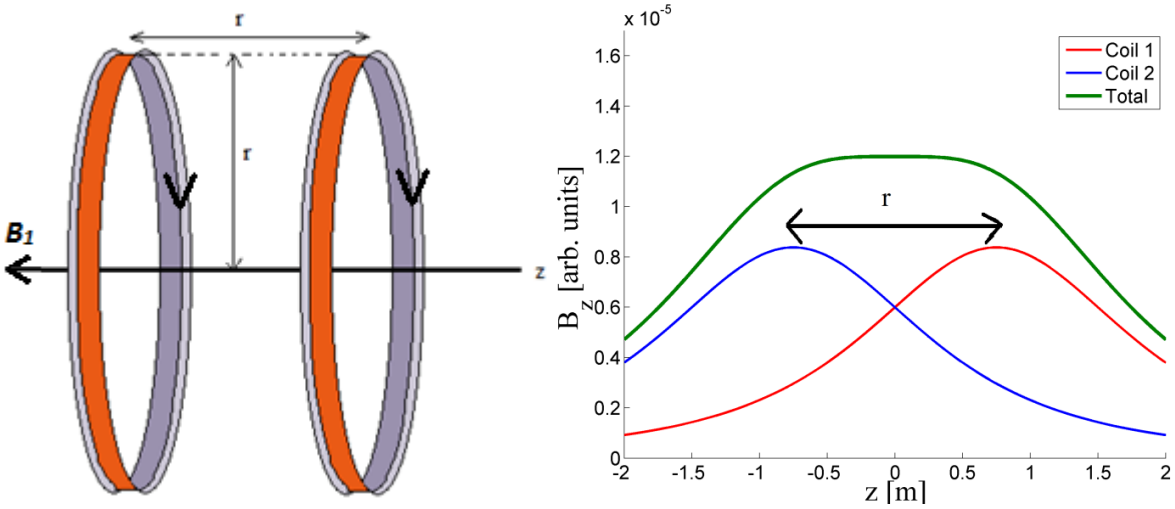

Figure 1.18. A simple a Helmholtz pair as well as its field map along the z - axis.

A slight variation of the Helmholtz pair coil is the saddle coil. Figure 1.19 shows the design of a one turn saddle coil, which produces a very homogeneous magnetic field in the area of interest in the direction of its cylindrical axis compared to that of a Helmholtz pair.

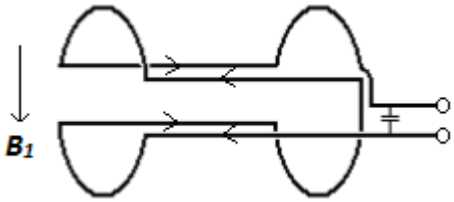

Figure 1.19 A saddle RF coil.

Volume transmit-receive coils

A solenoid coil (Fig. 1.20) is a volume transmit coil that produces a homogeneous magnetic field and produces higher signal-to-noise ratio compared to the surface coils above. However, a solenoid coil cannot detect signal if its axis is parallel to that of the static magnetic field (i.e. $B_1//B_0$). Thus it is only useful for small coils and samples, if the sample can sit orthogonal to the principal field. Also the high inductance, L, of the solenoid coil makes it impractical for large volume coils at high frequency.

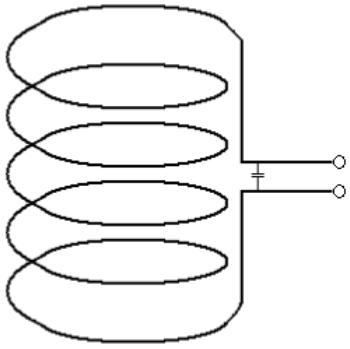

Figure 1.20. **A 5 loop multi-turn solenoid coil.**

A very common volumetric coil design is a birdcage coil (22) which has a number of conducting elements (rungs) running in the direction of its cylindrical axis (Fig. 1.20), and provides the best field homogeneity over most of the coil's volume compared to all the above coil designs described. Since most of the energy is stored near the conductors, the sensitivity of the birdcage coil near the centre is inherently lower. The coil will resonate at a number of modes depending on the number of legs and configuration (low/high/band – pass) with only one mode that produces a homogeneous B_1 field. For a low-pass configured birdcage coil, the lowest mode is the NMR mode, whereas the third highest is the NMR mode for a high-pass configured birdcage coil since the two highest modes are produced by the currents in the end rings (23) (Fig. 1.21). The major advantage of this coil design is that it acts as a transmission line with one complete cycle of standing wave around the end rings. By driving this coil at two points on the end rings 90° out of phase

in a quadrature fashion, the two orthogonal B_1 fields results in a circularly polarised B_1 field, rotating with the same frequency and direction as the nuclei's Larmor frequency, resulting in a more efficient use of input power, a factor of √2 higher than a linear B_1 field described earlier in Section 1.2.2. Detection in quadrature demodulates the complex signal into real and imaginary components, and combines the signals with their phase difference of 90° and increase in sensitivity by the same factor of √2. A quadrature hybrid circuit is a symmetric circuit required to drive a coil in quadrature (Figure 1.23), where any port can be used as an input port (i.e. port (a)), and signal outputs from the opposite two ports (in this case port (b) and (c)) are 90° out of phase when all ports are matched to the intrinsic impedance of the transmission line of Z_0. The design and application of an asymmetrical birdcage coil will be discussion in more details in Chapter 4 of this thesis.

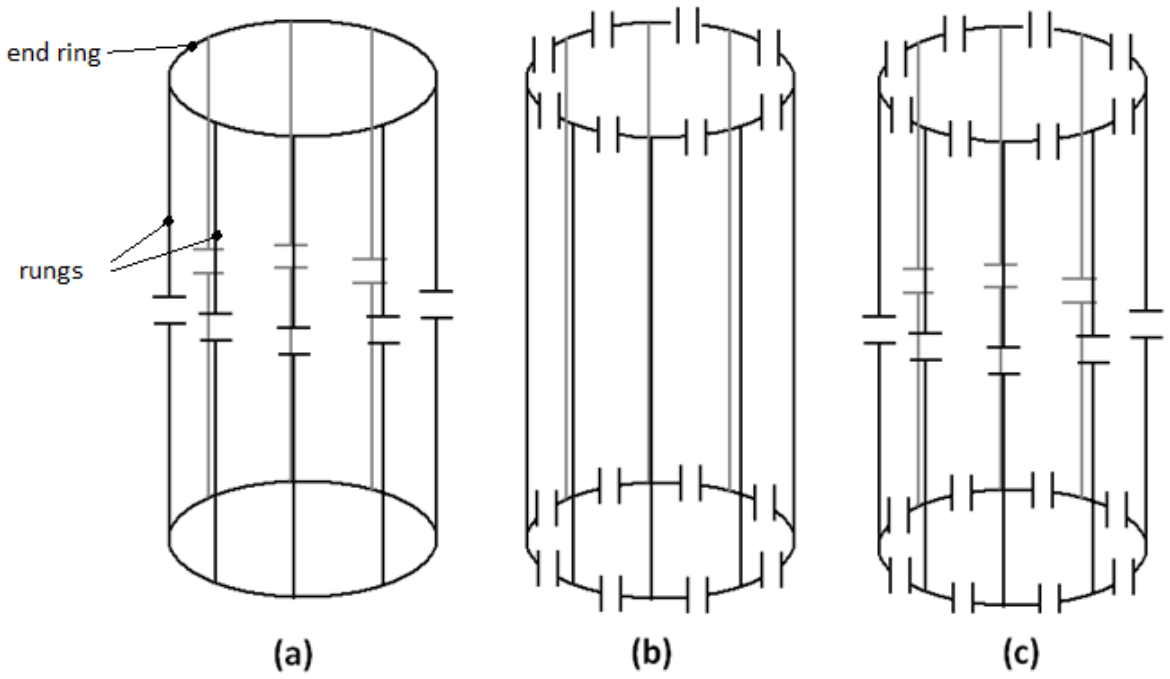

Figure 1.21. A symmetric birdcage coil of 8-legs of a low pass (a), high pass (b) and band pass (c) design coil.

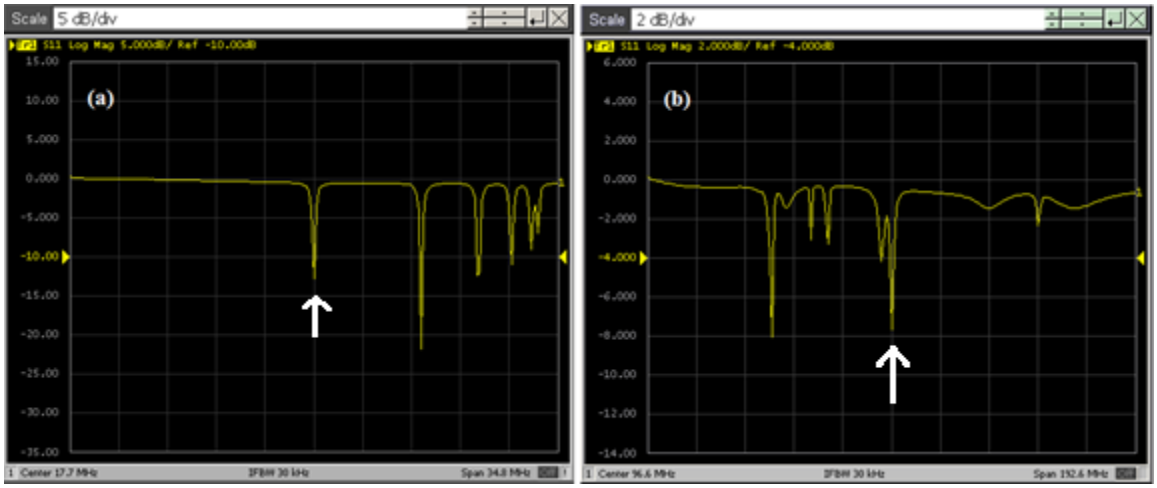

Figure 1.22. Network analyser tracers of (a) a low pass ^{129}Xe birdcage coil at 1.5 T resonates at 17.7 MHz and (b) a high pass ^{3}He birdcage coil (Fig. 1.24 (d)) at 3 T resonates at 97.3 MHz.

All the above coils can be used for transmission of the B_1 RF pulse as well as receiving NMR signals as *transmit-receive coils*. To protect the receiver pre-amplifier from the high RF power during transmission, diodes and blocking circuits are put between transmit port and pre-amplifier in a transmit-receive (T/R) switch circuit, which differ for linear and quadrature driven coils.

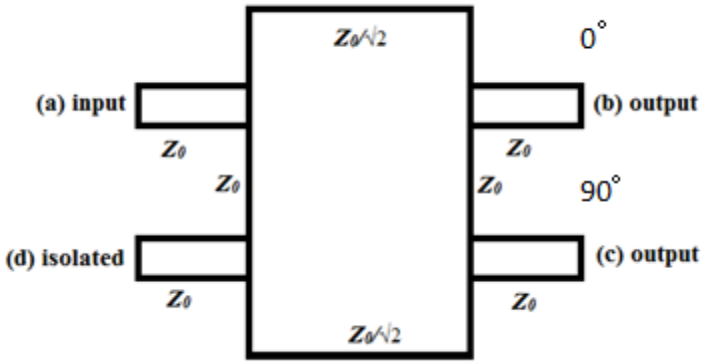

Figure 1.23. a quadrature hybrid used to drive a coil in quadrature mode.

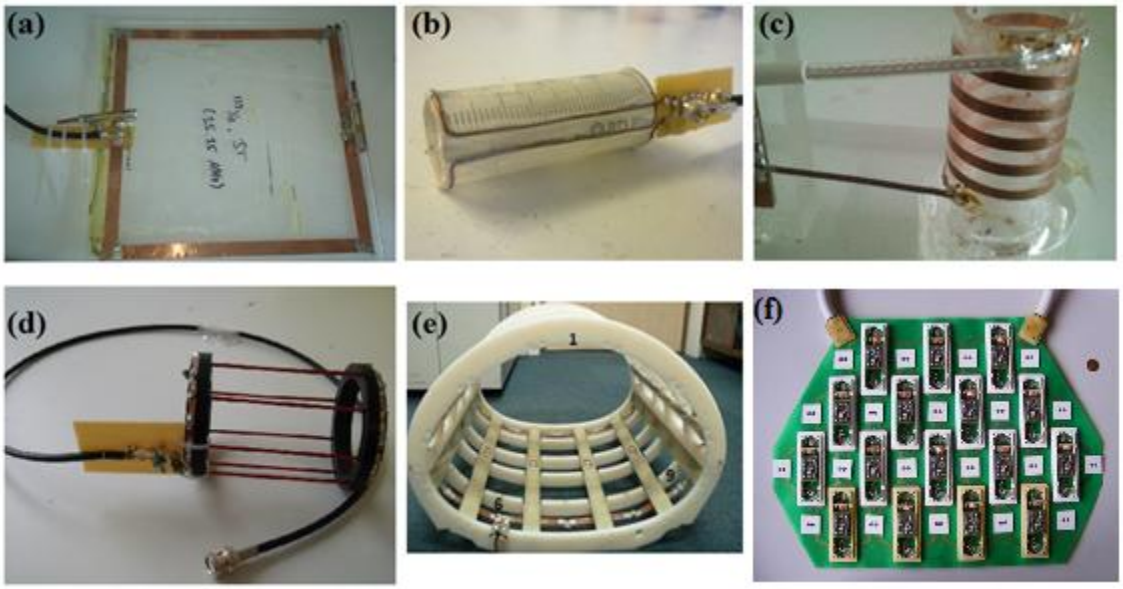

Figure 1.24. Examples of the RF coils from (a) surface coil, (b) saddle coil, (c) solenoid coil, (d) high-pass symmetric birdcage coil, (e) band-pass asymmetric birdcage coil, and (f) half of a 32 element array coil (24).

Array Coils

Phased arrays consist of several receive-only surface coils (Fig. 1.24 (f)). Unlike with transmit-receive coils, a separate coil is used to excite and a set of smaller, automatically well coupled to the decoupled array coils are used to receive signals simultaneously. The data from the separate receive coils are then combined and yield a final image with higher SNR over a large FOV because smaller coils produce higher SNR due to the principle of reciprocity. The most straightforward approach to reconstruction is called the root sum-of-squares (RSS) given by:

$$P = \sqrt{p^T R^{-1} p^*} \tag{1.61}$$

where p is the vector of pixel values from an individual image, R is the noise correlation matrix, resulting in a combination pixel value of P (25). It was soon realised after the initial introduction of phased array to cover large FOV that it can also be used to accelerate imaging speed; parallel imaging utilises the fact that multiple receive array coils

hold different spatial sensitivities, thus by combining multiple k-space data sets, only a subset of k-space is necessary from each receive coil for reconstruction, speeding up imaging acquisition times. There are many methods in k-space sampling in parallel imaging with sensitivity encoding (SENSE) (26) and generalised auto-calibrating partially parallel acquisitions (GRAPPA) (27) being widespread. Figure 1.24 shows some examples of the coils described in this section of the chapter.

Matching

After the completion of a coil resonating at the target frequency, it must be connected to a transmission line for NMR detection. The impedance of a transmission line depends on the dielectric properties of the insulator separating the two conductors and is conventionally equal to 50 Ω in the MRI community. The coil impedance must be matched to the transmission line to avoid signal losses by using a matching capacitor (Fig. 1.25). This process adjusts the impedance so that they are equal to be joined at an interface, but does not alter the resonating frequency of the RF coil. Lastly, since a coaxial cable is by definition unbalanced (the two conductors are not geometrically identical), balanced-unbalanced (baluns) transformers, also known as the *LC* or lattice baluns (Fig. 1.26) are introduced to avoid common mode currents, which are currents on the outer shield of an unbalanced coaxial cable when connected to a balanced coil.

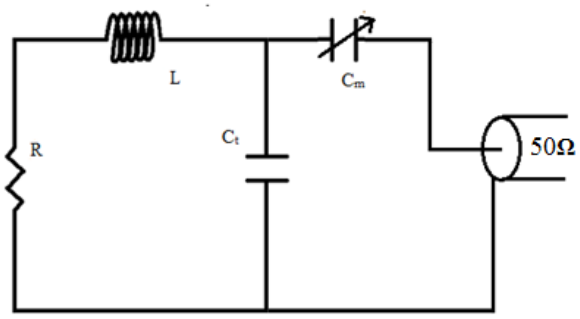

Figure 1.25. The matching capacitor C_m, which matches the impedance of the coil to the transmission coaxial cable, which is usually a variable capacitor.

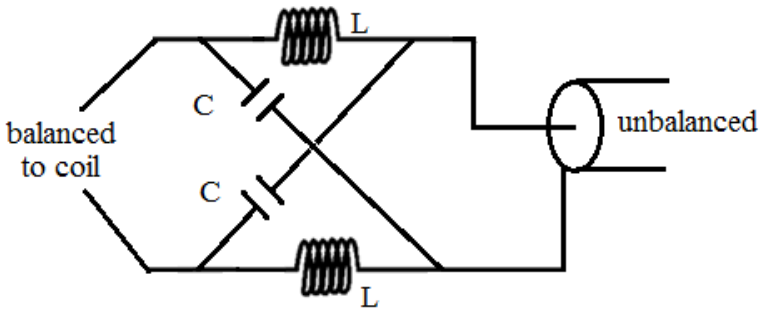

Figure 1.26. **A common balanced – unbalanced transformer, also known as the LC or lattice balun.**

1.3 Hyperpolarisation

By introducing a gaseous atom, MR imaging of the gas can reveal anatomical and functional information about the lung. Gases, however, have low spin density due to their physical density. A typical dose used in hyperpolarised ^{129}Xe imaging is about 500 - 1000 m*l* of gas in 5 – 6 *l* total lung volume (0.0037 moles of atoms in 1 *l*) in comparison to protons in water (110 moles of ^{1}H in 1 *l*). Considering that thermal nuclear polarisation is only about 1 in 100 000, the signal from thermally polarised gas is therefore very weak. By increasing the polarisation of ^{129}Xe with spin exchange optical pumping (SEOP), this density disadvantage can be counter balanced (Figure 1.27), and we can obtain a polarisation *P* in the order of 10% (equation 1.7).

1.3.1 Spin Exchange Optical Pumping (SEOP)

One method by which the polarisation of the noble gas atoms can be increased is by spin exchange optical pumping (28) in a glass cell containing an alkali metal, a noble gas, and buffer gases. The cell is heated with an oven that ensures saturated vapour pressure of alkali metal, where the following two steps occur:

Optical pumping is the excitation of an electron of an intermediate alkali metal into a higher excited state with a circularly polarised laser light of a specific wavelength determined by the difference in the energy levels between excitation states (Fig. 1.28 (A)). Even though any alkali metal can be used as the intermediate nucleus, rubidium (Rb) is usually used. It allows a reasonable temperature due to its high vapour pressure, and its excitation resonating frequency to excite valence electron falls within a region of spectrum where many tuneable lasers readily exist. A 794.77 nm polarised laser light is used to spin-polarise both the electron spin as well as the nuclear spin of Rb, resonant with the transition of $^2S_{½}$ ground state electron to the lowest excited state of $^2P_{½}$. The populations of the excited electrons in the $^2P_{½}$ state are evenly distributed in the spin -½ and ½ states through collisional mixing; therefore, the relaxation back to the ground state is of the same probability. Due to continued depletion of only the spin -½ state in the ground state, a net polarisation results in excess of the spin ½ state. The Pressure broadening gives the laser absorption linewidths of 30 GHz or more, well over that of Rb, to ensure adequate polarisation of Rb atoms.

Photons radiated by Rb are nearly un-polarised, thus can be reabsorbed by the Rb atoms, de-polarising the Rb atoms several times in a long cell. Nitrogen serves as a buffer gas removes this damaging mechanism and prevents radiation trapping from polarised photons, thus a N_2 gas density of 0.1 amagat or more is usually required in a SEOP system. The energy emitted from Rb is transferred to N_2 gas into vibrational and rotational motion with nitrogen moledules' large quenching absorption cross section. The nuclear spin of the alkali atom is conserved between excitation by a pumping photon and de-excited by a quenching collision with nitrogen, ready for another cycle. Through this method within a static magnetic field, the excited rubidium electron populates in the electron spin Zeeman ground state (see Sec. 1.1.1 for Zeeman splitting) . This is where the second part of SEOP (i.e. spin exchange) occurs.

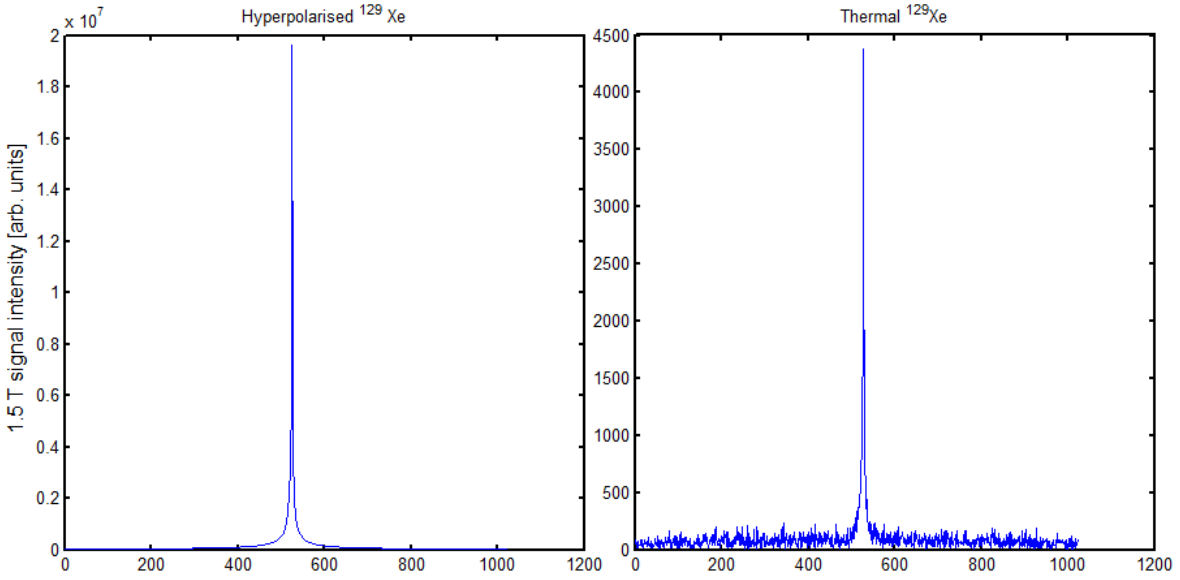

Figure 1.27. Left: hyperpolarised signal: 10 ml Xe (86% ^{129}Xe) with a 10 degree flip angle, single acquisition, Right: thermal signal: 5 ml Xe (86% ^{129}Xe, 5 ml O_2) with a 90 degree flip angle, averaged over 64 pulses.

The transfer of spin polarisation occurs when the two atoms are bound in van der Waals molecules or simple binary collision. The time for a binary collision is on the order of 10^{-12} s. Whereas binary collisions between Rb atom and helium atom are essential to the transfer of polarisation, the occurrence of van der Waals is also dominant with ^{129}Xe. The spin exchange cross-sections are quite large, typically 2 x 10^{-14} cm^2 , making this process efficient as the electron spins rotate about each other many times during a single collision. The electron spin of the Rb atoms can then exchange its polarisation with the nucleus of ^{129}Xe, populating positive ½ nuclear spin states in the gas atoms (Fig. 1.28 (B)). The rate of collisions is between 10^4 and 10^6 every second.

To increase the efficiency, N_2 and He are used in the cell as buffer gases. While the nitrogen prevents radiative emissions of circularly or linearly polarised photons, He, with a smaller Rb spin-destruction rate increases the linewidth of the laser absorption line by

collisional broadening. A magnetic field of a few hundred Gauss is also needed during this process to sufficiently suppress the relaxation due to van der Waals molecules at these low pressures.

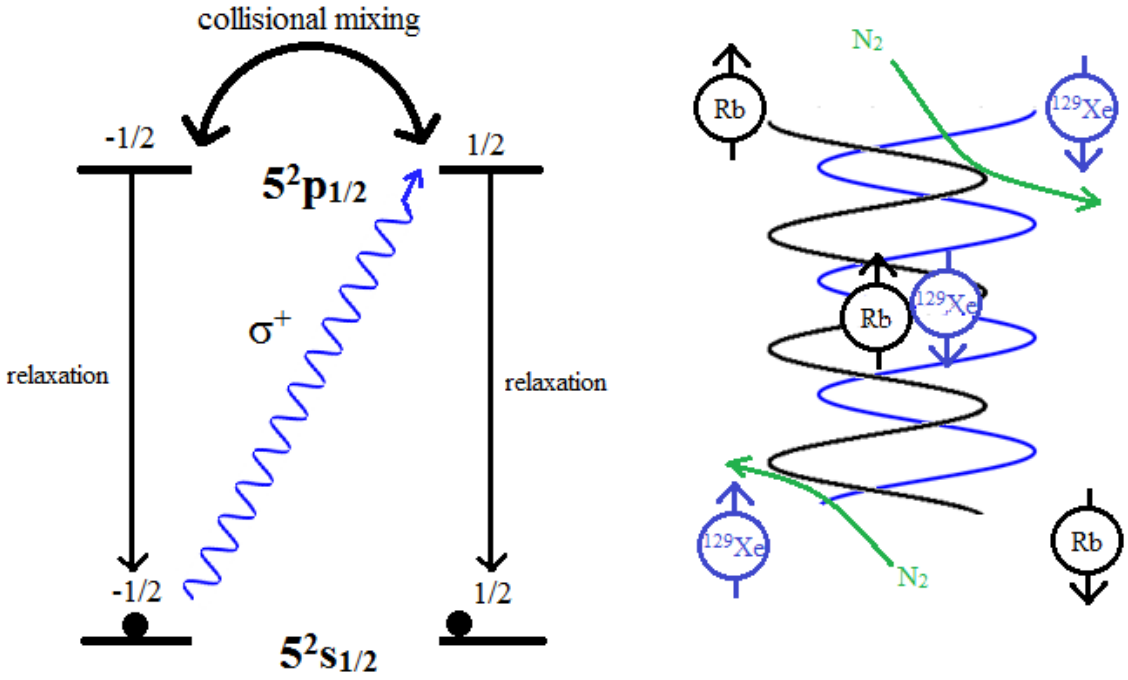

(A) (B)

Figure 1.28. (A) Excitation of an electron from a rubidium atom to an excited state. When the electron relaxes back to its original orbital, it stays in the positive ½ spin state. (B) the exchange of spin with the ^{129}Xe with N_2 as a buffer gas.

The process of spin exchange optical pumping increases the polarisation of ^{129}Xe to an excess of 10%, which is an increase of approximately five orders of magnitude higher compared to the thermal polarisation via Boltzmann distribution. This process provides a hyperpolarised $^{3}He/^{129}Xe$ signal comparable to that obtainable to that of water thermally polarised NMR and is thus detectable in physiologically feasible concentrations when inhaled.

Even though both ^{3}He and ^{129}Xe can be polarised via SEOP, the practical implementations are different. ^{3}He hyperpolarisation can take place at high pressure (> 5 Bar), which increases laser absorption by broadening the rubidium absorption line, while not effecting polarisation. A batch of ^{3}He can typically be polarised to ~30% polarisation in 18 h via rubidium SEOP. Recent improvement of hybrid SEOP involves using a mixture of potassium and rubidium as the alkali metals, which show significant improvement on efficiency (29,30). ^{129}Xe, optical pumping by spin exchange on the other hand, has a few more considerations. Since the electron cloud of ^{129}Xe is distorted easily upon collision with the cell wall and other atoms, the T_1 relaxation time of ^{129}Xe is very short, in order of minutes. Also, the chance of collision of ^{129}Xe with the cross-section of an optically pumped alkali vapour is very large and thus also lowers the achievable polarisation. Xenon requires lower partial pressures in the optical pumping mixture as spin-relaxation mechanism with the rubidium atom valence electron is more potent than for ^{3}He, therefore xenon is typically polarised in lower concentration under flow with cryogenic freeze out. The method of hyperpolarising ^{129}Xe in "continuous flow" was first introduced by Driehuys (31) operating with a high gas density with buffer gases N_2 and ^{4}He, collected cryogenically. Another method more recently by Hersman et al (32) was developed operating at low gas density and has proven to be a very efficient xenon polariser suitable for clinical use.

1.3.2 Sheffield polariser

Our group has developed an in-home "continuous flow" polariser which is described in full by Norquay et al(33). The system operates at a total gas pressure inside the cell of 2 bar at the iso-centre of Helmholtz pair coils of diameter 80 cm, with a B_0 ~2.7 mT. The Pyrex optical cell (25 cm in length and 5 cm in diameter) is filled with <1 g of molten rubidium inside a non-magnetic ceramic hot-air oven operating at 373 K. Optical pumping is achieved by the use of an external cavity diode laser with laser emission centred on

794.77 nm with a full width at half max of 0.09 ± 0.01 nm. The gas mixture consist of 3% isotopically enriched Xe (86% ^{129}Xe), 10% N_2, and 87% He (Spectra Gases, UK), and is collected cryogenically within a glassware (Fig. 1.29 (b)) at a magnetic holding field with a field strength of ~0.3 T using liquid nitrogen and collected in the solid state. The high freezing point of xenon make it possible to separate xenon from the other gases as they exit collection as gases and the magnetic field is used to achieve a long solid xenon relaxation time during the accumulation process, which limits the loss of polarisation in the freezing process.

After 30-40 minutes accumulation, the frozen xenon was then melted and collected in a 1 / Tedlar bag and filled up with medical grade N_2 gas. This system has been in use with consistently over 10% polarisation for the past year at a production rate of 10 ml of hyperpolarised ^{129}Xe / min (Fig. 1.29). For polarisation level estimates, the signals from 10 ml HP Xe samples were compared to a reference signal (100 acquisition-average) from a 10 ml thermal xenon sample containing 50 % O_2 (T_1 ~ 6 s) using a small saddle coil.

This system has been optimised with the following parameters: (a)temperature, (b) flow rate, (c) frozen xenon decay, (d) accumulation time, and is described fully in details by Norquay et al (33) to a polarisation level excess of 13%

Imaging using the home polariser have shown consistency over the past year in over 100 in vivo lung imaging studies in small doses (<400 ml) and can provide high quality images of the lungs (SNR range 21–53 with a spatial resolution of 15 mm × 4 mm × 4 mm voxel).

Also note that all xenon polarised in this study was done under a special UK MHRA regulating license.

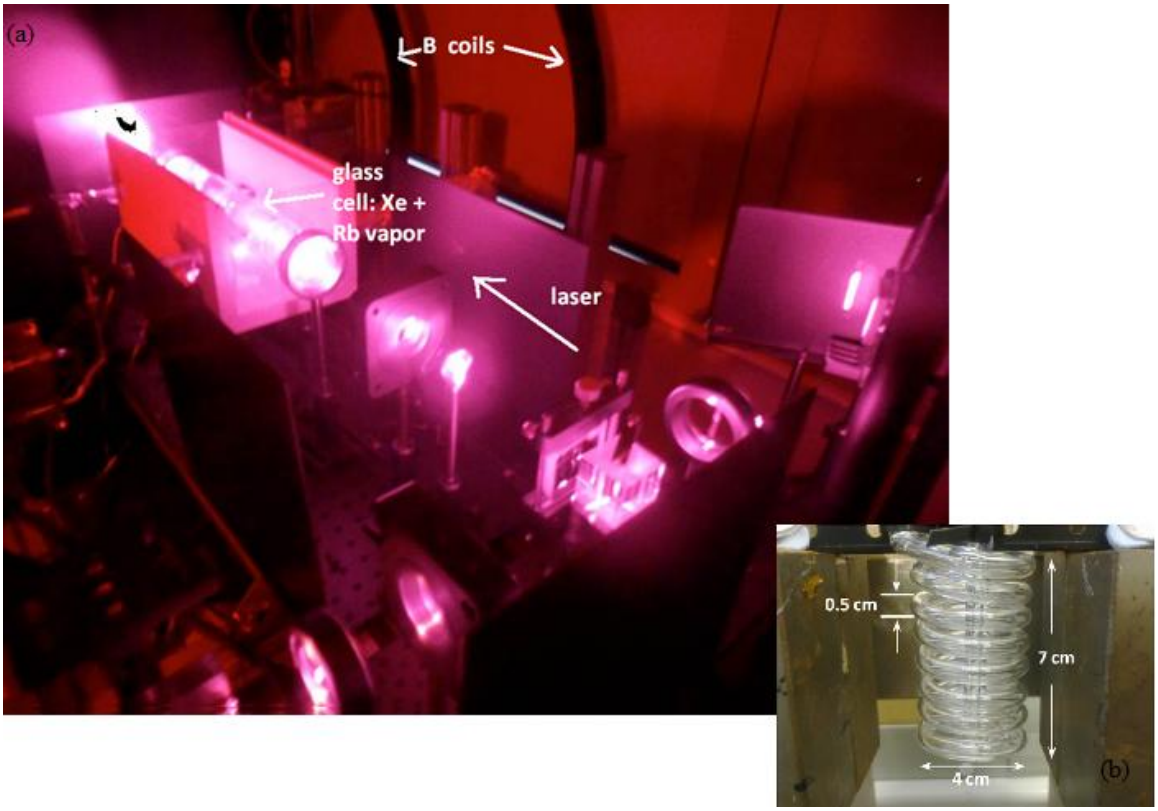

Figure 1.29. **Apparatus of a homebuilt regulatory-approved polariser system for ^{129}Xe, where gas is accumulated within the spiral glassware (b) cryogenically at a holding magnetic field of ~0.3 T (33).**

CHAPTER 2: Hyperpolarised Gas Magnetic Resonance Imaging in Human Lungs – A Brief Overview

2.1 Introduction

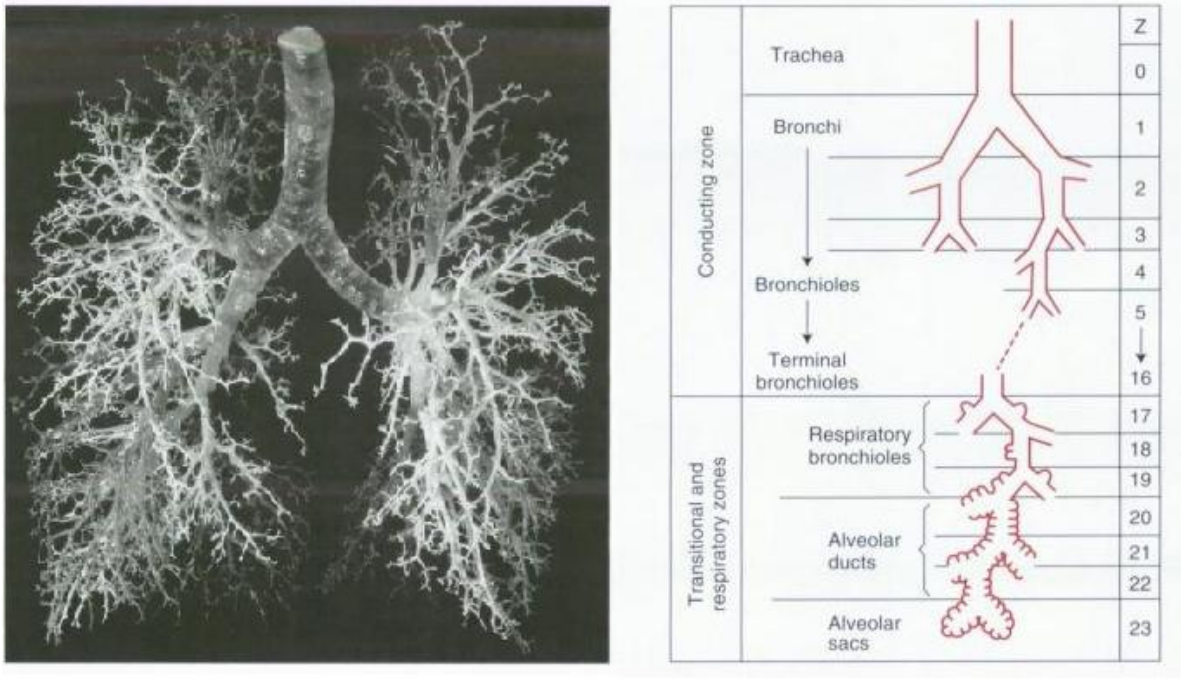

Figure 2.1. Left: cast of the airways of a human lung less alveoli, showing conducting airways from trachea to terminal bronchioles. Right: Model of the human airways proposed by Weibel into conducting zone (16 generations) and transitional and respiratory zones (Taken from (34), Fig 1-3 and Fig 1-4).

The lungs make up an essential organ primarily used for gas exchange to allow oxygen into the venous blood and remove carbon dioxide. The lungs branch off from the trachea into narrower and shorter branches of bronchi (also known as the conducting airways (Fig. 2.1

(right)) where no gas exchange takes place and they constitute the anatomic dead space of about 150 ml. The airways continue to divide until reaching terminal bronchioles, and eventually terminate at the alveoli after 25 generations of tree-like branching (Fig 2.1 after Weibel). The lungs have a large surface area between 50 to 100 m^2, made possible by ~500 million terminal alveoli, each about 0.33 mm in diameter and 0.2 – 0.3 µm in wall thickness (34).

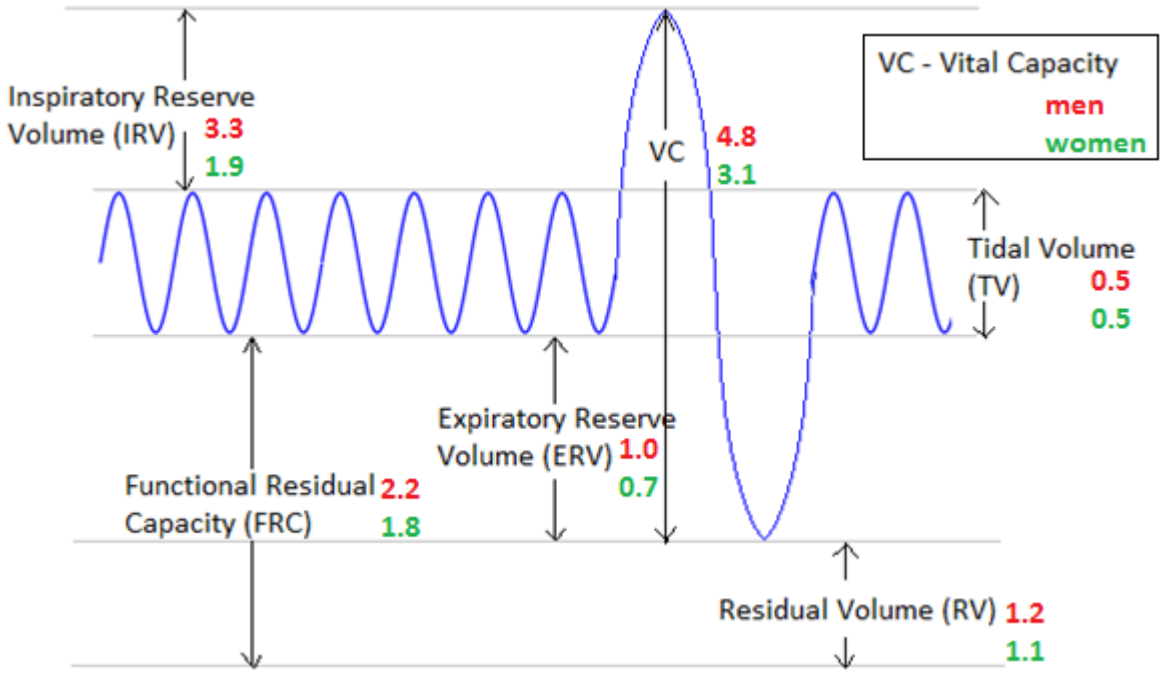

Figure 2.2. Lung volumes of interest for adult men (red) and women (green) in litres. Some of the key lung volumes that are used in this thesis are TLC (the volume of the lungs at maximum inflation, RV + VC), RV (the volume of the lungs at maximum exhalation) and FRC (the volume of the lungs after normal exhalation).

The most common technique currently used for diagnosing abnormalities in lung function is spirometry (35,36), a global whole lung pulmonary function test using a spirometer to measure the volume and flow of inhalation and exhalation at the mouth. The basic form of the test is performed using a flow sensor with a filter mouthpiece and a nose clip to

prevent breathing through the nose. The patient is asked to inhale as much in as possible and exhale as hard as possible into the detector for as long as possible. The most important measured parameters in spirometry are:

(a) Forced vital capacity (equivalent to VC in Figure 2.2): Volume of air, measured in litres that can be forcefully blown out after a full inspiration.

(b) Forced expiratory volume in one second (FEV_1): Volume of air, measured in litres that can be forcefully blown out in one second after a full inspiration. Healthy adult male/female has a normal value decreases almost linearly with age from 4.5 *l*/3.25 *l* at age of 20. A value that falls 80 – 120 % of that value is diagnosed as normal. (37)

(c) Forced expiratory flow (FEF) 25-75%: The mean flow/speed of air coming out of the lung from 25% of FVC expired to 75% of the FVC expired.

(d) Diffusion capacity (DL_{CO}): Carbon dioxide uptake in a single inspiration of ~10 s. A measurement of the trace quantities of CO at the end of a breathing cycle determines how much is absorbed by the lung during breathing, which can pick up diseases that lead to diffusion obstruction, like ones in pulmonary fibrosis.(38)

Since spirometry measures the whole lung function (39,40), it lacks regional information and can have a large range of variation based on patient co-operation, effort and techniques (35,41). Spirometry can therefore miss subtle changes in lung patho-physiology. Figure 2.2 shows some of the normal lung volumes of interest in healthy adults (42). Note that these values are highly variable depending on many co-founding factors; a few examples are subject height, weight, and elevation. These factors can be normalised for by expressing the spirometry measurements in percentage of predicted values.

Spirometry thus has no sensitivity to regional lung function. Medical imaging can help provide regional and structural information; Computed Tomography (CT) has been used to obtain structural information of the lungs with high resolution (43-47) (Fig. 2.3). This modality provides soft tissue contrast for the lungs, as well as the surrounding tissues based on different tissue density relative to air and water. Significant correlations have been found between emphysema morphology of the lungs and CT emphysema score in determining severity of the disease (48-51). CT is also the modality of choice for structural imaging of the lungs in lung cancer although the poor soft tissue contrast of CT makes structural delineation of tumours and mediastinal abnormality difficult. The radiation dosage required for CT imaging, however, is not ideal for longitudinal studies at the moment or assessment of short term changes in response to respiratory therapy evaluation. This is a particular concern in children. The health risk of a 10 mSv whole body CT scans was estimated to increase the risk of death from radiation-related cancer to 1 in 1250 (52). Many studies in recent years have been focused on lowering the radiation dosage substantially (53,54), with volume CT chest studies now possible with doses of 3-4 mSv (comparable with the annual background radiation dose) so future use for longitudinal imaging is still under investigation. Previous studies showed good concordance between CT and emphysema physiology, however, there are still variations that underestimate mild emphysema and overestimate severe emphysema (51). Nuclear medicine uses injected or inhaled radiopharmaceuticals to externally detect emitted radiation to form images. ^{99m}Tc is used in lung scintigraphy (Fig. 2.4) and the emitted gamma ray radiation provides functional information (i.e. ventilation, perfusion). In the ventilation phase of the procedure, the patient is asked to inhale through a mouthpiece a gaseous technetium pentetic acid in an aerosol form, which remains in place for sufficient time to allow imaging of the distribution of the aerated lung volume. The perfusion phase of the procedure is done by intravenous injection of the radioactive technetium (^{99m}Tc) macroaggregated albumin (MAA), which localises by the mechanism of capillary blockade. In healthy subject, less than 1 in 1000 of the capillaries is blocked, thus a large number of

particles must be injected for a meaningful statistical distribution of functional blood vessels (55). Images are obtained from the emitted gamma rays in both cases. Nuclear medicine imaging suffers from poor spatial resolution (56), cannot reveal small airway changes, and is also associated with radiation deposition (dose ~1mSv).

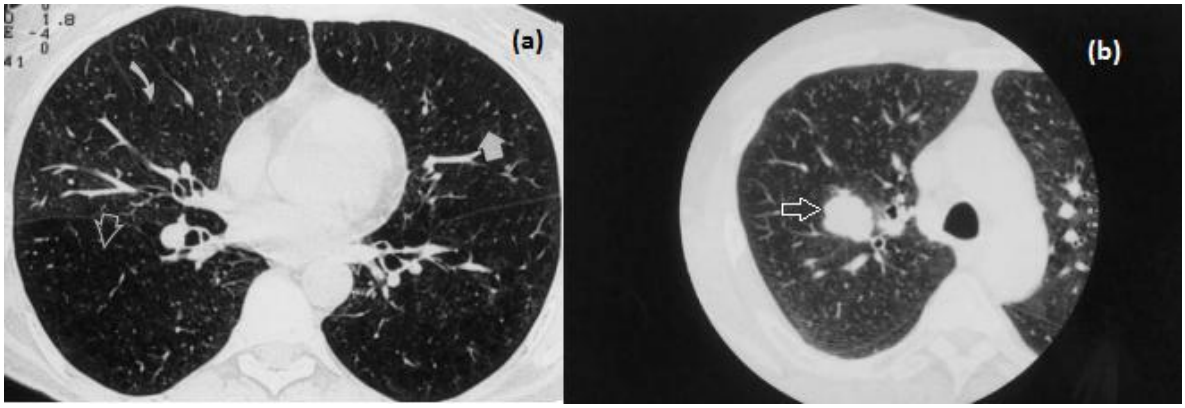

Figure 2.3. **(a) High resolution Computer Tomography (CT) image of an emphysema patient where lung tissues appears darker (white arrow)(57) ; (b) CT image of a cancer patient showing a solid nodule in the lungs (white arrow) (58)** .

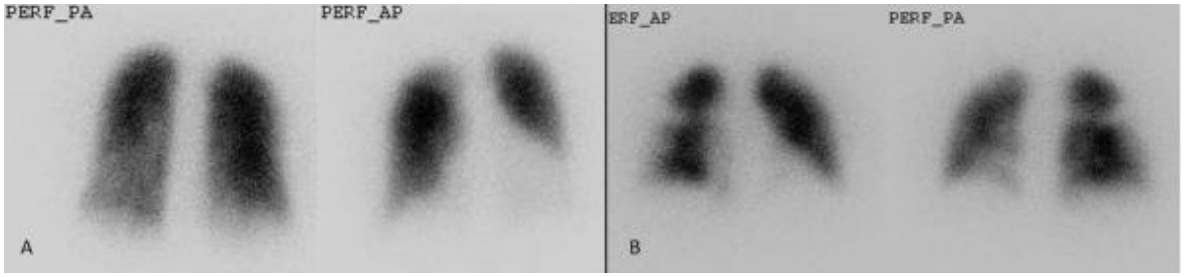

Figure 2.4. **Anterior and posterior view of perfusion scintigraphy of: (A) a patient with normal lung perfusion; (B) a patient with chronic thromboembolic pulmonary hypertension with bilateral segmental perfusion defects (59).**

Proton magnetic resonance (MR) imaging (60) and variants such as oxygen-enhanced proton MRI (61) have also been used to image the lungs. Although motion artefacts

caused by cardiac and respiratory systems can degrade MR images, this can be corrected by cardiac (62) and respiratory (63) gating. Therefore, the biggest challenge of proton MR imaging of the lungs comes from the magnetic susceptibility due to the large number of air-tissue interfaces (64), as well as the low density of protons (~0.2 g/cm^3) in the lung, producing limited imaging signal and resolution. Nevertheless with the use of short echo times and parallel imaging methods (65), proton lung MRI is starting to make an impact as a functionally sensitive (66-68) alternative to CT (69) (Fig. 2.5 (a)), particularly in the detection of mucus, consolidated masses and tumours where elevated proton density and T_1 and T_2 contrast can provide pathological insight, examples of proton MRI in diseased lungs are shown in Figure 2.5 (b) and (c) (70).

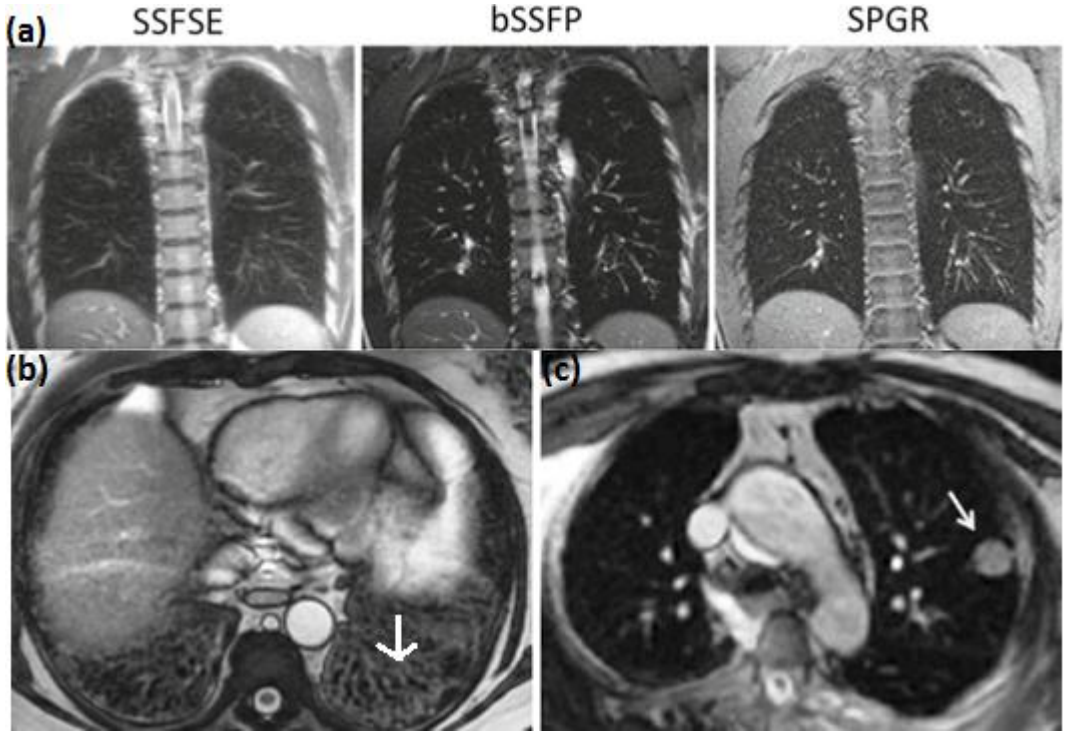

Figure 2.5. 1.5 T proton anatomical images from SSFSE (single shot fast spin echo), bSSFP (balanced steady-state free precession, and SPGR (spoiled gradient echo) sequences of a healthy volunteer (a), as well as bSSFP MR images of: (b) a patient with fibrosis in the lung bases and (c) a patient with a peripheral 12-mm lung nodule, indicated by white arrows (70).

2.2 Clinical Hyperpolarised Gas MR Imaging

In the relatively new imaging modality of hyperpolarised (HP) gas imaging (71-73), noble gases such as ^{3}He and ^{129}Xe can be inhaled to visualise air spaces within the lungs regionally. After first demonstration of the potential of the method for imaging the airspaces with ^{129}Xe in rodent lungs (74), ^{3}He soon became the preferred noble gas used in clinical lung imaging research due to its large gyromagnetic ratio offering higher imaging SNR. A comparison of a ^{3}He ventilation image with a CT image of the same patient with COPD-emphysema is shown side by side in Fig. 2.6.

^{3}He and ^{129}Xe can be both hyperpolarised via spin exchange optical pumping (SEOP) (28) which significantly increases the signal strength (typically five orders of magnitude lager than that of thermal magnetisation at 3T). Correlations have been shown between the two noble gases with apparent diffusion coefficient (ADC) values (75) , ventilation defects, as well as changes after treatment (76).

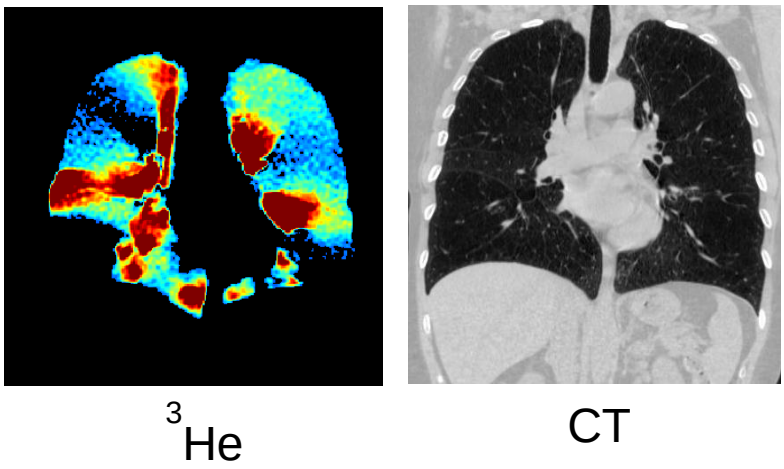

Figure 2.6 ^{3}He ventilation image and CT image of the same slice of the same volunteer. Ventilation defects are seen in the upper and lower right lung with evidence of reduced parenchymal density (emphysema) in the CT in the same regions (77)

MRI of HP ^{3}He gas has been evaluated in pre-clinical studies for different lung diseases (78,79) and has been shown to have high sensitivity to early stage lung disease such as

early presymptomatic smoking related emphysema (80) and early obstruction of the airways in paediatric cystic fibrosis patients (81) who have normal spirometry test results.

The safety of the technique (82) and its inherent sensitivity to regional lung ventilation and function make it an ideal imaging tool for the assessment of novel lung therapies (83-85).

There are a number of limitations associated with hyperpolarised gas MRI. The foremost limitation is the nature of hyperpolarisation prior to imaging, opposed to relying on thermal polarisation in proton imaging. The RF excitation pulses and T_1 decay will continue to deplete signal intensity until it is exhausted, therefore each RF pulse used must be considered and the k-space trajectory optimised. Secondly, most of the studies done using hyperpolarised MRI are acquired in a static single breath hold, thus limiting the imaging time to under 20 s, especially for patients with lung diseases. Experiment setup will be shown in Section 3.2. Next, commercially built RF coils are made for proton imaging, thus many modifications are needed such as the receiver bandwidth, pulse sequence development, as well as custom made coils needed for hyperpolarised nuclei of different resonating frequencies. When it comes to the cost of hyperpolarised gas MRI, both ^{3}He (~$850 per litre (86)) and isotopically enriched ^{129}Xe (~$100 per litre for >80% (87)) to this day are still very expensive to purchase. There is only 5.2 ppm helium by volume in the Earth's atmosphere, of which the natural abundance for ^{3}He in helium gas as an isotope is 1.38 ppm, thus 7.2 parts per trillion of the atmosphere (88), so it remains expensive as its source is through tritium decay as the by-product of nuclear industry. Currently all ^{3}He in use for clinical lung imaging research is administered and released from the USA Department of Energy via the National Institute for Health. This release is allowing ^{3}He MRI to be used for well-defined clinical research questions but being used as a routine clinical diagnostic lung-imaging agent is not realistic.

Recent studies (89) have shown that similar qualitative ventilation images can be achieved using the more readily available inert gas ^{129}Xe (90). Xenon has the added functionality of

being soluble in blood and thus can be used to image lung ventilation perfusion (91) and alveolar-capillary gas exchange (92).

^{129}Xe is 26.44% naturally abundant as an isotope of xenon and can be extracted from the Earth's atmosphere (87 ppm) (93), but the cost is currently also high for enriched (86% ^{129}Xe) xenon (~$170 per litre) compared to natural abundance xenon (~$30 per litre) (86). Enriched ^{129}Xe is what has been used for the *in vivo* imaging in this thesis.

2.3 Ventilation Weighted Imaging (static breath-hold imaging)

2.3.1 ^{3}He

For the most basic evaluation and diagnosis of obstructive airway diseases, patients are asked to inhale a fixed volume of hyperpolarised gas after a full exhalation and hold their breath for a few seconds while ventilation images can be obtained. The images show polarised gas density and position of ventilation defects as dark void areas where gas cannot penetrate (78,94,95), providing regional insight into lung ventilation in obstructive respiratory diseases such as cystic fibrosis (85) and asthma (96). Image SNR is directly proportional to gas spin density, which in turn is proportional to lung ventilation.

If 3D pulse sequences are used, the whole lung volume can be imaged allowing direct calculation of the ventilated lung volume (97) (Fig.2.7).

Disease diagnosis from the 3D information can still be very difficult, especially at the borders and edges of the lungs where susceptibility artefacts and B_1 coil inhomogeneity can cause non-uniformity in image SNR and lead to mis-diagnosis of ventilation defects (98,99). Efforts can be made to counter the lung border artefacts by using registration of Helium images to that of proton MRI (81) or CT images (100). The visual impact of these

ventilation images in lung disease is striking when compared to alternative methods such as the nuclear medicine ventilation scan.

Figure 2.7. Surface-rendered 3D lung volume data set obtained from a 3D in vivo imaging experiment (taken from (97) Fig. 4).

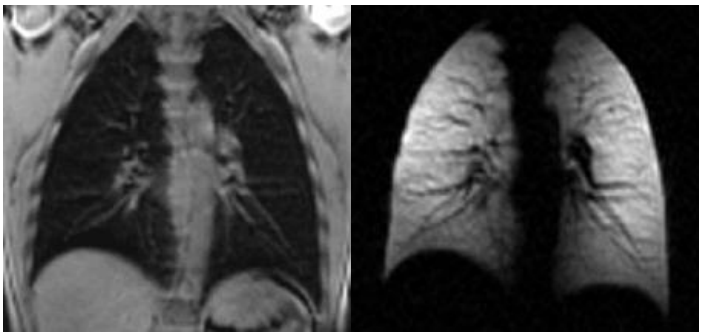

Figure 2.8. Left: a proton image of a healthy volunteer, the pulmonary vessels are prominent due to their higher density but the airspaces are predominantly dark due to the low proton tissue density and magnetic field inhomogeneity. Right: ^{3}He HP gas image of the same healthy volunteer acquired from the same slice in the same breath-hold, notice the homogeneous distribution of the gas density in the airspace.

Figure 2.9 shows the proton and ^{3}He images of a healthy volunteer. One of the useful parameters we can obtain from the two images is percentage ventilation volume or %vV, calculated by using ventilated volume from segmented ^{3}He images divided by the total

lung capacity from the proton scan (Fig. 2.9 (c)). The immediate problem rises as the lung inflation level is not constant between scans, thus co-registered images obtained within a single breath-hold is preferable, and has been implemented and used with success (101).

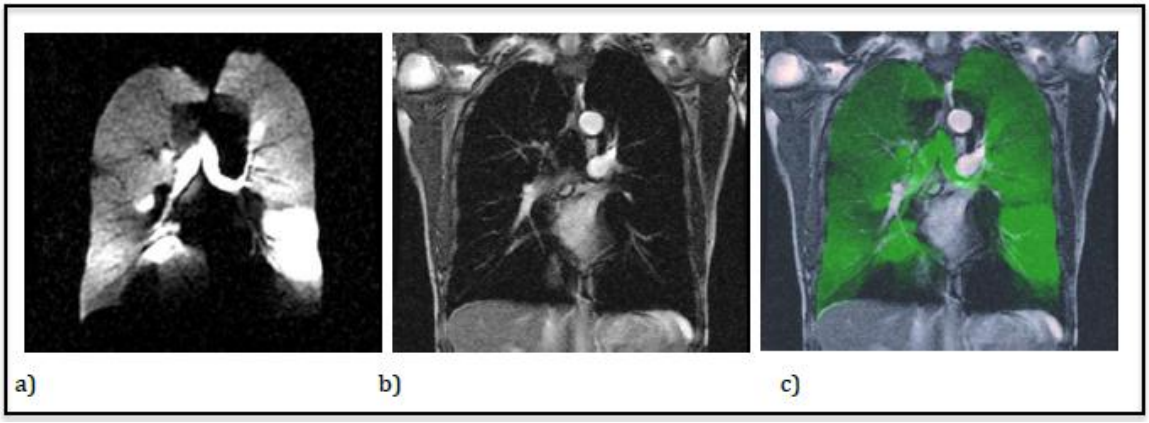

Figure 2.9. (a)^{3}He ventilation image, (b) registered proton image, (c) overlapping proton and ^{3}He images (102). Image courtesy Sam Janoff BMedSci Thesis University of Sheffield 2012.

2.3.2 ^{129}Xe

^{3}He is not the only gaseous noble gas used in HP gas MR imaging. The techniques and methods may also be applied to other gases, such as ^{129}Xe (103,104). The disadvantage of using ^{129}Xe is that its gyromagnetic ratio is only one third of that of ^{3}He (Table 1.1), and since SNR is roughly proportional to gyromagnetic ratio in hyperpolarised gas MRI (see Chapter 3 for proof), ^{129}Xe would have around a 3 fold lower SNR than ^{3}He if the amount of gas used and polarisation were identical. The smaller gyromagnetic ratio, however, does decrease dephasing due to off-resonance effects from magnetic-susceptibility interfaces. To maximise the image SNR of ^{129}Xe, we must maximise polarisation, use enriched ^{129}Xe mixtures, and optimised RF-coil technology and pulse sequence design. It is also important to note the physical differences between the two nuclei, as ^{3}He is a lighter, smaller atom compared to air whereas ^{129}Xe is heavier and denser which in turn

would affect the flow and distribution of the gases upon inhalation. The quality of ^{129}Xe imaging has improved as the polarisation levels possible with ^{129}Xe improved in the last fifteen years (105), giving results comparable to those with ^{3}He. The first MR image of the lungs using hyperpolarised ^{129}Xe was obtained in 1997 with a polarisation of 2% with voxel size of 0.9 cm^2, and had a SNR of 28 using 1 *l* of gas (Fig 2.10, top). Today, with improved polarisation of the gas, MR images can be obtained for 0.25 cm^2 voxel size using 300 m*l* of ^{129}Xe with SNR of ~50 (Fig 2.10, bottom, see Chapter 3 – 4 for more images). The significant increase in SNR is due to the increase of polarisation and optimisation of image acquisition methods. These images show homogenous signal distribution same as those from ^{3}He in healthy volunteers.

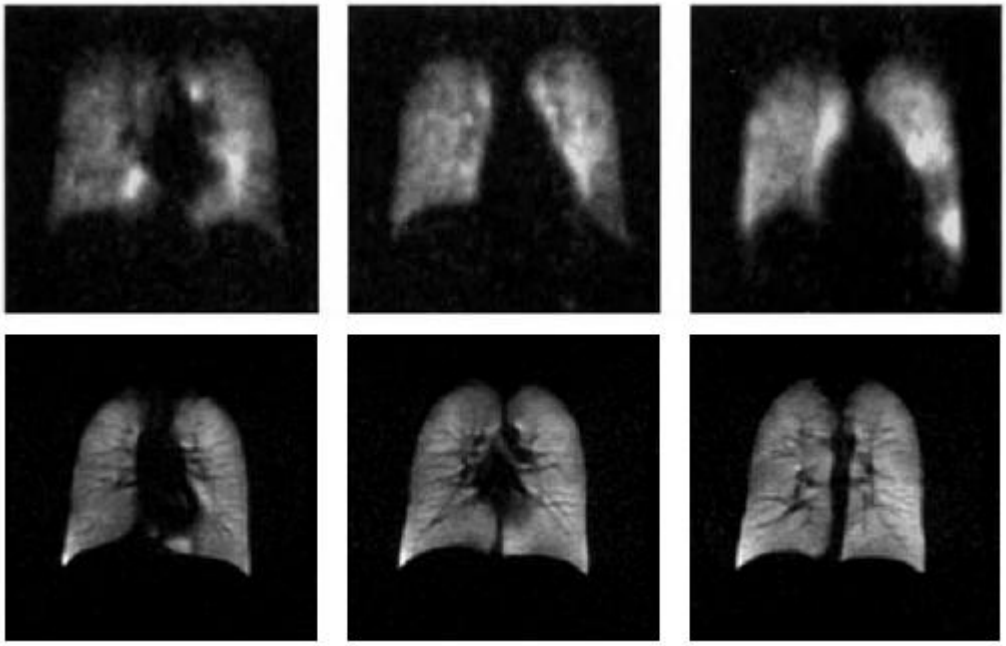

Figure 2.10. Coronal ventilation images of healthy human lungs using hyperpolarised ^{129}Xe. Top: the first MR images of the lungs using hyperpolarised ^{129}Xe in voxel size of 0.9 cm^2 (SNR of 28) in 1997 using 1 *l* of gas taken from (105); bottom: MR images obtained in this thesis from 0.25 cm^2 voxel size using 300 m*l* of ^{129}Xe (SNR of 50)(90).

Ventilation defects and functional abnormalities can also been seen using hyperpolarised ^{129}Xe. The images show qualitatively similar results to defects seen in ^{3}He images. ^{129}Xe,

however, is a much larger atom, therefore, direct comparisons between the two noble gases have shown that the signal distribution may be more sensitive to detection of mild disease using ^{129}Xe than that of ^{3}He (87,106) as it is less diffusive (see Section 2.4). There are partial obstructions observed in ^{129}Xe images that appear better ventilated in ^{3}He images of the same volunteers, indicating the more diffusive nature of ^{3}He (107) (Fig 2.11).

Despite its known anaesthetic effect, ^{129}Xe is well tolerated (108,109) in doses of 500 m*l* – 1 *l* in healthy subjects and in those with mild or moderate COPD with symptoms consistent with its anaesthetic properties such as dizziness, euphoria and hypoesthesia. All symptoms typically resolve within 2 minutes with no clinical intervention. Functional defects through ventilation imaging using ^{129}Xe have shown sensitivity to subjects with asthma, COPD and cystic fibrosis (91).

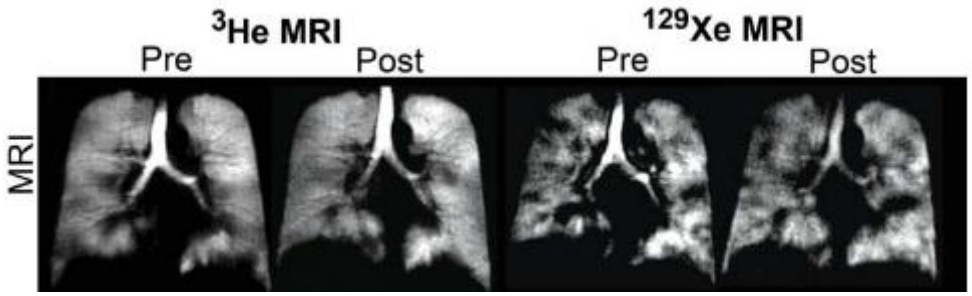

Figure 2.11. ^{3}He and ^{129}Xe ventilation images of the same subject pre and post salbutamol (taken from (107) Fig. 1). Note the more heterogeneous ventilation seen with ^{129}Xe in the same subject.

2.4 Diffusion Studies

2.4.1 Free Diffusion

The measurement of the Brownian diffusion of hyperpolarised gases in the lungs with magnetic resonance imaging can reveal information on lung micro-structure. The root mean square distance, l_0, travelled by particles by diffusion in free space over a time, δ, can be calculated from the Einstein diffusion equation:

$$l_0 = \sqrt{2D_0\delta} \qquad (2.1)$$

where D_0 is the free diffusion coefficient at a specific temperature and δ is the diffusion time. ^{3}He, for example, has a D_0 value of ~ 0.88 cm^2/s at body temperature of 37 ^{o}C within a mixture of typical of the concentration found when inhaled in the lungs (110). Protons (^{1}H), in water, have a D_0 value of 1.1 x 10^{-5} cm^2/s in comparison (111).

2.4.2 Restricted Diffusion

When diffusion becomes restricted in a porous medium due to collisions with the walls, movement of the atoms becomes limited and the root mean square distance shortens. The airways, walls, and alveoli in the lungs serve as obstacles to restrict the movement of gas atoms.

With such restrictions, diffusion is now characterised by an apparent diffusion coefficient (ADC), which is always less than the free diffusion coefficient (which is limited by the mean free path from kinetic theory) and highly dependent on the geometry of the medium (Fig. 2.12). Restricted diffusion for equation 2.1 can be expressed as:

$$l_0 = \sqrt{2ADC \cdot \delta} \qquad (2.2)$$

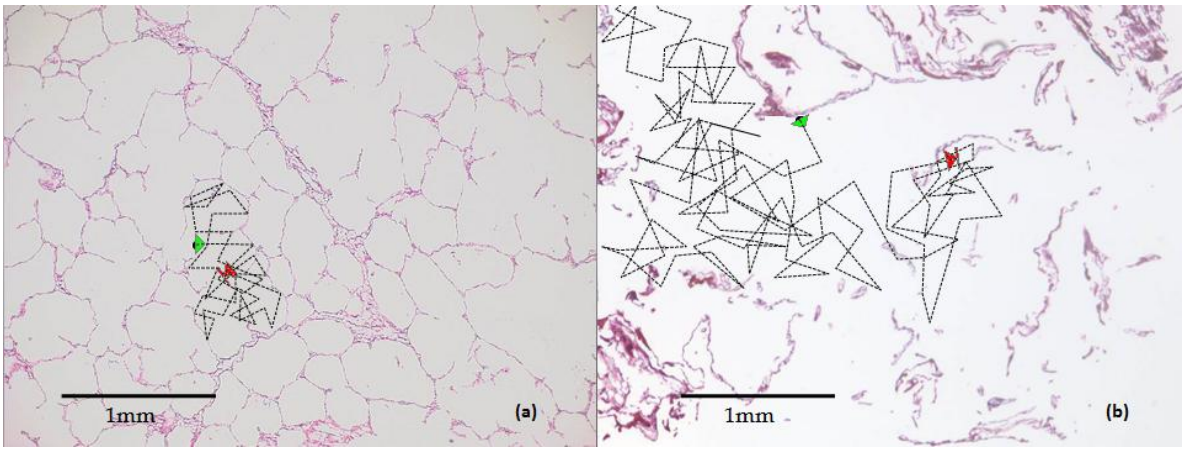

Figure 2.12. Schematics of restricted diffusion in healthy lung tissue (left) and emphysematous lung airspace (right). Image from Xiaojun Xu, MSc Thesis, University of Western Ontario 2009.

The ADC of ^{3}He in healthy, human lungs is 0.20 cm^2/s at a 1.8 ms of diffusion time (30), and ^{3}He nucleus may travel across the alveoli of 300 μm in diameter in a short period of 1 ms.

Diffusion leads to enhanced transverse relaxation (dephasing) of the MR gradient echo signal (Eq. 1.28). Signal decay due to diffusion in MR imaging is related to the diffusion coefficient and the b-value by:

$$S = S_0 e^{-\frac{TE}{T_2^*}} e^{-\frac{TR}{T_1}} e^{-b \cdot ADC} \tag{2.3}$$

where TE and TR are echo time and repetition time respectively, and b-value is a parametric representation of diffusion dephasing in MR to incorporate the effects of both gradient strength and diffusion time of the pulse sequence. S_0 is the initial signal, and ADC is the apparent diffusion coefficient. For a bipolar gradient echo sequence, the b-value is given by (29):

$$b = (\gamma G_{\max})^2 \delta^2 \left[\left(\Delta - \frac{\delta}{3} \right) + \tau \left(\delta^2 - 2\Delta\delta + \Delta\tau - \frac{7}{6}\delta\tau + \frac{8}{15}\tau^2 \right) \right] \tag{2.4}$$

with a corresponding gradient shape shown in Fig. 2.13, where γ is the gyromagnetic ratio.

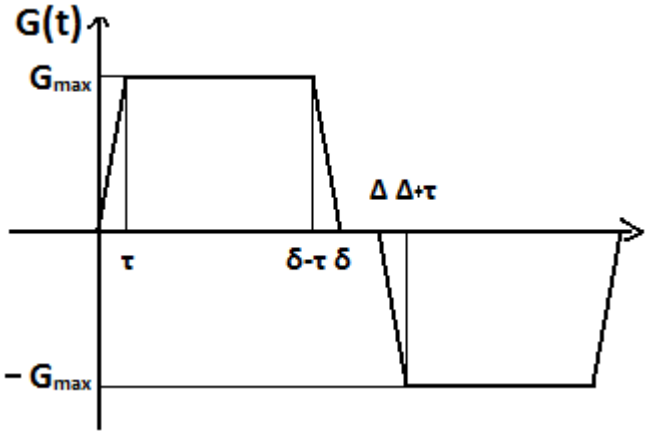

Figure 2.13. **A bipolar gradient waveform**

In a simplified bipolar gradient where there is no delay between the two lobes, $\delta = \Delta$, then equation 2.4 can be simplified to:

$$b = \gamma^2 G_{\max}{}^2 \left(\frac{2}{3}\delta^3 + (\tau - 2)\delta^2 - \frac{1}{6}\tau^2\delta + \frac{8}{15}\tau^3 \right) \tag{2.5}$$

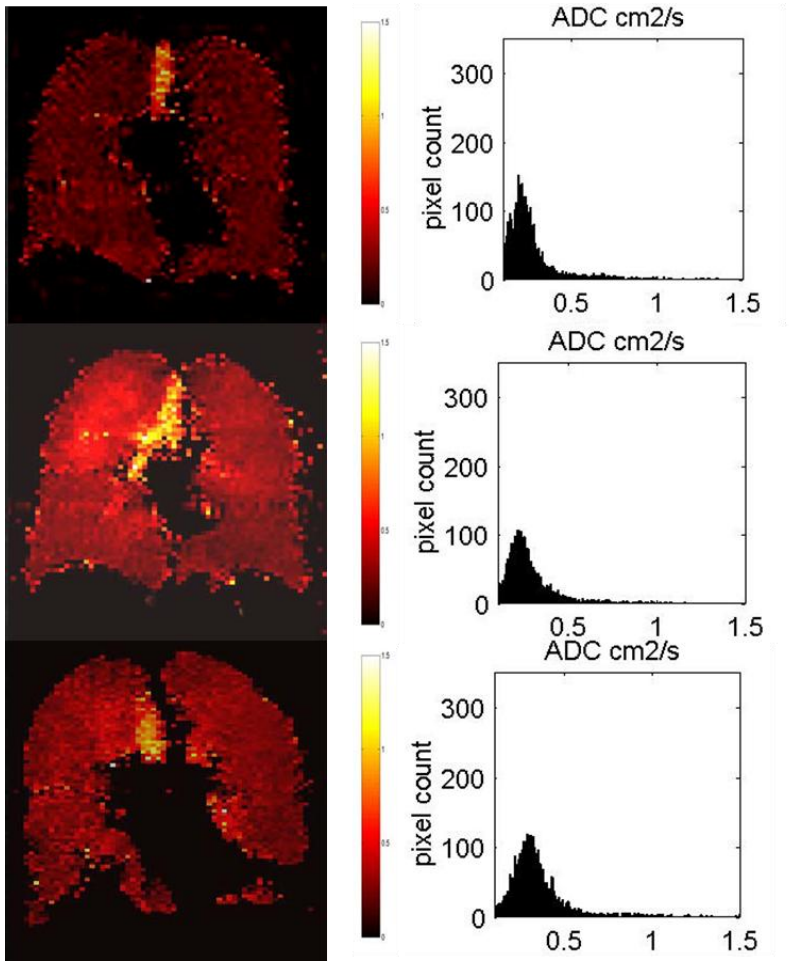

Figure 2.14. Apparent diffusion coefficients (ADC) with the ^{3}He are mapped out pixel-by-pixel in the second column, and an increase of ADC is visible. Lastly, the ADCs are plotted in histograms in the third column, clearly show the broadening and increase of ADCs in the smoker and emphysema patient. A: 48-year-old, female, healthy, non-smoker; B: 51-year-old, female, healthy, smoker with normal spirometry; C: 62-year-old, male, emphysema/COPD patient.

Clinically, diffusion mapping in the lungs is usually computed assuming a mono-exponential decay from two images with either variable gradient (G_{max}) or variable diffusion time (δ), which generates two signals $S_{norm1} = Ae^{-b_1 \cdot ADC}$, and $S_{norm2} = Ae^{-b_2 \cdot ADC}$. A is a common factor in both images due to electronic factors, flip angle and relaxation. The ADC can then be calculated by subtracting the logarithms of the two normalised signals and divide by the change in b-value:

$$S_{norm1} / S_{norm2} = e^{-\Delta b \cdot ADC}$$
$$ADC = -\frac{\ln S_{norm1} - \ln S_{norm2}}{\Delta b} \quad (2.6)$$

Diffusion is always a factor for consideration in hyperpolarised gas MR imaging due to the high diffusivity of gas atoms, thus it is important to have a thorough understanding of the physics behind it to know when its effect is negligible, and when the effect has to be taken into consideration. The experiments of this thesis will not be directly linked to diffusion measurements, but it is appropriate to discuss it here in detail for discussions in later chapters around transverse relaxation as it plays a role in these mechanisms.

2.4.3 ^{3}He

Diffusion of ^{3}He is so sensitive to the lung alveolar geometry that it can detect changes from aging (112,113) and has been shown to correlate well with alveolar surface area to volume ratios from histology (114). Although diffusion-weighted images (Fig. 2.14) do show significant correlation with FEV_1 (forced expiratory volume in 1 second) for diagnosing emphysema (115), more interesting in terms of early diagnostic potential is the ability of the ^{3}He ADC to detect early alveolar destruction in smokers with normal spirometry and individual FEV_1% predicted (116). ADC gradients in the anterior and posterior direction show differences between healthy volunteers and severe COPD subjects with FEV_1 predicted between 30% and 50% (117,118). Such regional differences were also observed in another study (116) that suggested less homogeneity in diffusion

coefficient in emphysema patients, especially in the distal regions of the lungs. Since diffusion behaviour is also highly sensitive to diffusion times, various studies have focused on a specific time scale, from sub-millisecond for the study of small airway and alveolar abnormality, such as emphysema (119), to the diagnosis of large airway and branching changes, such as bronchitis and asthma, in long range diffusion studies of the order of seconds (120,121).

2.4.4 ^{129}Xe

Since ^{129}Xe atoms are larger and heavier than ^{3}He atoms, its diffusion coefficient is about 6 times less than ^{3}He in air, thus ADC measurements with ^{129}Xe would be expected to be sensitive to different length scales. Studies have been done to examine its sensitivity toward lung morphology changes in a similar fashion as has been done for ^{3}He. The first diffusion comparison study has shown that ^{129}Xe is sensitive enough to distinguish healthy volunteers from subjects with emphysema, and can detect age- and posture-dependent changes (89). Much like preliminary ventilation images, preliminary diffusion measurements using ^{129}Xe have yielded similar clinical information to that from ^{3}He (122,123) where uniform and lower ADCs are calculated in healthy subjects, whilst subjects with COPD demonstrate inhomogeneous distribution and significantly elevated ADCs. A mean parenchymal ADC of 0.036 ± 0.003 cm^2/s for healthy volunteers compared to the elevated 0.056 ± 0.008 cm^2/s for COPD subjects with emphysematous condition(122). As previous studies have shown with ^{3}He, long-range diffusion studies can provide sensitivity to certain micro-structural changes. Preliminary studies show similar methods are feasible using ^{129}Xe in long range diffusion measurements in the order of ~1 s (124).

2.4.5 Mixed gas studies

Mixed gases can also be used for experiments as another alternative for further diffusion weighted studies, where ^{3}He is mixed with heavier gases like ^{129}Xe. This procedure would slow down ^{3}He (decrease the apparent diffusion coefficient), without substantial loss of signal to noise ratio (SNR) (125).

2.5 Other imaging techniques with ^{3}He and ^{129}Xe

2.5.1 pO_2 mapping

As described in Chapter 1, T_1 relaxation constants of pure ^{3}He and ^{129}Xe can be hours, but this relaxation is greatly enhanced upon mixing with paramagnetic oxygen, reducing T_1 to seconds - minutes in the healthy human lung, and is inversely proportional to oxygen concentration (see equations 1.33 and 1.34). $P_{A,O2}$ measurements using ^{3}He provide functional information of the oxygen concentration within the lung space (126) where regions of abnormal oxygen pressure were observed in lung transplant patients (127). Regional ventilation-to-perfusion ratios can also be calculated from the $P_{A,O2}$ data (128). This can also be adapted into 3D mapping (97), to measure partial pressure of oxygen (129) (Fig. 2.15). This method has been challenging due to the combined effect of T_1 relaxation with RF pulse depletion in signal decay, thus technical development has been aimed to produce reproducible approaches for measuring pO_2 (126,127,129,130). This method has also been preliminarily applied to ^{129}Xe (103,131) and yields similar information. ^{129}Xe, however, differs fundamentally from ^{3}He as gas exchange and dissolution into the blood and tissue plays a part in polarisation decay, which produces an over-estimation of pO_2 unless it is corrected for (103,131).

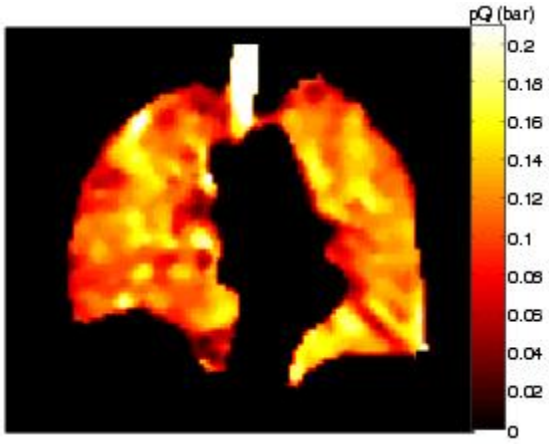

Figure 2.15. pO_2 mapping from a 3D image slice of a healthy volunteer. The imaging sequence was performed after inhalation of 1 *l* of gas (400 ml / 600 ml of $^3He/N_2$) followed by tidal breathing of room air.(132)

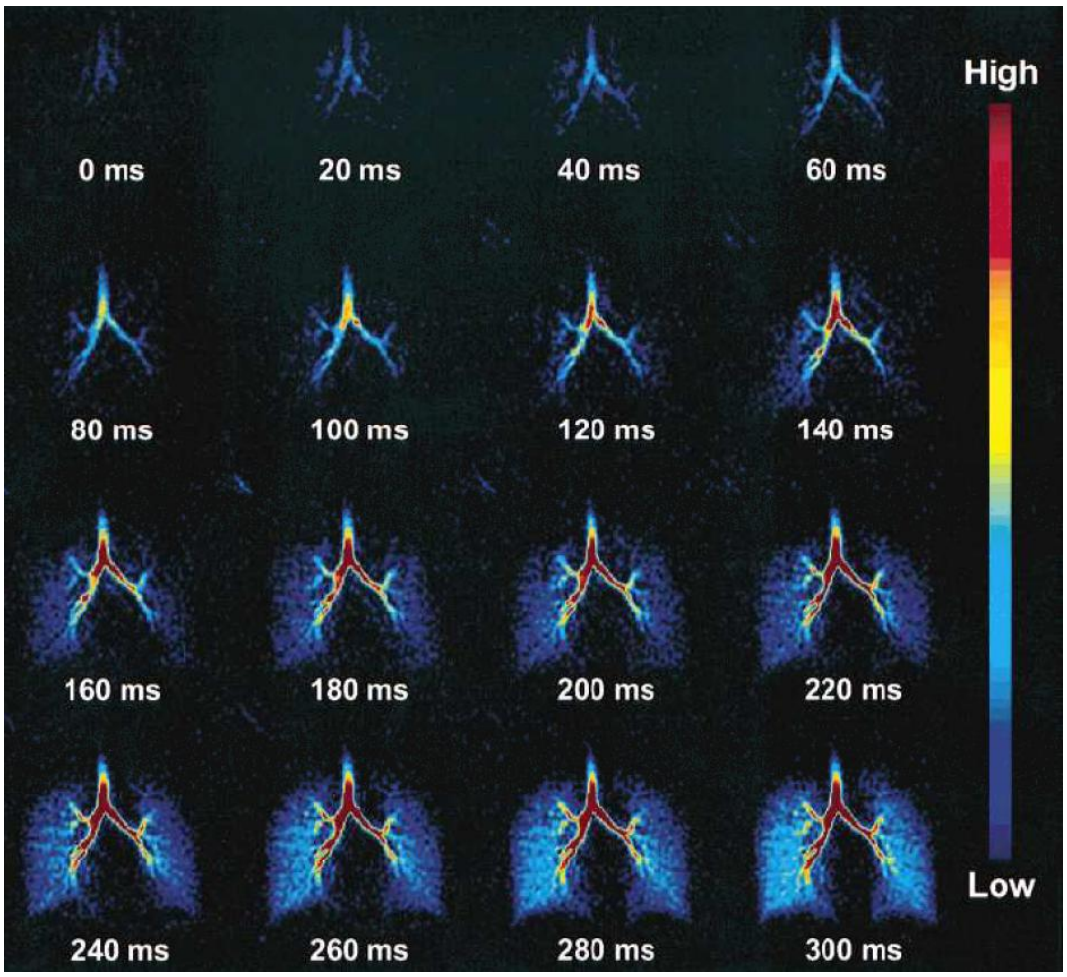

Figure 2.16. Dynamic imaging of a healthy volunteer on selected time intervals using 300ml 40% polarised ^{3}He HP gas (133).

2.5.2 Dynamic Imaging

Dynamic imaging is possible when images are taken temporally while the volunteer/patient is in the process of inhalation or exhalation (73) (Fig. 2.16); this technique shows the air flow within the lungs and can be used to diagnose air trapping in asthma (134) and also lung recoil dynamics that manifest in emphysema (115). Cystic fibrosis (CF) is another disease sensitive to dynamic ^{3}He MR imaging according to a study of children who were in the early stages of CF (135) with no permanent lung obstruction , showing animation of ventilation oppose to static ventilation images (136). By measuring the speed of the airflow (signal rise over time) in the peripheral lung region, dynamic ventilation can provide quantitative parametric maps of gas flow in the lungs (137) and these quantitative parametric mapping approaches have been applied in early stages of CF patients (138) with more homogeneously ventilated lungs.

2.6 Clinical Imaging Studies with HP gas MRI

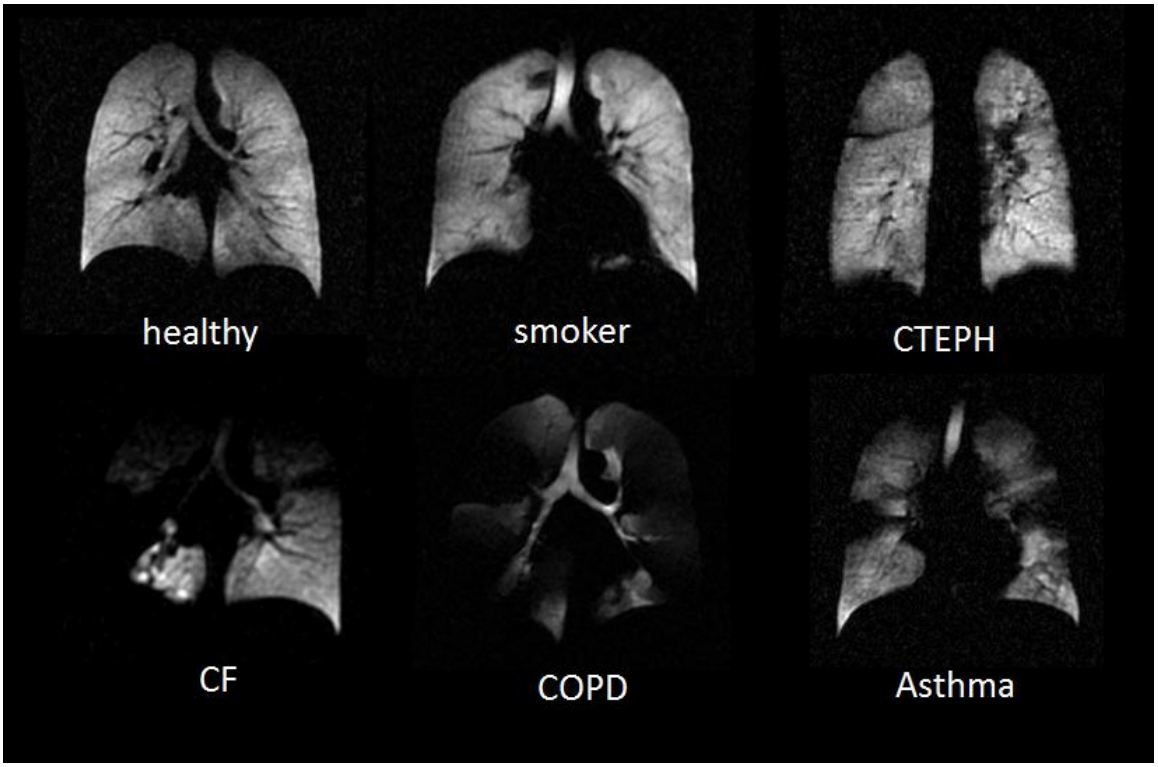

Figure 2.17 Example ventilation images of healthy as well as diseased lungs using hyperpolarised ^{3}He.

2.6.1 Cystic Fibrosis

HP gas imaging has been used to clearly diagnose cystic fibrosis with ventilation mapping (139,140) by scoring the percentage of ventilation as CF patients experience obstruction thus less ventilated volume. These clinical experiments correlate with HRCT results very well without concerns for radiation deposition in tissues(139). This method also agrees well with standard clinical diagnostic parameters and scores from both spirometry and chest radiograph in children with CF. A significant correlation was found between MRI score and spirometry (FEV_1% predicted and FVC%), as well as trends of correlation between MRI score and chest radiograph (Shwachman score) (141). It also has a great advantage for respiratory disease diagnosis in children, where ionising radiation should be

minimised (136) The technique has also been used to assess the efficacy of chest physiotherapy for regional mucus clearance and airways opening in paediatric CF (83,85).

2.6.2 Chronic Obstructive Pulmonary Disease (COPD)

For diagnosis of COPD, ventilation mapping is used to visualise ventilation defects as dark voids from obstruction. Hyperpolarised ^{3}He MRI has been used clinically for the investigation and diagnosis of COPD longitudinally (142) in an age-matched group and is well tolerated by stage II and III COPD subjects with a high 7- day rescan reproducibility for ADC measurements (143).

Recently, clinical trials showed that ^{129}Xe is well tolerated (108,109) in mild or moderate COPD patients, and ventilation imaging has shown functional defect sensitivity to COPD subjects (91). Preliminary diffusion studies have yielded similar clinical information to that from ^{3}He (122,123), where subjects with COPD demonstrated less homogeneous distributed and significantly elevated ADCs compared to that of healthy volunteers.

2.6.3 Asthma

Using hyperpolarised ^{3}He, ventilation defects per slice (VDS) for asthmatics showed significant increase when compared to control subjects and correlated to FEV_1/FVC. Many asthmatics, however, with normal spirometric indexes, had elevated VDS, indicating the sensitivity of the imaging modality (95). Fain et al., shown overlapping results of multi-detector CT images to ventilation defects measured using hyperpolarised ^{3}He (134).

Recently, both hyperpolarised ^{3}He and ^{129}Xe were used to study the effect of bronchodilator in asthmatics. Pre-salbutamol inhalation, ^{129}Xe ventilation images show significantly greater VDS than ^{3}He. Even though images post-salbutamol inhalation for

both gases improved, the improvement (i.e. greater percentage decrease in VDS) using ^{129}Xe is significantly higher, making ^{129}Xe the more sensitive detector (107). Using dissolved ^{129}Xe, MXTC (see Section 2.7.2) mapping after saturation of dissolved xenon showed elevation of depolarisation in all delay times compared to that of the healthy volunteers (144).

2.6.4 Post-Surgery Complications

In lung transplant patients, the current longitudinal monitoring using spirometry is not sensitive enough to detect bronchiolitis obliterans syndrome (BOS), the deterioration of graft function and obstructive airflow, at an early stage (145), which effects 60% of the recipients post-surgery within five years (146). Preliminary results show a sensitivity to lung function decline noticeable via ^{3}He imaging that is not detectable even with thin-slice CT images, as well as a correlation between the severity of the BOS and HP helium ventilation defects (147).

Even though ^{3}He MR and CT diagnosis of fibrosis post transplantation were comparable with little differences, the sensitivity towards emphysema and airways obstruction is quite significant as MR images show more ventilation defects (148). This suggests MR to be a better modality to demonstrate the decline in ventilated lung volume (149). Lung volume can also be obtained and is found to be a useful method in determining areas of the lungs being hyperventilated post-surgery (150). Regional studies with lung transplant patients in an anterior/posterior fashion also shows HP gas imaging useful in detecting abnormal ventilation (151).

2.6.5 Other Potential Applications

There are many other potential applications for HP gas imaging. It is anticipated to be useful in pulmonary embolism and chronic thromboembolic pulmonary hypertension, to investigate the physiological knock on effect on gas exchange from pulmonary vessel

blockage, for initial diagnosis (152). It has also been demonstrated as a feasible method for radiotherapy planning (81) as a mean of sparing radiation damage to viable and healthy lung tissue and more focused irradiation of tumours.

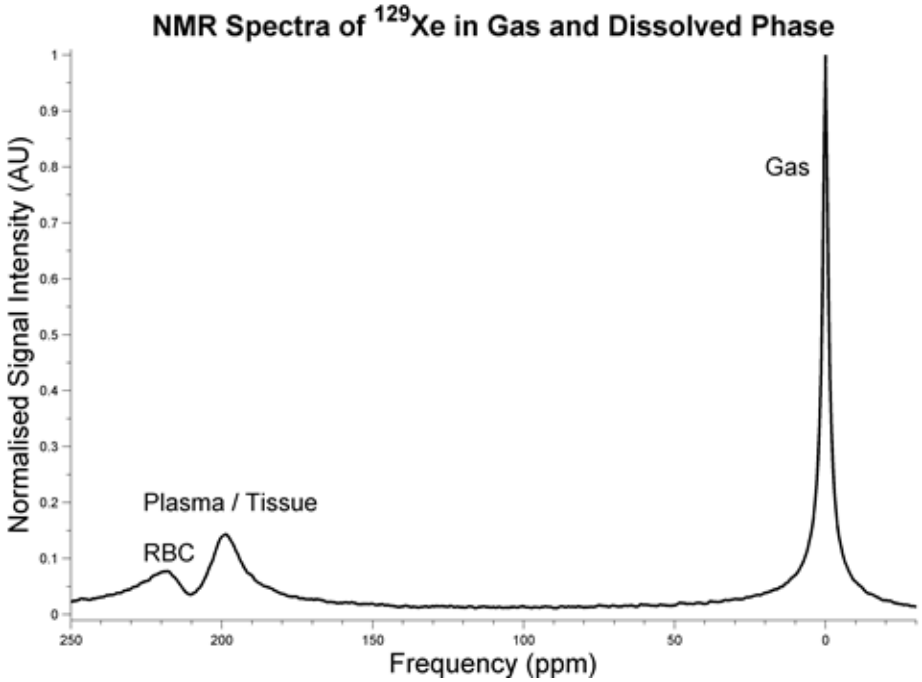

Figure 2.18. ^{129}Xe spectroscopy in healthy human lungs where RF pulse is a sinc-gaussian pulse shape centred on dissolved phase xenon. Notice the two distinct dissolved peaks from both RBC and plasma/tissue compartments.

2.7 Dissolved ^{129}Xe studies

Unlike ^{3}He, ^{129}Xe dissolves as it diffuses into the blood stream and undergoes constant exchange with the gas phase driven by diffusion across the alveolar wall. With a chemical shift of ~200 ppm in resonating frequency from the gas phase ^{129}Xe (~60 times larger than water-fat shift), information on the chemical composition of the gas exchange compartments can be obtained (Fig. 2.18). It has additional chemical shift sensitisation by virtue of its solubility in the blood, allowing direct access to the lung gas exchange pathways (153).

Upon inhalation, ~2% of the ^{129}Xe dissolved into tissue and blood, where dissolved ^{129}Xe NMR results in multiple peaks associated with distinct compartments are observed in spectroscopy (105,154-156) (Fig. 2.18) from gas, blood, and tissue depending on the interactions within the compartments. Spectroscopic scans *in vivo* have shown success in characterising gas uptake, exchange and transport by Patz et al. (103,157,158). One of the spectroscopic experimental methods is the study of xenon uptake rate by varying the repetition time between RF pulses through chemical shift saturation recovery (CSSR) type experiment, more details can be found in Chapter 6.

Due to the limited amount of ^{129}Xe in the dissolved phase, imaging directly is challenging in producing high spatially resolved images. A few imaging techniques have been adopted to overcome this limitation in the following section.

2.7.1 Xenon polarisation transfer contrast technique (XTC)

This method proposed by Ruppert et al (159) uses a low-flip-angle gradient echo pulse sequence twice with RF excitation centred at gas-phase xenon frequency to obtain two ventilation images of the gas-phase ^{129}Xe. A series of saturation high degree flip angles (ideally, 90 degrees) are applied in between the two imaging acquisitions to deplete xenon polarisation from gas exchange. During this intermediate step, longitudinal magnetisation of the gas will decrease in proportion to the amount of xenon exchange between the airspaces and tissue/plasma. The saturation RF pulses are centred at either 202 ppm (XTC, between the Xe_{RBC} and Xe_{plasma} peaks) or -202 ppm as a means of obtaining a controlled image. The controlled experiment pulses 404 ppm away from the dissolved frequency, thus not disturbing the dissolved phase xenon signal. This can then be used to correct for any other changes during the experiment (i.e. T_1 relaxation, blood transport, residual RF). Using the data from both XTC and Control experiments, a parameter called fractional depolarisation, f_{Depol}, can be calculated from (159):

$$f_{DEPOL} = 1 - \left(\frac{\frac{S_{XTC,after}}{S_{XTC,before}}}{\frac{S_{Control,after}}{S_{Control,before}}} \right)^{\frac{1}{N}} \quad (2.7)$$

where *N* is the number saturation RF pulses, and *S* is the signal intensity. By computing the equation above on a pixel-by-pixel basis, a XTC map is produced, proving a regional map which reflects the degree of exchange between gas and dissolved xenon.

This method was first introduced in small animal experiments in multiple breath-holds. From the high sensitivity of this polarisation-transfer pulse sequence technique, gas exchange and diffusion were measured in animal models indicating that gas exchange time is within milliseconds with an effective diffusion coefficient of 3.3×10^{-6} cm^2/s in the lung parenchyma. Patz et al. first demonstrated single breath-hold XTC for application in human lung imaging, where the fractional gas exchange appears homogeneous and uniform in healthy volunteers, and is sensitive to detect small changes in lung volume (160).

2.7.2 Multiple-exchange time XTC (MXTC)

Since the fractional depolarisation of xenon is highly dependent on the delay time between saturation pulses, a method of multiple delay time XTC is then used to study the xenon transfer behaviour. The experimental setup is similar to that of XTC, where the first set of RF pulses is the controlled data set (RF pulse centred at ~-200ppm), applied between $Image_1$ and $Image_2$, followed by the first set of saturation pulses on dissolved phase Xe (~200ppm) of a single delay time, τ_1, between $Image_2$ and $Image_3$, this is then followed by a second set of saturation pulses on dissolved phase Xe (~200ppm) of a second delay time, τ_2, between $Image_3$ and $Image_4$.

The gas depolarisation as a function of delay time τ can then be estimated by the curve defined by (161):

$$f(\tau) = F\left(1 - \frac{8}{\pi^2}\exp\left(-\frac{\tau}{\tau_c}\right)\right) \quad (2.8)$$

Where *F* is the parameter MXTC-F, the maximum depolarisation value i.e. $f(\tau)\ as\ \tau \to \infty$ and τ_c is the xenon exchange time constant. The maximum depolarisation value map (MXTC-*F* map) can be obtained by fitting the two delay times, τ_i, through the origin using equation 2.8, after normalisation using the controlled set of images obtained initially. From the parameter *F*, one can extract tissue-to-alveolar-volume of the lungs using the xenon blood-gas partition coefficient, *λ* (161).

Now from equation 2.1, diffusion length, in this case alveolar wall thickness, can be calculated by:

$$a_{thickness} \propto \sqrt{\tau_c D_m} \quad (2.9)$$

where D_m is the diffusion coefficient of xenon in the alveolar membranes (3.33 x 10^{-6} cm^2/s) (153). The factor$\sqrt{\tau_c}$, is then another measureable parameter in MXTC, which describes the thickness and composition of the alveolar septa (MXTC-S) (161) (Fig. 2.19).

MXTC-F is generally uniform within each coronal slice in healthy volunteers, and increases towards the posterior slices in supine position, consistent with the gravitational effect which reflects the higher tissue density towards posterior lung tissues. In COPD patients, MXTC-F maps show much more variation within each coronal slice, with lower values in the apices, but no significant gravitational effect can be observed in the anterior to posterior direction.

MXTC-S also shows homogeneous signal intensity within each coronal slice with a significant increase towards posterior lung tissue in healthy volunteers. In COPD patients,

gravitational effect is again not observed, with an overall increase in MXTC-S values, indicating the thickening of the septal walls.

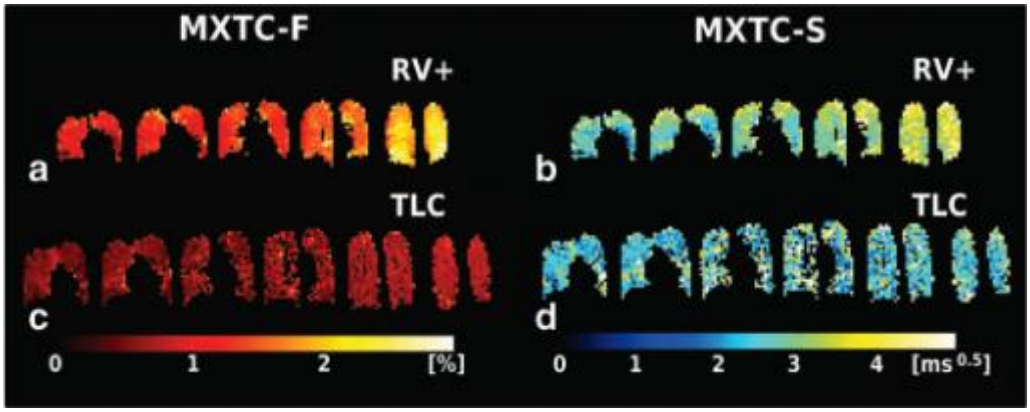

Figure 2.19 MXTC-F (a) & (c) and MXTC-S (b) & (d) maps obtained from curve fitting to equation 2.6 at low lung inflation (a) & (b) where tissue density is greater in the posterior regions of the lungs, producing a gravitation effect; as well as high lung inflation level (TLC) in (c) & (d) where parameter values appear more homogeneous (taken from (161) Fig. 3).

2.7.3 Direct dissolved phase ^{129}Xe imaging

Direct imaging of the dissolved-phase ^{129}Xe has been difficult until the improvement of polarisation where litres at polarisation levels of 10 % and above ^{129}Xe can be produced. Cleveland et al and Mugler et al showed in vivo images of dissolved phase ^{129}Xe in the human lungs in 2010 (162,163). Because the dissolved xenon undergoes constant exchange and replenishment from the airspace, high flip angles can be used to maximise signal intensity taken into consideration of the large chemical shift. Signal intensity from the direct imaging of dissolved phase xenon is uniform within a single coronal slice in healthy volunteers and show gravitational effect due to tissue density change much like ones observed in XTC maps, and increases in posterior regions of the lungs. More images of dissolved phase xenon are shown in Chapter 5 and 6.

2.7.4 Simultaneous dissolved and gas phase ^{129}Xe imaging

Mugler et al (163) had shown that by carefully selecting the readout bandwidth, one can image dissolved and gas - phase ^{129}Xe simultaneously (Fig. 2.20).

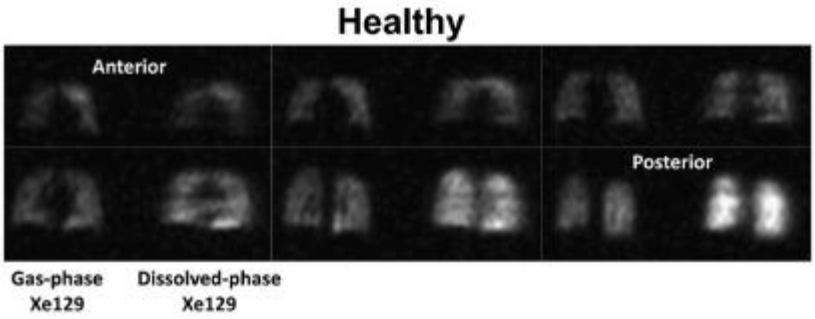

Figure 2.20. Simultaneous gas- and dissolved-phase ^{129}Xe imaging of the lungs of a healthy volunteer ((163) Fig. 2). Notice the gravitational effect of the dissolved-phase xenon, which is insignificant in the ventilation images.

With matched spatial resolution, one can quantify regional diffusion/ventilation information by normalising the dissolved signals by the gas signals. Here, a distinction between perfusion and diffusion should be made. The physiological definition of ventilation/perfusion ratio (V/Q ratio) is a measurement used to assess the efficiency of respiratory function defined by the ratio of the amount of air reaching the alveoli to the amount of blood reaching the alveoli. In nuclear medicine (discussed earlier in section 2.1), perfusion provides information on the whereabouts of blood capillary beds in the lungs as the radioactive tracer is injected intravenously and is trapped in the capillaries in the lungs. Dissolved xenon MR, however, shows the direct alveolar-capillary gas exchange in the ventilated area of the lungs. This information cannot indicate the lack of functional capillaries around those ventilation defects, thus dissolved phase xenon has similar sensitivity to the D_{LCO} measurement in pulmonary function tests in that it is sensitive to the gas exchange surface (see Section 2.1), with the additional benefit of regional information. When using the same imaging parameters, much lower dissolved signal intensity is observed in COPD subjects in the anterior slices compared to the gas signal,

which is not observed in healthy volunteers, suggesting a poorer lung perfusion function or low tissue density. Signal intensity/ventilation defects also occur differently regionally, indicating regions of the lungs that can be ventilated but are not viable for gas exchange. Also, by comparing the normalised dissolved phase image to ADC maps, one can see a correlation between reduced dissolved phase signals to elevated ADC values indicating a loss of gas exchange surface in emphysema. A closer look at this technique of simultaneous imaging is demonstrated experimentally in Chapter 6.

Most recently, multi-echo 3D radial imaging within one breath hold enabled the imaging of not only gas and dissolved ^{129}Xe, but is able to separate dissolved ^{129}Xe in blood and tissue/plasma in both healthy subjects and subjects with asthma and COPD(164). Even though these preliminary works with dissolved ^{129}Xe imaging provide relatively low spatial resolution, we can anticipate improvement with better sequence optimisation and polarisation in the future.

This thesis now focuses on the development of xenon imaging methods for human lung imaging on 1.5 T and 3 T whole body scanners in the upcoming Chapters.

2.8 Conclusions

Hyperpolarised noble gas in magnetic resonance imaging has been shown to be sensitive for diagnosing pulmonary diseases with zero ionising radiation dosage and no known adverse effects. It is a structural and functional imaging modality that can be used in numerous applications with high resolution with added physiological sensitivity that is not provided by other lung imaging modalities. This makes it a powerful tool for assessment of earlier stages of lung diseases such as CF (139,141) and COPD (41) that cannot be detected by standard means of spirometry and as a marker of response to therapy for these lung diseases. To date, hyperpolarised gas imaging is still only used in a handful of academic

centres (Table 2.1) due to the business policies of US companies whom held very broad patents in the field in the mid-1990s, therefore, polarisers were limited either home-built or on loan. In 2011, however, Polarean (Research Triangle Park, NC) re-obtained the patents and for the first time, offered polarisation systems for sale, which provides opportunities for new research groups and academic centres to become involved in this field to ensure a faster development in the field of hyperpolarised noble gas MRI.

Known clinical hyperpolarised noble gas MRI sites worldwide	
^{3}He	University of Sheffield, Sheffield, UK University of Virginia, Charlottesville, US University of Washington, Seattle, US Duke University, South Carolina, US University of Western Ontario, London, CA University of Wisconsin, Madison, US University of Iowa, Iowa, US University of Pennsylvania, Philadelphia, US Lakehead University, Thunder Bay, CA Mainz University, Mainz, Germany University of Lyon, France University Paris Sud, Orsay, France University of Copenhagen, Denmark
^{129}Xe	University of Sheffield, Sheffield, UK Univerisity of Virginia, Charlottesville, US Duke University, South Carolina, US University of Cincinnati, Cincinnati, US University of Western Ontario, London, CA University of Oxford, Oxford, UK University of Pennsylvania, Philadelphia, US Lakehead University, Thunder Bay, CA

Table 2.1. Hyperpolarised noble gas MRI sites around the world.

CHAPTER 3: Imaging of Hyperpolarised gas phase ^{129}Xe in lung MRI – B_0 field strength comparisons at 1.5 T and 3 T

3.1 Introduction

Hyperpolarised ^{129}Xe lung MRI (103) provides a potentially cheaper and more abundant alternative to ^{3}He. Preliminary clinical studies (89,104) with gas phase ^{129}Xe lung MRI suggest the gas could have comparable functional sensitivity for imaging lung ventilation in lung diseases as ^{3}He MRI. From an experimental and clinical perspective, it is important to know what magnetic field strengths are feasible and optimal for ^{129}Xe lung MRI.

Signal-to-noise ratio (SNR) in MRI is affected by many factors including pulse sequence parameters, sample noise, magnetic field strength, and coil noise. If the coils are large with large samples such as the human thorax, the SNR is typically dictated by the sample noise dominant regime at frequencies typical for standard clinical MRI (60 – 130 MHz), whereas experiments with small coils with a higher resistance from the coil rather than the sample tend to fall under the coil noise dominant regime (165), especially at lower frequencies typical of ^{129}Xe MRI at 17.7 MHz and 35.5 MHz at 1.5 and 3 T respectively .

Thermal noise, also termed Johnson-Nyquist noise, is the electronic noise inside an electrical conductor and the sample from thermal agitation of the charge carriers at equilibrium regardless of the voltage input as the charge carriers are vibrating due to temperature and resistance alone. Thermal noise is associated with the tuned circuit losses and sample dissipation, v_t and v_s respectively, are given by the Johnson noise formula where the units are $\frac{V^2}{Hz}$ (166):

$$v_t^2 = 4R_t kT \tag{3.1}$$

$$v_s^2 = 4R_s kT \tag{3.2}$$

where k is Boltzmann's constant, T is temperature in degrees Kelvin, and R_t and R_s are resistive losses in the tuned circuit and sample respectively, and the noise is proportional to the frequency bandwidth in Hz. Since thermal noise extends over a very wide spectrum, it is usually treated as a white noise source, and we can then simplify eq. 3.1 and 3.2 to:

$$v_t = \sqrt{4R_t kTBW} \tag{3.3}$$

$$v_s = \sqrt{4R_s kTBW} \tag{3.4}$$

where BW is the bandwidth in Hz and the units are now in V.

In NMR, the signal, S, from the total transverse magnetisation, M, from the sample, precessing at a frequency, ω, satisfies:

$$S \propto \frac{dM}{dt} \propto \omega M \tag{3.5}$$

In conventional thermally polarised ^{1}H MRI, both ω (Eq. 1.15) and M (Eq. 1.9) are proportional to the static magnetic field B_0, such that:

$$S \propto B_0^2 \tag{3.6}$$

Coil resistance, R_t, from the conductor generally scales with $\sqrt{B_0}$ because of the RF skin depth effect of the conductor. Sample resistance, R_s, comes from eddy currents generated in the lossy sample, and much like the induced emf of the signal, scales with B_0^2 (equation 3.6). Therefore, the noises associated with tuned circuit loss (v_t) and sample (v_s) are related to the magnetic field strength by:

$$v_t \propto B_0^{1/4} \tag{3.7}$$

$$v_s \propto B_0 \tag{3.8}$$

and a general expression of SNR can be written as (165)

$$SNR \equiv \psi \propto \frac{S}{\sqrt{v_s^2 + v_t^2}} \propto \frac{B_0^2}{\sqrt{\alpha B_0^2 + \beta\sqrt{B_0}}} \tag{3.9}$$

where α and β are sample and coil contributions respectively. A simplified expression assuming a high enough frequency where sample noise dominates ($\beta \ll \alpha$) is given by:

$$\psi \propto B_0 \tag{3.10}$$

Now at low frequency, coil resistance generally becomes more significant, so under the coil dominant noise regime (α = 0), SNR is given by:

$$\psi \propto B_0^{\frac{7}{4}} \tag{3.11}$$

Now if we consider the case for a hyperpolarised gas MR experiment where the polarisation and longitudinal magnetisation is independent of B_0, then signal is now linearly proportional to B_0 since the longitudinal magnetisation is a function of the polarisation (equation 1.6) alone, which is determined by the SEOP process. So expression (3.6) for hyperpolarised gas MR becomes:

$$S \propto \frac{dM}{dt} \propto \omega M \propto B_0 \tag{3.12}$$

And equations 3.10 and 3.11 for the hyperpolarised sample can thus be expressed as:

$$\begin{cases} \psi \; is \; independent \; of \; B_0 & \text{in sample dominant regime} \\ \psi \propto B_0^{\frac{3}{4}} & \text{in coil dominant regime} \end{cases} \tag{3.13}$$

Signal to noise ratio (SNR) is also affected by the imaging pixel size as (1):

$$SNR \equiv \psi = K \cdot \left(\frac{FOV_x}{N_x} \cdot \frac{FOV_y}{N_y} \cdot \Delta z \right) \cdot \sqrt{N_x \cdot N_y \cdot \frac{NEX}{rBW}} \tag{3.14}$$

where K is a constant from hardware dependent factors and sequence parameters, N_x and N_y are number of frequency and phase encoding steps, NEX is the number of averages, rBW is the receiver bandwidth, and FOV_x and FOV_y are field of view in x and y direction respectively.

So far, we have an indication that SNR in hyperpolarised magnetic resonance imaging (MRI) is less dependent upon static magnetic field strength, B_0, due to the B_0-independent polarisation (167) (eqn. 3.13). Indeed, low field imaging of hyperpolarised gases has been realised in multiple research centres (168-170). The apparent transverse relaxation time, T_2^* is however field dependent and is largely affected by magnetic susceptibility at tissue/gas interfaces with a bulk susceptibility difference between the airspace and tissue

(^{1}H) of $\Delta\chi \approx 9$ ppm (171). Experimental results have shown that the T_2^* of ^{3}He is about twice as long at 1.5 T (27.8 ± 1.2 ms) when compared to at 3 T (14.4 ± 2.6 ms). (172), which suggests a static dephasing regime (173), opposed to a motional averaging / narrowing dominated relaxation, where diffusion is so fast compared to *TE* that all spins undergo similar averaged accumulative phase, thus little signal attenuation. In the static dephasing regime, the phase accumulation is mainly induced by the static magnetic field inhomogeneity, which is much greater than through diffusion in the presence of field gradients in the time course of the experiment (i.e. slow diffusion where spins can be treated as stationary and accumulation of phase comes from localised field inhomogeneity mainly). The static dephasing regime criterion is as followed defined in Yablonskiy and Haacke (173):

$$(\varsigma \cdot \delta\omega)^{-1} \ll \frac{\left(\frac{\bar{r}}{2}\right)^2}{2 \cdot d \cdot D} \qquad (3.15)$$

where ς is the relative fraction volume of the dephasing sources from air-tissue interfaces in the case of the lungs, $\delta\omega$ is the frequency shift, $\bar{r}$ is the characteristic distance of magnetic field change, *D* is the diffusion coefficient, and *d* = 1, 2, 3 for 1-, 2- , and 3-dimensional diffusion respectively. This was first proposed by Yablonskiy et al, for a two-compartment model where magnetised objects such as blood vessels and red blood cells are embedded in an isotropic medium of tissue in which water molecules are diffusing. The application of such criterion for the static dephasing regime has not been extended to hyperpolarised noble gases in the lungs due to the complexity in structure of the acinar space. The limited experimental data suggests a static dephasing regime with ^{3}He from two clinical MR field strengths (172). However, theoretical simulations (167,174) suggested a non-linear dependence of T_2^* for xenon closer to 3 T magnetic field strength. Further modelling and experiments are needed to understand in more depth of the key contributors, including susceptibility, lung micro-geometry and diffusion.

It has also been predicted for hyperpolarised gas lung imaging that a higher SNR could be achieved at low B_0 due to the longer T_2^* by the use of a low readout bandwidth (167), thus enabling imaging with hyperpolarised gases at field strengths as low as 3 mT (175). This benefit has limited scope with ^{3}He gas due to its highly diffusive nature introducing significant diffusion dephasing in the presence of a long readout gradient associated with the low bandwidth readout gradient (176), but has potential advantages for ^{129}Xe.

Despite the possibilities at low B_0, for HP gas lung MRI to translate to clinical practice, it really needs to be feasible at the B_0 field strengths currently used for routine clinical ^{1}H MRI, namely 1.5 T and 3 T. Three previous experimental studies with hyperpolarised ^{3}He have shown comparable SNR observed at various field strengths. Deppe et al. (172) reported comparable SNR at 3 T and 1.5 T, although different RF coil designs were used. Dominguez et al., in a later study also concluded that SNR is independent of field strength for human lung ^{3}He imaging at 1.5 T and 3 T using RF coils of the same design (16 rungs, rigid transmit-receive elliptical chest coil). They also proposed a thermal phantom normalisation procedure to account for the non-field-strength dependent contribution to the SNR (177). Salerno et al. in a study where a 1.5 T system was ramped down to 0.5 T, compared ^{3}He lung MRI SNR at the two field strengths using flexible chest RF coils where they found the SNR values at 0.54 T were similar to, but generally lower than that at 1.5 T (168). No systematic evaluation of the coil performance was done in that empirical study.

The aim of this study was to perform systematic experiments at the clinically relevant field strengths of 1.5 T and 3 T to compare the SNR of inhaled hyperpolarised ^{129}Xe lung MRI using radiofrequency (RF) coils of the same geometrical design. Image SNR and gas T_2^* were measured using ventilation images from healthy volunteers at both field strengths. In addition, the assessment of the non-B_0 dependent hardware dependent contribution was also assessed using thermally polarised ^{129}Xe and hyperpolarised gas phantoms.

3.2 Materials and Methods

Experiments were performed on whole-body clinical MR systems: (i) a 1.5 T Signa HDx (GE, Milwaukee, WI, USA, Fig. 3.1(b)) equipped with a 2kW broadband RF amplifier and (ii) a 3 T Philips Achieva equipped with a 4kW broadband RF amplifier. A flexible twin Helmholtz

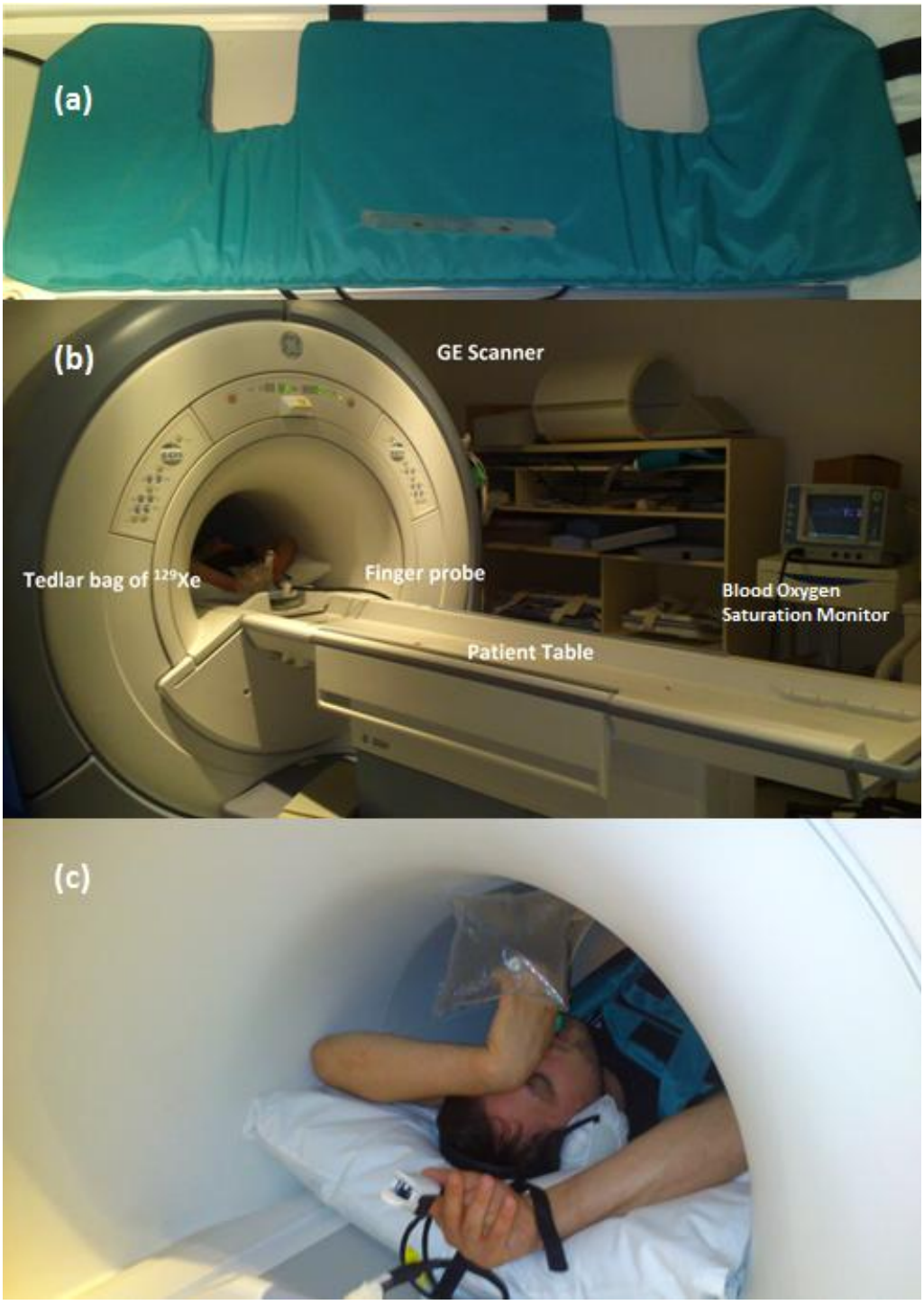

Figure 3.1 **Experimental set up for in vivo ^{129}Xe experiments using a custom vest coil (a) subject in a 1.5 T GE scanner constantly being monitored for vital signs with blood oxygen saturation monitor attached via a finger probe (b) and the subject inhales 1 *l* of mixed ^{129}Xe and N_2 from a 1*l* Tedlar bag (c).**

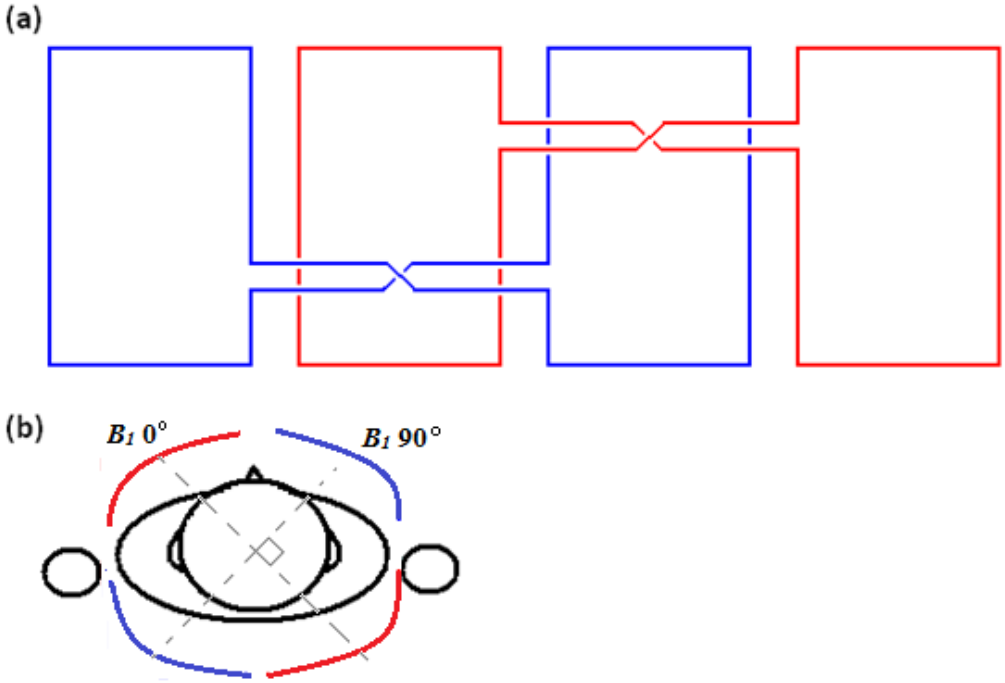

Figure 3.2 **Schematic of the geometry of the double Helmholtz transmit-receive vest coil (a) and how it is wrapped around the subject during experiments ideally with B_1 fields 90˚ out of phase (b).**

quadrature transmit-receive coil (CMRS, USA, Fig. 3.1(a), Fig. 3.2) was used at both field strengths, resonating at 17.7 MHz and 35.4 MHz for 1.5 T and 3 T, respectively. The coils had exactly the same geometrical form and were fitted with passive trap circuits tuned to the ^1H frequency for blocking induced currents during ^1H body coil transmission. In addition, tuned transmit-receive switches with custom tuned pre-amplifiers were used for both experiments. Measurements of both of the coils' impedances were made with a network analyser (Agilent Technologies E5061A, CA, US) from the S_{11} Smith chart when unloaded (but geometrically formed, Fig 3.3 (a)) and loaded with volunteers of 50 kg (b)

and 88 kg (c) in the bore of the magnets (Fig. 3.3). The fact the locus of the Smith chart and the measured impedances change very little even at 3 T indicates that the sample coupling is not the dominant source of noise in these experiments.

Three volunteers participated in the *in vivo* imaging study at 1.5 T and 3 T, (female 25 years old, 50 kg; male, 40 years old, 88 kg; male, 41 years old, 88 kg). Written consent was acquired from all volunteers and approval was obtained from the national research ethics committee.

As a parallel means to assess the contribution to the SNR measurements from factors that are not directly related to the polarisation (e.g. the rate of precession of the transverse magnetisation, the coil's intrinsic sensitivity and resistive noise at the different radio frequencies, the T-R switch insertion loss, cable losses and preamplifier noise), experiments were performed using both a thermally-polarised and a hyperpolarised ^{129}Xe phantom with the same loading as experiments with the same volunteer following the method of Dominguez et al (177). The thermally polarised phantom was a 1 *l* glass cell containing 2 *l* of natural abundance xenon (26% ^{129}Xe) mixed with 1 *l* of oxygen at a total pressure of around 3 bar with a measured T_1 of 1.6 s. The hyperpolarised phantom was a 1 *l* Tedlar bag containing 3% of isotopically-enriched xenon (86% ^{129}Xe), 10% N_2, and 87% ^{4}He. The ^{129}Xe was polarised to around 10% as described in Section 1.3.

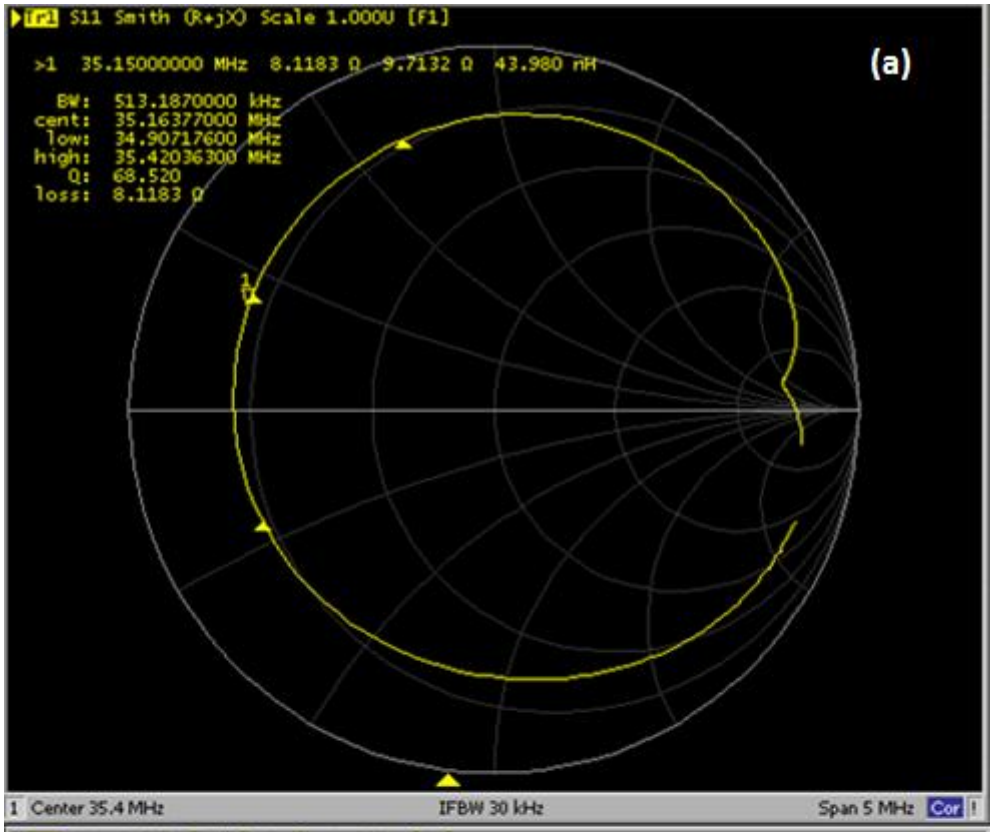
Tr1 S11 Smith (R+jX) Scale 1.000U [F1]
>1 35.15000000 MHz 8.1183 Ω -9.7132 Ω 43.980 nH
BW: 513.1870000 kHz
cent: 35.16377000 MHz
low: 34.90717600 MHz
high: 35.42036300 MHz
Q: 68.520
loss: 8.1183 Ω
(a)
1 Center 35.4 MHz
IFBW 30 kHz
Span 5 MHz
Cor

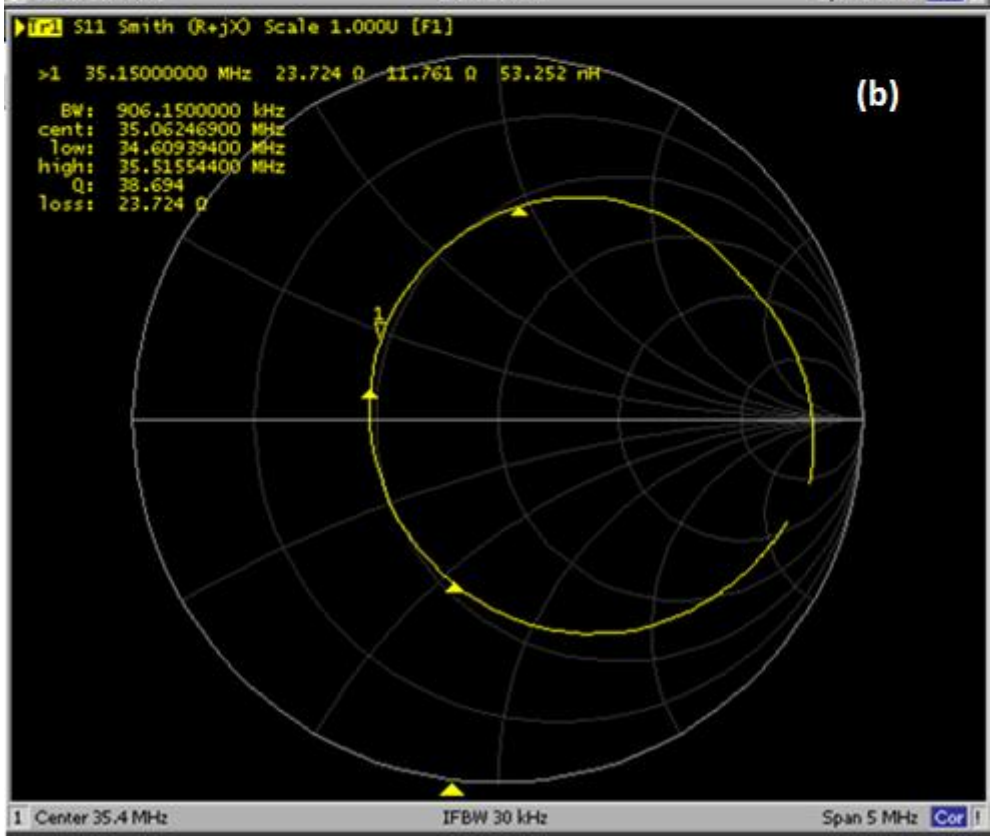
Tr1 S11 Smith (R+jX) Scale 1.000U [F1]
>1 35.15000000 MHz 23.724 Ω 11.761 Ω 53.252 nH
BW: 906.1500000 kHz
cent: 35.06246900 MHz
low: 34.60939400 MHz
high: 35.51554400 MHz
Q: 38.694
loss: 23.724 Ω
(b)
1 Center 35.4 MHz
IFBW 30 kHz
Span 5 MHz
Cor

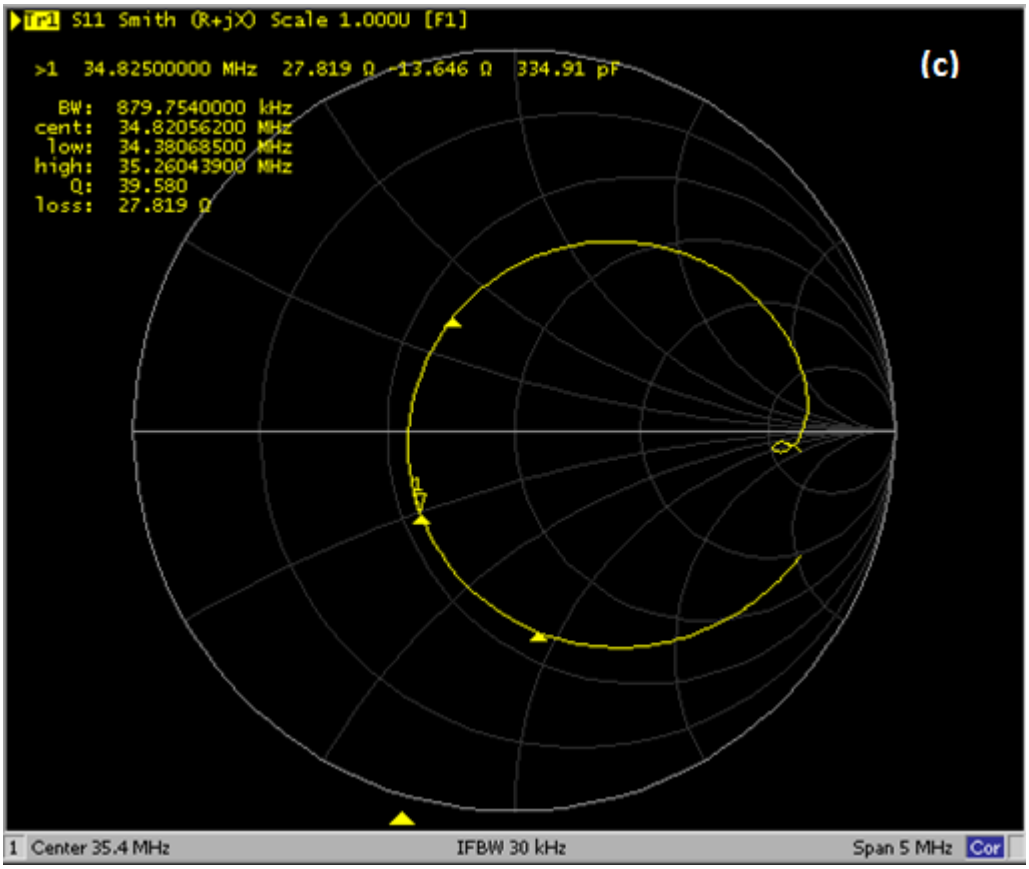

Figure 3.3. S_{11} measurement on smith charts of the quadrature transmit-receive coil at 3 T when unloaded (a), loaded with (b) a 50 kg volunteer, and (c) loaded with an 88 kg volunteer. Notice the locus of the Smith chart changes very little between the volunteers.

3.2.1 MR measurements

3.2.1.1 Phantom SNR assessment

For the phantom SNR assessment calculations, the female volunteer (50kg) was positioned supine in the chest coil at both field strengths. The hyperpolarised gas phantom was then placed on top of the volunteer's chest above the lungs inside the coil. Flip-angle calibration was performed on the phantom using a non-slice-selective pulse-acquire sequence of 20 free-induction decay (FID) acquisitions with spoiler gradient

applied between repetitions at 500 ms TR. The mean flip angle from that volume of the coil was calculated using:

$$S(n) = S(0)\cos^{n-1}\alpha \tag{3.16}$$

where *S(n)* is measured signal after *n* RF pulses, *S(0)* is the initial signal, and α is the flip angle. The thermally polarised phantom was then placed in the same position on the volunteers chest above the lungs inside the coil (Fig 3.4), and the SNR of the signal was calculated from the average of 100 pulse-acquire FID acquisitions with a 50° flip angle, TR of 6 s, receiver bandwidth 2 kHz and 512 samples.

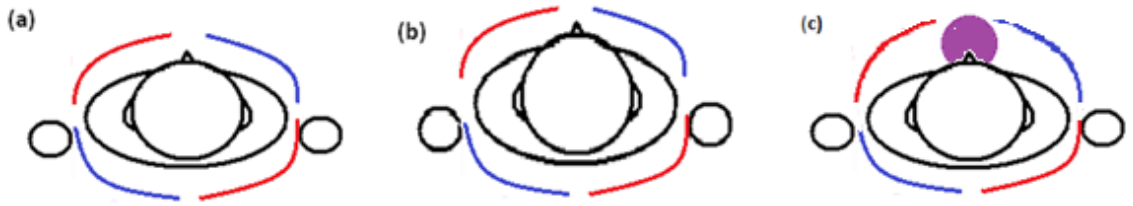

Figure 3.4. Coil geometry is dependent on patient and experimental setup in (a) a small volunteer, (b) a larger volunteer, and (c) a small volunteer with a thermally polarised ^{129}Xe phantom (purple) on top of the chest during the thermal phantom assessment.

3.2.1.2 Ventilation imaging

A global (whole lung) flip-angle calibration was calculated for each volunteer in the RF coil at both field strengths with data acquired from the same 2D spoiled gradient echo imaging sequence as detailed below, but with the phase-encoding gradient and slice select gradient turned off. Each volunteer inhaled a 50 m*l* dose of hyperpolarised ^{129}Xe and the flip angle was calculated using Eq. 3.12. ^{129}Xe ventilation images were then obtained at both field strengths using a multi-slice 2D spoiled gradient echo sequence. Images were acquired following inhalation of a 1 *l* Tedlar bag filled with 700 m*l* N_2 and 300 m*l* isotopically enriched Xe (86% ^{129}Xe) from a position of relaxed expiration. Gas was polarised as described in Chapter 1, Section 1.4.

(a)

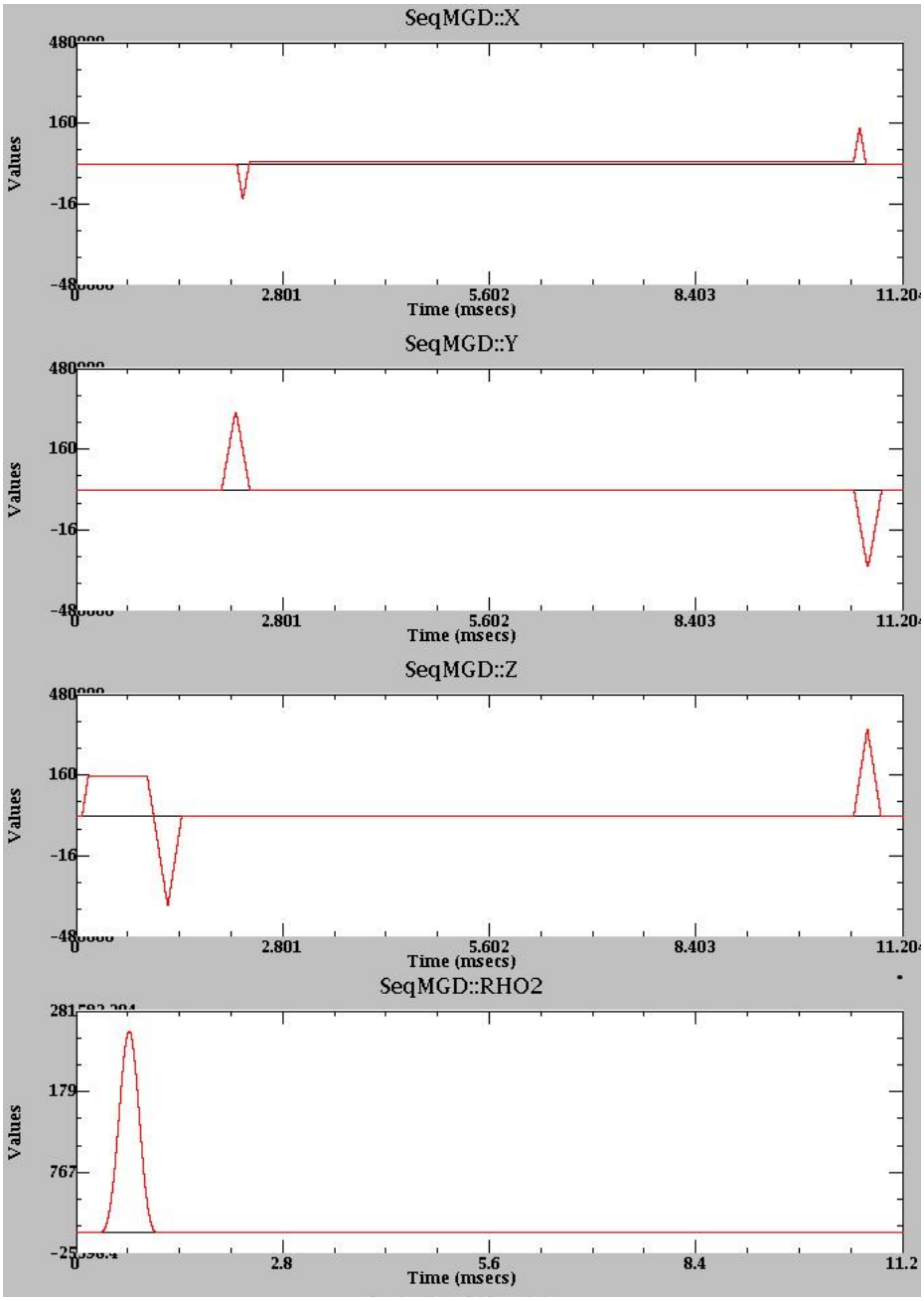

Figure 3.5 (a) Pulse sequence of a 2D spoiled gradient echo from 1.5 T EPIC psd plotter and (b, next page) 3 T Philips pulse sequence simulator.

(b)

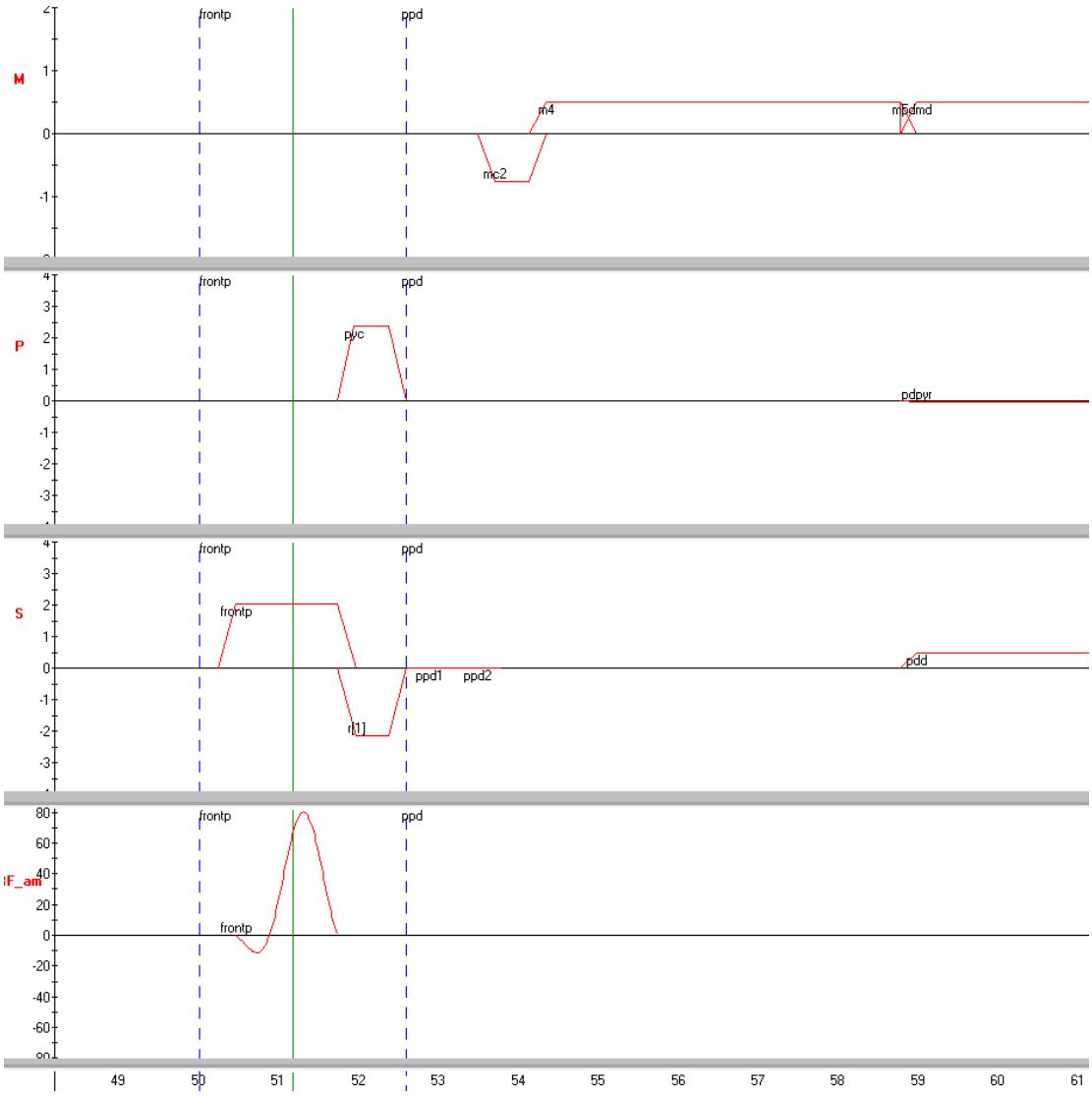

Pulse-sequence parameters were kept consistent between the two MR systems: 9 coronal slices of 15 mm thickness acquired from anterior to posterior covering the whole lung, field of view (FOV) of 38.4 cm x 38.4 cm, resolution of 96 x 96 matrix, receiver bandwidth (BW) of 4 kHz, echo time / repetition time (TE / TR) of 4.15 / 18 ms for volunteer one and 3.0 / 6.2 ms for volunteer two. The parameters were kept constant for each volunteer on both scanners, but not identical to each other because a larger bandwidth was adopted for the larger volunteer for a smaller echo time, which should not affect the systematic comparison between the two scanners. Centric phase encoding was used to maximise the

SNR, and a constant flip angle of 9° was used, the pulse sequence diagrams from the GE EPIC and Philips PARADISE pulse sequence programming interfaces are shown in Fig. 3.5. The B_1 field homogeneity of the coil is dependent on coil geometry; as shown in Fig 3.4, the coil geometry changes from a small healthy volunteer (a), a larger volunteer (b), as well as (c) the same smaller volunteer with a thermally polarised ^{129}Xe phantom, which was used for thermal phantom SNR assessment.

3.2.1.3 Pulse sequence for T_2* measurement

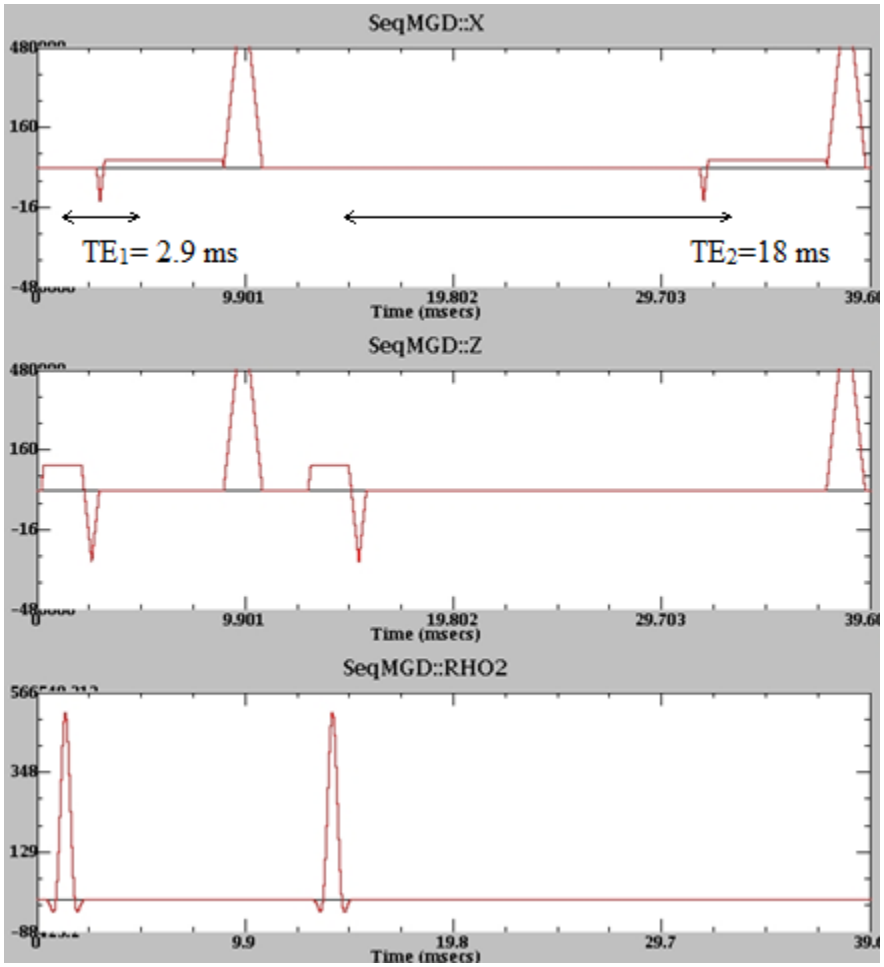

Figure 3.6. Sequence diagram of an interleaved dual echo time 2D spoiled gradient echo pulse-sequence used for T_2^* measurement at 1.5 T on the GE system.

An interleaved dual echo time 2D spoiled gradient echo pulse-sequence (Fig. 3.6) was used for T_2^* calculation as detailed in (172), fitting to a mono-exponential T_2^* relaxation decay. Since the T_2^* in the lungs is highly dependent on the lung volume (see discussion on effect of lung inflation level in Section 3.3.3), and breath-hold time limits our capability to acquire many TE values, a mono-exponential decay of the signal is assumed and we did not adopt a bi-exponential/multi-exponential fit for T_2^* measurements in this experiment. In reality, however, it is more likely that the transverse decay of xenon within the lungs is may not be mono-exponential due to factors related to the existence of different compartments like e.g. one undergoing a long slow decay (free diffusion and motional narrowing away from the walls), and one undergoing a faster short decay (restricted diffusion proximal to by the air/tissue micro-structural interface), as well as a possible decay component associated to with dissolved phase xenon exchange. Note that this chapter focuses on the first attempt to our understanding of T_2^* relaxation of gas xenon for imaging purposes, thus an assumption of mono-exponential decay is suffice, which will further enable the development of sequences and measurements.

Sequence parameters were: 6 coronal slices of 30 mm thickness covering the whole lung, FOV of 38.4 cm x 38.4 cm, resolution of 64 x 64 matrix, BW of 16 kHz, centric encoding, and a flip angle of 7°. TE_1/TE_2 values used at 1.5 T were 2.9 ms / 18 ms, and the TE_1/TE_2 values used at 3 T were 4.4 ms/ 11 ms. TE_1 values were chosen as the minimum attainable for the given RF pulse and bandwidth, whereas TE_2 values were chosen based more on the expected smaller T_2^* values at 3 T. Each volunteer was asked to breathe either to Residual Volume (RV) + 1 *l* from the Tedlar bag or to the Total Lung Capacity (TLC) after inhaling 1 *l* from the Tedlar bag. The sequence diagram for the 1.5 T interleaved sequence is shown in Fig. 3.6.

3.3 Results and Discussion

3.3.1 SNR Assessment

Since the comparisons made in this chapter were between two completely different system, we debated a more systematic assessment in hope to reduce the effect. This SNR assessment procedure was suggested in (177) for normalisation of all signals based on the fact that the phantom is fixed and should produce signal intensities proportional to field strength differences on thermally polarised xenon. After averaging 100 FID acquisitions from the thermally polarised phantom loaded with the volunteer (Fig.3.4 (c)), the SNRs at 3 T and 1.5 T were 105 and 42, respectively. This gives a relative sensitivity factor *k* of 1.25, from the calculation described in full detail in (177) using equation 3.10.

$$k = \frac{SNR_{Thermal}^{3T}}{SNR_{Thermal}^{1.5T}} \cdot \frac{\sin\left(\alpha^{1.5T}\right)B_0^{1.5T}}{\sin\left(\alpha^{3T}\right)B_0^{3T}} \qquad (3.17)$$

This k-factor also makes the assumption that the scanner/coil combination from both scanners would pick up all of the gas with a homogenous flip angle spatially. This, however, is hard to manipulate due to the changes in the exact position of the phantom with respect to loading/coil as well as coil geometry consistency.

3.3.2 Ventilation imaging comparisons

Fig. 3.7 shows typical ventilation images from the female volunteer acquired following inhalation of 300 ml of ^{129}Xe at both 3 T and 1.5 T. Images were reconstructed from raw k-space data in MATLAB (MA, USA) with no additional k-space or image domain filtering to exclude differences between the image processing algorithms of the respective scanners.

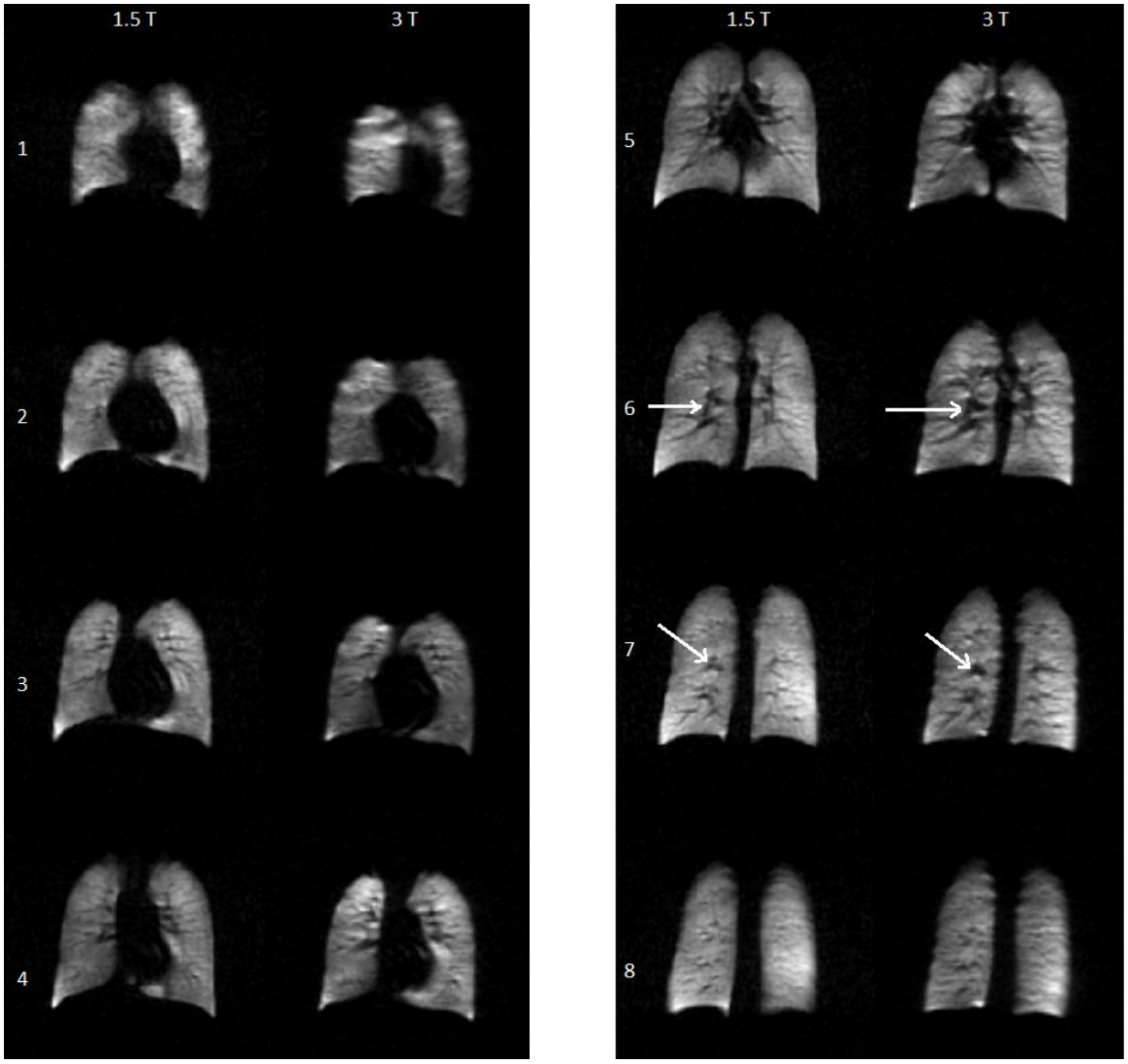

Figure 3.7. Slice-by-slice comparison of images from the lungs of volunteer 1 obtained with ^{129}Xe ventilation sequences at 3 T and 1.5 T. Spatial resolution in the images is 15 mm × 4 mm × 4 mm. Note the increased texture in the images due to increased susceptibility dephasing at 3 T around the blood vessels (arrows).

For each slice, two regions of interest (ROIs), consisting of the whole lung less major airways, were selected from the left and right lungs; a ROI containing background noise was also selected. The mean SNRs were then calculated using the average of the signal divided by the standard deviation of the noise, and are plotted in Fig. 3.8 slice by slice at both field strengths. The general trend of decreasing SNR from anterior to posterior is

likely to be partly due to T_1 decay during the breath-hold (105) as the multi-slice imaging order is anterior to posterior and the posterior slices are thus more exposed to T_1 relaxation. Previous studies with 3D ^{3}He MRI (97) and ^{129}Xe MRI (162,163) have shown higher SNR in posterior slices which is consistent with the physiology of preferential ventilation of the posterior lungs. These trends were not obvious in this work although the slight rise in SNR in the most posterior slices may be partially due to this effect in combination with the higher B_1 transmit and receive sensitivity of the close fitting vest coil at the back (see Chapter 4 . Fig. 4.18).

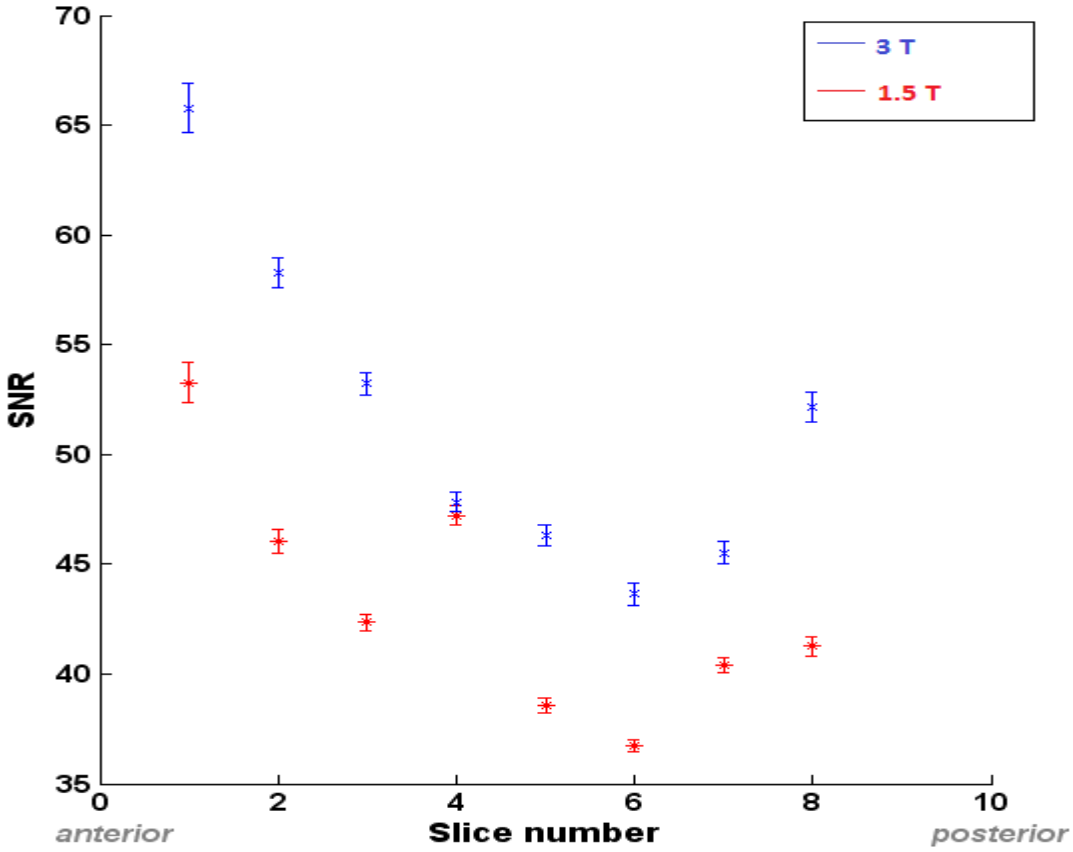

Figure 3.8. Comparison of the mean SNR from the images of the left and right lung as a function of slice number for regions of interest at 1.5 T and 3 T. Note the higher SNR in anterior slices, which is probably indicative of T_1 decay resulting from the anterior to posterior imaging order. The slight rise in signal in the posterior slices is likely a result of higher B_1 transmit–receive sensitivity close to the coil.

The mean SNR values from two volunteers are summarised in Table 3.1. These results, obtained using these RF coil designs of the same geometry, suggest that the SNR of hyperpolarised ^{129}Xe MRI is slightly higher at 3 T by factors of 1.16 and 1.31 for the two subject-loads of 50 kg and 88 kg, respectively. However, the B_1 homogeneity of the coil could be different from patient loading differences and coil geometry can change from subject to subject as shown in Fig. 3.4. This is the same trend in increased SNR with B_0 as is seen with thermal phantom experiments following normalisation for the B_0 dependent longitudinal magnetisation (k = 1.25). Going back to the SNR calculations at the beginning of this chapter, equation 3.13 predicts that SNR should be independent of the field strengths if the noise is dominated by the sample, and would increase by a factor of $3^{3/4}/1.5^{3/4}$ =1.68 at 3 T if the system is in a coil noise dominated regime. From this result, it appears that due to the relatively low resonant frequency of xenon, there is some contribution of coil noise, and both contributions (coil and sample) affect the SNR outcome. Following experiments with ^{3}He SNR 1.5 T and 3 T using bird-cage body coils of the same geometry, Dominguez et al. (177) proposed a normalisation process using the thermal phantom signal ratio, k from Eq. 3.10. They used this factor to normalise the ^{3}He lung image SNR for system hardware-dependent SNR effects. This factor, however, still contains an intrinsic weighting from the B_0, in that firstly the induced EMF is proportional to the precessional frequency of the transverse magnetisation (which is proportional to B_0), and secondly, that frequency-dependent noise characteristics of the RF coil and sample load are removed by this process of normalisation. It is debatable that this procedure can in fact be used to separate system noise not originating from the RF coil and sample from frequency-dependent signal and noise factors related to the higher precessional frequency and different coil electromagnetic sensitivities at 3 T and 1.5 T. As such, this normalisation process was not used in the work here with ^{129}Xe. Instead the thermal phantom procedure was used to evaluate the relative spectroscopic SNR of the two systems in parallel to the lung imaging experiments.

The higher SNR observed at 3 T could be attributed to the collective contribution to the SNR from several different factors including:

(i) the transverse magnetisation (precessing at 17.65 MHz and 35.35 MHz, respectively) which is directly linked to measured current.

(ii) the noise is a combination of coil and sample resistance noise with both of these coils with possibly more coil noise dominated regime environment at 1.5 T since the frequency is less at 17.65 MHz.

(iii) the ''back-end'' system noise (preamplifier, T–R switch and hybrid insertion loss, receiver chain, etc). These factors are difficult to accurately quantify for in-vivo RF coil comparisons with these kind of coils which are fitted with cables and have additional losses from the resistance of the ^{1}H trap blocking circuits, where measurements of coil Q when loaded and unloaded are not really a meaningful assessment of the working coils sensitivity with respect to factor (ii).

(iv) Small variation in controlled parameters such as gas polarisation/amount, volunteers' lung inflation consistency.

Gender, age,[weight]	Sequence parameters (TR/TE)	SNR at 1.5 T	SNR at 3 T
F, 25, [50 kg]	18 ms / 4.2 ms	44.1	51.3
M, 40, [88 kg]	6.2 ms / 3.0 ms	27.1	35.7

Table 3.1. Mean SNRs from slice-by-slice ROI calculations of the whole lung of two volunteers. The differences between volunteers are due to differences in sequence parameters, which were kept constant for each volunteer across both scanners.

The central message from this comparison is both field strengths provide a near equally sensitive environment for lung MRI studies with ^{129}Xe with this coil design with 3 T providing slightly higher SNR. The fact that SNR did not scale with $B_0^{3/4}$ (predicted higher SNR in the sample dominated noise regime from equation (3.13)) indicates the imaging

regime for human ^{129}Xe lung MRI with this coil design at 1.5 T and 3 T lies somewhere in between the coil noise dominated and sample noise dominated regimes.

The SNRs achieved in practice at these two field strengths within the time course of a breath-hold are likely to match or exceed those at lower field strengths. An additional factor worth consideration when deciding upon B_0 is the power available from the RF amplifier to deliver a given flip angle with a short duration pulse. This could become an issue when imaging with sequences such as balanced steady-state free precession, which require short duration high flip angle pulses. As required RF power and deposited SAR scale quadratically with Larmor frequency, imaging at 1.5 T is less constrained by this factor than at 3 T.

3.3.3 T_2^* measurements

Example T_2^* histograms from all slices from the two male volunteers acquired at functional residual capacity (FRC) + 1 *l* are shown in Fig. 3.9 (a) & (c), with median values of 25 ± 13 ms and 18 ± 6 ms at 1.5 T and 3 T, respectively. The uncertainty was measured as the full-width at half maximum of the T_2^* histogram. These values are shorter than the only other previously reported values in the conference literature (178) of 50.4 ms and 27.4 ms at 1.5 T and 3 T respectively. However, repeated measurements with the lungs filled up with room air to total lung capacity (TLC) instead of FRC + 1 *l* show T_2^* with median values of 52 ± 20 ms and 24 ± 11 ms at 1.5 T and 3 T, respectively, which are consistent with (178) to within limits of agreement. This is shown in Fig. 3.9 (b) & (d), and indicates a dependence of the transverse relaxation constant T_2^* on lung inflation level that was previously seen with ^{3}He (179).

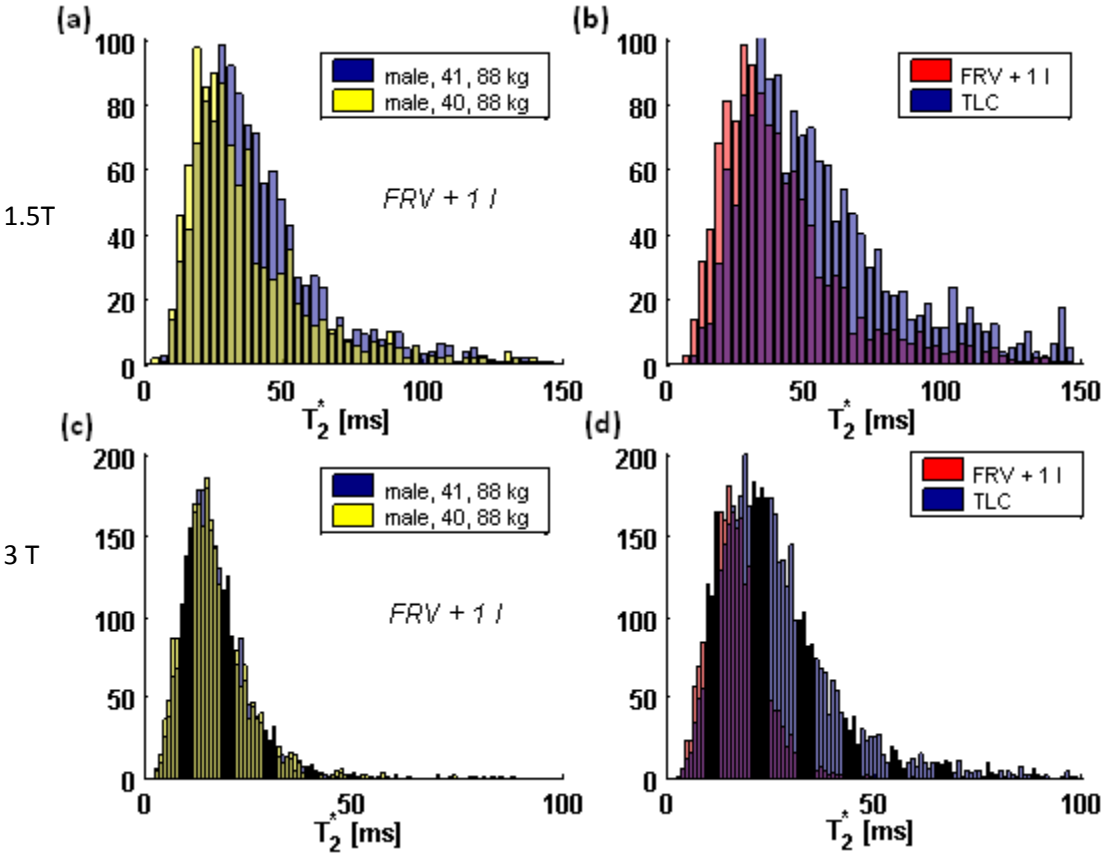

Figure 3.9. The distribution of T_2^* of two healthy volunteers (40 years old , 88 kg; 41 years old, 88 kg) as measured from all coronal lung slices with hyperpolarised ^{129}Xe at B_0 field strengths of 1.5 T (a) and 3 T (c) showing healthy subject consistency at FRV + 1 *l*; as well as the distribution of T_2^* while imaging at forced residual volume (FRV) +1 *l* and total lung capacity (TLC) as measured from all coronal slices at B_0 field strengths of 1.5 T (b) and 3 T (d) from one healthy volunteer (41 years old, 88 kg).

Example ventilation images of the lungs of a healthy volunteer at lung inflation levels of TLC as well as RV +1 *l* are shown in Fig. 3.9 at both TEs. It is observed that, the SNR is lowered at TLC at TE_1 due to the larger lung volume at TLC as to be expected. From these interleaved sequences, the two images obtained can be used to map out T_2^* of each individual slice, slice-by-slice maps are shown in Fig. 3.11.

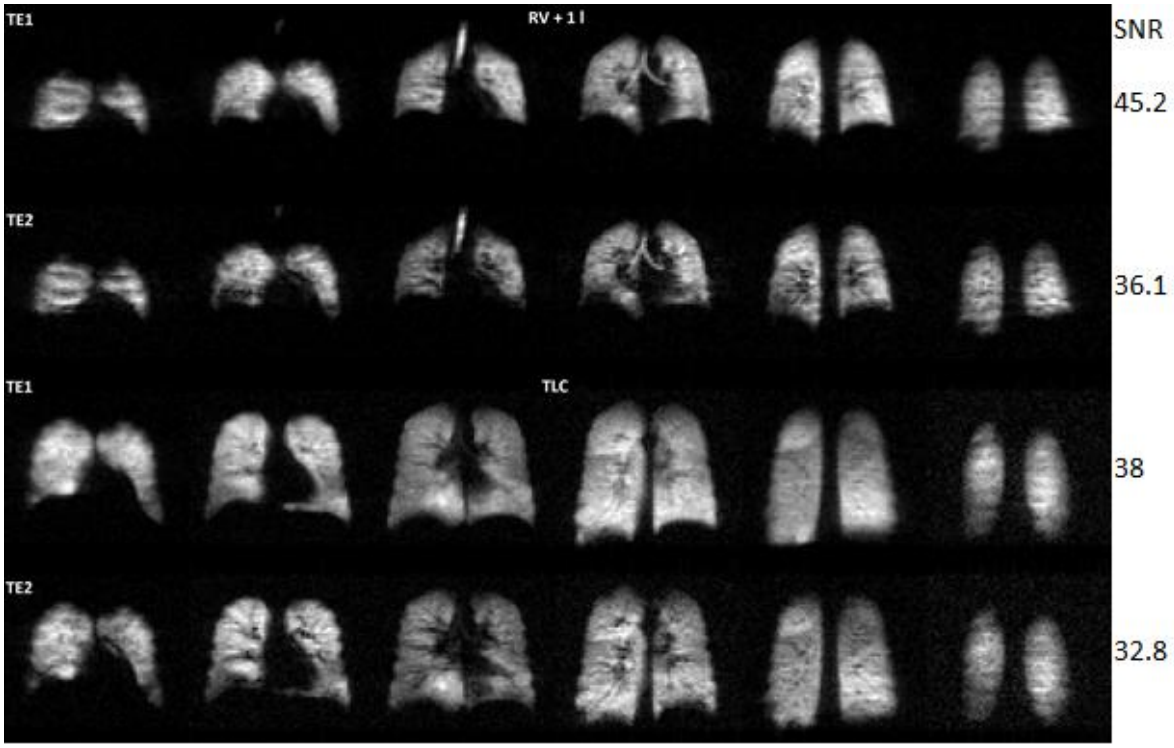

Figure 3.10. Typical slice-by-slice comparison of the lungs of a volunteer (40 year old male, 88 kg) obtained with ^{129}Xe at RV + 1 *l* and TLC at 3 T at TE_1 = 4.4 ms and TE_2 = 11 ms.

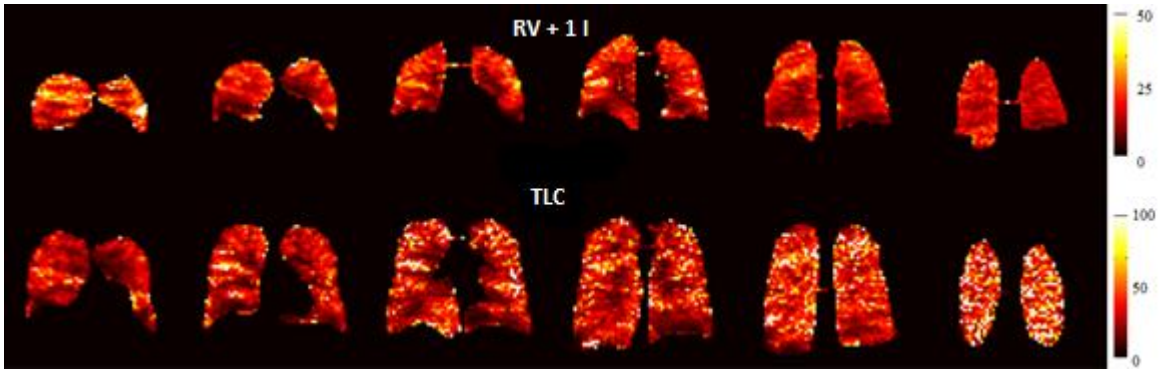

Figure 3.11. Slice by slice T_2^* maps generated by two point exponential fits from the images in Figure 3.10 at 3 T

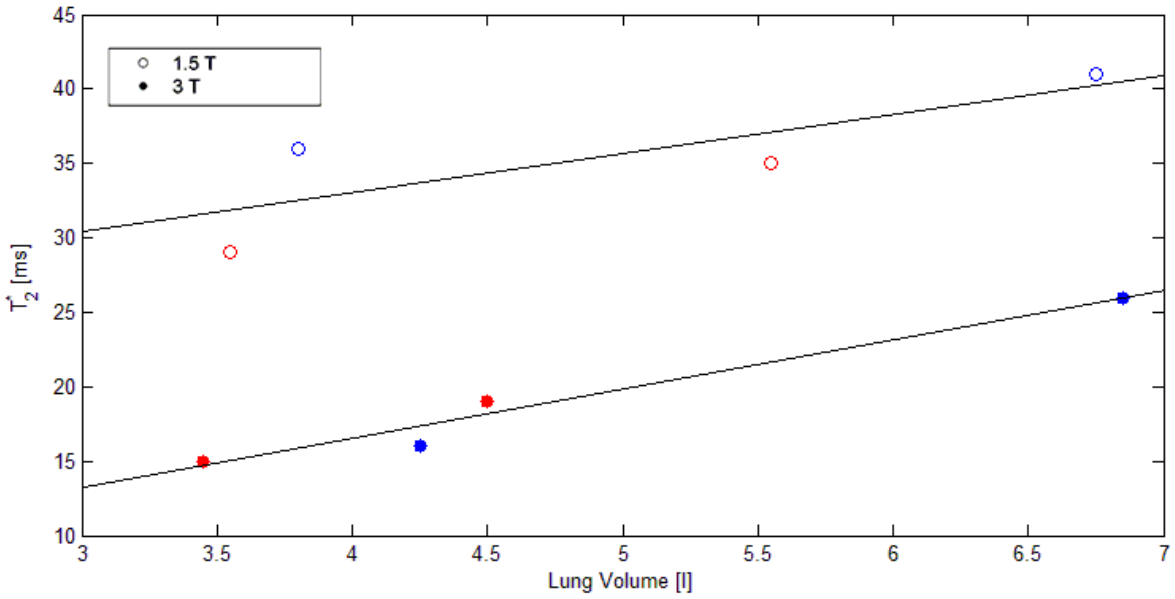

Figure 3.12. Mean T_2^* of the ^{129}Xe in the lungs of the two healthy volunteers averaged from all coronal slices against measured ventilation volume of the lung since the two volunteers (blue and red) are age, sex, and weight matched (the four data points corresponds to two volunteers at two lung inflation level, or four lung volumes).

Gender, age,[weight]	Lung inflation level	T_2^* at 1.5 T [ms]	T_2^* at 3 T [ms]
M, 41, [88 kg]	FRV + 1 ℓ TLC	36 ± 19 41 ± 21	16 ± 8 26 ± 10
M, 40, [88 kg]	FRV + 1 ℓ TLC	29 ± 12 35 ± 18	15 ± 6 19 ± 9

Table 3.2. Mean T_2^* of the two healthy volunteers from all coronal slices at two different lung inflation levels at two B_0 field strengths. The uncertainty was measured as the full-width at half maximum of the histogram.

The mean T_2^* values were then plotted against the measured ventilated volume by multiplying the number of all ventilated voxels from all slices by the voxel size of 6 × 6 × 30 mm^3 in Fig. 3.12, and summarised in Table 3.2.

The trend of these total lung capacity values of T_2^* being inversely proportional to B_0 suggests a pseudo-static dephasing regime (see Section 3.1 above). This was previously observed for inhaled ^{3}He T_2^* of 27.8 ± 1.2 ms at 1.5T compared to 14.4 ms ± 2.6 ms at 3T. (169). The dependence of T_2^* on lung inflation volume has also previously been observed with ^{3}He (180). Whereas T_2^* is inversely proportional to the magnetic field strength in the static dephasing regime, xenon is theoretically in that regime at 1.5 T but not at 3 T. This is however, hard to verify with only two clinical field strengths available. All the T_2^* values appear to scale inversely with B_0 at both lung inflations of FRC + l *l* and TLC as predicted in static-dephasing regime. Another effect in xenon measurements that needs to be considered is the dissolution of xenon into blood/tissue. It is thought possible that the increased alveolar SA/V ratio for gas exchange at lower lung inflation level may mean that a higher fraction of the gas in the alveolus samples the dissolved septal/blood compartment (162,163). However, exchange time of 100 – 150 ms (161) is much longer than that of T_2^* values, which would suggest a slow exchange during T_2^* decay, thus should have negligible effects.

As a result of the longer T_2^* values of ^{129}Xe at 1.5 T, it is likely to be more useful for experiments involving longer TE, e.g., diffusion studies (89) and EPI (181). A longer T_2^* can enable a narrower readout bandwidth that requires a longer *TE* due to the decrease of gradient strength (frequency encoding in Section 1.1.7). This leads to an improvement in SNR by equation 1.47, as predicted by theory (167) (Fig. 3.13). In Figure 3.13, an expected increase in SNR of less than $\sqrt{2}$ is expected from equation 1.47 as the receiver bandwidth is halved. The slight discrepancy in the measured SNR may be due to experimental precision and variability in gas polarisation/volume. How advantageous this is in practice is debatable as very low imaging bandwidths incur longer acquisition times, which prevents complete volume coverage at higher resolution within a breath-hold. Furthermore, the associated need for weak readout gradients means that the background B_0 inhomogeneity in the lungs may become significant in comparison. Lastly, the longer

echo time results in more dephasing due to diffusion action of the readout gradients, and should be taken into consideration.

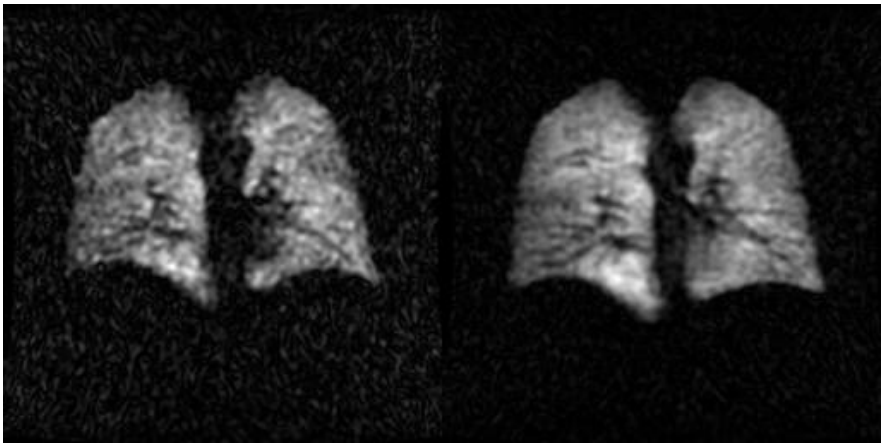

Figure 3.13. 15 mm central slice of a healthy volunteer at 1.5 T. Left: receiver bandwidth of 8 kHz with TE of 2.4 ms (SNR of 11.4/13.3 for the left/right lungs) . Right: receiver bandwidth of 4 KHz with TE of 3.6 ms (SNR of 27.6/28.6 for the left/right lungs).

3.4 Conclusion

In this study, the feasibility of high quality hyperpolarised ^{129}Xe gas ventilation imaging has been demonstrated at both of the clinically relevant field strengths of 1.5 T and 3 T, using small (300 m*l*) volumes of inhaled Xe gas (isotopically enriched to 86% ^{129}Xe). The high quality images obtained (SNR range 21–53) with a spatial resolution of 15 mm × 4 mm × 4 mm voxel, bode well for future clinical studies of lung ventilation at either clinical scanner field strength using modest volumes of ^{129}Xe gas. This is demonstrated below with comparable results from ^{3}He (Fig. 3.14) in healthy volunteers as well as sensitivity to lung regional functions as seen in Fig. 3.15 in a healthy smoker.

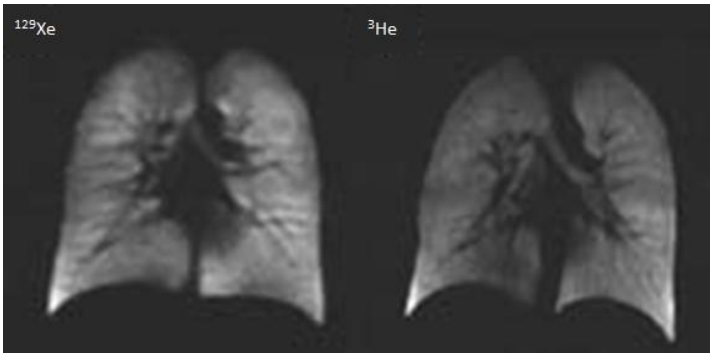

Figure 3.14. Comparable slice of the same volunteer (F, 26) with 300 ml ^{129}Xe (left, centric, 96 x 96 x15 mm) and ^{3}He (right, sequential, 192 x 192 x 10 mm) at 1.5 T.

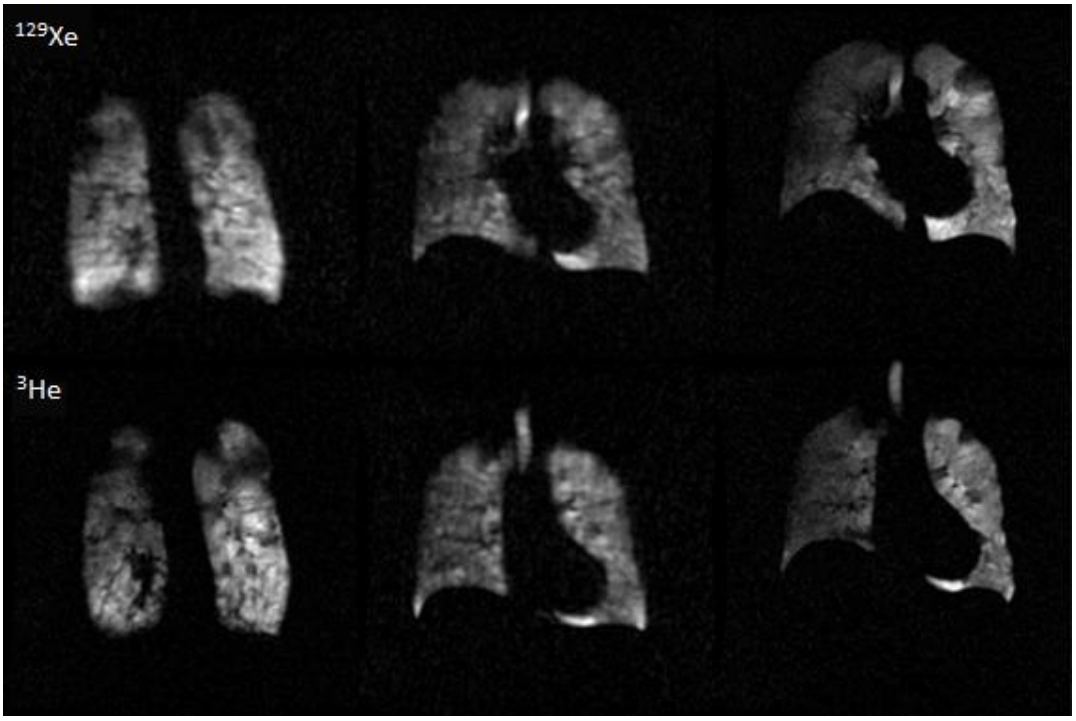

Figure 3.15. Central slice-by-slice comparison of the lungs of a healthy smoker with ^{129}Xe ventilation sequences at 1.5 T. Spatial resolution 15 mm × 4 mm × 4 mm.

CHAPTER 4: An Unshielded Asymmetric Split Insert Quadrature Birdcage Coil for Hyperpolarised ^{129}Xe Lung MRI at 1.5 T

(to be submitted to Magnetic Resonance in Medicine)

4.1 Introduction

Hyperpolarised gas MRI requires special RF hardware that can transmit and/or receive at the resonant frequencies of at the respective nucleus; 17.67 MHz and 48.65 MHz for ^{129}Xe and ^{3}He respectively (Table 1.1) at 1.5 T. In Chapter 3, work was carried out with flexible RF transmit-receive coils of double Helmholtz design. Whilst providing good sensitivity, the B_1 field homogeneity of such a coil design is not optimum and can change from subject to subject due to geometrical distortion and subject-dependent loading. Birdcage coils in comparison provide the best spatial homogeneity in B_1 fields. The objective of the work in this Chapter was to develop and demonstrate an insert body transmit-receive birdcage RF coil tuned to 17.7 MHz for imaging of hyperpolarised ^{129}Xe in the human lungs. The coil was designed for use on a whole body GE Signa HDx 1.5 T (GE, Milwaukee, WI, USA) system, and the field strength was chosen because the skeleton of the coil was made identical to the 1.5 T home built ^{3}He coil to fit the MR system. The design considerations and criteria include the following:

(i) Since the coil is designed for imaging the lungs, the size of the coil must be large enough to provide a uniform excitation across the FOV of the upper torso.

(ii) In addition, there must be enough room for future accommodation of either a ^{129}Xe and/or ^{1}H multiple receiver array.

(iii) In light of the above, the coil diameter was maximised, making full use of the magnet bore (60 cm in diameter).

(iv) The rigid body of the coil ensures a consistent homogeneous magnetic field with less potential variation due to differences in subject size than when using flexible transmit-receive vest coil designs (Fig. 3.4) which are closely coupled to the torso.

(v) Coupling with the MRI scanner's built-in proton body coil was to be taken into account in the design process by making all possible measurements inside the magnet bore. This was to enable anatomical ^{1}H imaging of the chest with the ^{129}Xe coil in-situ which allows acquisition of co-registered ^{1}H and ^{129}Xe images in the same breath hold (182).

(vi) Due to the non-recoverable ^{129}Xe polarisation, small flip angles are typically used in a spoiled gradient echo (SPGR) sequence in gas phase ^{129}Xe lung MRI. ^{129}Xe, however, can also be imaged in its dissolved phase in the blood using the gas in the lungs as a polarisation reservoir, in which case a much larger flip angle is typically used to image the dissolved ^{129}Xe signal. Thus, this coil must be able to deliver a wide range of flip angles in a homogeneous and linear fashion with delivered RF pulse power.

4.2 Materials and Methods

4.2.1 Coil design:

To satisfy all requirements mentioned above, an asymmetrical elliptical design was adopted based upon a geometrical mesh of copper conductors with an asymmetric oval cross-section (Fig 4.1) developed previously for ^{3}He lung MRI by the Sheffield group (183), which fits onto the patient table 16 cm below the 1.5 T magnet bore's centre line. A conformal mapping approach transforms evenly-distributed positions from the circumference of a circle onto a cylinder of arbitrary cross-section to produce a uniform

magnetic field by means of continuous current density on the surface of the cylinder, in this case, an elliptical cross-section. Assume that $f(w)$ is an analytical function of the transform, the transformation must include regions outside of the cylinder with known optimal current distribution (i.e. distortion approaches zero at infinity so the field's amplitude is the same) to satisfy $\lim_{w\to\infty}\frac{f(w)}{w}=1$. The conformal transformation *f(w)* can be solved using power series expansion and is given by:

$$f(w)=w+\sum_{k=1}^{\infty}\frac{c_k}{w^k} \tag{4.1}$$

where c_k are transformation complex coefficients and w is the coordinate in the circle plane. This calculation was performed by Nick deZanche using software developed previously (184).

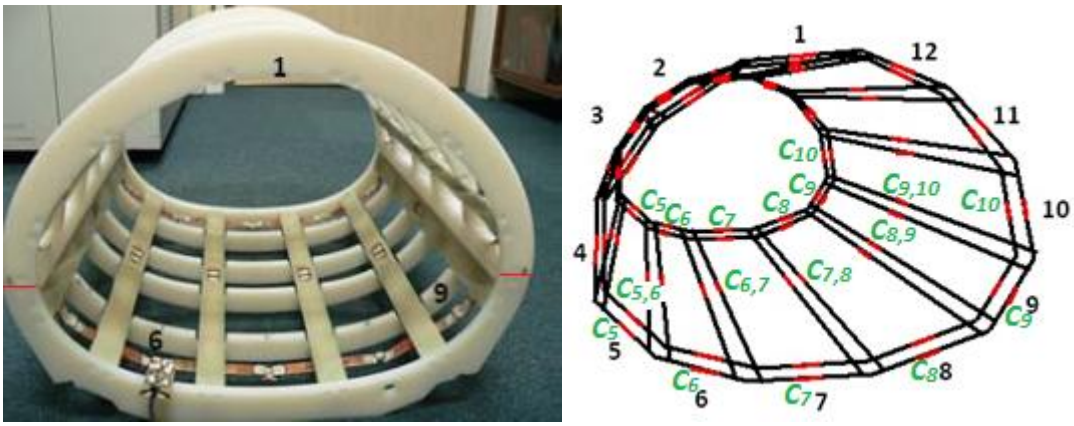

(a) (b)

Figure 4.1 **^{129}Xe body coil mesh with copper conductors with 12 rungs (a) which separate into two parts at the red line indicators. Schematics of the conducting mesh (b) with its corresponding mesh numbers, the thick solid black lines indicate the placement of the copper conducting bars of the mesh and the red sections indicates the placement of capacitors, and the annotation for bottom half capacitors are labelled in green.**

The mechanical support of the coil's conducting elements is designed to be separable into two parts, following the pattern of the coil previously developed for ^{3}He (183), to allow a

subject to enter conveniently by lying down after removal of the anterior portion with patient-accessible space 50 cm wide and 36 cm high. The ribs and spars of the coil are made of machined fibre-glass epoxy (FR4), which offers high mechanical and dielectric strength, while being flame-retardant. The copper bars that make up the network are 3 mm × 20 mm. Reliable, nonmagnetic beryllium copper lug connectors join the upper and lower half of the coil. The coil is connected to coaxial cables by non-magnetic BNC bulkhead connectors at meshes 6 and 9 (Fig 4.1 (a)) 90 degrees to one another for a quadrature coil design (Section 1.2.2). The outside of the coil is covered with a 3–mm-thick Acrylonitrile butadiene styrene (ABS) cover sheet for protection of the coil. Details of the materials, geometrical design, as well as technique for the capacitance estimation are described in full in (183).

The key differences of this coil are: firstly, it is not shielded therefore it is designed to be transparent to ^{1}H RF transmit-receive with the scanner body coil, and secondly the coil has a band-pass design, with capacitors located on both the rungs and the end rings, in order to have maximal control of coil tuning at this lower frequency of 17.7 MHz compared to 48.6 MHz for the previous ^{3}He design.

4.2.2 Inductance measurements

First, to determine the approximate capacitor starting values, an algebraic method was used. This method first requires knowledge of the ladder network's complete matrix of self and mutual inductances of the 12 meshes. These were obtained by measuring the resonant frequency or frequencies when single or pairs of meshes were populated with known capacitance values. The inductance measurements were performed inside the bore of the magnet to account for mutual inductance and coupling of the mesh with the ^{1}H body coil and other cables in the bore. In making these measurements, all other mesh elements were left open (183) (see Fig. 4.2) except the meshes being probed. By using a

known, fixed capacitor (5 pF), inductances were calculated based on the measured S_{21} network analyser frequency using equation (1.59) for an LCR network. This process requires the removal of copper tapes for shorting/capacitors and the re-soldering of them onto the next mesh in between each measurement. The soldering in between takes approximately 15 – 20 min, and the copper was allowed 5 – 10 min to cool down before taking any measurement since it affects the measured impedance values. This initial process of measuring inductances therefore took 2-3 weeks to complete in the magnet bore. The calculated inductances are summarised in table 4.1 in units of μH. By inversion of Leifer's expression (23) for the eigenmodes of the coil, the resulting calculated capacitance values for each of the elements provided the first iteration. The theoretical field maps were then generated in MATLAB using the capacitance values, shown in Fig. 4.3. Upon completing the second iteration of the coil, the field maps were plotted (Fig. 4.4 (b)) and a uniform, optimal magnetic field can be observed. Then it was noted that the centre frequency of each linear mode differed from the first iteration. Upon revisiting the initial capacitance values with the new resonating frequencies, the theoretical field maps of the first iteration were plotted (Fig. 4.4 (a)) and the result confirmed the field inhomogeneity of the first iteration observed experimentally. These simulations were performed using code written by Nicola deZanche at the University of Alberta using MATLAB code developed previously (183).

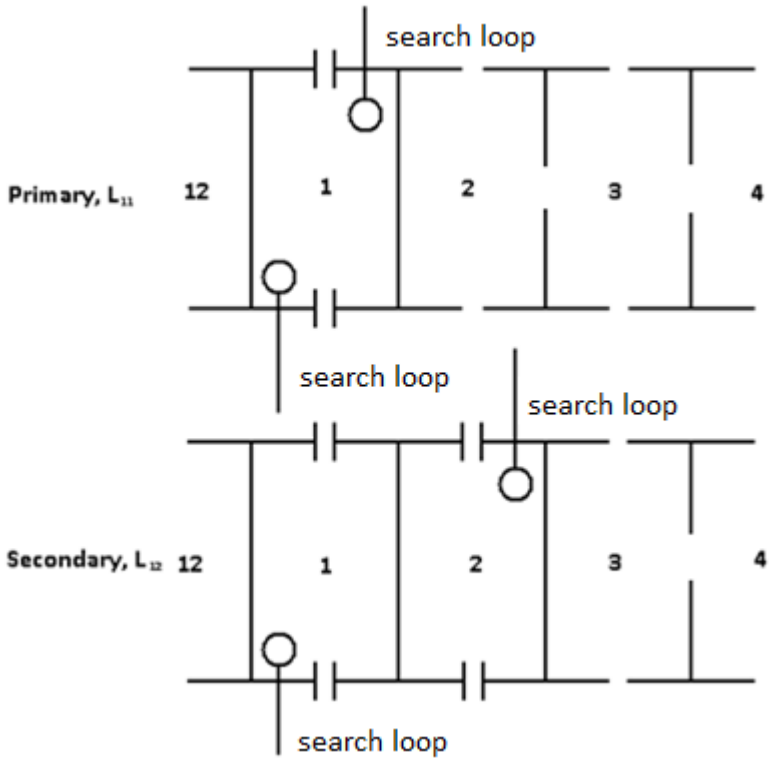

Figure 4.2. Schematics showing the technique for measurement of inductances between two elements of the coil with known capacitors and open circuits on all other meshes. Both search loops are connected to a network analyser for an isolation measurement (S_{21}) where one serves to transmit, and the other search loop receives.

4.2.3 Coil Tuning:

Since this is an un-shielded coil, coupling with the proton body coil must be carefully controlled and taken into consideration when tuning and matching the coil; imperfections including geometrical positioning, subject loading, finite capacitor tolerances, and mutual inductances between non-adjacent meshes, must be considered. Thus, all of the empirical iterative capacitance determination and coil tuning measurements were made inside the magnet bore.

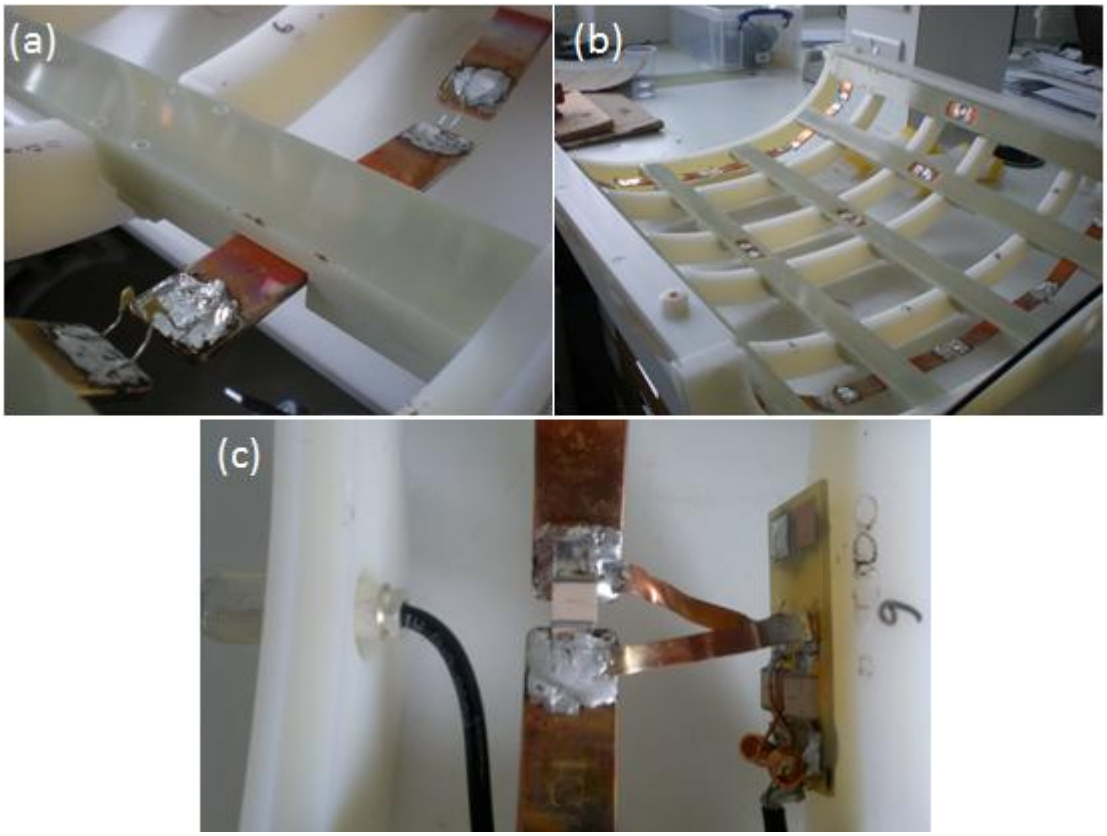

Figure 4.3. (a) Initial capacitors used in the building process with regular capacitors, which were then replaced by ATC capacitors (b), and completed with a BALUN cabled at meshes 6 and 9 (c).

With the first iteration of calculated capacitance values for the coil, it was first tested using low-tolerance, non-heat-resistant electrolytic capacitors (Fig. 4.3 (a)) just for the frequency measurements since no power was transmitted into the coil. Once the desired frequency has been achieved, high power RF tolerated capacitors were ordered from American Technical Ceramics (ATC). Once the ATC capacitors were received, they were soldered onto the coil (Fig. 4.3 (b)). This resulted in a change in the resonant frequency perhaps due to the extra capacitance in the capacitor legs, and differences in tolerances, etc. This step was omitted for the second iteration as it did not provide an accurate enough values. All capacitors were then iteratively adjusted to achieve the desired frequency of 17.7 MHz for both linear modes to allow quadrature operation. Due to the

effect of additional inductance from coupling between the ^{129}Xe coil mesh and ^{1}H body coil and cables, a systematic decrease in all of the capacitor values from the values simulated, was needed. The final values were approximately 91 ± 30 pF (10 – 13% difference) less than the calculated values after the first major iteration of a working coil, and are summarised in table 4.2 (top). The values after the second major iteration of a working coil are summarised in table 4.2 (bottom). There are between 0.4 and 29 % differences between simulated and empirically optimised capacitor values.

	1	2	3	4	5	6	7	8	9	10	11	12
1	594.9	194.3	12.2	-1						-1	12.2	194.3
2	194.3	614.3	199.9	-1	-1							14.2
3	12.2	199.9	589	223.3	16.4							
4	-1	-1	223.3	543	182.3	-1						
5		-1	16.4	182.3	564	195.2	30.5					
6				-1	195.2	657	206.2	18				
7					30.5	206.2	701.3	206.2	30.5			
8						18	206.2	657	195.2	-1		
9							30.5	195.2	564	182.3	16.4	-1
10	-1							-1	182.3	543	223.3	-1
11	12.2								16.4	223.3	589	199.9
12	194.3	14.2							-1	-1	199.9	614.3

Legend:
- measured
- formula gave complex value;
- symmetry of coil
- symmetry of matrix
- not measured

Table 4.1 Primary and secondary inductance values (in units of µH) of the xenon body coil calculated from the frequency of the S_{21} reading from a network analyser (in units of MHz) and the known capacitor value (5 pF) by equation 1.59. These table values were then used to calculate for all the capacitor values for all 12 meshes.

Note that some of the secondary simulated capacitance values on the coil rungs (the longest length conductors that connect the two end rings) are all very large and in practice were shorted with copper strips (e.g. $C_{4,5}$, $C_{5,6}$, $C_{6,7}$).

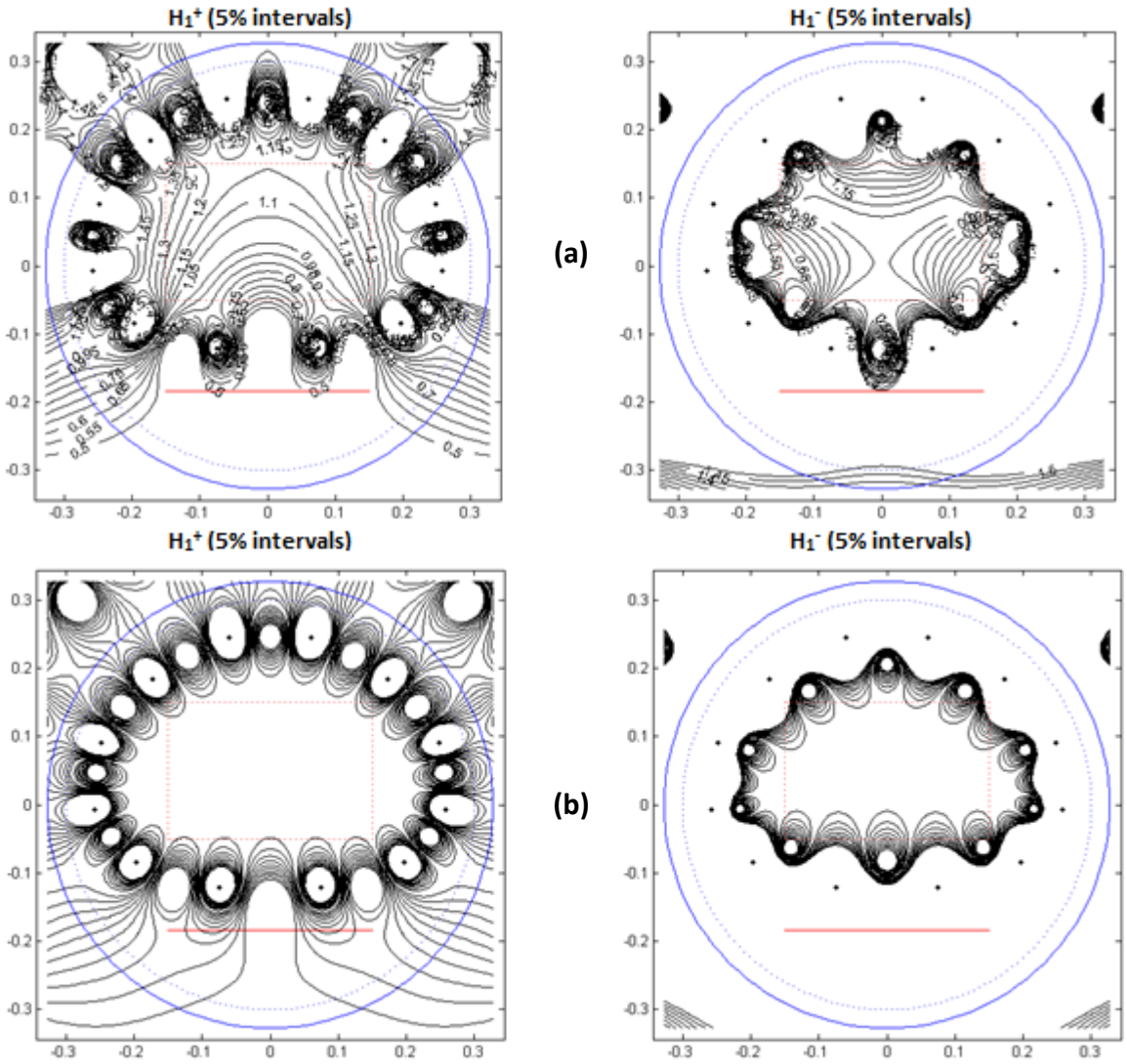

Figure 4.4. Transmit field contour maps through the transverse plane through centre of the coil of the first initial iteration of capacitor values from simulation (a) and second initial iteration values (b), which shows improved homogeneity and uniformity. The black dots in each individual graph correspond to the 12 legs of the coil, the blue circle is the proton body coil inside the scanner, and the red line is the scanner table where the body coil is positioned.

Lastly, after the final iteration of the tuning, the quadrature coupling to the ladder network was achieved through standard lattice baluns (Fig. 4.5) across one of the end

rings at elements 6 and 9. This process was performed on the bench top prior to connecting to the coil with a network analyser to ensure the lattice balun resonates at the Larmor frequency of ^{129}Xe at 17.7 MHz.

Mesh Position	C_1	C_2	C_3	C_4	C_5	C_6	C_7	$C_{1,2}$	$C_{2,3}$	$C_{3,4}$	$C_{4,5}$	$C_{5,6}$	$C_{6,7}$
First major iteration													
Calculated capacitor values [pF]	681	624	807	873	779	570	555	2815	8018	1981	∞	2189	1028
Final capacitor value [pF]	620	640	790	820	979	640	550	1700	8820	2220	∞	1860	840
Second major iteration													
Calculated capacitor values [pF]	725	665	873	986	851	602	502	2625	3931	1419	∞	∞	∞
Final capacitor value [pF]	880	510	620	820	680	575	500	2610	4400	1440	∞	∞	∞

Table 4.2. Capacitor values at their corresponding mesh positions in the xenon body coil after the first and second major iterations, where a single subscript denotes one of the primary capacitors of its corresponding mesh number on the end rings, and the double subscript denotes one of the capacitors on the rungs of the coil (Fig. 4.1 (b)). Due to symmetry about the y-z plane, only half of the values are shown (i.e. $C_1 = C_{12}$, $C_6 = C_9$, and $C_{1,2}=C_{1,12}$).

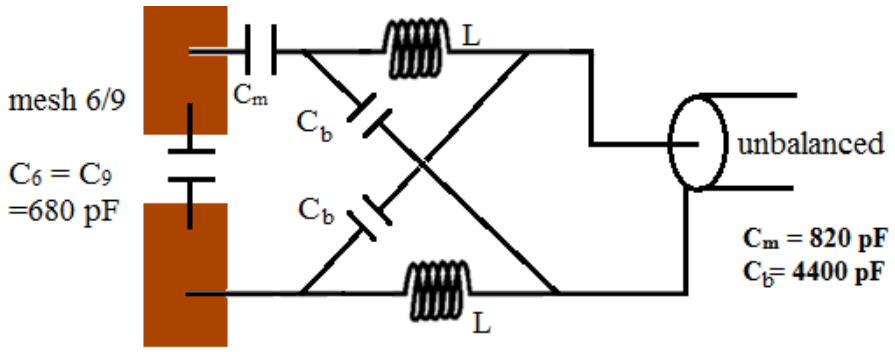

Figure 4.5. Lattice balun design connected at mesh 6 and 9 (680 pF, see Table 4.2). The lattice balun was tuned on the bench top, wire wound solenoid inductors were manually adjusted so the circuit resonates at ^{129}Xe frequency of 17.7 MHz.

4.3 Coil testing

4.3.1 Network Analyser measurements

Fig. 4.6 (a) & (b) shows the S_{11} measurements of the coils' two resonant linear modes of 17.45 MHz and 17.71 MHz when loaded with the same healthy volunteer after the first major iteration. The plots are centred at a frequency of 17.7 MHz with a 3 MHz span.

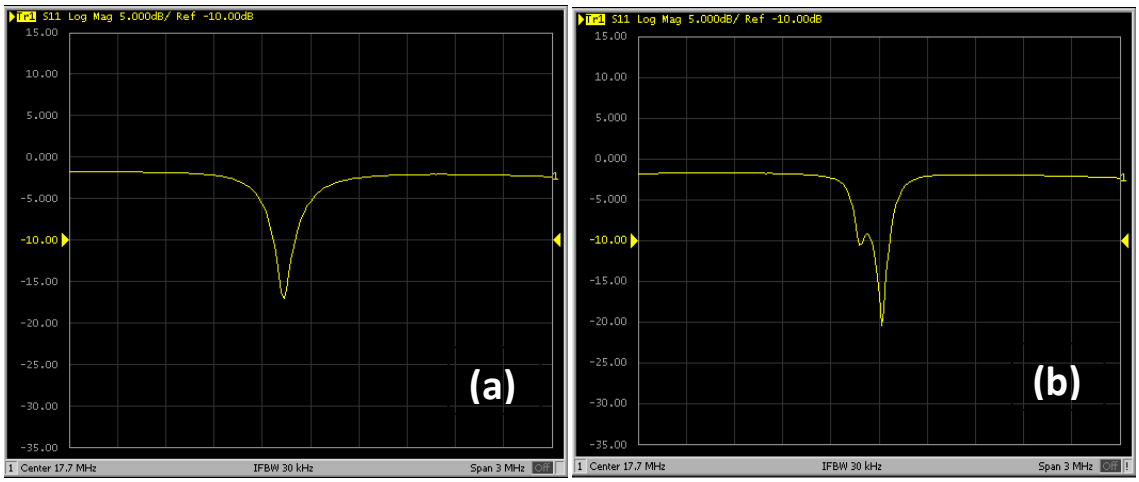

Figure 4.6. S_{11} measurements of the coil's resonating frequency inside the proton body coil for the two ports (meshes 6 (a) and 9 (b)) centred at 17.7 MHz with a 3 MHz span after the first major iteration.

Despite a high degree of spatial homogeneity seen at the centre of the imaging field, spatial inhomogeneity was found in the left distal lung of the first round of test images (white arrows in Fig. 4.12) as well as in the anterior to posterior direction of the coil. It was then retuned and the S_{11} measurements from the second major iteration are shown in Fig. 4.7 (a) & (b). The plots are centred at a frequency of 17.65 MHz with a 3 MHz span.

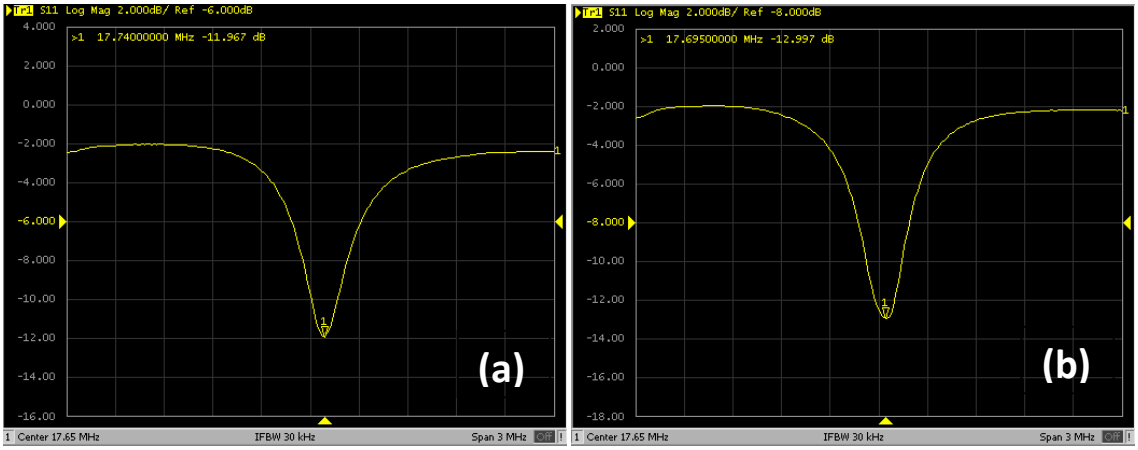

Figure 4.7. S_{11} measurements of the coil's resonating frequency inside the proton body coil for the two ports (meshes 6 (a) and 9 (b)) centred at 17.6 MHz with a 3 MHz span after the second major iteration. Note the slight splitting in the second port measurement has now been resolved.

To investigate the matching of the coil, Fig. 4.8 shows the return loss (S_{11}) measurements (Agilent Technologies E5061A, CA, US) of the unloaded (a) and loaded (b) coil, notice the quality factor Q (as discussed in Chapter 1) is greatly improved with loading from $Q_{unloaded}$ = 44 to Q_{loaded} = 121. Note also that the centre frequency changes very little with loading. Note that for accurate Q measurement, a two-port isolation S_{21} measurement is needed.

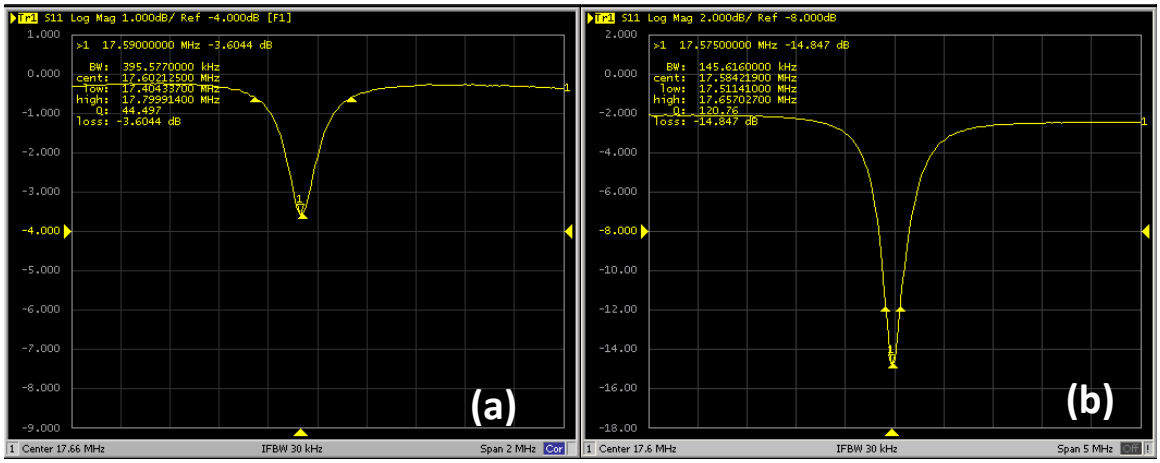

Figure 4.8. S_{11} measurement of unloaded (a) and loaded (b) coil with a healthy volunteer with a quality factor of 44 and 121 respectively.

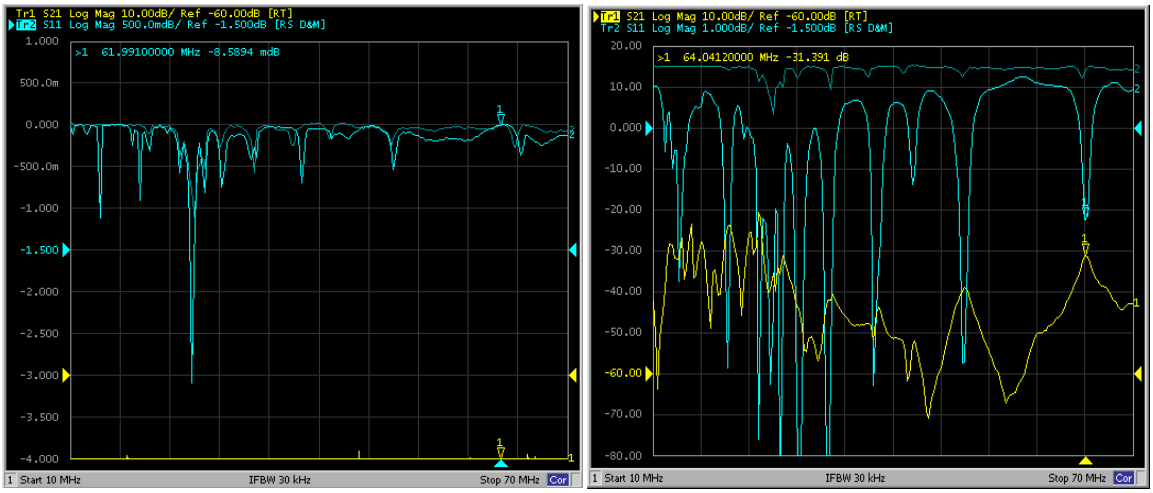

Figure 4.9. Left: S_{11} measurements of ^{1}H body coil without xenon body coil (memory trace in thinner blue) and with xenon body coil (brighter blue) inside the magnet bore.
Right: S_{21} isolation measurement between the proton body coil and the xenon body coil with < -20 dB isolation at both frequencies.

Lastly, to ensure the compatibility of the xenon body coil with the proton body coil of the clinical scanner, coupling between the two coils was determined by the isolation measurement (S_{21}) from the network analyser. Coupling is the electromagnetic interaction of two RF resonators that can cause change in coil resonant frequency (Fig. 4.9 left), and affect the performance of one or both of the coils. The coupling for the xenon body coil was taken into consideration and the coil was tuned in the coupled state. The proton coils, however, cannot be re-tuned, thus this measurement is important to see if proton imaging is achievable while coupled to the xenon body coil. The measurement was done with two cables directly connected to the proton coil and the xenon body coil, where one transmits signal and the other receives, outputting isolation, S_{21} measurement (Fig. 4.9 right). This is a more important issue in transmit/receive coils of the same resonating frequency. Fig. 4.9 shows the S_{21} of the xenon coil and the proton body coil as measured as the RF amplifier output cable and port on element 6 on the xenon birdcage. S_{21} < -20 dB was measured at both resonating frequencies (17.7 MHz for ^{129}Xe and 63.87 MHz for ^{1}H), indicating only a weak coupling. Using the S_{21} measurement of -31 dB at the proton

resonating frequency, a 0.08% attenuation ($10^{-3.1}$), which means 1kW x 0.08 % = 0.8 W is deposited for every kW. It was concluded that the unshielded xenon coil can safely be used inside the ^{1}H body coil while imaging low-flip-angle proton localiser scans without fear of significant induced currents in the xenon coil.

The final assembled birdcage coil with the covers on is shown in a photograph in Fig. 4.10, operating in the 1.5 T GE clinical scanner with a subject inside.

Figure 4.10. The coil setup on the clinical 1.5 T system with subject in position ready to be located at the bore centre.

4.3.2 MRI tests:

MRI was performed on three healthy volunteers (26 years old, female, 50 kg; 30 years old, female, 60 kg; 42 years old, male, 88 kg). Written consent was acquired from the volunteers and approval was obtained from the local ethics committee. The process of hyperpolarising ^{129}Xe was described in full in Chapter 1.

^{1}H MRI tests

Flip-angle calibration for proton imaging was performed with the ^{129}Xe coil in-situ since the ^{129}Xe and ^{1}H body coils do couple slightly to each other (S_{21} < -20 dB), and some ^{1}H body coil detuning was also induced (Fig.4.9 left). The flip angle for proton scans without the ^{129}Xe coil in-situ was first determined prior to imaging using a water phantom. Scout images were obtained using a fast GRE sequence with a resolution of 128 × 128 matrix,

BW of ± 62.5 kHz, FOV of 40 cm × 40 cm. The ^{129}Xe coil was then placed inside the bore with the same phantom using the same auto prescan transmit gain (TG) value of 116 that was returned from the auto prescan without the coil in-situ. The same sequence was performed and the SNRs of both images with and without xenon coil *in situ* were recorded. We can estimate the flip angle while the xenon body coil is inside the proton body coil from:

$$\alpha_{withcoil} = \sin^{-1}\left[\sin\left(\alpha_{withoutcoil}\right) \cdot \frac{SNR_{withcoil}}{SNR_{withoutcoil}}\right] \qquad (4.2)$$

Using this method, we can determine the nominal flip angle (transit gain setting) needed in order to achieve comparable SNR with the xenon body coil inside the bore of the magnet. The relative image quality was then tested with a 2D spoiled gradient echo pulse sequence with a resolution of 128 × 128 matrix, BW of ± 62.50 kHz, FOV of 40 cm × 40 cm, flip angle of 5° calculated using equation (4.2), and 10 mm slices. Negligible change is seen in the quality and SNR of proton imaging, as seen in Fig. 4.11.

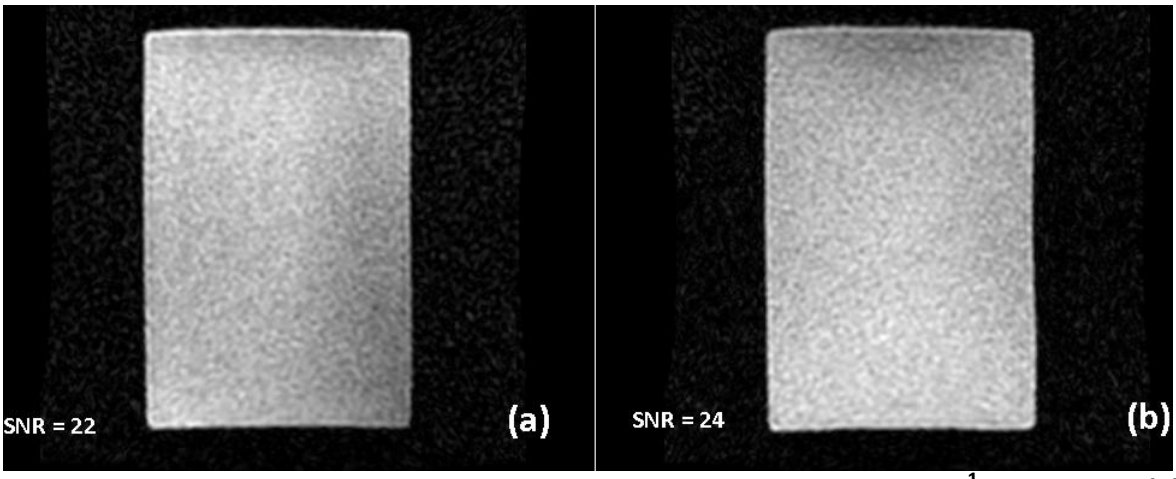

Figure 4.11. Image of the same aqueous phantom using the system's ^{1}H body coil (a) with the insert xenon body coil in place and (b) without the xenon coil following flip angle calibration from equation (4.2).

^{129}Xe MRI tests

Two-dimensional (2 D) ^{129}Xe coil B_1 maps were first obtained using ventilation images obtained during a breathhold with four-image acquisitions per slice. The sequence was a 2D spoiled gradient echo with parameters: 20 mm coronal slices, field of view (FOV) of 40 cm × 40 cm, resolution of 64 × 64 matrix, receiver bandwidth (BW) of 8 kHz, TE/TR of 4/10.2 ms, Cartesian centric phase encoding, with TG of 120 (corresponding to an approximate flip angle of 5°, was used for SNR purposes (176).

Xenon ventilation imaging was also performed using the same 2D spoiled gradient echo sequence as used in Chapter 3 with the CMRS vest coil as used in Chapter 3, with parameters: 96 × 96 matrix size resolution, BW of ± 2 kHz, FOV of 40 cm × 40 cm, TE/TR of 3.6 / 18.9 ms, flip angle of 9°, 15 mm slices, TG of 120, and Cartesian centric encoding.

4.4 Results and Discussion

4.4.1 Imaging with the xenon body coil

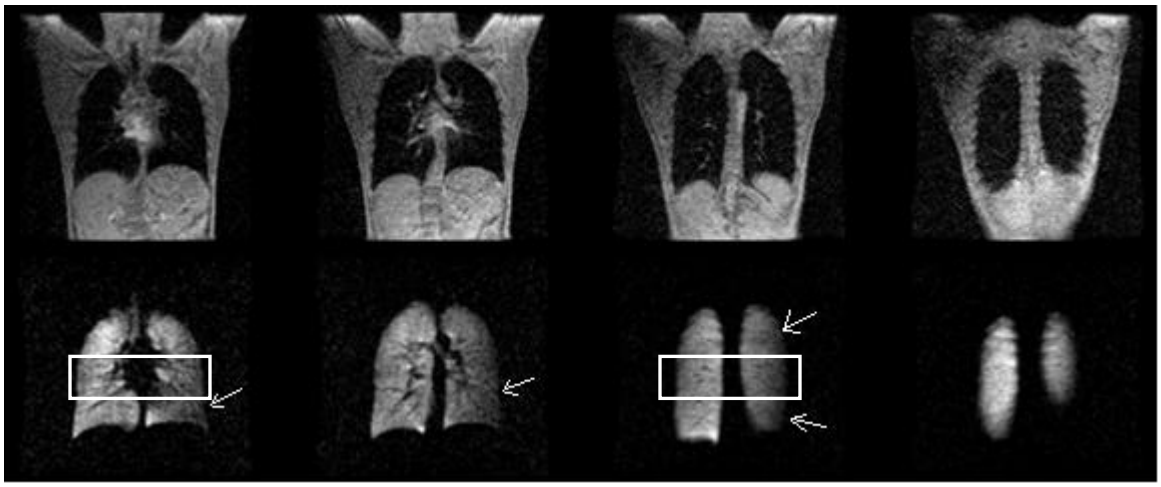

Figure 4.12. Central slices of 2D coronal ventilation images obtained after the first iteration of coil tuning from a healthy volunteer (F, 26 years old, 50 kg) with the corresponding localiser proton images. Note the shading inhomogeneity in the left lung.

Typical ventilation images from a healthy volunteer are shown in Fig. 4.12 along with the proton localiser performed prior to ^{129}Xe imaging follows the first iteration of the coil

tuning. A high degree of spatial homogeneity is seen at the centre of the imaging field with a small but consistent inhomogeneity distal from the centre in the lung (arrows) is seen in the ventilation images after the first major iteration. After the second major iteration, ventilation images are much more homogeneous (Fig. 4.13), and the signal intensity profiles of the ROIs selected in these images are shown in Figure 4.14, note the signal intensity uniformity within each lungs after the second iteration (Fig. 4.14 (b)). These ventilation images are comparable in terms of SNR to those obtained in Chapter 3 with the flexible vest coil (see Section 3.4.2).

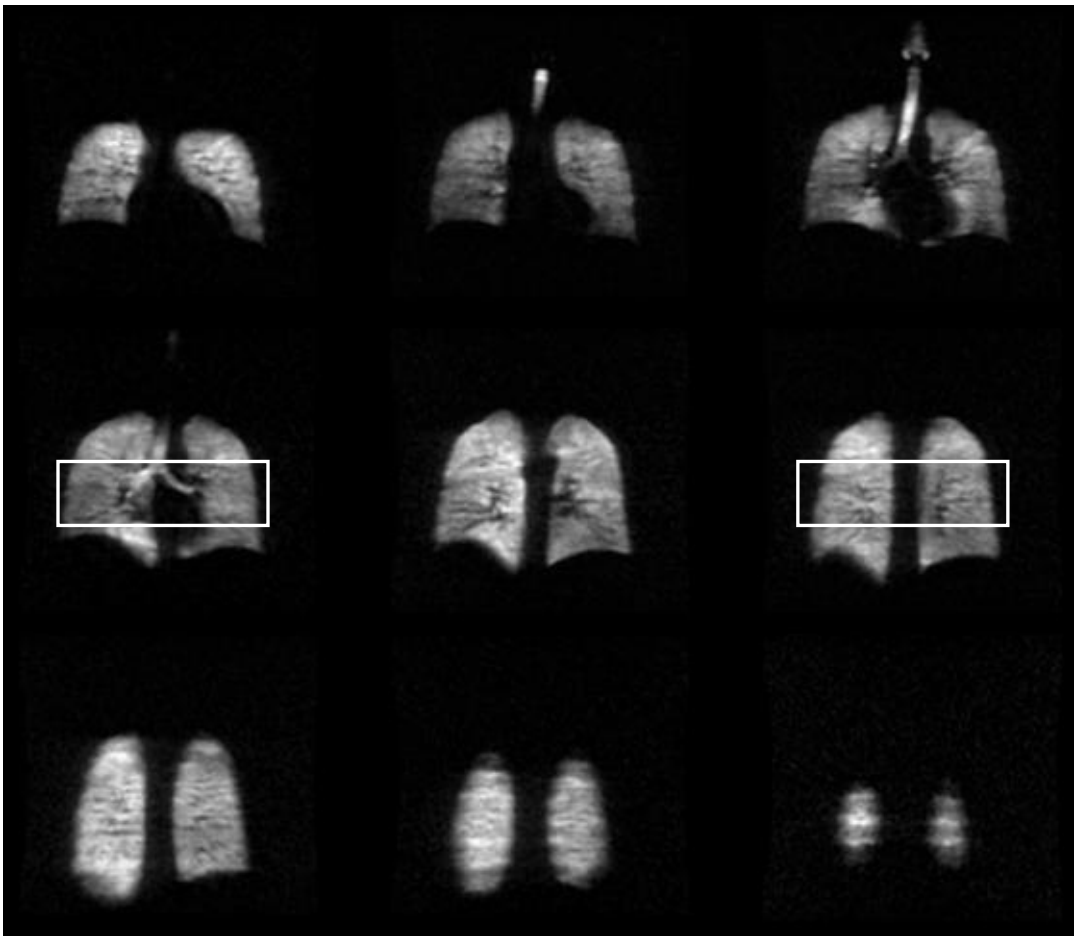

Figure 4.13 2D coronal ventilation images of a healthy volunteer (41 years old, 88 kg) after second iteration of the coil. Notice the improved homogeneity in both left right, anterior to posterior direction compared to those in Fig. 4.11.

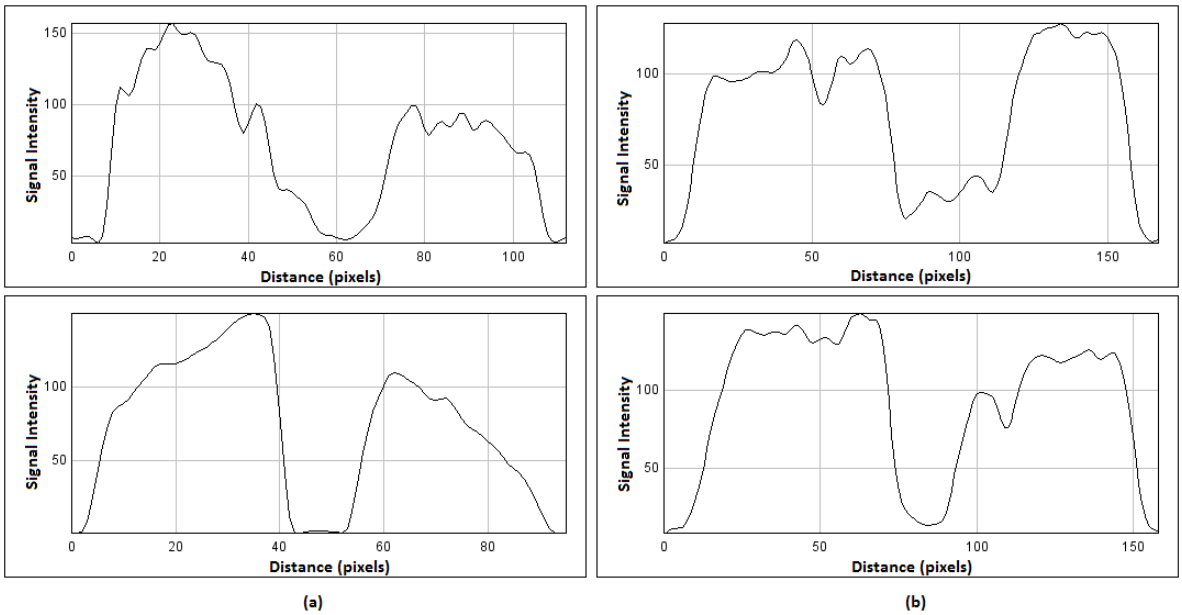

Figure 4.14. Signal intensity profiles of the ROIs selected in Fig. 4.12 (slice 1 top, slice 3 bottom) and Fig. 4.13 (slice 4 top, slice 6 bottom) in comparison of similar slices. Note the lack of homogeneity of imaging signal intensity within the lung regions after the first iteration (a) with signal drop offs on both distal regions of the lungs especially in the more posterior slice (bottom (a)). In contrast, signal intensity profiles after the second iteration produce almost uniform signal intensity across each lung in forms of plateaus (b), indicating a higher imaging uniformity.

4.4.2 B_1 maps

Flip angle maps of the xenon body coil can better quantitatively demonstrate field homogeneity. B_1 maps were calculated from the four images obtained per slice, each pixel has four decaying signal intensities governed by the flip angle, α, of the RF pulses by $S(n) = S_0 \cos^{\mathrm{n}} \alpha$. B1 maps of each slice were obtained by fitting for the flip angles from the four data points on a pixel-by-pixel basis.

Corresponding B_1 maps are shown with their ventilation images in Fig. 4.13 for the first (a) and second (b) major iteration. Again, note the inhomogeneity associated to the edge of

the lungs after the first iteration, and improvement of homogeneity post second major iteration.

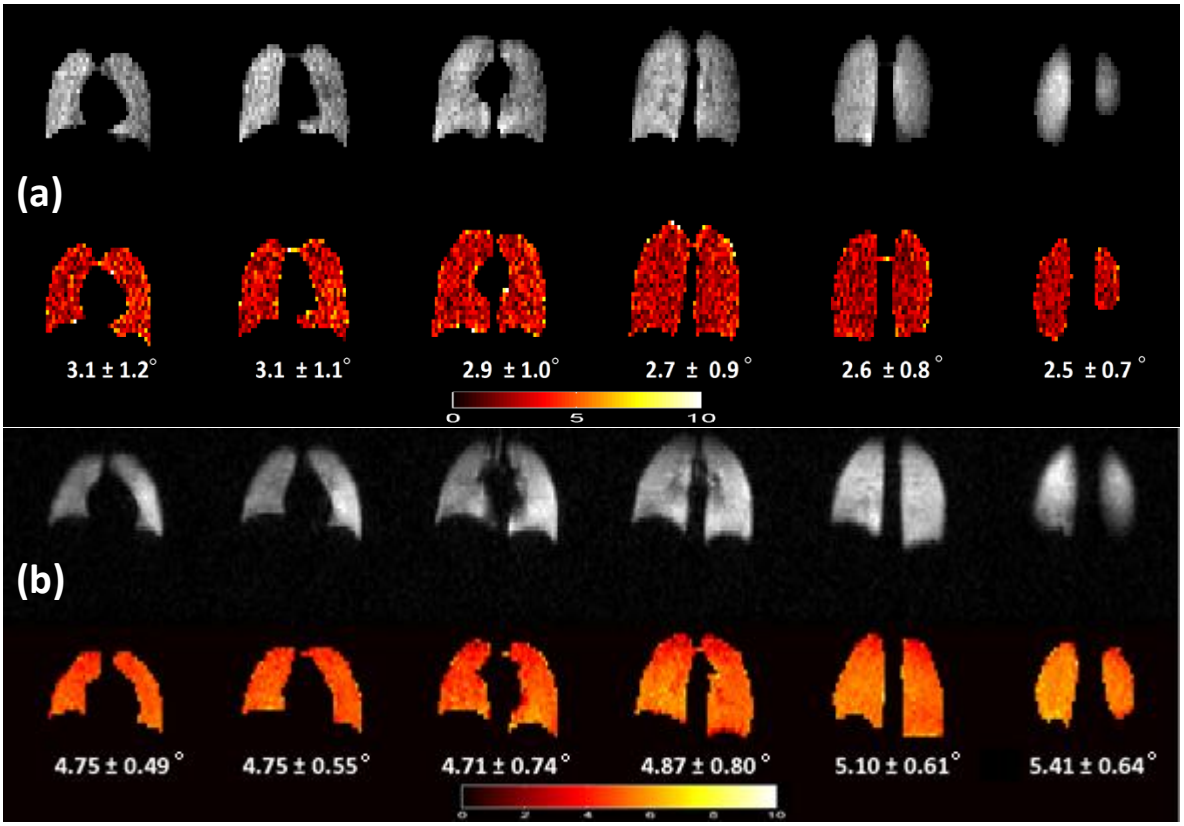

Figure 4.15. First of four consecutive 20 mm coronal ventilation image slices of a healthy volunteer (F, 30 years old, 60 kg) used for B_1 flip angle mapping (top) and the corresponding B_1 maps (bottom) with the corresponding mean and one standard deviation values (in degrees) after the first (a) and second (b) major iterations.

4.4.3 Comparison with CMRS quadrature flex coil (as used in Chapter 3).

To further test the imaging quality, as well as field homogeneity produced by the new asymmetrical ^{129}Xe birdcage body coil, the ventilation image SNR and B_1 flip angle maps were compared to the performance of the CMRS quadrature double Helmholtz flex coil as used in Chapter 3.

Ventilation images

By calculating the signal-to-noise ratio using the average of the ROI of the signal divided by the standard deviation of the ROI of the background (Fig. 4.14) on a slice-by-slice basis, a comparison of the SNRs of the two coils are shown in Fig. 4.15. The SNRs of the vest coil and the birdcage coil are 43.2 ± 5.3 and 29.8 ± 2.6 (mean ± standard deviation) respectively, showing a slightly lower, yet more uniform SNR from the whole body rigid birdcage coil when used as a transmit-receive coil. This is consistent with the concept of filling factor since a coil that is "filled" by the imaging target as close to the coil as possible produces the ideal SNR. Using the average female's lung residual volume + 1 *l* under experimental condition (See Fig 2.2), the birdcage coil inevitably has a lower filling factor ($2.8\ l\ /\ V_{xbc} > 1/2$, see Fig.4.16 (a)) compared to that of the CMRS vest coil ($2.8\ l\ /\ V_{CMRS} < 1/4$, see Fig. 4.16 (b)), thus lower SNR.

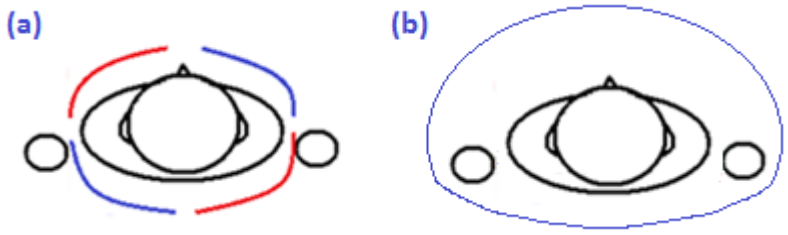

Figure 4.16. Schematics of the same volunteer in the CMRS vest coil (a) compared to the birdcage body coil (b). Notice the considerable differences in the coil volume, denoted by V_{CMRS} (volume of the CMRS vest coil) (a) and V_{xbc} (volume of the xenon body coil) (b).

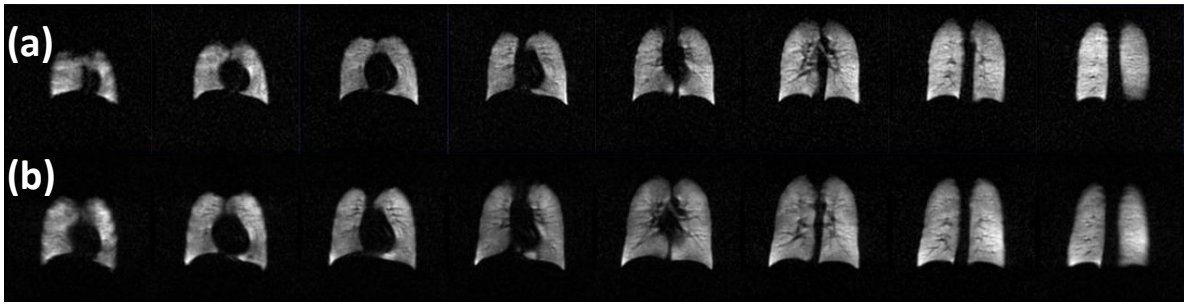

Figure 4.17. Slice-by-slice comparison of the lungs of a healthy volunteer (26 years old, 50 kg) obtained with ^{129}Xe ventilation sequences using a vest coil (a) and the asymmetrical home-built birdcage coil (b). Spatial resolution in both sets of images is 15 mm × 4 mm × 4 mm.

(a)

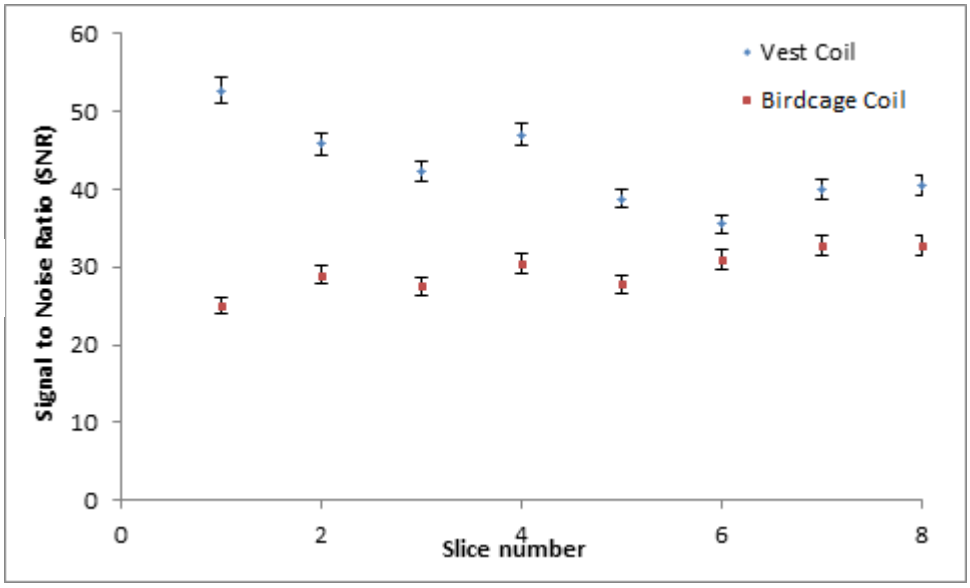

(b)

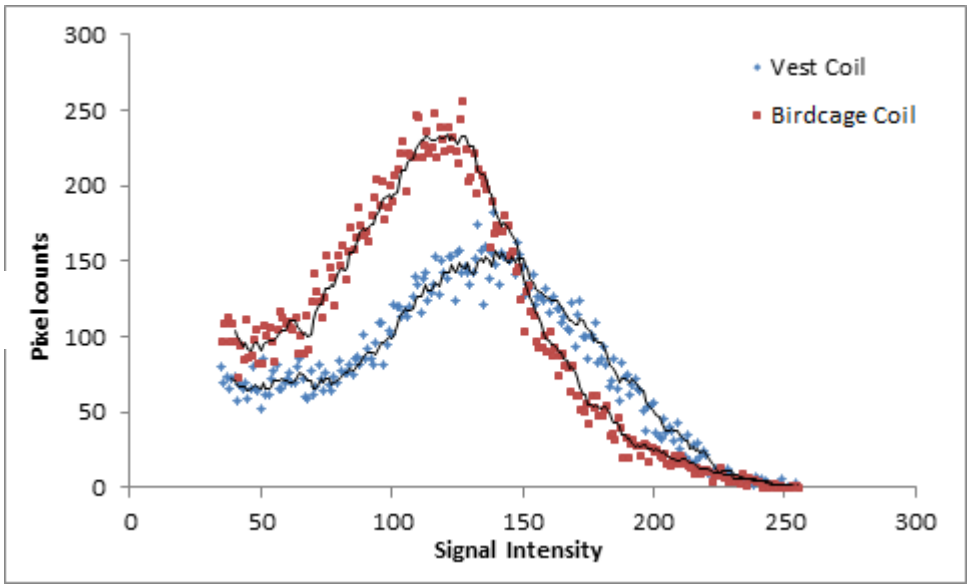

Figure 4.18 **Slice-by-slice SNR comparison between asymmetrical birdcage coil (a) and CMRS vest coil (b) used in Chapter 3 with the same imaging sequence, same volunteer, as well as comparable inhaled ^{129}Xe volume and polarisation (300 ml @ ~10%). The bottom graph shows the histogram of all imaging pixels from all slices from figure 4.17, showing a narrower distribution with a FWHM of 75 using the birdcage coil compared to that of the vest coil with a FWHM of 100 as suggested theoretically.**

B_1 maps

After comparing the SNR of the two coils, B_1 maps were also compared between the two coils with the same volunteer and imaging sequence, shown in Fig. 4.19.

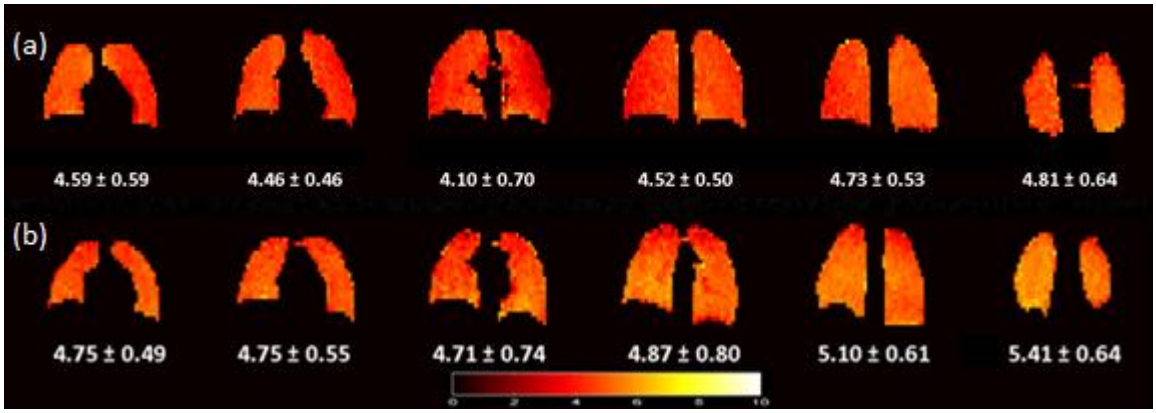

(c)

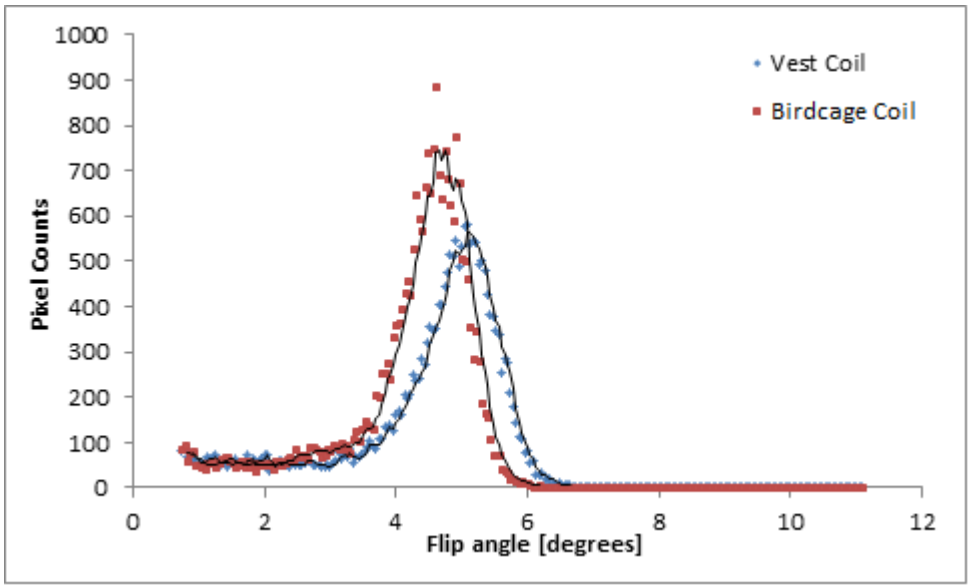

Figure 4.19. ***B_1*** **map comparison between the asymmetric birdcage coil (a) and the vest coil (CMRS, USA) (b) and their mean flip angle and its associated standard deviation. In (c), all flip angle calculated from all pixels from all slices are displayed in a histogram fashion comparing the two coils. Note again the narrower distribution from the birdcage coil with a FWHM of 0.91 from 1.26 of the vest coil. Again, this suggests a higher degree of homogeneity of the rigid coil.**

4.4.4 Co-registered $^{1}H/^{129}Xe$ imaging

The ability to image protons in the thorax with minimal interaction with the xenon coil enables co-registered $^{1}H/^{129}Xe$ imaging in the same breath-hold (182). This is shown in Fig. 4.20 with *in vivo* ^{1}H and ^{129}Xe images obtained back to back from a healthy volunteer in the same breath-hold.

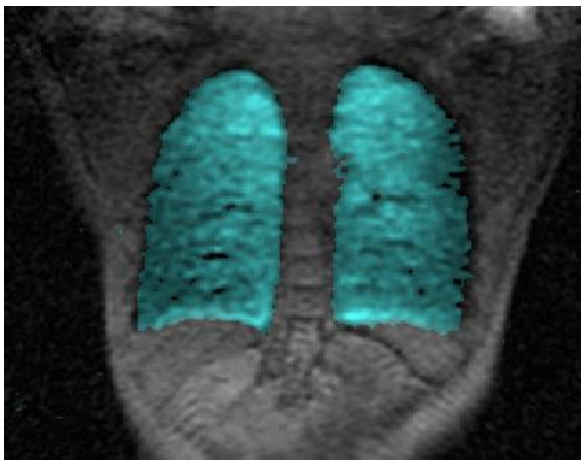

Figure 4.20. ^{129}Xe image (blue) superimposed on the coregistered ^{1}H image that was acquired in the same breath with the ^{129}Xe coil in-situ in the ^{1}H body coil.

4.5 Conclusion

We have described the design, construction and demonstrated the *in vivo* uses of a whole-body insert asymmetric birdcage transmit-receive coil for hyperpolarised ^{129}Xe MR lung imaging. Due to the initial calculation estimation errors, the first iteration of the coil led to noticeable inhomogeneity in B_1 magnetic field. After the second major iteration of the coil, the coil can now provide a homogeneous magnetic field and its feasibility for high quality hyperpolarised ^{129}Xe ventilation imaging as a transmit-receive coil has been demonstrated through ventilation images and B_1 maps.

Some of the drawbacks of this design of coil include:

(i) Band-pass design of the coil introduces more variables into tuning of the coil. This introduced more changes during the building process to preserve the field homogeneity (i.e. symmetry has to be preserved and usually all capacitors must be decreased/increased to preserve the field homogeneity). Perhaps a low-pass design would have been a simpler solution for a coil resonating at 17.7 MHz.

(ii) Un-shielding the coil also made the construction process harder. By introducing this large amount of copper into the clinical scanner bore, an unshielded coil will couple to the proton coil, thus impossible to tune on a bench top, perhaps a simpler way to enable proton imaging is to construct a proton transmit/receive vest coil to be used inside a shielded xenon body coil.

The initial motivation of this design was governed by the previous coil design of a ^{3}He coil using the same body constructed of a band-pass design, which resonates at 48 MHz. Xenon, however, has a lower gyromagnetic ratio and resonates at a much lower frequency of 17.7 MHz. This influenced an initial decision to opt for a low-pass configuration since a low-pass configuration typically yields a higher performance, whereas a band-pass design is usually adopted at higher frequency as it minimises the electrical field loss and maximises the loading factor. Most published birdcage designs, however, are smaller in size where inductance distribution is much less of an issue, thus being able to distribute among considerably more points on the coil in a band-pass design might be the better choice for this torso coil. Taken into consideration of the above, a birdcage coil design would still be suggested to someone who is aiming to build a xenon whole body birdcage coil for 1.5 T. The empirical tuning of the coil took a considerable amount of time due to coupling to the proton coil, but this allowed the coil to be transparent to the scanner's proton body coil, enabling proton localiser imaging prior to xenon lung imaging as well as co-registered ^{1}H/^{129}Xe images in a single breath hold. The band-pass coil design also made the process more complicated, however, enabled more precise tuning and the design is

also more optimal for proton RF transmission through the coil during localising/co-registered proton imaging as the capacitors are more evenly distributed throughout the coil. In the process of tuning this xenon body coil, step-by-step of RF engineering from ground up gave me the right learning experience to understand the basics of practical RF engineering, as well as producing a functional coil that can be used for future experiments. The entire process of building this coil took a year to complete and was a worthwhile experience. Even though the filling factor of such a large coil is small, the asymmetric coil has enough space to accommodate a receive array and can be used as a transmit-only coil in conjunction, hopefully providing higher SNR and parallel imaging capability in future work (See Chapter 6).

CHAPTER 5: Apparent dissolved-Phase ^{129}Xe T_2^* in the Human Lungs at 1.5 T and 3 T

(to be submitted as a Note to Magnetic Resonance in Medicine)

5.1 Introduction

One of the potential attractions of using hyperpolarised ^{129}Xe in pulmonary imaging is its solubility in blood, producing two distinct peaks attributed to xenon dissolved in red blood cells and in tissue/plasma in the lungs. Imaging dissolved ^{129}Xe in blood and tissue, thus has the potential for studying gas exchange pathways (92,103,153), whilst simultaneous gas/dissolved ^{129}Xe imaging allows exploration of lung ventilation and perfusion (163). Both dissolved peaks (about 20 ppm apart from one another) are found at a chemical shift 200/220 ppm from the gas resonance (105,185) and both are small (about 2%) when compared to the gas peak, due to the low solubility and chemical exchange effects between these two compartments (186). The Ostwald solubility coefficients of xenon in plasma and red blood cells at body temperature of 37 °C are 0.0939 ± 0.0009 and 0.2710 ± 0.0094 m*l* / m*l* respectively (187). Thus the small signal from ^{129}Xe that is dissolved in the lungs at any given time (188), necessitates careful choice of pulse sequence and parameters must be considered carefully for optimum imaging quality. The T_2^* of the gas phase of ^{129}Xe in the human lungs was recently measured in fully inflated human lungs to be 52 ms and 24 ms at 1.5 T and 3 T, respectively (90), which suggested a smaller bandwidth is more beneficial than a shorter TE for higher signal to noise ratio (SNR) ^{129}Xe ventilation MRI. An accurate measurement of the apparent T_2^* of the dissolved signal of ^{129}Xe at these field strengths would provide similar insight into optimal pulse sequence parameters for imaging dissolved phase xenon.

The aim of this Chapter was to measure the apparent T_2^* of ^{129}Xe dissolved in human lungs at both 1.5 T and 3 T. Since the signal decay measured for the dissolved-phase T_2^* comes from both $^{129}Xe_{RBC}$ and $^{129}Xe_{plasma}$, which have different T_2^* of their own, the T_2^* derived in this Chapter from imaging experiments is thus a combination of both dissolved peaks, producing an apparent T_2^* in the imaging sequence.

5.2 Materials and Methods

Experiments were performed on two whole-body clinical MR systems; a 1.5 T Signa HDx (GE, Milwaukee, WI, USA) and a 3 T Philips Achieva (Best, Netherlands). Flexible twin Helmholtz quadrature transmit-receive coils (CMRS, USA) of the same geometry were used at both field strength (90) as described in full in Chapter 3. ^{129}Xe was polarised using the method described in Chapter 1.

Three healthy (never smoked) volunteers participated in this study at both 1.5 T and 3 T, (female, 26 years old, 50 kg; female, 31 years old, 60 kg; male, 26 years old, 80 kg). Written consent was obtained from all volunteers and approval was obtained from the national research ethics committee. An interleaved dual echo time 2D spoiled gradient echo pulse-sequence was used for apparent T_2^* measurements (Fig. 5.1). Sequence parameters were: 1 coronal whole lung projection interleaved with two TEs at a TR of 200 ms, FOV of 40 cm^2, resolution of 32 × 32 matrix, centric k-space encoding, and bandwidth of 8 kHz. The RF pulse waveform used was a Sinc pulse at 1.5 T and a Sinc-Gaussian pulse at 3 T with durations of 3.6 ms and 1.8 ms respectively.

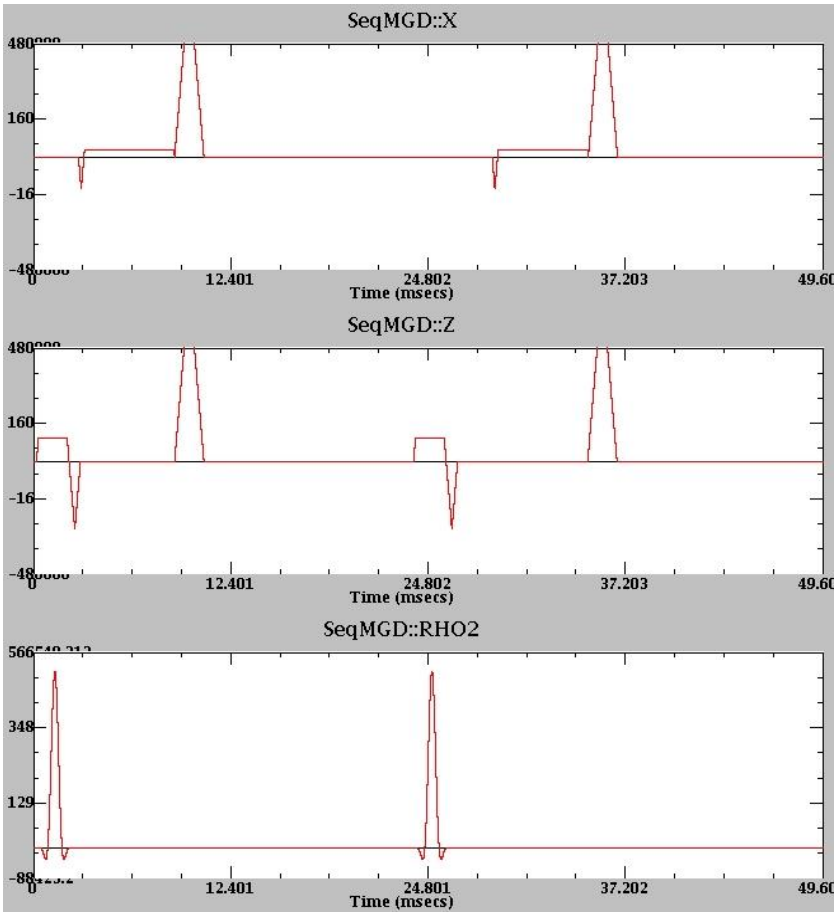

Figure 5.1 Pulse sequence used to image dissolved T_2^* of ^{129}Xe. Note the TR is shortened from 400 ms to 50 ms to show the sequence clearly.

The flip angle was set up to 33°/45° at 1.5 T / 3 T respectively due to hardware limitations on the respective RF amplifiers (2 kW and 4 kW maximum powers respectively). The TE_1/TE_2 used at 1.5 T were 2.9 ms / 5.2 ms, and the TE_1/ TE_2 used at 3 T were 1.7 ms / 2.9 ms (see Section 5.2.1 for determination of choice of echo times). Total imaging time was 15 s.

5.2.1 Determination of Echo Times

Much like the chemical shift phase evolution that results in the water-fat shift in ^{1}H MRI (189), dissolved phase ^{129}Xe imaging is sensitive to the same effects due to the two

distinct peaks from xenon dissolved in red blood cells (RBCs) and plasma (Fig. 5.2). To accurately measure the chemical shift difference, whole lung spectroscopy measurements were performed on the same healthy volunteers with the following parameters: sinc-windowed Gaussian RF pulse of flip angle of 45°, the delay time between excitation and readout was 100 µs, a readout bandwidth of 4 kHz was used and the RF pulse was centred on the RBC resonance at 17.66 MHz, TR of 3 s.

An initial chemical shift of 23.5 ppm between the two peaks was observed in all volunteers. This is important to note since this chemical shift between $^{129}Xe_{RBC}$ and $^{129}Xe_{plasma}$ can depend upon oxygenation (190,191) due to the paramagnetic state of the haemoglobin in the RBC. With knowledge of the frequency separation between the two peaks, the time for the signals to re-phase after a complete phase cycle can be calculated:

$$\Delta TE = \frac{1}{\frac{ppm * \gamma \left[\frac{MHz}{T}\right] * B_0[T]}{10^6}} \qquad (5.1)$$

Now, by taken into consideration of chemical shift due to de-oxygenation during experiment breath-hold, an extreme case of a 2 ppm shift would change the optimal ΔTE from 2.4 ms to 2.3 ms at 1.5 T and 1.2 ms to 1.1 ms at 3 T, which translate to changes in the apparent T_2^* of approximately less than 5 %. We, of course minimised this effect already by minimising the breath-hold to that of the spectroscopic breath-hold, having an accurate chemical shift to begin with, thus oxygenation effect is not taken into consideration for the remaining of this chapter.

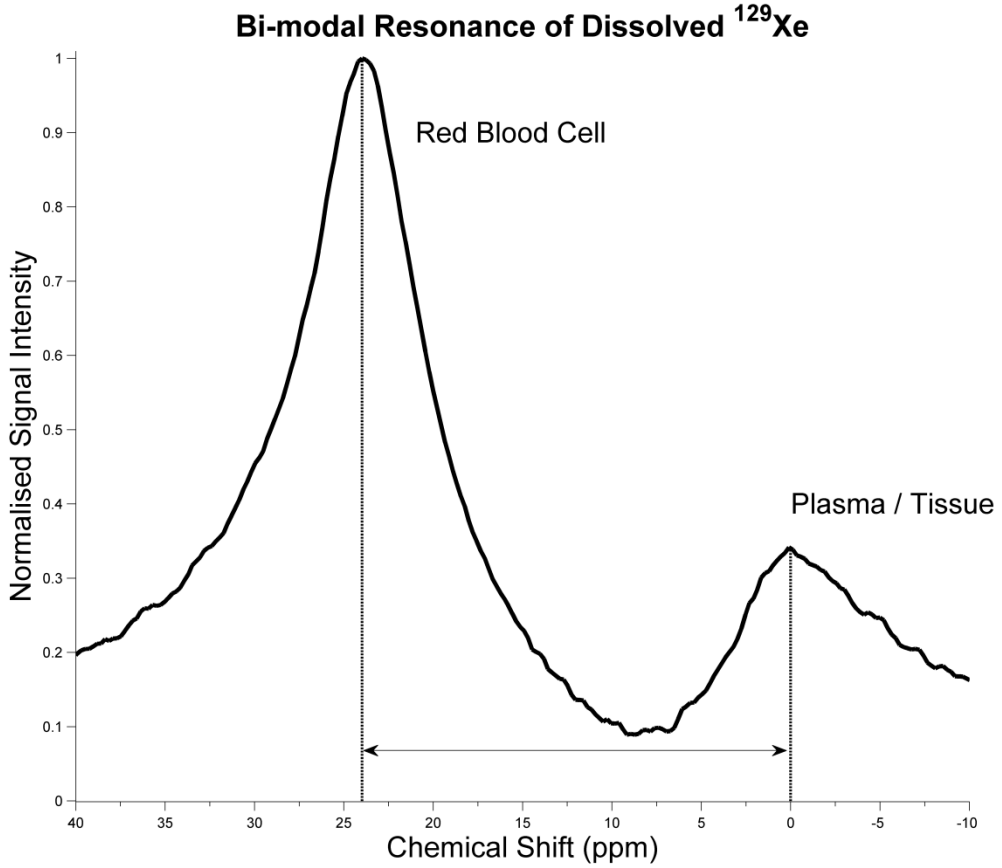

Figure 5.2. Spectrum of dissolved ^{129}Xe in RBC (left peak) and plasma/tissue (right peak) from the lungs of a healthy volunteer 15 s post inhalation with the RF pulse centred at the $^{129}Xe_{plasma}$ frequency.

Fig. 5.3 shows the simulated signal decay of the $^{129}Xe_{RBC}$ signal and the signal of $^{129}Xe_{plasma}$ with a phase shift based on their chemical shift separation. T_2^* values of 1.26 ms and 0.94 ms of the respective compartments was assumed in these simulations from Lorentzian fitting of the whole lung spectra acquired at 3 T.

Another factor for consideration when imaging these resonances is relaxation and phase coherence evolution during the RF pulse. To minimise excitation of the gas phase signal of ^{129}Xe in the lungs, (which acts in these experiments as a reservoir of longitudinal magnetisation via gas exchange across the alveolar-capillary interface), a narrow

bandwidth, long RF pulse was used (3.6 ms pulse width and 1.8 ms pulse width for 1.5 T and 3 T respectively). The pulse duration affects the initial phase difference between the $^{129}Xe_{plasma}$ signal and the $^{129}Xe_{RBC}$ signal. From the simulation results, it is safe to assume that even though the optimum TEs from the simulation (Fig. 5.3 (a)) are at 1.15 ms/ 2.3 ms for 1.5 T and 2.3 ms / 4.6 ms for 3 T, as long as the two signals are in-phase with each other at the echo times used, the resulting envelope of the FID (and hence the measured apparent T_2^*) should not depend critically upon RF pulse duration (Fig. 5.3 (b)).

5.2.2 Chemical Exchange

In a two-site exchange between sites A and B defined by:

$$\boldsymbol{A} \underset{\boldsymbol{k_b}}{\overset{\boldsymbol{k_a}}{\rightleftarrows}} \boldsymbol{B} \tag{5.2}$$

The modified Bloch equation, also known as the Bloch-McConnell equation is given by (192,193):

$$\frac{d}{dt}\boldsymbol{M}^+(t) = [\Lambda + \Gamma]\boldsymbol{M}^+(t) \tag{5.3}$$

Where $\boldsymbol{M}^+(t) = [M_a^+(t), M_b^+(t)]^T$, and Λ, Γ are given by:

$$\Lambda = \begin{pmatrix} \Lambda_a & 0 \\ 0 & \Lambda_b \end{pmatrix} \tag{5.4}$$

$$\Gamma = \begin{pmatrix} -k_a & k_b \\ k_a & -k_b \end{pmatrix} \tag{5.5}$$

$$\Lambda_a = i\Omega_a - R_{2a} \tag{5.6}$$

$$\Lambda_b = i\Omega_b - R_{2b} \tag{5.7}$$

The chemical exchange simulations are shown in Figure 5.3.

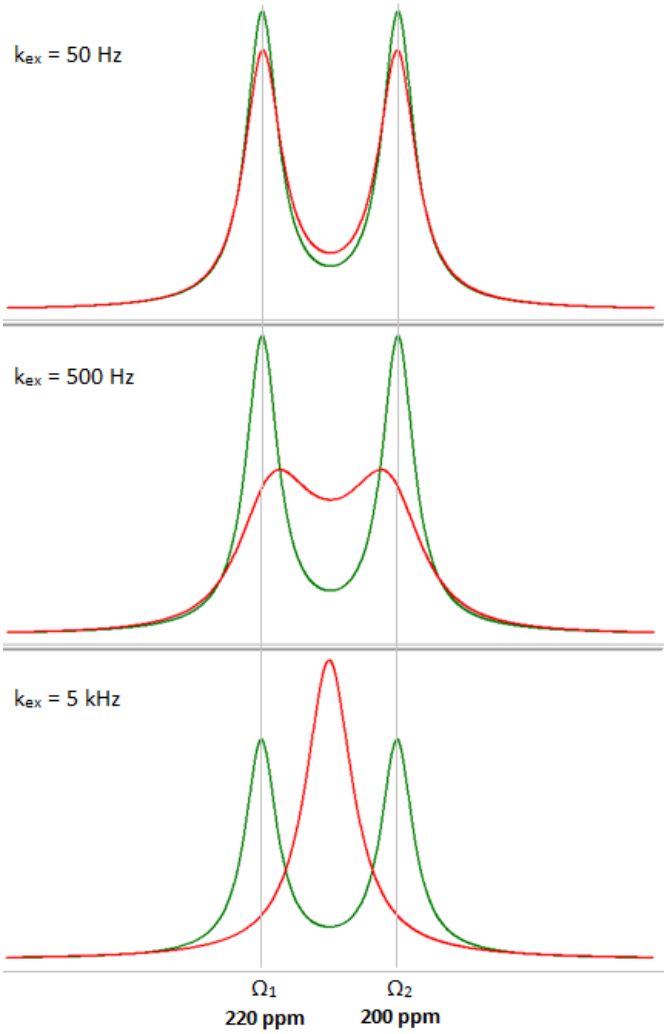

Figure 5.3. Chemical exchange regimes for two site exchange using linewidth and frequency separation of the two Lorentzian fitted dissolved xenon peaks at 1.5 T with exchange rate k_{ex} of 50, 500, and 5000 Hz in the slow (top), intermediate (middle) and fast (bottom) regimes. The green lines are the initial baseline of the two sites.

5.2.3 Assessment of the role of the gas signal on dissolved phase ^{129}Xe apparent T_2^*

To further examine the effect of gas depletion on dissolved phase xenon T_2^* measurement, the imaging sequence was used again but without the spatial gradients to observe the signal decay from pulse to pulse.

5.3 Results and Discussion:

5.3.1 Simulations of the effect of echo time on apparent T_2^*

Reproducible dissolved phase ^{129}Xe spectroscopy measurements at both 1.5 T and 3 T confirm that the initial chemical shift between $^{129}Xe_{plasma}$ and $^{129}Xe_{RBC}$ is 23.5 ppm. Fig. 5.2 shows a single spectrum acquired at B_0 = 1.5 T, from the lungs of volunteer 1 with the RF pulse centred at the dissolved $^{129}Xe_{plasma}$ frequency. Fig. 5.4 (a) shows the simulated beating FID as a result of the slight frequency shift between the ^{129}Xe dissolved in plasma/tissue and red blood cells. The phase difference between the $^{129}Xe_{plasma}$ and $^{129}Xe_{RBC}$ evolves as soon as the RF pulse tips magnetisation into the transverse plane; however, it can be seen in Fig. 5.4 (b) that the overall envelope of the beating FID follows T_2^*, thus the measured apparent T_2^* should not be affected if the TE's are chosen with the knowledge of this phase evolution.

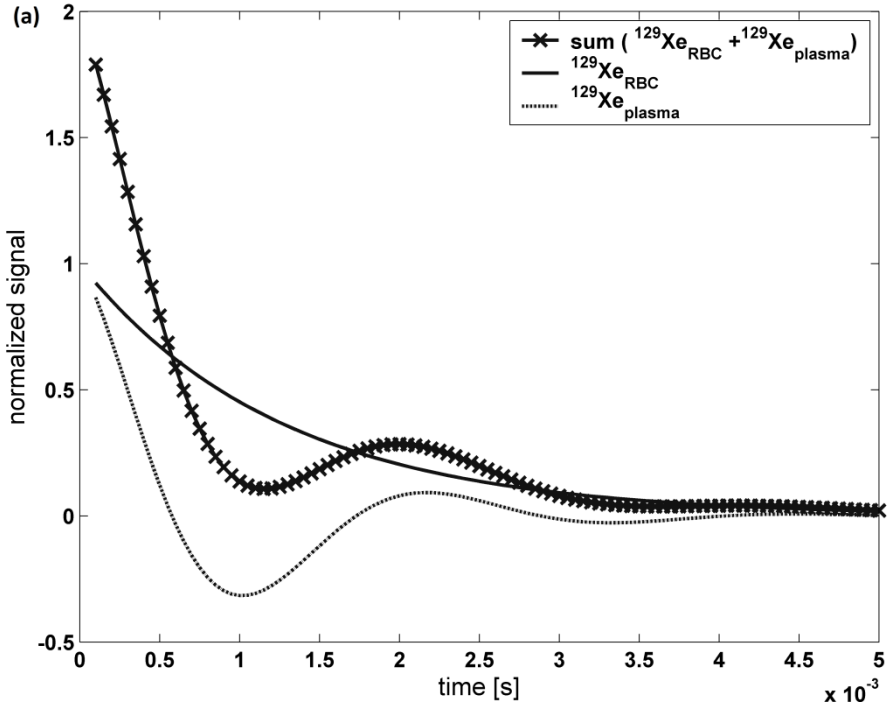

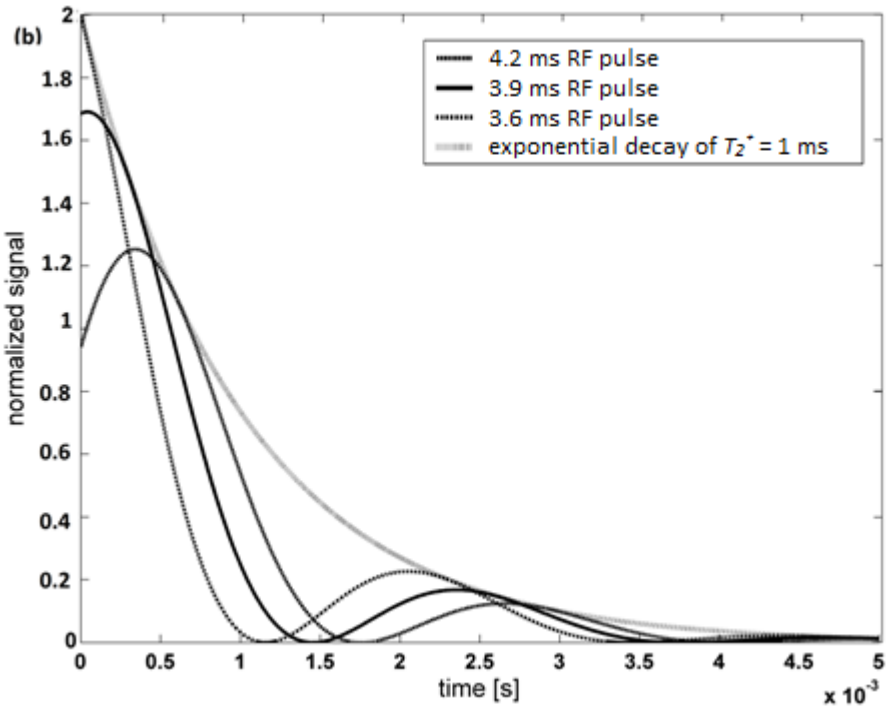

Figure 5.4. Simulations of (a) the beating signal decay caused by difference in phase of ^{129}Xe dissolved in RBC and tissue/plasma due to their different resonant frequencies 23.5 ppm apart; (b) signal decay with different RF pulse durations assuming the original RF pulse produces a completely in-phase $^{129}Xe_{RBC}$ and $^{129}Xe_{plasma}$ post RF pulse at 3 T.

5.3.2 *In vivo apparent* T_2^* measurements

The apparent T_2^* values derived from the imaging experiments from all three volunteers are summarised in Table 5.1 with median values of 1.6 ms and 1.0 ms at 1.5 T and 3 T, respectively. Examples of the images obtained at 3 T at both TEs are shown in Fig. 5.5. Notice that aliasing of the images at the bottom of the lungs from the apex of the lungs of the gas phase ^{129}Xe due to the superior-inferior readout gradient fold-over of the gas signal. Some off-resonance excitation of the gas signal is inevitable with the RF pulse used (1200 Hz and 2500 Hz RF pulse width for 1.5 T and 3 T respectively). The two compartments are separated in the frequency encoding direction, much like an exaggerated water-fat chemical shift in ^{1}H MRI. Indeed this separation has been proposed for simultaneous imaging by Mugler et al (163) to obtain ventilation/perfusion

information. This is an artefact due to the bandwidth selection which ensured shorter TEs (8 kHz) but is more than the chemical shift between gas and dissolved phase ^{129}Xe (7 kHz). The effect is much more visible at TE_2 because the gas phase ^{129}Xe has a much longer T_2^* of 24 ms compared to the dissolved compartment so the off-resonance signal appears more prominent.

The results were reproducible, when experiments were repeated with volunteer 1, an average apparent T_2^* from the left and right lung region of interest were 1.6 ms and 1.0 ms at 1.5 T and 3 T respectively. However, due to flip angle limitations due to the RF hardware power limitations at these pulse widths (maximum 45° F.A. in smaller subject down to 30° F.A. in larger subjects) and the longer time period required for rephasing at 1.5 T, the signal of the second interleave images (TE = 5.2 ms), which is about 3 times the T_2^* value, were at the noise level in the lungs of the larger volunteers at 1.5 T, and thus are not shown in the table.

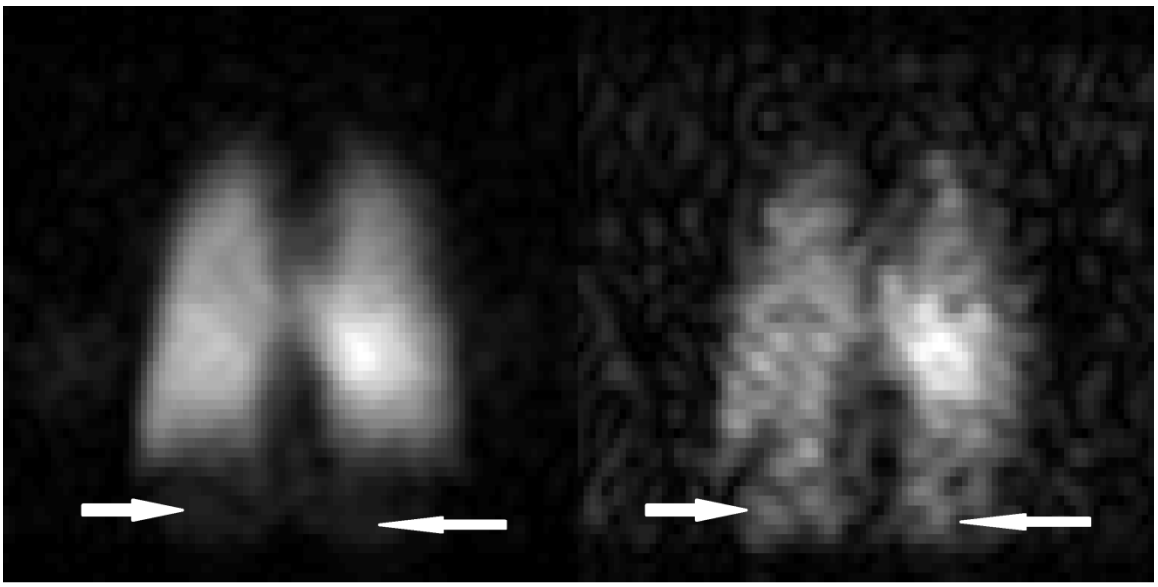

TE_1 = 1.7 ms **TE_2 = 2.9 ms**

Figure 5.5. An example of ventilation images at 2 *TE*s collected in an interleaved fashion with of a healthy volunteer at 3 T. Notice the simultaneous imaging of the gas phase ^{129}Xe (163) at the bottom of the lungs (arrows) which is most visible at TE_2 as a result of a much longer T_2^* of the gas phase ^{129}Xe.

Gender, age,[weight]	Region of Interest	T_2^* at 1.5 T [ms]	*SNR of* TE_1 *SNR of* TE_2	T_2^* at 3 T [ms]	*SNR of* TE_1 *SNR of* TE_2
F , 26 , [50 kg]					
Repeat 1	Left lung	**1.65 ± 0.06**	**22**	**0.9 ± 0.03**	**37**
	Right lung	**1.61 ± 0.12**	**7**	**1.0 ± 0.05**	**12**
Repeat 2	Left lung	**1.62 ± 0.12**	**25**	--	
	Right lung	**1.58 ± 0.12**	**7**	--	
F, 31, [60 kg]					
	Left lung	--		**1.0 ± 0.03**	**35**
	Right lung	--		**1.0 ± 0.03**	**8**
M, 26, [80 kg]					
	Left lung	--		**1.1 ± 0.05**	**33**
	Right lung	--		**1.0 ± 0.03**	**7**
Spectroscopic measurements					
	$^{129}Xe_{RBC}$	**1.76**		**1.65**	
	$^{129}Xe_{plasma}$	**1.22**		**1.3**	

Table 5.1. Mean T_2^* values measured from the left and the right lung region of interest (whole lung from either side with its standard deviation) as well as T_2^* measured from linewidth of spectroscopic experiments.

To our knowledge, these are the first reports of dissolved xenon apparent T_2^* in human lungs. Previously, T_2^* of dissolved xenon has been measured in animal lungs through NMR spectroscopy to be 2 ms at 2 T (194), 0.67 ± 0.30 ms at 9.4 T using slice selective spectroscopy in rat lungs (195) and 0.7 ± 0.1 ms at 9.4 T in mouse lungs with imaging (196). These results are within reasonable agreement with our data, and suggest that static dephasing (197,198) is not the sole mechanism influencing the transverse relaxation constant since T_2^* is not inversely proportional to the magnetic field strength B_0 as one would expect in a static dephasing regime.

The other significant contribution towards the transverse relaxation constant of the dissolved ^{129}Xe is chemical exchange between the $^{129}Xe_{RBC}$ and $^{129}Xe_{plasma}$ peaks (with an exchange time of 12 ms (199), much longer than the apparent T_2^* of dissolved xenon). Millet et al (200) showed that R_{ex}, the exchange contribution to relaxation, whose dependence on static magnetic field was assumed to be proportional to B_0^{α}, is given by:

$$\frac{\delta R_{ex}}{R_{ex}} = \alpha\left(\frac{\delta B_0}{B_0}\right) \tag{5.8}$$

where α is a constant between 0 and 2, and δB_0 is the change in static magnetic field strength. If k_{ex} is the exchange rate constant calculated by taking the rate exchange time constants of hyperpolarised ^{129}Xe measured by Bifone et, al. in RBC (τ_{RBC}) and plasma (τ_{plasma}) solutions in-vitro (188). Then the three regimes can be defined according to:

$$\begin{cases} 0 \le \alpha < 1 & \frac{k_{ex}}{\Delta\omega} < 1 \\ \alpha = 1 & \frac{k_{ex}}{\Delta\omega} = 1 \\ 1 < \alpha \le 2 & \frac{k_{ex}}{\Delta\omega} > 1 \end{cases} \tag{5.9}$$

where $k_{ex} = k_{RBC} + k_{plasma} = \frac{1}{\tau_{RBC}} + \frac{1}{\tau_{plasma}} = \frac{1}{20.4\,\text{ms}} + \frac{1}{29.1\,\text{ms}} = 83\,\text{Hz}$.

Since $\Delta\omega = 2720\,\text{rad/s}$ and $5440\,\text{rad/s}$ at 1.5 T and 3 T respectively, both of our experiments would then take place in the slow exchange regime where $\frac{k_{ex}}{\Delta\omega} \ll 1$.

α is in this case much less than 1, which suggests no exchange contribution of chemical exchange to T_2^* relaxation constant upon B_0, and this is confirmed by our spectroscopy measurements, as the linewidth of both $^{129}Xe_{RBC}$ (1.76 ms / 1.65 ms) and $^{129}Xe_{plasma}$ (1.22 ms / 1.3 ms) peaks are not significantly different at 1.5 T and 3 T respectively (see Table 5.1).

The key contribution, therefore, to dissolved xenon apparent T_2^* in the lungs that has a dependence upon B_0 field strength is static dephasing, with little effect from chemical

exchange. This suggests a direct and linear dependence of the transverse relaxation constant upon B_0. We, however, only observed a decrease of only 60% in the imaging apparent T_2^* values from 1.5 T to 3 T in B_0 strengths.

This discrepancy between the spectroscopy and the imaging T_2^* could be due to the following: (i) the imaging T_2^* is an apparent T_2^* with a combination of both $^{129}Xe_{RBC}$ and $^{129}Xe_{plasma}$ signals, opposed to the linewidth measurement for spectroscopy T_2^* for individual dissolved peaks. This might affect the T_2^* measured value through imaging due to the faster dephasing of spins with larger frequency difference (more inhomogeneous spins) between the two peaks at 3 T oppose to 1.5 T. (ii) Signal-to-noise-ratio at the second TE, due to the small T_2^*, is very low, for both 1.5 T and 3 T (Table 5.1), which can lead to inaccuracy of the measurements. To account for this problem, a pulse sequence with smaller first TE is needed to ensure accurate signal measurements from both TEs. (iii) We observed more gas signals from 3 T imaging measurements, which might indicate a higher rate of depletion of polarised signals in the gas reservoir, which can lead to parallel decrease of the dissolved signals that is independent of T_2^*, a more detailed analysis of this effect will be looked at in the following section. (iv) Lastly, the imaging T_2^* values from a given pixel represent magnetic field inhomogeneity over a pixel length scale whereas the spectroscopic linewidth tells us something about the field inhomogeneity over the whole lungs.

5.3.3 Assessment of the role of the gas signal on dissolved phase ^{129}Xe apparent T_2^*

Even though the RF excitation pulse width (1200 Hz and 2500 Hz RF pulse width for 1.5 T and 3 T respectively) is much less than the chemical shift difference between dissolved and gas peaks (3500 Hz and 7000 Hz for 1.5 T and 3 T respectively), the gas phase ^{129}Xe still makes up 98% of the total xenon inhaled; thus even a small off-resonance gas

excitation can result in a measureable signal. The effect of which can be seen in the images in Figure 5.5 (white arrows).

The envelope of the RF excitation is shown in Fig. 5.6 from the Fourier Transform of the truncated Sinc pulse enveloped used at 1.5 T, where the RF pulse was centred to excite the dissolved phase ^{129}Xe at the dissolved frequency with a large flip angle. Nevertheless, the tail of the RF pulse excites the gas phase frequency with a small flip angle, and needs to be taken into consideration.

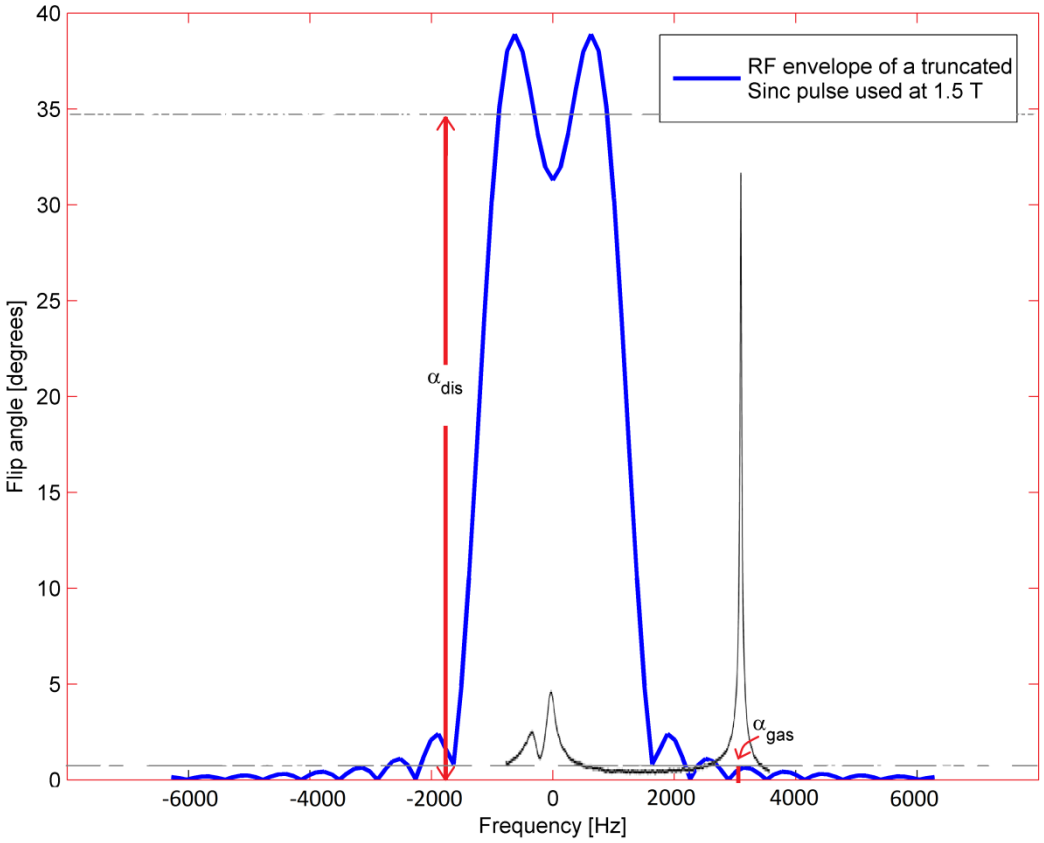

Figure 5.6. RF pulse excitation envelope of a truncated Sinc pulse used at 1.5 T and its effect on both gas and dissolved ^{129}Xe. The simulated flip angle at the gas frequency is 0.44 degrees. Superposed spectrum in black show the dissolved and gas peaks acquired with such RF pulse centred on dissolved frequency.

At the beginning of an experiment, the volunteers are asked to breath in the ^{129}Xe gas prior to holding their breath. This process of inhalation takes approximately 3-5 s to complete, which gives xenon enough time to saturate into the dissolved phase from the inhaled gas phase. During this time, the dissolved phase ^{129}Xe has a comparable polarisation to the xenon gas reservoir neglecting dissolved T_1 decay. Thus, for the initial 3 RF pulses (Fig. 5.7), a rapid decay is observed as xenon does not fully saturate prior to the next RF pulse with a TR of 200 ms (time for about 70% of dissolved signal to recover (157)), and the initially fully saturated dissolved xenon signal is being depleted. The constant chemical exchange between the xenon compartments leads to a steady state effect during the latter part of imaging which can been seen in Fig. 5.7. For the remaining RF pulses used to build up the image, the dissolved phase ^{129}Xe does not completely re-saturate and equilibrate with the gas phase ^{129}Xe polarisation (i.e., the exchange time T_{ex} <*TR*). It does, however, reach a steady state between RF depletion and replenishment by chemical exchange.

During the first five RF pulses, the dissolved phase ^{129}Xe signal shows a rapid drop towards a more steady subsequent decay, which results from the dissolved signal tracking the RF depletion of the gas due to off-resonance excitation and some gas T_1 decay. Assuming negligible decay from the 2% dissolved phase xenon signal during the 15 s (with a T_1 of 10 ms (199)), the signal decay of the gas phase xenon would decay in the same fashion as dissolved xenon in a pseudo steady state due to RF depletion and T_1 decay. This effect can be quantified from equation (5.4) with an off-resonance flip angle at the gas xenon frequency (α_{gas}= 3.2°) calculated by solving equation (5.4) for the steadily decaying portion of the curve starting from the 6th data point where TR = 200 ms and T_1 = 20 s (dotted line, only one of the two interleaves is shown, thus the 3rd point corresponds to the 6th RF pulse):

$$S_{n\ (n>6)} = S_6 \left(\cos\left(\alpha_{gas}\right)^{n-1} \exp\left(-\frac{n\,TR}{T_1}\right)\right) \qquad (5.10)$$

The residual dissolved signal after the application of a 45° flip angle on the dissolved resonance would leave only 29% (1-cos45°) of the initial magnetisation remaining in the

longitudinal plane which would then undergo T_1 decay. Now the T_1 of the dissolved compartment is measured at ~10 ms (199), so with an inter-pulse TR of 200 ms, this residual longitudinal magnetisation from the previous RF excitation can be neglected and we assume the only factors effecting the signal between TRs come from the RF depletion of the gas polarisation and its associated T_1 decay and T_2^* related to the echo time. The actual flip angle delivered at the gas frequency is going to be lower without the above assumption, which is the case in the RF envelope simulated earlier (Fig. 5.6).

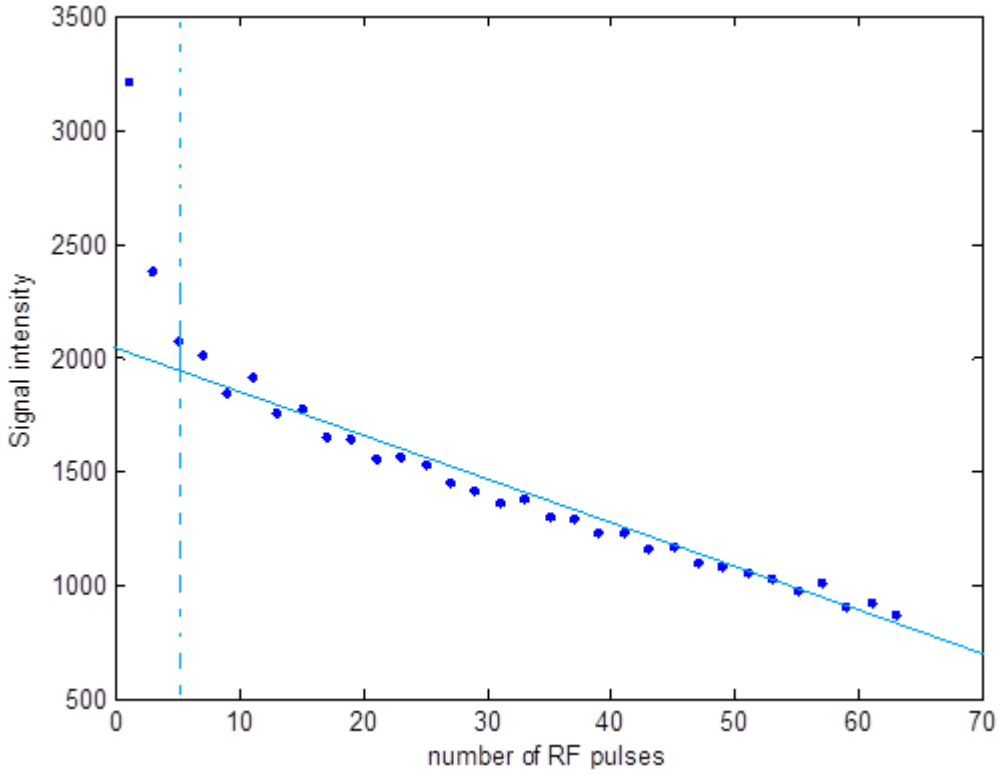

Figure 5.7. Signal decay of dissolved ^{129}Xe using the T_2^* imaging sequence with the same imaging TR of 200 ms without spatial encoding gradients. Notice that a steady decay is achieved by the 3rd RF pulse, thus will show minimal effect if the image was obtained with a sequential phase ordering, because the k-space filler has no discontinuities (results at 1.5 T).

To obtain the highest SNR possible, centric encoding during acquisition was used whenever possible. This would mean a change in the weighting of k-space from the centre to edge following the k-space filter of Fig 5.7, which is defined by the off-resonant

RF excitation of the gas peak and the xenon gas T_1. Taking these factors into account, k-space raw data from one of the volunteers was normalised on a RF view-view basis accordingly and T_2^* was re-calculated which resulted in a difference of 0.1 ms. This difference, however, is less than the standard deviation of the distribution of the imaging T_2^* values (Fig. 5.8) (between 0.03 and 0.12 ms), and as such we consider it negligible. This is especially the case when we consider the increase of noise in the post normalisation images, which results from amplification of the noise in the edges of k-space. This effect would be even less insignificant when sequential encoding is used (which is the case at 1.5 T). Centric encoding was only used at 3 T and this normalisation process was not taken into consideration in the final results due to the small differences considered.

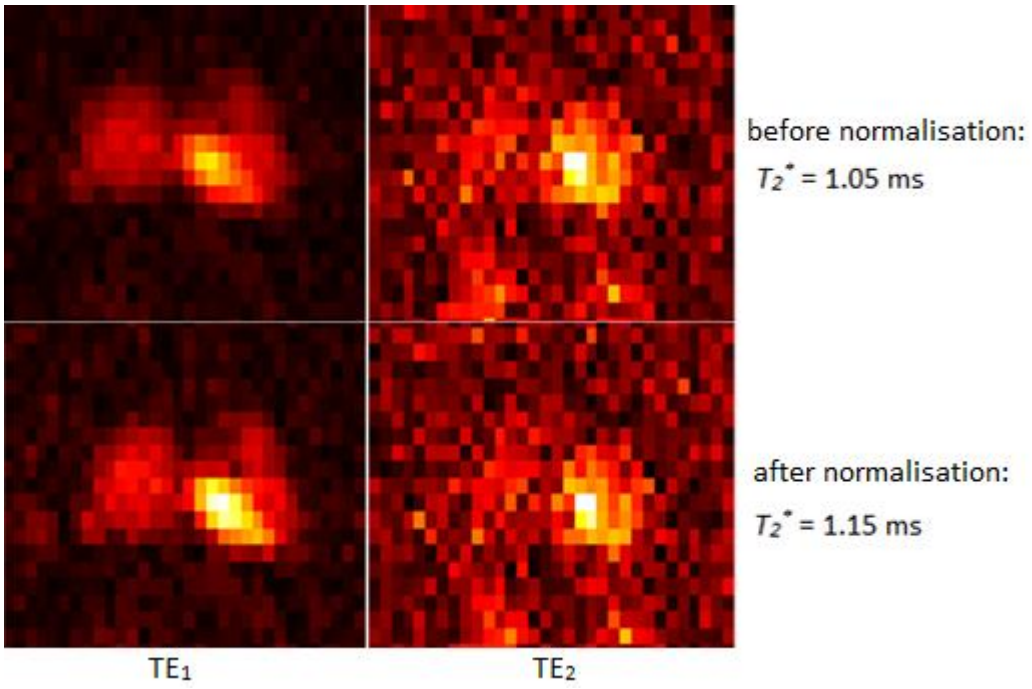

Figure 5.8 **Dissolved xenon images from a healthy volunteer at 3 T acquired centrically prior and post normalisation procedure using the signal decay curve from Fig. 5.7. Note the bright spot in the middle of the lungs, where the heart is situated (presumably the left atrium and ventricle where oxygenated blood is received and pumped out). This can also be seen in Fig. 5.4, which is only observed in dissolved xenon images.**

5.4 Conclusion

In this Chapter, the transverse relaxation times, apparent T_2^*, of dissolved ^{129}Xe gas in the human lungs at both 1.5 T and 3 T were measured at 1.6 ms and 1.0 ms respectively in three healthy volunteers. This is in rough agreement with whole lung spectroscopy results reported previously at 1.5 T of 1.5 – 2.4 ms (162) as well as our spectroscopic results from a healthy volunteer. Since the dissolved ^{129}Xe has two distinct peaks 23.5 ppm apart, the signal cannot be treated as one , but two signals precessing in and out of phase with each other, thus specifically calculated TEs were used for a more accurate T_2^* measurement to account for this in-out of phase signal. The effects from both chemical exchange and RF excitation of the gas reservoir were also taken into consideration and described.

Even though dissolved xenon imaging does not provide the same resolution and details compared to that of gas phase xenon, it provides very interesting functional information about gas exchange. This technique can be used to quantify the amount of gas exchange in relationship to a given time by acquiring at different TRs (157). This provides a regional mapping and spatial information of pulmonary function sensitive to gas exchange (160), similar to the respiratory physiological test parameter of D_{LCO} mentioned in Chapter 2. This sensitivity could be used to investigate pulmonary diseases associated with membrane thickening such as pulmonary fibrosis and prolonged interstitial lung disease where excess connective tissues are formed in the lungs that impair gas exchange.

These short T_2^* values demonstrate that one of the most important parameters needed to achieve better dissolved-phase ^{129}Xe images is the minimisation of echo time (TE). Partial echo should be used and imaging sequences that minimise *TE* such as spiral (73), UTE (201), or radial (133,162) are of obvious choice for the direct imaging of dissolved ^{129}Xe.

Improvement in RF excitation pulses could be another way to optimise the pulse sequences for dissolved phase xenon imaging. As pointed out previously, the two main problems with imaging dissolved xenon is the disturbance of the gas phase reservoir and

the hardware limitation on dissolved RF pulse magnitude. For example, one can design a hard pulse on dissolved frequency with 1st zero crossing at gas frequency to ensure the Fourier transformed RF envelope of a Sinc function has a zero amplitude at gas frequency. To achieve a higher flip angle (up to 90˚) for dissolved xenon RF pulses, one can consider using composite or adiabatic pulses, with the careful consideration of pulse duration (202).

In future work, it would be beneficial to use such methods combined with more inhaled ^{129}Xe to measure regional T_2^* with a higher degree of accuracy.

Chapter 6: Ongoing and Future Works

Introduction

In this final Chapter of my thesis, I will describe a few ongoing projects on which I worked in addition to the projects described in Chapter 3 to 5 linked to the advances made in hyperpolarised ^{129}Xe imaging by the rest of my colleagues in the group. The results of the thesis will be briefly summarised in Section 6.4.

6.1 Retuning an 8 Channel Cardiac Array Coil

6.1.1 Motivation

One of the many methods to accelerate imaging time in hyperpolarised gas magnetic resonance lung imaging is the use of parallel imaging (26,65,203), which was first introduced in the late 1980s for conventional MRI. There are two major benefits for parallel imaging in the field of hyperpolarised gas lung MRI (204): (1) imaging is usually done within one single breathhold, thus any imaging acceleration that reduces the breathhold requirement is useful for patients with lung diseases, whom might have difficulties holding their breath. (2) The disadvantage of using parallel imaging in proton MRI is not present with the hyperpolarised media in the fashion of √N with respect to SNR of the image, and it has been shown that the drop in SNR due to less RF pulses can be compensated simply by increasing the flip angle (204). This is the key motivation for tuning a receive array after the completion of the asymmetric xenon body coil (Chapter 4). The idea is to use it as a transmit coil in conjunction with a multi-array chest coil as the receive coil.

6.1.2 Methods and preliminary results

The array coil consists of two flexible halves, each containing 4 receive channels (Fig. 6.1 (a)). It is placed on the subject one half on the anterior and one half on the posterior side

(Fig 6.1 (c)), and fits inside the xenon body coil inside a clinical 1.5 T GE scanner (Fig. 6.1 (b)). Since it was retuned from a GE commercially built 8 channel cardiac ^{1}H coil, the design was enclosed in semi-flexible and comfortable. With the help of GE engineers in Cleveland Ohio, the coil was taken apart and retuned for each element as well as each pre-amplifier to resonate at ^{129}Xe frequency of 17.7 MHz for a 1.5 T clinical GE MR system. This RF engineering work was conducted by myself, Martin Deppe and my supervisor Jim Wild and has subsequently been completed and tested by Madwesha Rao.

Figure 6.1. **(a) Photo of the inside of the array coil. (b) Photo of one half of the 8 channel arrays of a GE custom build proton chest coil. (c) Array coil inside the transimit ^{129}Xe body coil inside a clinical 1.5 T MR scanner. (d) Close up of the assembly of the array coil inside the transmit body coil with a hollow cylindrical proton phatom inside.**

Preliminary experiments have been carried out in the magnet bore using a network analyser. Figure 6.2 shows two S_{11} traces measured inside the magnet bore attached to the asymmetrical xenon body coil from Chapter 4. The thick, brighter yellow trace shows the detuned body coil when the array is tuned to xenon frequency which then couples strongly to the nearby xenon body coil. The light yellow trace on the other hand is acquired after transmitting a signal (when the array coil is detuned), and the trace shows a single resonate peak at the ^{129}Xe Larmor frequency at 1.5 T from the xenon body coil, indicating no coupling with the receive array.

The next step in this project was to edit software compatibility to the GE system through its coil configuration file and add necessary control parameters as well as an ID recognisable by the GE clinical MR scanner.

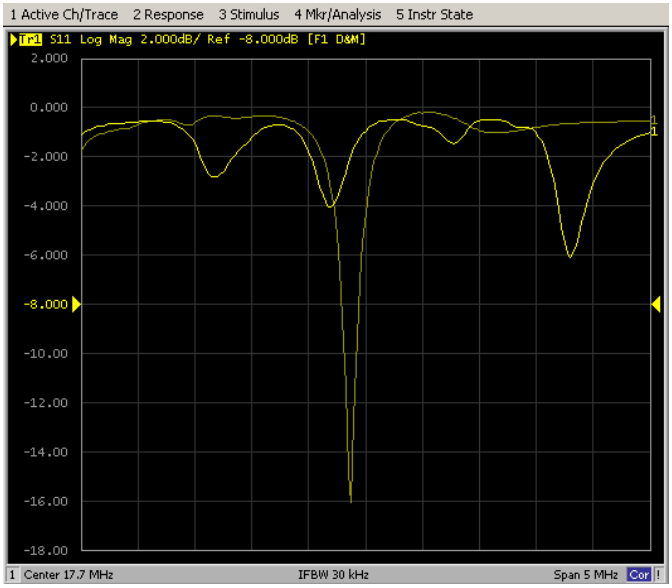

Figure 6.2. Tuned (un-coupled, light yellow) and detuned (coupled, bright yellow) S_{11} tracer on a network analyser of the xenon body coil when the array coil is inside the xenon body coil.

The SNR from the 8-channel array is comparable to that of transmit/receive from the whole body coil (Chapter 4) and vest coil (Chapter 3). A systematic comparison is however not included in this thesis because the coil was completed after my thesis write up. The

images from 6.4 are obtained one/two years post imaging from Chapter 3 – 4, thus there would be systematic differences such as polarisation, volunteer differences as well as hardware differences.

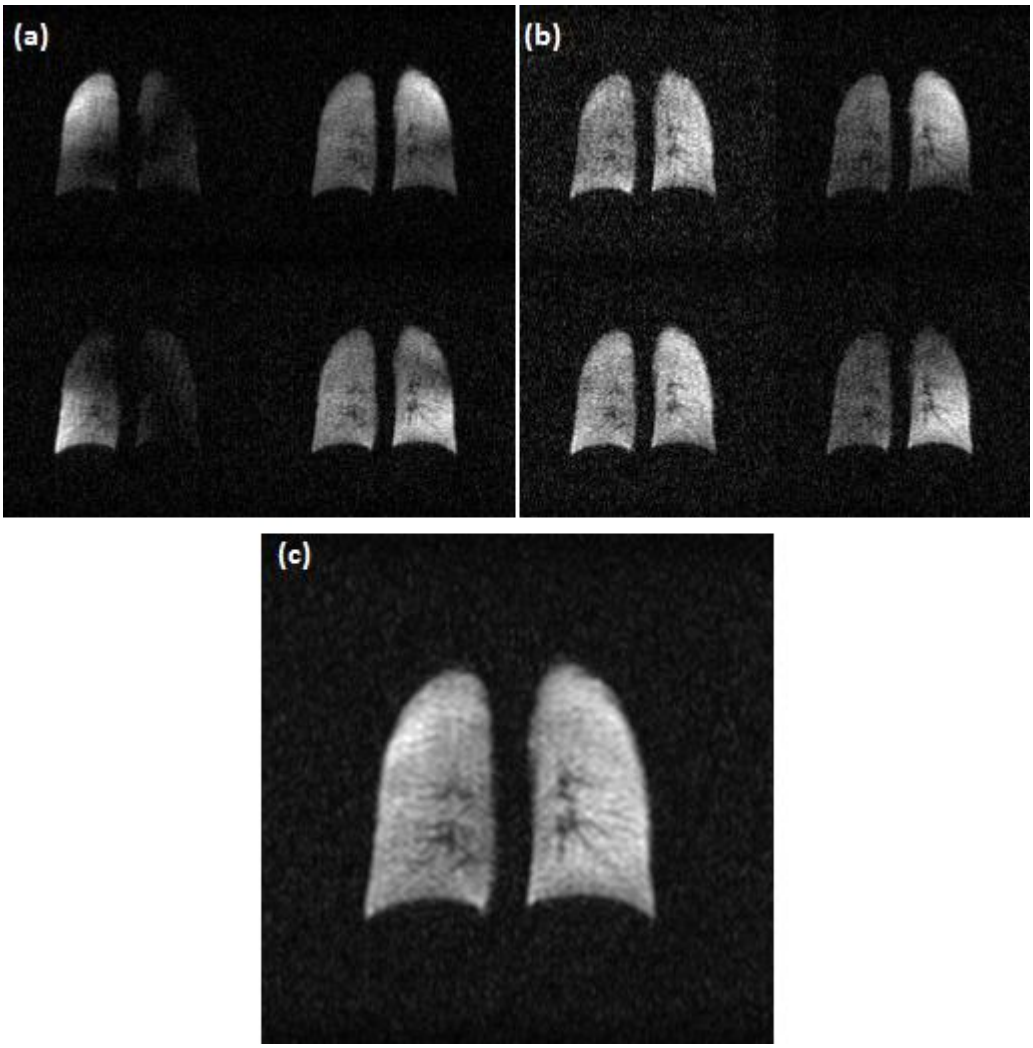

Figure 6.3. **Reconstructed ^{129}Xe image (c) using individual images of the anterior (a) and posterior (b) elements of the 8-channel array coil. Imaging is performed on a healthy volunteer (27 years old, 50 kg) with 400 ml of ~10% polarised ^{129}Xe gas with a resolution of 4 mm x 4 mm x 15 mm voxel size. (Courtesy of Madhwesha Rao, PhD student at University of Sheffield).**

6.1.3 Discussion

During the initial testing phase, a signal was not acquired from the thermal phantom. To study the nature of the behaviour being an indication of coil malfunction or tuning inaccuracy, an RF synthesiser was used (which produces a much larger signal than the thermal phantom), where a measurable signal was acquired, indicating a working coil. This also led us to believe there was something wrong with the connections to the pre-amplifiers, which proved to be correct. Upon carefully examining the coil hardware, it has come to our attention that the supply power for the pre-amplifiers were not connected to the coil feedboard. My colleague Madhwesha Rao has suggested to do one of the following : (1) Using RF chokes to hard-wire the 10 V to the RF line coming from the pre-amplifier after shorting all capacitors if any. (2) Use a multi-strand DC wire from the feedboard to every pre-amplifier. Any changes, however, could come with risks of pre-amplifier becoming unstable. The next step in this project of using an array coil as a receive coil for the xenon body coil will be carried out by my colleague Madhwesha Rao. Recently, it has been used successfully to image the human lungs (Fig. 6.3). In recent years, many efforts has been made to better register hyperpolarised images onto proton images to acquire the border of the lungs, especially in diseased lungs, where borders are usually associated with ventilation defects. It has been possible to image both ^{3}He and ^{1}H in a single breath hold (182) using a whole body transmit/receive coil. This, however, is not possible yet using a 2D SPGR sequence for xenon imaging since the imaging time for xenon is longer for an optimised sequence. Parallel imaging can be the solution to shorten the imaging time without losing SNR , thus enabling coregistering for ^{129}Xe and ^{1}H imaging within a single breathhold.

6.2 Ventilation/Perfusion Measurements using Simultaneous Gas-/Dissolved- ^{129}Xe Imaging Technique

6.2.1 Motivation

Following Chapter 5, where dissolved ^{129}Xe T_2^* was imaged and measured, we explored the possibility of simultaneously imaging both ventilation of ^{129}Xe in gas phase as well as perfusion of ^{129}Xe in dissolved phase in a single acquisition. This method was proposed by Mugler et al (163), and we are aiming to work towards a quatifiable measurement of the ventilation/perfusion of the lungs using this method.

6.2.2 Methods and preliminary results

Experiments were performed on whole-body clinical MR systems, a 1.5 T Signa HDx (GE, Milwaukee, WI, USA) and a 3 T Philips Achieva (Best, Netherlands). Flexible twin Helmholtz quadrature transmit-receive coils (CMRS, USA, described in Chapter 3) were used at both field strengths. ^{129}Xe was polarised by means described in Chapter 1.

A 2D spoiled gradient echo pulse-sequence (described in Chapter 3) was used for the simultaneous imaging of two healthy volunteers (female, 27 years old, 50 kg; female, 31 years old, 60 kg). Sequence parameters were: 1 coronal slice covering the whole lung, FOV of 48 cm × 48 cm, resolution of 64 × 32 matrix, centric encoding, TR of 200 ms, RF pulse width of 800 µs / 1600 µs, maximum flip angle allowed by the scanners of 33° / 45°, minimum TE of 2 ms /1.34 ms for 1.5 T and 3 T respectively. The readout direction and bandwidth is very important in this imaging sequence since the frequency shift of the dissovled phase ^{129}Xe is ultilised to separate the two phases, which are 200 ppm apart. To make sure full coverage is achieved as well as no overlapping between the two images, one must ensure the readout bandwidth is twice the frequency shift between the two compartments. Bandwidth is 7 kHz and 14 kHz for 1.5 T and 3 T respectively, and RF pulses are centred on the dissolved ^{129}Xe frequency. Readout direction was not kept constant because lung shapes are different. To satisfy the bandwidth requirement mentioned above, the readout direction is chosen such that the length of the lungs in that direction only occupies half of the FOV on the localising scan. For example, when imaging

narrower, longer lungs (Fig. 6.4), the readout direction is left to right, where overlapping may occur if the readout direction is top to bottom. Same applies to wider, short lungs (Fig. 6.5), an overlapping would occur here if the readout/frequency direction is left to right.

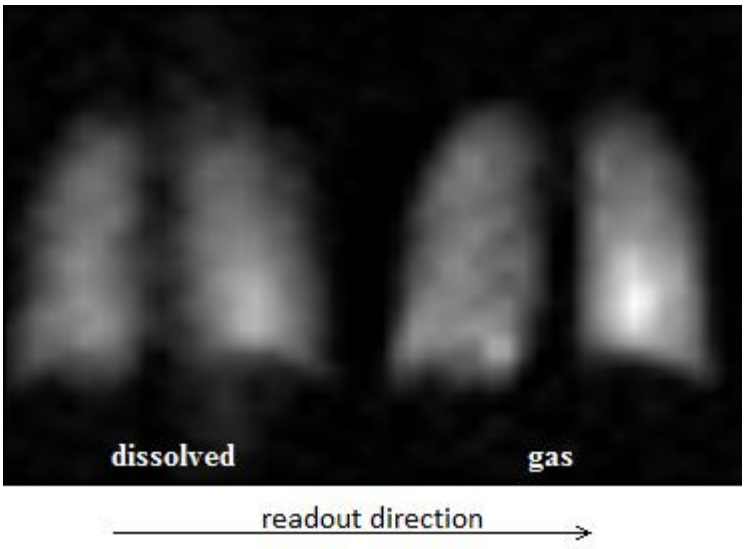

Figure 6.4 Simultaneous dissolved- /gas- phase ^{129}Xe at 3 T of a healthy volunteer (female, 27 years old, 50 kg), readout direction is left to right.

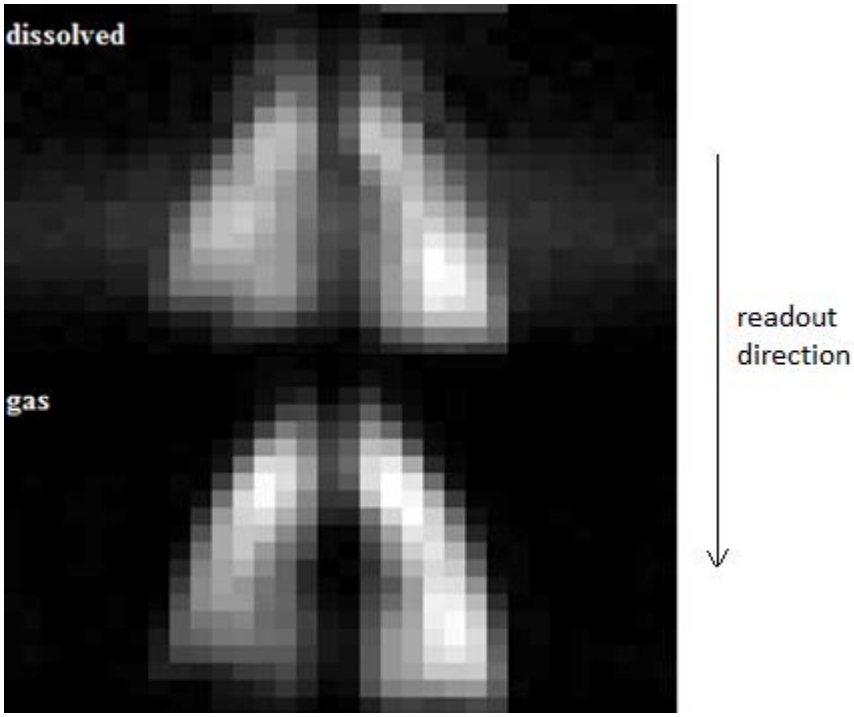

Figure 6.5. Simultaneous dissolved- /gas- phase ^{129}Xe at 1.5 T of a healthy volunteer (female, 32 years old, 60 kg), readout direction is superior to inferior.

Figure 6.4 and Figure 6.5 show preliminary results from the simultaneous imaging of both dissolved and gas – phase ^{129}Xe at 3 T and 1.5 T respectively. Notice the brighter signal in lower left lung area of the dissolved phase images, suggesting a higher uptake around the heart region in perfusion signals, which was also observed in Chapter 5 dissolved images (Fig. 5.5 and Fig. 5.8).

Lastly, in an attempt to quantify the ventilation/perfusion ratio, the gas signal was divided by the dissolved signal on a pixel by pixel basis, shown in Figure 6.6. There is a fairly homogeneous distribution between values of 1 to 2. There were regions of little ventilation but high perfusion (dark blue) as well as high ventilation with little perfusion (dark red, near the bottom diaphragm of the right side of the lungs).

Note here that the control experiment portion in an XTC experiment is used to normalise for T_1 relaxation, blood transport, residual RF when mapping the gas image at a later time (see section 2.7.1). Simultaneous imaging here, however, only is concerned with the visualisation of both gas and dissolved states of ^{129}Xe, which is only acquired once (not twice or more like in XTC type experiments for mapping purposes), thus a control image here was not acquired but may be needed if absolute quantification of lung V/Q were to be sought in the future with this method. As for the realness of these dissolved images, they were acquired on both scanners with the FOV prescribed in the wrong direction (frequency encoding from dissolved frequency to +200 ppm as well as from dissolved frequency to - 200ppm), and in the wrong direction, only the dissolved phase image was observed and no gas phase xenon image.

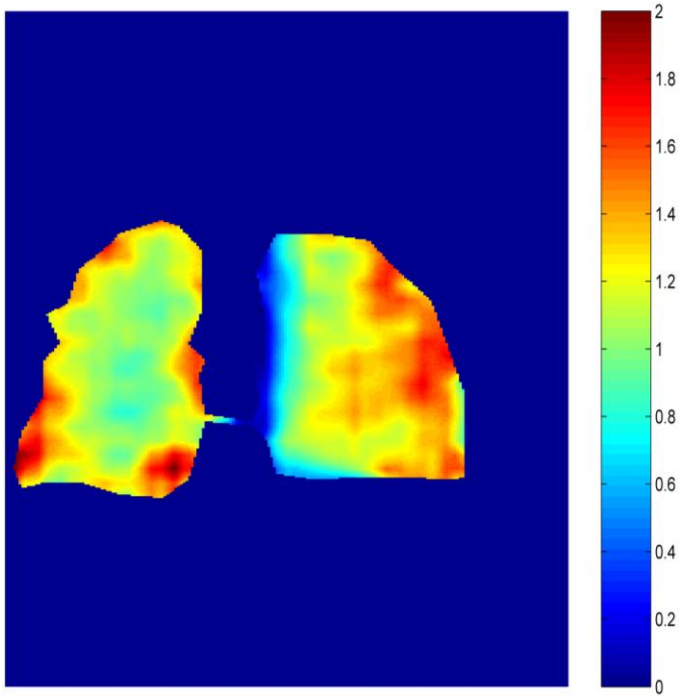

Figure 6.6 First attempt to quantify ventilation/perfusion using images from Figure 6.4.

6.2.3 Discussion

There are a few problems in the attempt to quantify V/Q from the images: (1) there is a blurring effect on both set of images in the dissolved phase image in the phase encoding direction. This is caused by the initial RF pulses when the dissolved ^{129}Xe is fully saturated. After a few RF pulses, it then reaches a steady state signal attenuation guided mostly by the depletion of the gas magnetisation (see Fig.5.7). There are two solutions to lessen this effect, one of which suggests a longer TR to ensure ^{129}Xe saturation between all RF pulses, which would increase the scan time. The other one is to disregard the initial data points, in which case sequential encoding must be used, which would then lower the measured SNR. (2) Because V/Q is measure on a pixel by pixel basis, the pixels of the dissolved signals must match the gas signals exactly. This problem can be avoided by using a more precise frequency shift between the two signals at each scanner when defining the receiver bandwidth. Still, this is very difficult since the dissolved signal comes from both RBC and plasma/tissue, which has a slight chemical shift of their own. My colleague Neil Stewart has taken over this project for further investigation. (3) Lastly, the most important problem associated with quantifying V/Q from dissolved xenon images lies with the fundamental definition of ventilation/perfusion measurement. From nuclear medicine V/Q measurement, the perfusion phase of the procedure is done by intravenous injection of the radioactive technetium (^{99m}Tc) macroaggregated albumin (MAA). As mentioned in Chapter 2, MAA is localises by the mechanism of capillary blockade. A minimum of 100,000 particles are injected in general, but optimally anywhere between 200,000 and 600,000. In a healthy subject, less than 1 in 1000 of the capillaries is blocked, which increases significantly in pulmonary hypertension, thus less MAA would be injected in those cases. Images are obtained from the emitted gamma rays of the ^{99m}Tc, thus this is a measurement of functional blood vessels around the lungs, which is different from dissolved xenon measurement. The dissolved xenon indicates functional tissue in well ventilated lung regions, which does not indicate functional blood vessels. In comparison

to other pulmonary measurements such as V/Q in nuclear medicine, dissolved xenon signal is more similar to D_{LCO} measurement in functional lung tests (See section 2.1). Thus, when V/Q values are quoted in hyperpolarised xenon imaging, one should note its difference to V/Q measurements in nuclear medicine.

6.3 Chemical shift saturation recovery (CSSR) type experiments.

6.3.1 Motivation

The dissolved and gas phase ^{129}Xe are constantly exchanging, providing replenishment for the dissolved phase ^{129}Xe during the imaging process. Chemical shift saturation recovery (CSSR) type experiment uses the saturation of ^{129}Xe magnetisation in the dissolved phase followed by the measurement of its recovery from the gas in the lungs (Fig. 6.7). Figure 6.8 shows an example of the saturation recovery of both $^{129}Xe_{plasma}$ and $^{129}Xe_{RBC}$ with changing TR in a spectroscopic sequence. This type of experiment has demonstrated to be able to provide surface area per unit gas volume in humans at 0.2 T (157), quantitative values of the parenchymal and blood compartment thickness and perfusion information (205), as well as the thickness of the parenchymal layer that separates gas and blood compartment (92). The purpose of this project was to try and repeat such experiments in a clinical imaging setting with the 3 T Philips Achieva hardware. This project was cut short due to the removal and upgrade of the 3 T MR scanner in Autumn 2011.

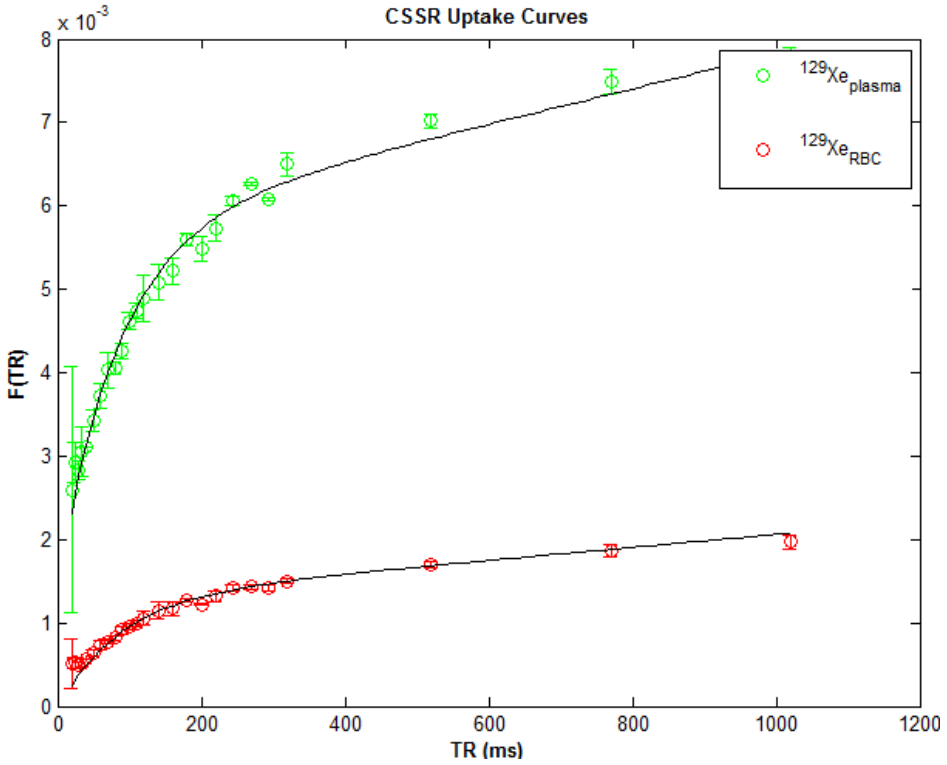

Figure 6.7. Chemical shift saturation recovery (CSSR) of xenon in red blood cells (red) and plasma / tissue (green) with respect to repetition time (TR) in a spectroscopic sequence (thanks to Neil Stewart, PhD student at University of Sheffield).

6.3.2 Methods and preliminary results

A systematic sweep through of RF power was performed using a thermally polarised pressured ^{129}Xe phantom (described in Chapter 3) on a 3 T Philips Achieva (Best, Netherlands) scanner. Flexible twin Helmholtz quadrature transmit-receive coil (CMRS, USA, described in Chapter 3) was used. The phantom was loaded and averaged with the following sequence parameters: TR of 6 s, 30 averages from on screen flipangle of 25 to 270 (maximum) with a spectroscopy sequency (Fig. 6.8).

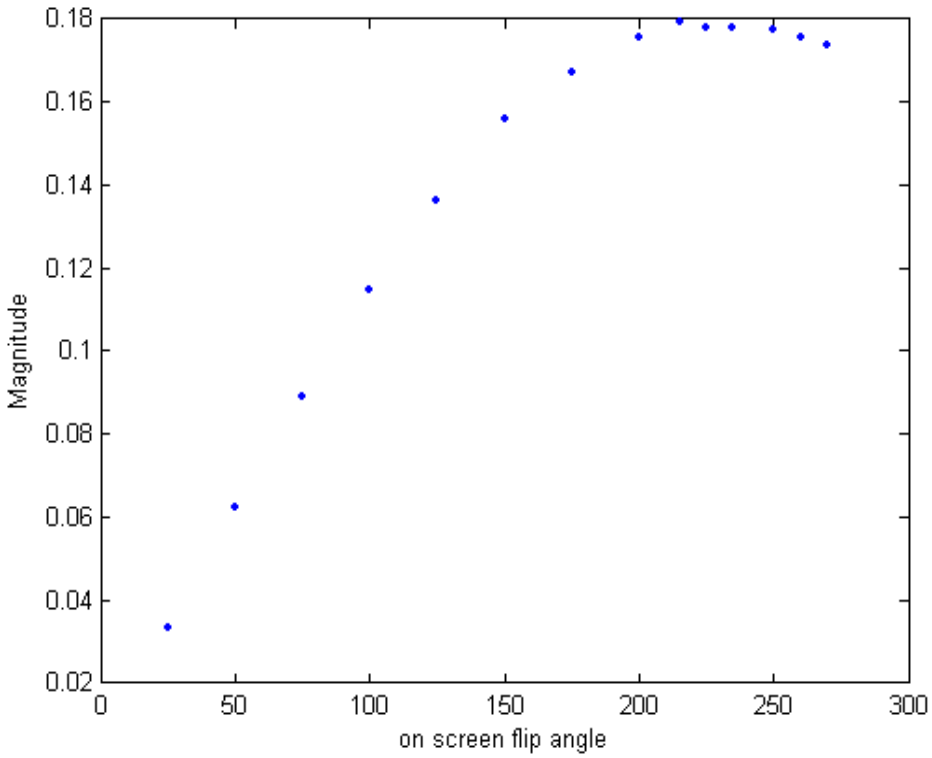

Figure 6.8. Flip angle sweep on a 3 T Philips scanner with a loaded thermal phantom using a spectroscopy sequence.

The maximum on screen flip angle of 270, however, is not valid for imaging sequences as the 3 T MR scanner has a maximum on screen flip angle of 150 for imaging sequences. Thus the maximum flip angle achievable is around 65 ˚ (Fig. 6.8) depending on the loading of the subject.

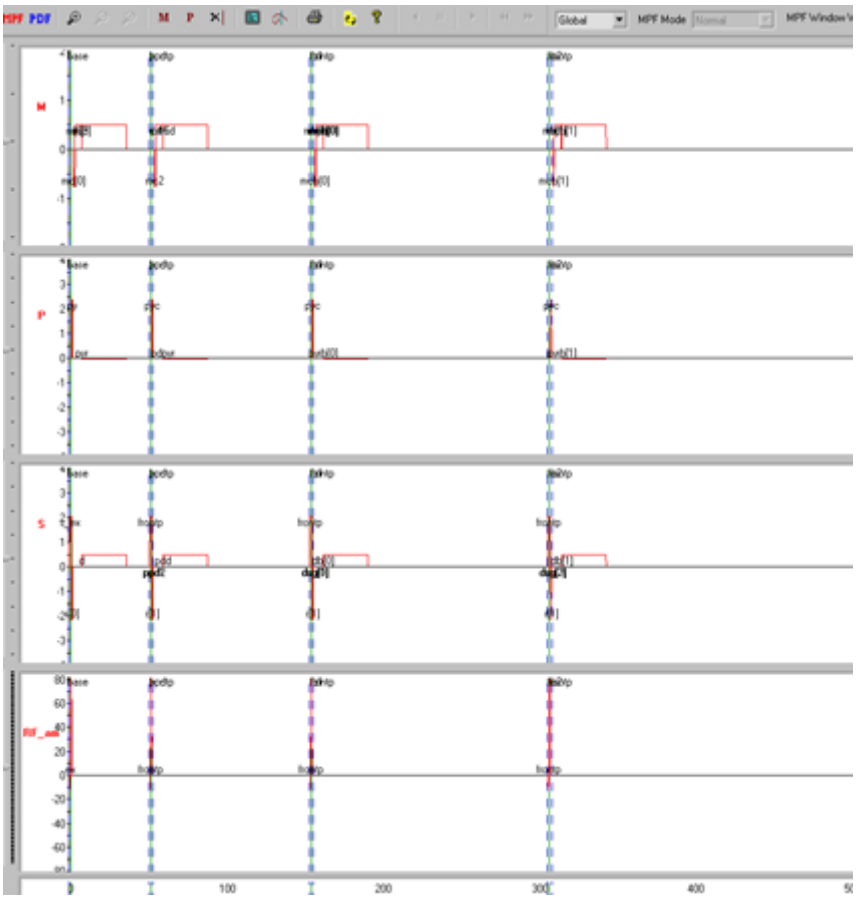

Figure 6.9. Interleaved CSSR imaging sequence, which was programmed on the Philips PARADISE pulse sequence programming environment at 3 T.

Experiments were performed on the same clinical MR system, ^{129}Xe was polarised by means described in Chapter 1. A four interleaved 2D spoiled gradient echo pulse-sequence (Fig. 6.9) was used on one healthy volunteer (female, 26 years old, 50 kg). Sequence parameters were: TR_1 = 70 ms, TR_2 = 100 ms, TR_3 = 130 ms, TR_4 = 200 ms, TE = minimum = 1.33 ms. On screen maximum flip angle of 150, FOV of 48 cm × 48 cm, resolution of 32 × 32, centric encoding.

Figure 6.10 shows the images obtained from the healthy volunteer. The images are organised in such a way that the recovery time is increasing.

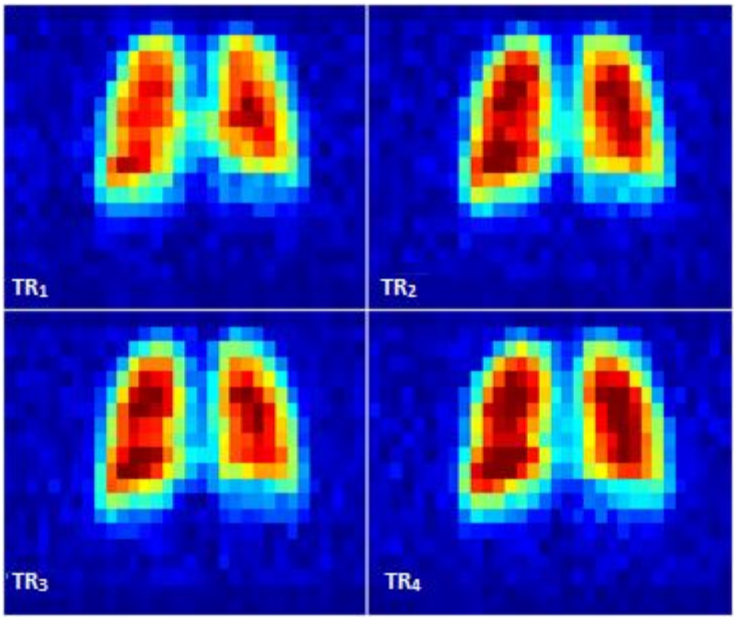

Figure 6.10. Images obtained from the CSSR sequence described in Fig. 6.9.

6.3.3 Discussion

Ideally, a 90° flip angle should be applied for the dissolved phase ^{129}Xe to kill all magnetisation before replenishment from exchange to ensure the signal from the next RF pulse comes from only the recovery process. One of the major limitations we ran into while scanning dissolved ^{129}Xe is the RF amplifier power limitation of 4 kW, as a 90° RF pulse is hard to achieve in a short duration (taken into consideration that dissolved ^{129}Xe T_2^* is very short from Chapter 5) on the clinical scanners. This leads to a numerical problem where the measured signal each time is a combination of saturation recovery as well as the remaining magnetisation prior and is hard to be separated. For example, in Figure 6.10, one would expect an increase of signal in each interleave shown, however, the signal from TR_4 (130 ms recovery time) is less than that of TR_3 (100 ms recovery time). One of the solutions is to achieve a complete saturation by other means, such as multiple RF pulses post readout to kill the remaining transverse magnetisation. This is still difficult due to the finite pulse width of the RF and the constant exchange of gas and dissolved

xenon signal. Thus during the RF excitations, the exchange is still happening between the multiple RF excitations, making complete saturation difficult. So the optimal way is still finding a way to achieve the 90° RF excitation through different RF pulses. My colleague Neil Stewart, with the help of another colleague General Leung has been trying to use composite RF pulses to achieve a 90° flip angle for further exploration of the CSSR experiment. Once again, this project was cut short due to the scanner upgrade in 2011

This type of experiment can be very useful for clinical purposes as the functional information are associated to specific diseases. It has been demonstrated that at 0.2 T, the recovery magnetisation can provide surface area per unit gas volume in humans (157), which can be a very helpful indicator for emphysema as the surface area to volume ratio in those patients can decrease by up to six folds in severe emphysema(206). Another very useful, quantitative value one can obtain from a CSSR type experiment is information of the parenchymal and blood compartment thickness.(205), as well as the thickness of the parenchymal layer that separates gas and blood compartment (92). Both of these sets of information are of interest for diseases associated to associated to membrane thickness change in conditions such as pulmonary fibrosis and prolonged interstitial lung disease where excess connective tissue are formed in the lungs. Further separation of $^{129}Xe_{RBC}$ and $^{129}Xe_{plasma}$ even shows that for fibrotic lung tissues, only dissolved signal from barrier is observed and not in the RBCs(207). As we can see, even with only 2% of the gas dissolved, which is 3000 fold less dense than tissue, useful and functional structural information can be obtain without radiation using hyperpolarised xenon MRI of the lungs.

6.4 Thesis Summary

This thesis has mainly focused on methods for ^{129}Xe imaging in human lungs at both 1.5 T and 3 T clinical scanners. The results can be summarised briefly as followed:

- ^{129}Xe human lung imaging is feasible on both 1.5 T and 3T clinical scanners and the ventilation images obtained show comparable SNR and qualitative images (Chapter 3) with slightly higher SNR observed at 3 T. The susceptibility effect, however, does increase at a higher field strength of 3 T, resulting in smaller T_2^* values in the gas phase ^{129}Xe in a static dephasing regime, and are highly dependent on lung inflation level.
- A whole body, unshielded, asymmetric, insert birdcage transmit receive xenon coil was developed for the in-vivo imaging of the human lungs for hyperpolarised ^{129}Xe MRI at 1.5 T. It provides a homogeneous magnetic field and high quality hyperpolarised ^{129}Xe ventilation images. The transparency of the coil to the proton body coil is utilised for localiser imaging prior to xenon lung imaging as well as co-registered ^{1}H/^{129}Xe images in a single breath hold. This coil has also been shown to work with an 8 Channel array coil.
- T_2^* of dissolved ^{129}Xe gas in the human lungs at both 1.5 T and 3 T are very short, were measured at 1.6 ms and 1.0 ms respectively. To achieve better dissolved-phase ^{129}Xe images, one must ensure the minimisation of echo time (TE), and taken into consideration of the chemical shift between $^{129}Xe_{RBC}$ and $^{129}Xe_{plasma}$.

In conclusion, all findings of this thesis resulted in development and more understanding into the relatively new field of hyperpolarised ^{129}Xe lung imaging. The work built the groundwork towards improvement of ^{129}Xe MRI as a useful and reliable imaging modality.

References

1. Haacke EM. Magnetic resonance imaging : physical principles and sequence design. New York: Wiley; 1999. xxvii, 914 p. p.
2. Zeeman P. The effect of magnetisation on the nature of light emitted by a substance. Nature 1897;55(1424):347-347.
3. Slichter CP. Principles of magnetic resonance: Springer; 1996.
4. Pule JV. The Bloch equations. Communications in Mathematical Physics 1974;38(3):241-256.
5. Fitzsimmons WM, Harness E. Attempts, by blood transfusion, to replace blood loss due to Haemonchus placei infection. The Veterinary record 1969;84(2):49-50.
6. Driehuys B, Cates GD, Happer W. Surface relaxation mechanisms of laser-polarized 129Xe. Physical review letters 1995;74(24):4943-4946.
7. Chann B, Nelson IA, Anderson LW, Driehuys B, Walker TG. 129Xe-Xe molecular spin relaxation. Physical review letters 2002;88(11):113201.
8. Saam B, Happer W, Middleton H. Nuclear relaxation of 3He in the presence of O2. Physical review A 1995;52(1):862-865.
9. Jameson CJ, Jameson AK, Hwang JK. Nuclear-Spin Relaxation by Intermolecular Magnetic Dipole Coupling in the Gas-Phase - Xe-129 in Oxygen. J Chem Phys 1988;89(7):4074-4081.
10. Gamblin RL, Carver TR. Polarization and Relaxation Processes in He3 Gas. Phys Rev 1965;138(4A):A946-&.
11. Schearer LD, Walters GK. Nuclear Spin-Lattice Relaxation in Presence of Magnetic-Field Gradients. Phys Rev 1965;139(5A):1398-&.
12. Cates GD, White DJ, Chien TR, Schaefer SR, Happer W. Spin Relaxation in Gases Due to Inhomogeneous Static and Oscillating Magnetic-Fields. Physical Review A 1988;38(10):5092-5106.
13. Newbury NR, Barton AS, Cates GD, Happer W, Middleton H. Gaseous He-3 He-3 Magnetic Dipolar Spin Relaxation. Physical Review A 1993;48(6):4411-4420.
14. Torrey HC. Chemical Shift and Relaxation of Xe129 in Xenon Gas. Phys Rev 1963;130(6):2306-&.
15. Hunt ER, Carr HY. Nuclear Magnetic Resonance of Xe129 in Natural Xenon. Phys Rev 1963;130(6):2302-&.
16. Vogt FM, Ladd ME, Hunold P, Mateiescu S, Hebrank FX, Zhang A, Debatin JF, Göhde SC. Increased Time Rate of Change of Gradient Fields: Effect on Peripheral Nerve Stimulation at Clinical MR Imaging1. Radiology 2004;233(2):548-554.
17. Edelstein WA, Hutchison JMS, Johnson G, Redpath T. Spin Warp Nmr Imaging and Applications to Human Whole-Body Imaging. Phys Med Biol 1980;25(4):751-756.
18. Wild JM, Paley MN, Viallon M, Schreiber WG, van Beek EJ, Griffiths PD. k‐space filtering in 2D gradient‐echo breath‐hold hyperpolarized 3He MRI: spatial

resolution and signal‐to‐noise ratio considerations. Magnetic resonance in medicine 2002;47(4):687-695.
19. Noll DC, Nishimura DG, Macovski A. Homodyne detection in magnetic resonance imaging. Medical Imaging, IEEE Transactions on 1991;10(2):154-163.
20. Peters DC, Korosec FR, Grist TM, Block WF, Holden JE, Vigen KK, Mistretta CA. Undersampled projection reconstruction applied to MR angiography. Magnetic Resonance in Medicine 2000;43(1):91-101.
21. Cahan D. Hermann von Helmholtz and the foundations of nineteenth-century science: University of California Press; 1994.
22. Leifer MC. Quadrature elliptical birdcage coil for NMR. Google Patents; 1999.
23. Leifer MC. Resonant modes of the birdcage coil. J Magn Reson 1997;124(1):51-60.
24. Deppe MH, Parra-Robles J, Marshall H, Lanz T, Wild JM. A Flexible 32-channel Receive Array Combined With a Homogeneous Transmit Coil for Human Lung Imaging With Hyperpolarized He-3 at 1.5 T. Magnetic Resonance in Medicine 2011;66(6):1788-1797.
25. Roemer PB, Edelstein WA, Hayes CE, Souza SP, Mueller OM. The Nmr Phased-Array. Magnetic Resonance in Medicine 1990;16(2):192-225.
26. Pruessmann KP, Weiger M, Scheidegger MB, Boesiger P. SENSE: sensitivity encoding for fast MRI. Magnetic Resonance in Medicine 1999;42(5):952-962.
27. Griswold MA, Jakob PM, Heidemann RM, Nittka M, Jellus V, Wang J, Kiefer B, Haase A. Generalized autocalibrating partially parallel acquisitions (GRAPPA). Magnetic Resonance in Medicine 2002;47(6):1202-1210.
28. Walker TG, Happer W. Spin-Exchange Optical Pumping of Noble-Gas Nuclei. RMP 1997;69:629-642.
29. Babcock E, Nelson I, Kadlecek S, Driehuys B, Anderson LW, Hersman FW, Walker TG. Hybrid spin-exchange optical pumping of 3He. Physical review letters 2003;91(12):123003.
30. Walter DK, Griffith WM, Happer W. Energy transport in high-density spin-exchange optical pumping cells. Physical review letters 2001;86(15):3264-3267.
31. Driehuys B, Cates GD, Miron E, Sauer K, Walter DK, Happer W. High-volume production of laser-polarized Xe-129. Appl Phys Lett 1996;69(12):1668-1670.
32. Ruset IC, Ketel S, Hersman FW. Optical pumping system design for large production of hyperpolarized. Physical review letters 2006;96(5):053002.
33. Norquay G, Parnell SR, Xu X, Parra-Robles J, Wild JM. Optimized production of hyperpolarized 129 Xe at 2 bars for in vivo lung magnetic resonance imaging. Journal of Applied Physics 2013;113(4):044908-044908-044909.
34. West JB. Respiratory physiology: the essentials: Lippincott Williams & Wilkins; 2011.
35. Eaton T, Withy S, Garrett JE, Mercer J, Whitlock RML, Rea HH. Spirometry in Primary Care Practice: The Importance of Wuality Assurance and the Impact of Spirometry Workshops. CHEST 1999;116:416-423.

36. Casaburi R, Briggs DD, Donohue JF, Serby CW, Menjoge SS, Witek Jr TJ. The Spirometric Efficacy of Once-Daily Dosing with Tiotropium in Stable COPD: A 13-Week Multicenter Trial. CHEST 2000;118:1294-1303.
37. Stanojevic S, Wade A, Stocks J, Hankinson J, Coates AL, Pan H, Rosenthal M, Corey M, Lebecque P, Cole TJ. Reference ranges for spirometry across all ages: a new approach. American journal of respiratory and critical care medicine 2008;177(3):253.
38. Vc DD. Session 11: Acute and Chronic Fibrotic States. Chest 1976;69(2).
39. Bartolome RC. The Importance of Spirometry in COPD and Asthma. CHEST 2000;117:5.
40. Celli BR. The Importance of Spirometry in COPD and Asthma: Effect on Approach to Management. CHEST 2000;117:5.
41. Schermer TR, Jacobs JE, Chavannes NH, Hartman J, Folgering HT, Bottema BJ, van Weel C. Validity of Spirometric Testing in a General Practice Population of Patients with Chronic Obstructive Pulmonary Disease (COPD). Thorax 2003;58:861-866.
42. Ganong WF. Review of medical physiology: McGraw-Hill Medical New York:; 2005.
43. Bergin CJ, Muller NL, Vedal S, Chan-Yeung M. CT in Silicosis: Correlation with Plain Films and Pulmonary Function Tests. American Journal of Radiology 1985;146:477-484.
44. Lee E-S, Gotway MB, Reddy GP, Golden JA, Keith FM, Webb WR. Early Bronchiolitis Obliterans Following Lung Traspantation: Accuracy of Expiratory Thin-Section CT for Diagnosis. Radiology 2000;216:472-477.
45. Gurney JW, Jones KK, Robbins RA, Gossman GL, Nelson KJ, Daughton D, Spurzem JR, Rennard SI. Regional Distribution of Emphysema: Correlation of High-Resolution CT with Pulmonary Function Tests in Unselected Smokers. Thoracic Radiology 1992;183:457-463.
46. Gevenois PA, Vuyst P, Sy M, Scillia P, Chaminade L, de Maertelaer V, Zanen J, Yernault J. Pulmonary Emphysema: Quantitative CT during Expiration. Radiology 1996;199:825-829.
47. Sakao S, Tatsumi K, Igari H, Watanabe R, Shino Y, Shirasawa H, Kuriyama T. Association of Tumor Necrosis Factor-a Gene Promoter Polymorphism With Low Patients Attenuation Areas on High-Resolution CT in With COPD. CHEST 2002;122:416-420.
48. M. Casio, H. Ghezzo, J. C. Hogg, R. Corbin, M. Loveland, J. Dosman, Macklem PT. The Relations Between Structural Changes in Small Airways and Pulmonary Function Test. 1978;298:1277-1281.
49. Wright JL, Lawson LM, Pare PD, Kennedy S, Wiggs B, Hogg JC. The Detecting of Small Airways Disease. Am Rev Respir Dis 1984;129:989-994.
50. Hogg JC, Wright JL, Wiggs BR. Lung Structure and Function in Cigarette Smokers. Thorax 1994;49:473-478.

51. Gelb AF, Hogg JC, Muller NL, Schein MJ, Kuei J, Tashkin DP, Epstein JD, Kollin J, Green RH, Hadjiaghai L. Contribution of Emphysema and Small Airways in COPD. CHEST 1996;109(2):353-359.
52. Brenner DJ, Elliston CD. Estimated Radiation Risks Potentially Associated with Full-Body CT Screening. Radiology 2004;10:735-739.
53. Vestbo J, Anderson W, Coxson HO, Crim C, Dawber F, Edwards L, Hagan G, Knobil K, Lomas DA, MacNee W, Silverman EK, Tal-Singer R. Evaluation of COPD Longitudinally to Identify Predictive Surrogate End-points (ECLIPSE). Eur Respir J 2008;31(4):869-873.
54. Zaporozhan J, Ley S, Weinheimer O, Eberhardt R, Tsakiris I, Noshi Y, Herth F, Kauczor HU. Multi-detector CT of the chest: influence of dose onto quantitative evaluation of severe emphysema: a simulation study. J Comput Assist Tomogr 2006;30(3):460-468.
55. Mettler FA, Guiberteau MJ. Essentials of Nuclear Medicine Imaging: Elsevier/Saunders; 2012.
56. Sanchez-Crespo A, Petersson J, Nyren S, Mure M, Glenny RW, Thorell JO, Jacobsson H, Lindahl SG, Larsson SA. A Novel Quantitative Dual-Isotope Method for Simultaneous Ventilation and Perfusion Lung SPET. . European Journal of Nuclear Medicine 2002;29(7):863-875.
57. Bankier AA, De Maertelaer V, Keyzer C, Gevenois PA. Pulmonary Emphysema: Subjective Visual Grading versus Objective Quantification with Macroscopic Morphometry and Thin-Section CT Densitometry1. Radiology 1999;211(3):851-858.
58. Nomori H, Watanabe K, Ohtsuka T, Naruke T, Suemasu K, Uno K. Evaluation of F-18 fluorodeoxyglucose (FDG) PET scanning for pulmonary nodules less than 3 cm in diameter, with special reference to the CT images. Lung cancer 2004;45(1):19-27.
59. Rajaram S, Swift AJ, Telfer A, Hurdman J, Marshall H, Lorenz E, Capener D, Davies C, Hill C, Elliot C. 3D contrast-enhanced lung perfusion MRI is an effective screening tool for chronic thromboembolic pulmonary hypertension: results from the ASPIRE Registry. Thorax 2013;68(7):677-678.
60. McFadden RG, Carr TJ, Wood TE. Proton Magnetic Resonance Imaging to Stage Activity of Interstitial Lung Disease. . CHEST 1987;92:31-39.
61. Vaninbroukx J, Bosmans H, Sunaert S, Demedts M, Delcroix M, Marchal G, Verschakelen J. The Use of ECG and Respiratory Triggering to Improve the Sensitivity of Oxygen-Enhance Proton MRI of Lung Ventilation. European Radiology 2003;13:1260-1265.
62. Lenz GW, Haacke EM, White RD. Retrospective cardiac gating: a review of technical aspects and future directions. Magnetic resonance imaging 1989;7(5):445-455.
63. Ehman RL, McNamara MT, Pallack M, Hricak H, Higgins CB. Magnetic resonance imaging with respiratory gating: techniques and advantages. American Journal of Roentgenology 1984;143(6):1175-1182.
64. Bergin CJ, Glovver GH, Pauly HM. Lung Parenchyma: Magnetic Susceptibility in MR Imaging. Radiology 1991;180:845-849.

65. Heidemann RM, Özsarlak Ö, Parizel PM, Michiels J, Kiefer B, Jellus V, Müller M, Breuer F, Blaimer M, Griswold MA, Jakob PM. A Brief Review of Parallel Magnetic Resonance Imaging. European Radiology 2003;13(10):2323-2337.
66. Jakob PM, Wang T, Schultz G, Hebestreit H, Hebestreit A, Hahn D. Assessment of Human Pulmonary Function using Oxygen-Enhanced T1 Imaging in Patients with Cystic Fibrosis. Magnetic Resonance in Medicine 2004;51(5):1009-1016.
67. Eichinger M, Puderbach M, Fink C, Gahr J, Ley S, Plathow C, Tuengerthal S, Zuna I, Müller F, Kauczor H. Contrast-Enhanced 3D MRI of Lung Perfusion in Children with Cystic Fibrosis—Initial Results European Radiology 2006;16(10):2147-2152.
68. Ley-Zaporozhan J, Ley S, Eberhardt R, Kauczor H, Heussel CP. Visualization of morphological parenchymal changes in emphysema: Comparison of different MRI sequences to 3D-HRCT Eur J Radiol 2010;73(1):43-49.
69. Failo R, Wielopolski PA, Tiddens HAWM, Hop WCJ, Mucelli RP, Lequin MH. Lung Morphology Assessment Using MRI: A Robust Ultra-Short TR/TE 2D Steady State Free Precession Sequence Used in Cystic Fibrosis Patients. Magnetic Resonance in Medicine 2009;61(2):299-306.
70. Rajaram S, Swift AJ, Capener D, Telfer A, Davies C, Hill C, Condliffe R, Elliot C, Hurdman J, Kiely DG. Lung morphology assessment with balanced steady-state free precession MR imaging compared with CT. Radiology 2012;263(2):569-577.
71. van Beek EJR, Wild JM. Hyperpolarized 3-Helium Magnetic Resonance Imaging to Probe Lung Function. American Thoracic Society 2005;2:528-532.
72. Kauczor HU, Chen XJ, van Beek EJR, Schreiber WG. Pulmonary Ventilation Imaged by Magnetic Resonance: at the Doorstep of Clinical Application. European Respiratory Journal 2001;17:1008-1023.
73. Salerno M, Altes TA, Brookeman JR, de Lange EE, Mugler III JP. Dynamic Spiral MRI of Pulmonary Gas Flow Using Hyperpolarized 3He: Preliminary Studies in Healthy and Diseased Lungs. Magnetic Resonance in Medicine 2001;46:667-677.
74. Albert M, Cates G, Driehuys B, Happer W, Saam B, Springer C, Wishnia A. Biological magnetic resonance imaging using laser-polarized 129Xe. 1994.
75. Salerno M, de Lange EE, Altes TA, Truwit JD, Brookeman JR, Mugler JP, 3rd. Emphysema: hyperpolarized helium 3 diffusion MR imaging of the lungs compared with spirometric indexes--initial experience. Radiology 2002;222(1):252-260.
76. Mentore K, Froh DK, de Lange EE, Brookeman JR, Paget-Brown AO, Altes TA. Hyperpolarized HHe 3 MRI of the lung in cystic fibrosis: assessment at baseline and after bronchodilator and airway clearance treatment. Acad Radiol 2005;12(11):1423-1429.
77. Marshall H, Deppe MH, Parra-Robles J, Hillis S, Billings CG, Rajaram S, Swift A, Miller SR, Watson JH, Wolber J, Lipson DA, Lawson R, Wild JM. Direct visualisation of collateral ventilation in COPD with hyperpolarised gas MRI. Thorax 2012;67(7):613-617.

78. Ebert M, Grossmann T, Heil W, Otten WE, Surkau R, Leduc M, Bachert P, Knopp MV, Schad LR, Thelen M. Nuclear magnetic resonance imaging with hyperpolarised helium-3. Lancet 1996;347(9011):1297-1299.
79. van Beek EJR, Wild JM, Kauczor HU, Schreiber W, Mugler JP, de Lange EE. Functional MRI of the lung using hyperpolarized 3-helium gas. Journal of Magnetic Resonance Imaging 2004;20(4):540-554.
80. Swift AJ, Wild JM, Fichele S, Woodhouse N, Fleming S, Waterhouse J, Lawson RA, Paley MNJ, Van Beek EJR. Emphysematous changes and normal variation in smokers and COPD patients using diffusion He-3 MRI. European Journal of Radiology 2005;54(3):352-358.
81. Ireland RH, Bragg CM, McJury M, Woodhouse N, Fichele S, van Beek EJ, Wild JM, Hatton MQ. Feasibility of image registration and intensity-modulated radiotherapy planning with hyperpolarized helium-3 magnetic resonance imaging for non-small-cell lung cancer. Int J Radiat Oncol Biol Phys 2007;68(1):273-281.
82. Lutey BA, Lefrak SS, Woods JC, Tanoli T, Quirk JD, Bashir A, Yablonskiy DA, Conradi MS, Bartel ST, Pilgram TK, Cooper JD, Gierada DS. Hyperpolarized 3He MR imaging: physiologic monitoring observations and safety considerations in 100 consecutive subjects. Radiology 2008;248(2):655-661.
83. Woodhouse N, Wild JM, van Beek EJR, Hoggard N, Barker N, Taylor CJ. Assessment of Hyperpolarized He-3 Lung MRI for Regional Evaluation of Interventional Therapy: A Pilot Study in Pediatric Cystic Fibrosis. Journal of Magnetic Resonance Imaging 2009;30(5):981-988.
84. Kirby M, Mathew L, Heydarian M, Etemad-Rezai R, McCormack DG, Parraga G. Chronic obstructive pulmonary disease: quantification of bronchodilator effects by using hyperpolarized (3)He MR imaging. Radiology 2011;261(1):283-292.
85. Bannier E, Cieslar K, Mosbah K, Aubert F, Duboeuf F, Salhi Z, Gaillard S, Berthezene Y, Cremillieux Y, Reix P. Hyperpolarized 3He MR for Sensitive Imaging of Ventilation Function and Treatment Efficiency in Young Cystic Fibrosis Patients with Normal Lung Function. Radiology 2010;255:225-233.
86. Stewart NJ, Norquay G, Marshall H, Wild JM. Feasibility of high quality lung MRI with naturally-abundant hyperpolarised 129Xe. European Respiratory Journal 2014;44(Suppl 58).
87. Mugler JP, Altes TA. Hyperpolarized 129Xe MRI of the human lung. Journal of Magnetic Resonance Imaging 2013;37(2):313-331.
88. Chen J, He S, Mao H, Sun C, Pan Y. Characterization of polyphenol compounds from the roots and stems of Parthenocissus laetevirens by high‐performance liquid chromatography/tandem mass spectrometry. Rapid Communications in Mass Spectrometry 2009;23(6):737-744.
89. Kaushik SS, Cleveland ZI, Cofer GP, Metz G, Beaver D, Nouls J, Kraft M, Auffermann W, Wolber J, McAdams HP, Driehuys B. Diffusion-Weighted Hyperpolarized (129)Xe MRI in Healthy Volunteers and Subjects With Chronic Obstructive Pulmonary Disease. Magnetic Resonance in Medicine 2011;65(4):1155-1165.

90. Xu X, Norquay G, Parnell SR, Deppe MH, Ajraoui S, Hashoian R, Marshall H, Griffiths PD, Parra-Robles J, Wild JM. Hyperpolarized (129) Xe gas lung MRI-SNR and T(2) (*) comparisons at 1.5 T and 3 T. Magn Reson Med 2012.
91. Altes TA, Mugler JP, Dregely IM. Hyperpolarized xenon-129 ventilation MRI: preliminary results in normal subjects and patients with lung disease. Proc 18th Annual Meeting ISMRM, Stockholm 2010:1
92. Driehuys B, Cofer GP, Pollaro J, Mackel JB, Hedlund LW, Johnson GA. Imaging alveolar-capillary gas transfer using hyperpolarized 129Xe MRI. Proc Natl Acad Sci U S A 2006;103(48):18278-18283.
93. Hwang SC, Lein RD, Morgan DA. Noble gases. Kirk-Othmer Encyclopedia of Chemical Technology 2005.
94. de Lange EE, Mugler III JP, Brookeman JR, Knight-Scott J, Truwit JD, Teates CD, Daniel TM, Bogorad PL, Cates GD. Lung Air Spaces: MR Imaging Evaluation with Hyperpolarized 3He Gas. Radiology 1999;210(851-7).
95. de Lange EE, Altes TA, Patrie JT, Gaare JD, Knake JJ, Mugler III JP, Platts-Mills TA. Evaluation of Asthma with Hyperpolarized Helium-3 MRI. CHEST 2006;130:1055-1060.
96. Fain SB, Korosec FR, Holmes JH, O'Halloran R, Sorkness RL, Grist TM. Functional Lung Imaging using Hyperpolarized Gas MRI. Journal of Magnetic Resonance Imaging 2007;25(5):910-923.
97. Wild JM, Woodhouse N, Paley MNJ, Fichele S, Said Z, Kasuboski L, van Beek EJR. Comparison Between 2D and 3D Gradient-Echo Sequences for MRI of Human Lung Ventilation With Hyperpolarized 3He. Magnetic Resonance in Medicine 2004;52:673-678.
98. Wild JM, Teh K, Woodhouse N, Paley MNJ, Fichele S, de Zanche N, Kasuboski L. Steady-state free precession with hyperpolarized He-3: Experiments and theory. J Magn Reson 2006;183(1):13-24.
99. Miller G, Altes T, Brookeman J, De Lange E, Mugler Iii J. Hyperpolarized 3 He lung ventilation imaging with B 1-inhomogeneity correction in a single breath-hold scan. Magnetic Resonance Materials in Physics, Biology and Medicine 2004;16(5):218-226.
100. Ireland RH, Woodhouse N, Hoggard N, Swinscoe JA, Foran BH, Hatton MQ, Wild JM. An image acquisition and registration strategy for the fusion of hyperpolarized helium-3 MRI and x-ray CT images of the lung. Phys Med Biol 2008;53(21):6055-6063.
101. Woodhouse N, Wild JM, Paley MN, Fichele S, Said Z, Swift AJ, van Beek EJ. Combined helium‐3/proton magnetic resonance imaging measurement of ventilated lung volumes in smokers compared to never‐smokers. Journal of magnetic resonance imaging 2005;21(4):365-369.

102. Janoff S. Quantification of Lung Ventilation and Treatment Effect with Hyperpolarised 3Helium Magnetic Resonance Imaging in Chronic Obstructive Pulmonary Disease and Asthma. 2012:146.
103. Patz S, Hersman FW, Muradian I, Hrovat MI, Ruset IC, Ketel S, Jacobson F, Topulos GP, Hatabu H, Butler AP. Hyperpolarized 129Xe MRI: A Viable Functional Lung Imaging Modality? European Journal of Radiology 2007;64:335-344.
104. Dregely I, Mugler JP, 3rd, Ruset IC, Altes TA, Mata JF, Miller GW, Ketel J, Ketel S, Distelbrink J, Hersman FW, Ruppert K. Hyperpolarized Xenon-129 gas-exchange imaging of lung microstructure: First case studies in subjects with obstructive lung disease. J Magn Reson Imaging 2011;33(5):1052-1062.
105. Mugler JP, 3rd, Driehuys B, Brookeman JR, Cates GD, Berr SS, Bryant RG, Daniel TM, de Lange EE, Downs JH, 3rd, Erickson CJ, Happer W, Hinton DP, Kassel NF, Maier T, Phillips CD, Saam BT, Sauer KL, Wagshul ME. MR imaging and spectroscopy using hyperpolarized 129Xe gas: preliminary human results. Magn Reson Med 1997;37(6):809-815.
106. Kabilan S, Lin CL, Hoffman EA. Characteristics of airflow in a CT-based ovine lung: a numerical study. J Appl Physiol 2007;102(4):1469-1482.
107. Svenningsen S, Kirby M, Starr D, Leary D, Wheatley A, Maksym GN, McCormack DG, Parraga G. Hyperpolarized 3He and 129Xe MRI: Differences in asthma before bronchodilation. Journal of Magnetic Resonance Imaging 2013.
108. Driehuys B, Martinez-Jimenez S, Cleveland ZI, Metz GM, Beaver DM, Nouls JC, Kaushik SS, Firszt R, Willis C, Kelly KT, Wolber J, Kraft M, McAdams HP. Chronic Obstructive Pulmonary Disease: Safety and Tolerability of Hyperpolarized Xe-129 MR Imaging in Healthy Volunteers and Patients. Radiology 2012;262(1):279-289.
109. Shukla Y, Wheatley A, Kirby M, Svenningsen S, Farag A, Santyr GE, Paterson NAM, McCormack DG, Parraga G. Hyperpolarized Xe-129 Magnetic Resonance Imaging: Tolerability in Healthy Volunteers and Subjects with Pulmonary Disease. Academic Radiology 2012;19(8):941-951.
110. Yablonskiy DA, Sukstanskii AL, Leawoods JC, Gierada DS, Bretthorst GL, Lefrak SS, Cooper JD, Conradi MS. Quantitative in vivo assessment of lung microstructure at the alveolar level with hyperpolarized 3He diffusion MRI. Proc Natl Acad Sci U S A 2002;99(5):3111-3116.
111. Pasternak O, Sochen N, Gur Y, Intrator N, Assaf Y. Free water elimination and mapping from diffusion MRI. Magn Reson Med 2009;62(3):717-730.
112. Fain SB, Altes TA, Panth SR, Evans MD, Waters B, Mugler III JP, Korosec FR, Grist TM, Silverman M, Salerno M, Owers-Bradley J. Detection of Age-Dependent Changes in Healthy Adult Lungs With Diffusion-Weighted 3He MRI. Academic Radiology 2005;12:1385-1392.
113. Altes TA, Mata J, de Lange EE, Brookeman JR, Mugler JP, 3rd. Assessment of lung development using hyperpolarized helium-3 diffusion MR imaging. J Magn Reson Imaging 2006;24(6):1277-1283.

114. Woods JC, Choong CK, Yablonskiy DA, Bentley J, Wong J, Pierce JA, Cooper JD, Macklem PT, Conradi MS, Hogg JC. Hyperpolarized 3He Diffusion MRI and Histology in Pulmonary Emphysema. Magnetic Resonance in Medicine 2006;56:1293-1300.
115. Fain SB, Panth SR, Evans MD, Wentland AL, Holmes JH, Korosec FR, O'Brien MJ, Fountaine H, Grist TM. Early Emphysematous Changes in Asymptomatic Smokers: Detection with 3He MR Imaging. Radiology 2006;239(3):875-883.
116. Swift AJ, Wild JM, Fichele S, Woodhouse N, Fleming S, Waterhouse J, Lawson RA, Paley MNJ, Van Beek EJR. Emphysematous Changes and Normal Variation in Smokers and COPD Patients Using Diffusion 3He MRI. European Journal of Radiology 2005;54:352-358.
117. Evans A, McCormack DG, Ouriadov A, Santyr GE, Parraga G. Anatomical Distribution of 3He Apparent Diffusion Coefficients in Severe Chronic Obstructive Pulmonary Disease. . Journal of Magnetic Resonance Imaging 2007;26:1537-1547.
118. Evans A, McCormack DG, Santyr GE, Parraga G. Mapping and Quantifying Hyperpolarized 3He Magnetic Resonance Imaging Apparent Diffusion Coefficient Gradients. J Appl Physiol 2008;105:693-699.
119. Xu X, Parra-Robles J, Ouriadov A, Santyr GE. Mapping of 3He Apparent Diffusion Coefficient Anisotropy at Sub-millisecond Diffusion Times in Healthy and Elastase Instilled Rat Lungs. Proceedings of the International Society for Magnetic Resonance in Medicine 2010.
120. Wang C, Miller GW, Altes TA, de Lange EE, Cates Jr GD, Mugler JPI. Time Dependence of 3He Diffusion in the Human Lung: Measurement in the Long Time Region using Stimulated Echoes. Magnetic Resonance in Medicine 2006;56:296-309.
121. Wang C, Miller GW, Altes TA, de Lange EE, Cates Jr GD, Mata JF, Brookeman JR, Mugler JPI. Extending the Range of Diffusion Times for Regional Measurement of the 3He ADC in Human Lungs. Magnetic Resonance in Medicine 2008;59:673-678.
122. Kaushik SS, Cleveland ZI, Cofer GP, Metz G, Beaver D, Nouls J, Kraft M, Auffermann W, Wolber J, McAdams HP. Diffusion‐weighted hyperpolarized 129Xe MRI in healthy volunteers and subjects with chronic obstructive pulmonary disease. Magnetic Resonance in Medicine 2011;65(4):1154-1165.
123. Flors L, Mugler III JP, Ruppert K, Ruset IC, Hersman FW, Altes TA. Hyperpolarized xenon-129 diffusion MRI of the lungs: a viable alternative to helium-3. 96th Scientific Assembly and Annual Meeting Program, Radiological Society of North America, Chcago 2010:5.
124. Wang C, Mugler III JP, De Lange EE. Measurement of the diffusion of hyperpolarized ^{129}Xe in human lungs over short and long time scales during one breath hold. Proc 18th Annual Meeting ISMRM Stockholm 2010:1.
125. Acosta RH, Blumler P, Agulles-Pedros L, Morbach AE, Schmiedeskamp J, Herweling A, Wolf U, Scholz A, Schreiber WG, Heil W, Thelen M, Spiess HW. Controlling

Diffusion of 3He by Buffer Gases : a Structural Contrast Agent in Lung MRI. Journal of Magnetic Resonance Imaging 2006;24:1291-1297.
126. Deninger AJ, Eberle B, Ebert M, Großmann T, Heil W, Kauczor H-U, Lauer L, Markstaller K, Otten E, Schmiedeskamp J, Schreiber W, Surkau R, Thelen M, Weiler N. Quantification of Regional Intrapulmonary Oxygen Partial Pressure Evolution during Apnea by 3He MRI. Journal of Magnetic Resonance Imaging 1999;141:207-216.
127. Miller GW, Mugler JP, 3rd, Altes TA, Cai J, Mata JF, de Lange EE, Tobias WA, Cates GD, Brookeman JR. A short-breath-hold technique for lung pO2 mapping with 3He MRI. Magn Reson Med 2010;63(1):127-136.
128. Rizi RR, Baumgardner JE, Ishii M, Spector ZZ, Edvinsson JM, Jalali A, Yu J, Itkin M, Lipson DA, Gefter W. Determination of regional VA/Q by hyperpolarized 3He MRI. Magn Reson Med 2004;52(1):65-72.
129. Wild JM, Fichele S, Woodhouse N, Paley MNM, Kasuboski L, van Beek EJE. 3D Volume-Localized pO2 Measurement in the Human Lung with 3He MRI. Magnetic Resonance in Medicine 2005;53:1055-1064.
130. Fischer MC, Spector ZZ, Ishii M, Yu J, Emami K, Itkin M, Rizi R. Single-acquisition sequence for the measurement of oxygen partial pressure by hyperpolarized gas MRI. Magn Reson Med 2004;52(4):766-773.
131. Miller GW, Mugler III JP, Altes TA. Motion-corrected pO_2 mapping in human lungs using hyperpolarised Xe-129 MRI. Proc 18th Annual Meeting ISMRM, Stockholm 2010:1.
132. Wild JM, Teh K, Woodhouse N, Ireland RH, Fichele S, van Beek EJ, Paley MN. Single Scan 3D pO2 Mapping with Hyperpolarized ^{3}He MRI Proc Annual Meeting ISMRM 2006:1.
133. Wild JM, Paley MNJ, Kasuboski L, Swift A, Fichele S, Woodhouse N, Griffiths PD, van Beek EJR. Dynamic Radial Projection MRI of Inhaled Hyperpolarized 3He Gas. Magnetic Resonance in Medicine 2003;49:991-997.
134. Fain SB, Gonzalez-Fernandex G, Peterson ET, Evans MD, Sorkness RL, Jarjour NN, Busse WW, Kuhlman JE. Evaluation of Structure-Function Relationships in Asthma Using Multi-Detector CT (MDCT) and Hyperpolarized (HP) He-3 MRI. Academic Radiology 2008;15(6):753-762.
135. Koumellis P, van Beek EJR, Woodhouse N, Fichele S, Swift AJ, Paley MNJ, Hill C, Taylor CJ, Wild JM. Quantitative Analysis of Regional Airways Obstruction Using Dynamic Hyperpolarized 3He MRI—Preliminary Results in Children With Cystic Fibrosis. Journal of Magnetic Resonance Imaging 2005;22:420-426.
136. Donnelly LF, MacFall JR, McAdams HP, Majure JM, Smith J, Frush DP, Bogonad P, Charles HC, Ravin CE. Cystic fibrosis: combined hyperpolarized 3He-enhanced and conventional proton MR imaging in the lung--preliminary observations. Radiology 1999;212(3):885-889.

137. Dupuich D, Berthezène Y, Clouet PL, Stupar V, Canet E, Crémillieux Y. Dynamic 3He imaging for quantification of regional lung ventilation parameters. Magnetic resonance in medicine 2003;50(4):777-783.
138. Koumellis P, van Beek EJ, Woodhouse N, Fichele S, Swift AJ, Paley MN, Hill C, Taylor CJ, Wild JM. Quantitative analysis of regional airways obstruction using dynamic hyperpolarized 3He MRI—preliminary results in children with cystic fibrosis. Journal of Magnetic Resonance Imaging 2005;22(3):420-426.
139. McMahon CJ, Dodd JD, Hill C, Woodhouse N, Wild JM, Fichele S, Gallagher CG, Skehan SJ, van Beek EJR, Masterson JB. Hyperpolarized 3Helium Magnetic Resonance Ventilation Imaging of the Lung in Cystic Fibrosis: Comparison with High Resolution CT and Spirometry. European Radiology 2006;16:2483-2490.
140. Donnelly LF, MacFall JR, McAdams HP, Majure JM, Smith J, Frush DP, Bogonad P, Charles HC, Ravin CE. Cystic Fibrosis: Combined Hyperpolarized 3He-enhanced and Conventional Proton MR Imaging in the Lung-Preliminary Observations. Radiology 1999;212:885-889.
141. van Beek EJR, Hill C, Woodhouse N, Fichele S, Fleming S, Howe B, Bott S, Wild JM, Taylor CJ. Assessment of Lung Disease in Children with Cystic Fibrosis using Hyperpolarized 3-Helium MRI: Comparison with Shwachman Score, Chrispin-Norman Score and Spirometry. European Respiratory Journal 2007;17:1018-1024.
142. Mathew L, Kirby M, Eternad-Rezai R, Wheatley A, McCormack DG, Parraga G. Hyperpolarized 3He Magnetic Resonance Imaging: Preliminary Evaluation of Phenotyping Potential in Chronic Obstructive Pulmonary Disease. European Journal of Radiology 2009;doi: 10.1016.
143. Mathew L, Evans A, Ouriadov A, Etemad-Rezai R, Fogel R, Santyr G, McCormack DG, Parraga G. Hyperpolarized 3He Magnetic Resonance Imaging of Chronic Obstructive Pulmonary Disease: Reproducibility at 3.0 Tesla. Academic Radiology 2008;15:1298-1301.
144. Isabel D, Kai R, Talissa AA, Iulian CR, John PM, William FH. Lung Function Imaging With Hyperpolarized Xenon MRI In Asthmatics. A29 NOVEL INSIGHTS INTO LUNG MECHANICS IN HEALTH AND DISEASE, American Thoracic Society International Conference Abstracts: American Thoracic Society. p A1265-A1265.
145. Al-Githmi I, Batawil N, Shigemura N, Hsin M, Lee TW, He GW, Yima A. Bronchiolitis Obliterans Follwing Lung Transplantation. European Journal of Cardio-thoracic Surgery 2006;30:846-852.
146. Boehler A, Kesten S, Weder W, Speich R. Bronchiolitis obliterans after lung transplantation: a review. CHEST 1998;114(5):1411-1426.
147. McAdams HP, Palmer SM, Donnelly LF, Charles HC, Tapson VF, MacFall JR. Hyperpolarized 3He-Enhanced MR Imaging of Lung Transplant Recipien ts: Preliminary Results. American Journal of Radiology 1999;173:955-959.
148. Gast KK, Viallon M, Eberle B, Lill J, Puderbach MU, Hanke AT, Schmiedeskamp J, Kauczor H. MRI in Lung Transplant Recipients Using Hyperpolarized 3He: Comparison With CT. Journal of Magnetic Resonance Imaging 2002;15:268-274.

149. Zaporozhan J, Ley S, Gast K, Schmiedeskamp J, Biedermann A, Eberle B, Kauszor H. Functional Analysis in Single-Lung Transpant Recipients. CHEST 2004;125:173-181.
150. Markstaller K, Kauczor HU, Ruderbach M, Mayer E, Viallon M, Gast K, Weler N, Thelen M, Eberle B. 3He-MRI-based vs. Conventional Determination of Lung Volumes in Patients After Unilateral Lung Transplantation: a New Approach to Regional Spirometry. Acta Anaesthesiol Scand 2002;46:845-852.
151. Bink A, Hanisch G, Darg A, Bogel A, Katsaros K, Mayer E, Gast KK, Kauczor H. Clinical Aspiects of the Apparent Diffusion Coefficient in 3He MRI: Results in Healthy Volunteers and Patients after Lung Transplantation. Journal of Magnetic Resonance Imaging 2007;25:1152-1159.
152. van Beek EJR, Wild JM, Fink C, Moody AR, Kauczor H, Oudkerk M. MRI for the Diagnosis of Pulmonary Embolism. Journal of Magnetic Resonance Imaging 2003;18:627-640.
153. Ruppert K, Mata JF, Brookeman JR, Hagspiel KD, Mugler III JP. Exploring Lung Function with Hyperpolarized 129Xe Nuclear Magnetic Resonance. Magnetic Resonance in Medicine 2004;51(4):676-687.
154. Sakai K, Bilek AM, Oteiza E, Walsworth RL, Balamore D, Jolesz FA, Albert MS. Temporal dynamics of hyperpolarized Xe-129 resonances in living rats. J Magn Reson Ser B 1996;111(3):300-304.
155. Ruppert K, Brookeman JR, Hagspiel KD, Driehuys B, Mugler JP. NMR of hyperpolarized Xe-129 in the canine chest: spectral dynamics during a breath-hold. Nmr Biomed 2000;13(4):220-228.
156. Wagshul ME, Button TM, Li HF, Liang Z, Springer CS, Zhong K, Wishnia A. In vivo MR imaging and spectroscopy using hyperpolarized 129Xe. Magn Reson Med 1996;36(2):183-191.
157. Patz S, Muradian I, Hrovat MI, Ruset IC, Topulos G, Covrig SD, Frederick E, Hatabu H, Hersman FW, Butler JP. Human pulmonary imaging and spectroscopy with hyperpolarized Xe-129 at 0.2T. Academic Radiology 2008;15(6):713-727.
158. Patz S, Muradyan I, Hrovat MI, Dabaghyan M, Washko GR, Hatabu H, Butler JP. Diffusion of hyperpolarized Xe-129 in the lung: a simplified model of Xe-129 septal uptake and experimental results. New J Phys 2011;13.
159. Ruppert K, Brookeman JR, Hagspiel KD, Mugler JP. Probing lung physiology with xenon polarization transfer contrast (XTC). Magnetic Resonance in Medicine 2000;44(3):349-357.
160. Muradyan I, Butler JP, Dabaghyan M, Hrovat M, Dregely I, Ruset I, Topulos GP, Frederick E, Hatabu H, Hersman WF, Patz S. Single-breath xenon polarization transfer contrast (SB-XTC): implementation and initial results in healthy humans. J Magn Reson Imaging 2013;37(2):457-470.
161. Dregely I, Ruset IC, Mata JF, Ketel J, Ketel S, Distelbrink J, Altes TA, Mugler JP, 3rd, Wilson Miller G, William Hersman F, Ruppert K. Multiple-exchange-time xenon polarization transfer contrast (MXTC) MRI: initial results in animals and healthy volunteers. Magn Reson Med 2012;67(4):943-953.

162. Cleveland ZI, Cofer GP, Metz G, Beaver D, Nouls J, Kaushik SS, Kraft M, Wolber J, Kelly KT, McAdams HP, Driehuys B. Hyperpolarized Xe-129 MR Imaging of Alveolar Gas Uptake in Humans. Plos One 2010;5(8).
163. Mugler JP, Altes TA, Ruset IC, Dregely IM, Mata JF, Miller GW, Ketel S, Ketel J, Hersman FW, Ruppert K. Simultaneous magnetic resonance imaging of ventilation distribution and gas uptake in the human lung using hyperpolarized xenon-129. P Natl Acad Sci USA 2010;107(50):21707-21712.
164. Qing K, Ruppert K, Jiang Y, Mata JF, Miller GW, Shim YM, Wang C, Ruset IC, Hersman FW, Altes TA, Mugler JP, 3rd. Regional mapping of gas uptake by blood and tissue in the human lung using hyperpolarized xenon-129 MRI. J Magn Reson Imaging 2014;39(2):346-359.
165. Edelstein WA, Glover GH, Hardy CJ, Redington RW. The intrinsic signal-to-noise ratio in NMR imaging. Magn Reson Med 1986;3(4):604-618.
166. Hoult DI, Richards RE. The signal-to-noise ratio of the nuclear magnetic resonance experiment. 1976. J Magn Reson 2011;213(2):329-343.
167. Parra-Robles J, Cross AR, Santyr GE. Theoretical signal-to-noise ratio and spatial resolution dependence on the magnetic field strength for hyperpolarized noble gas magnetic resonance imaging of human lungs. Med Phys 2005;32(1):221-229.
168. Salerno M, Brookeman JR, de Lange EE, Mugler JP. Hyperpolarized He-3 lung imaging at 0.5 and 1.5 tesla: A study of susceptibility-induced effects. Magnetic Resonance in Medicine 2005;53(1):212-216.
169. Durand E, Guillot G, Darrasse L, Tastevin G, Nacher PJ, Vignaud A, Vattolo D, Bittoun J. CPMG Measurements and Ultrafast Imaging in Human Lungs With Hyperpolarized Helium-3 at Low Field (0.1 T). Magnetic Resonance in Medicine 2002;47:75-81.
170. Mair RW, Hrovat MI, Patz S, Rosen MS, Ruset IC, Topulos GP, Tsai LL, Butler JP, Hersman FW, Walsworth RL. He-3 lung imaging in an open access, very-low-field human magnetic resonance imaging system. Magnetic Resonance in Medicine 2005;53(4):745-749.
171. Chen XJ, Moller HE, Chawla MS, Cofer GP, Driehuys B, Hedlund LW, MacFall JR, Johnson GA. Spatially resolved measurements of hyperpolarized gas properties in the lung in vivo. Part II: T *(2). Magn Reson Med 1999;42(4):729-737.
172. Deppe MH, Parra-Robles J, Ajraoui S, Parnell SR, Clemence M, Schulte RF, Wild JM. Susceptibility effects in hyperpolarized (3)He lung MRI at 1.5T and 3T. J Magn Reson Imaging 2009;30(2):418-423.
173. Yablonskiy DA, Haacke EM. Theory of NMR signal behavior in magnetically inhomogeneous tissues: The static dephasing regime. Magnetic resonance in medicine 1994;32(6):749-763.
174. Parra-Robles J, Viqueira WD, Xu XJ, Ouriadov A, Santyr GE. Theoretical prediction and experimental measurement of the field dependence of the apparent transverse relaxation of hyperpolarized noble gases in lungs (vol 192, pg 85, 2008). J Magn Reson 2008;195(1):121-121.

175. Bidinosti CP, Choukeife J, Tastevin G, Vignaud A, Nacher PJ. MRI of the Lung Using Hyperpolarized 3He at Very Low Magnetic Field (3mT). MAGMA 2004;16:255-259.
176. Wild JM, Paley MNJ, Viallon M, Schreiber WG, van Beek EJR, Griffiths PD. k-space filtering in 2D gradient-echo breath-hold hyperpolarized He-3 MRI: Spatial resolution and signal-to-noise ratio considerations. Magnetic Resonance in Medicine 2002;47(4):687-695.
177. Dominguez-Viqueira W, Ouriadov A, O'Halloran R, Fain SB, Santyr GE. Signal-to-noise ratio for hyperpolarized (3) He MR imaging of human lungs: A 1.5 T and 3 T comparison. Magn Reson Med 2011.
178. J. P. Mugler I IMD, T. A. Altes1, S. Ketel, I. C. Ruset, J. H. Distelbrink, Y. Chang, J. F. Mata, F. W. Hersman, and K. Ruppert. T2* for Hyperpolarized Xe129 in the Healthy Human Lung at 1.5T and 3T. Proceeding to ISMRM, Hawaii 2009.
179. Deppe MH, Ajraoui S, Marshall H, Wild JM. Lung Inflation State Dominates Over Intrapulmonary PO2 Regarding T2* of 3He in Human Lungs. Proc 18th Annual Meeting ISMRM, Stockholm 2010:2557.
180. Martin H. Deppe SA, Helen Marshall, Jim M. Wild. Lung Inflation State Dominates Over Intrapulmonary PO2 Regarding T2* of 3He in Human Lungs. Proceedings of ISMRM, Stockholm, Sweden 2011.
181. Saam B, Yablonskiy DA, Gierada DS, Conradi MS. Rapid imaging of hyperpolarized gas using EPI. Magn Reson Med 1999;42(3):507-514.
182. Wild JM, Ajraoui S, Deppe MH, Parnell SR, Marshall H, Parra-Robles J, Ireland RH. Synchronous acquisition of hyperpolarised He-3 and H-1 MR images of the lungs - maximising mutual anatomical and functional information. Nmr Biomed 2011;24(2):130-134.
183. De Zanche N, Chhina N, Teh K, Randell C, Pruessmann KP, Wild JM. Asymmetric quadrature split birdcage coil for hyperpolarized 3He lung MRI at 1.5T. Magn Reson Med 2008;60(2):431-438.
184. De Zanche N, Yahya A, Vermeulen FE, Allen PS. Analytical approach to noncircular section birdcage coil design: Verification with a Cassinian oval coil. Magnetic Resonance in Medicine 2005;53(1):201-211.
185. Albert MS, Cates GD, Driehuys B, Happer W, Saam B, Springer CS, Wishnia A. Biological Magnetic-Resonance-Imaging Using Laser Polarized Xe-129. Nature 1994;370(6486):199-201.
186. Ladefoge.J, Andersen AM. Solubility of Xenon-133 at 37 Degree C in Wateer Saline Olive Oil Liquid Paraffin Solutions of Albumin and Blood. Phys Med Biol 1967;12(3):353-&.
187. Chen RYZ, Fan FC, Kim S, Jan KM, Usami S, Chien S. Tissue-Blood Partition-Coefficient for Xenon - Temperature and Hematocrit Dependence. J Appl Physiol 1980;49(2):178-183.
188. Bifone A, Song YQ, Seydoux R, Taylor RE, Goodson BM, Pietrass T, Budinger TF, Navon G, Pines A. NMR of laser-polarized xenon in human blood. P Natl Acad Sci USA 1996;93(23):12932-12936.

189. Reeder SB, McKenzie CA, Pineda AR, Yu H, Shimakawa A, Brau AC, Hargreaves BA, Gold GE, Brittain JH. Water–fat separation with IDEAL gradient-echo imaging. Journal of Magnetic Resonance Imaging 2007;25(3):644-652.
190. Wolber J, Cherubini A, Leach MO, Bifone A. Hyperpolarized Xe-129 NMR as a probe for blood oxygenation (vol 43, pg 491, 2000). Magnetic Resonance in Medicine 2002;47(1):213-213.
191. Leung G, Norquay G, Wild JM. Measuring red blood cell oxygenation in vivo using hyperpolarized 129Xe MR. 2012.
192. Cavanagh J, Fairbrother WJ, Palmer III AG, Skelton NJ. Protein NMR spectroscopy: principles and practice: Academic Press; 1995.
193. Mcconnell HM. Reaction Rates by Nuclear Magnetic Resonance. J Chem Phys 1958;28(3):430-431.
194. Cleveland ZI, Moller HE, Hedlund LW, Nouls JC, Freeman MS, Qi Y, Driehuys B. In Vivo MR Imaging of Pulmonary Perfusion and Gas Exchange in Rats via Continuous Extracorporeal Infusion of Hyperpolarized Xe-129. Plos One 2012;7(2).
195. Imai H, Kimura A, Iguchi S, Hori Y, Masuda S, Fujiwara H. Noninvasive Detection of Pulmonary Tissue Destruction in a Mouse Model of Emphysema Using Hyperpolarized (129)Xe MRS Under Spontaneous Respiration. Magnetic Resonance in Medicine 2010;64(4):929-938.
196. Wakayama T, Narazaki M, Kimura A, Fujiwara H. Hyperpolarized 129Xe phase-selective imaging of mouse lung at 9.4T using a continuous-flow hyperpolarizing system. Magn Reson Med Sci 2008;7(2):65-72.
197. Yablonskiy DA, Haacke EM. Theory of Nmr Signal Behavior in Magnetically Inhomogeneous Tissues - the Static Dephasing Regime. Magnetic Resonance in Medicine 1994;32(6):749-763.
198. Brown RJ. Distribution of Fields from Randomly Placed Dipoles - Free-Precession Signal Decay as Result of Magnetic Grains. Phys Rev 1961;121(5):1379-&.
199. Wolber J, Cherubini A, Dzik-Jurasz AS, Leach MO, Bifone A. Spin-lattice relaxation of laser-polarized xenon in human blood. Proceedings of the National Academy of Sciences 1999;96(7):3664-3669.
200. Millet O, Loria JP, Kroenke CD, Pons M, Palmer AG. The static magnetic field dependence of chemical exchange linebroadening defines the NMR chemical shift time scale. J Am Chem Soc 2000;122(12):2867-2877.
201. Holmes JE, Bydder GM. MR imaging with ultrashort TE (UTE) pulse sequences: Basic principles. Radiography 2005;11:12.
202. Leung G, Norquay G, Schulte RF, Wild JM. Radiofrequency pulse design for the selective excitation of dissolved Xe. Magn Reson Med 2014.
203. Wang Y. Description of parallel imaging in MRI using multiple coils. Magnetic Resonance in Medicine 2000;44(3):495-499.
204. Lee RF, Johnson G, Grossman RI, Stoeckel B, Trampel R, McGuinness G. Advantages of parallel imaging in conjunction with hyperpolarized helium- A new approach to MRI of the lung. Magnetic Resonance in Medicine 2006;55(5):1132-1141.

205. Mansson S, Wolber J, Driehuys B, Wollmer P, Golman K. Characterization of diffusing capacity and perfusion of the rat lung in a lipopolysaccaride disease model using hyperpolarized Xe-129. Magnetic Resonance in Medicine 2003;50(6):1170-1179.
206. Coxson HO, Rogers RM, Whittall KP, D'Yachkova Y, Pare PD, Sciurba FC, Hogg JC. A quantification of the lung surface area in emphysema using computed tomography. Am J Respir Crit Care Med 1999;159(3):851-856.
207. Driehuys B, Hedlund LW. Imaging techniques for small animal models of pulmonary disease: MR microscopy. Toxicologic pathology 2007;35(1):49-58.

Publications and Conference Proceedings

Publications

Xiaojun Xu, General Leung, Graham Norquay, Helen Marshall, Juan Parra-Robles, and Jim M. Wild. T_2^* Measurements of Dissolved-Phase 129Xe in the Human Lungs at 1.5 T and 3 T. In preparation of submission to MRM.

Xiaojun Xu, Martin H Deppe, Nicola DeZanche and Jim M. Wild. An Unshielded Asymmetric Split Insert Quadrature Birdcage Coil for Hyperpolarized ^{129}Xe Lung MRI at 1.5 T. In preparation for submission to MRM.

Xiaojun Xu, Graham Norquay, Steven R. Parnell, Martin H. Deppe, Salma Ajraoui, Ralph Hashoian, Helen Marshall, Paul D. Griffiths, Juan Parra-Robles, Jim M. Wild. Hyperpolarized 129Xe gas lung MRI–SNR and T_2^* comparisons at 1.5 T and 3 T. DOI: 10.1002/mrm.24190 (2012)

Xiaojun Xu, Mathieu, Alexei Ouriadov, Giles E. Santyr. Mapping of ^{3}He apparent diffusion coefficient anisotropy at sub-millisecond diffusion times in an elastase-instilled rat model of emphysema. DOI: 10.1002/mrm.23098 (2011)

Graham Norquay, Steve Parnell, **Xiaojun Xu,** Juan Parra-Robles, Jim M. Wild. Optimized production of hyperpolarized 129 Xe at 2 bars for in vivo lung magnetic resonance imaging. J Appl Phys 2013;113(4):044908-044908-044909.

J. M. Wild, Helen Marshall, **Xiaojun Xu**, Graham Norquay, Steve Parnell, M. Clemence, Paul D.Griffiths, Juan Parra-Robles. Simultaneous Imaging of Lung Structure and Function with Triple-Nuclear Hybrid MR Imaging. Radiology 2013;267(1):251-255.

Juan Parra-Robles, Salma Ajraoui, Helen Marshall, Martin H. Deppe, **Xiaojun Xu**, and Jim M. Wild, "The influence of field strength on the apparent diffusion coefficient of 3He gas in human lungs," Magn Reson Med **67** (2), 322-325 (2012).

Mathieu Boudreau, **Xiaojun Xu,** and Giles E. Santyr, "Measurement of (129) Xe gas apparent diffusion coefficient anisotropy in an elastase-instilled rat model of emphysema," Magn Reson Med (2012).

Juan Parra-Robles, William Dominguez Viqueira, **Xiaojun Xu**, Alexei Ouriadov, Giles E. Santyr. Theoretical prediction and experimental measurement of the field dependence of the apparent transverse relaxation of hyperpolarized noble gases in lungs [J. Magn. Res. 192 (2008) 85–91]

Proceedings

Xiaojun Xu, Graham Norquay, Helen Marshall, Juan Parra-Robles, Jim M. Wild. T_2^* Measurements of Dissolved ^{129}Xe and Simultaneous Gas/Dissolved ^{129}Xe Imaging in the Human Lungs at 1.5 T and 3 T. Proceedings to XeMat 2012 (Dublin, Ireland), 21.

Xiaojun Xu, N. De Zanche, M.H.Deppe, and, Jim M. Wild. An Asymmetric Insert Quadrature Birdcage Coil for HP ^{129}Xe Lung MRI at 1.5 T. Proceedings to XeMat 2012 (Dublin, Ireland), 90.

Xiaojun Xu, Graham Norquay, Steven R. Parnell, Martin H. Deppe, Salma Ajraoui, Ralph

Hashoian, Helen Marshall, Paul D. Griffiths, Juan Parra-Robles, and Jim M. Wild. Hyperpolarized ^{129}Xe Gas Lung MRI—SNR and T_2^* Comparisons at 1.5 T and 3 T. Proceedings to XeMat 2012 (Dublin, Ireland), 91.

Xiaojun Xu, Martin H. Deppe, Nicola De Zanche, and Jim M. Wild. An Asymmetric Insert Quadrature Birdcage Coil for Hyperpolarised ^{129}Xe Lung MRI at 1.5 T. Proceedings to ISMRM 2012 (Melbourne, Australia), 2526.

Xiaojun Xu, Graham Norquay, Helen Marshall, Juan Parra-Robles, and Jim M. Wild. The Effect of Lung Inflation on the T_2^* of ^{129}Xe in the Human Lungs at 1.5 T and 3 T. Proceedings to ISMRM 2012 (Melbourne, Australia), 3987.

Xiaojun Xu, Graham Norquay, Steven R. Parnell, Martin H Deppe, Salma Ajraoui, Ralph Hashoian, Helen Marshall, Paul Griffiths, Juan Parra-Robles, and Jim M. Wild. Hyperpolarised ^{129}Xe gas lung MRI – B_0 field strength comparisons at 1.5 T and 3 T. Proceedings to ISMRM 2012 (Melbourne, Australia), 3989.

Xiaojun Xu, Juan Parra-Robles, Alexei Ouriadov, and Giles E. Santyr. Mapping of ^{3}He Apparent Diffusion Coefficient Anisotropy at Sub-Millisecond Diffusion Times in Sham-Instilled and Elastase-Instilled Rat Lungs. Proceedings to ISMRM 2010 (Stockholm, Sweden), 198.

Xiaojun Xu, Juan Parra-Robles and Giles E. Santyr. Optimization of Apparent Diffusion

Coefficient Measurements for Detection of Emphysema Using Hyperpolarized Noble Gas Magnetic Resonance Imaging (2008, Iowa)

Juan Parra-Robles, Graham Norquay, **Xiaojun Xu,** Helen Marshall, and Jim M Wild. Non-Gaussian ^{129}Xe Diffusion in Human Lungs. Proceedings of the XeMat 2012 (Dublin, Ireland), 7.

Helen Marshall, **Xiaojun Xu**, Graham Norquay, Steve R Parnell, Juan Parra-Robles, and Jim M Wild. Dynamic Radial Imaging of Inhaled ^{129}Xe and ^{3}He. Proceedings to ISMRM 2012 (Melbourne, Australia), 4000.

Juan Parra-Robles, **Xiaojun Xu**, Martin H Deppe, Steven R Parnell, Helen Marshall, and Jim M Wild. Experimental investigation of the non-Gaussian diffusion of ^{129}Xe in human lungs. Proceedings to ISMRM 2012 (Melbourne, Australia), 1856.

Juan Parra-Robles, Martin H Deppe, **Xiaojun Xu**, Helen Marshall, and Jim M Wild. The influence of diffusion time on the measurement of the short-range ^{3}He diffusivity in human lungs. Proceedings to ISMRM 2012 (Melbourne, Australia), 3993.

Martin H. Deppe, **Xiaojun Xu**, Steve R. Parnell, and Jim M. Wild. Imaging of localized inert gas washout rates with ^{3}He MRI. Proceedings to ISMRM 2011 (Montreal, Canada), 910.

Juan Parra-Robles, Steve R. Parnell, Salma Ajraoui, **Xiaojun Xu**, and Jim M. Wild. Finite Element Simulations of Short-Range ^{3}He Diffusion in a Model of Branching Acinar Airways: Implications for In Vivo Lung Morphmetry. Proceedings to ISMRM 2011 (Montreal, Canada), 917.

Juan Parra-Robles, Steve R. Parnell, Salma Ajraoui, **Xiaojun Xu,** and Jim M. Wild. Finite Element Simulations of ^{129}Xe Gas Diffusion in Models of Lung Airways. Proceedings to ISMRM 2011 (Montreal, Canada), 916.

Mathieu Boudreau, **Xiaojun Xu**, William Dominguez-Viqueira, and Giles E. Santyr. Measurement of ^{129}Xe Gas Apparent Diffusion Coefficient Anisotropy in an Elastase-Instilled Rat Model of Emphysema. Proceedings to ISMRM 2011 (Montreal, Canada), 885.

Giles Santyr, Ryan Kraayvanger, **Xiaojun Xu** and W. Dominguez-Viqueira. Measurement of Apparent Long-Range Diffusion of 3He using Pulsed Gradient Spin Echo T2 in the Rat Lung at Low Magnetic Field Strength. Proceedings to ISMRM 2009 (Toronto, Canada), 1424.

Juan Parra-Robles, William Dominguez Viqueira, **Xiaojun Xu**, Alexei Ouriadov and Giles E. Santyr. Theoretical Prediction and Experimental Measurement of the Field Dependence of the Apparent Transverse Relaxation of Hyperpolarized Noble Gases in Lungs (2007, master's)

Juan Parra-Robles, **Xiaojun Xu,** W. Lam, Alexei Ouriadov, D. McCormack, and Giles E. Santyr. Finite Element Modeling and Experimental Validation of Transverse Relaxation and Apparent Diffusion Coefficients of Hyperpolarized Noble Gases in Rodent Lung (2007, undergraduate).

List of Figures